ABSTRACT

BROWN, CAMERON SCOTT. Spectral Cascade-Transport Turbulence Model Development for Two-Phase Flows. (Under the direction of Igor A. Bolotnov.)

Turbulence modeling remains a challenging problem in nuclear reactor applications, particularly for the turbulent multiphase flow conditions in nuclear reactor subchannels. Understanding the fundamental physics of turbulent multiphase flows is crucial for the improvement and further development of multiphase flow models used in reactor operation and safety calculations. Reactor calculations with Reynolds-averaged Navier-Stokes (RANS) approach continue to become viable tools for reactor analysis. The on-going increase in available computational resources allows for turbulence models that are more complex than the traditional two-equation models to become practical choices for nuclear reactor computational fluid dynamic (CFD) and multiphase computational fluid dynamic (M-CFD) simulations. Similarly, increased computational capabilities continue to allow for higher Reynolds numbers and more complex geometries to be evaluated using direct numerical simulation (DNS), thus providing more validation and verification data for turbulence model development. Spectral turbulence models are a promising approach to M-CFD simulations. These models resolve mean flow parameters as well as the turbulent kinetic energy spectrum, reproducing more physical details of the turbulence than traditional two-equation type models. Previously, work performed by other researchers on a spectral cascade-transport model has shown that the model behaves well for single and bubbly two-phase decay of isotropic turbulence, single and two-phase uniform shear flow, and single-phase flow in a channel without resolving the near-wall boundary layer for relatively low Reynolds number. Spectral models are great candidates for multiphase RANS modeling since bubble source terms can be modeled as contributions to specific turbulence scales.

This work focuses on the improvement and further development of the spectral cascade-transport model (SCTM) to become a three-dimensional (3D) turbulence model for use in M-CFD codes. To aid in SCTM development and validation a spectral analysis of single and two-phase bubbly DNS data in different geometries was performed with investigation of the modulation of the turbulent kinetic energy spectrum slope due to the presence of bubbles. A new spectral analysis technique was developed to show that modifications to the energy spectrum slope are due to the

presence of bubble wakes. Spectral analysis results are essential aids in turbulence model development and validation. Further work on the one-dimensional (1D) SCTM formulation was performed to improve model behavior for higher Reynolds number channel flow than previously examined, where the boundary layer close to the solid wall is now resolved and good agreement was achieved between the SCTM and DNS data. The SCTM was then implemented into the 3D M-CFD package NPHASE-CMFD and tested for turbulent single-phase, monodispersed bubbly two-phase, and polydispersed bubbly two-phase flow in various geometries. The SCTM predictions were compared with the k-ε model, experimental data, and DNS data. The objective of the work is to improve and develop the SCTM and subsequently provide the numerical framework for the SCTM to be used in M-CFD predictions of multiphase flow in complex nuclear reactor geometries.

Spectral Cascade-Transport Turbulence Model Development for Two-Phase Flows

by
Cameron Scott Brown

A dissertation submitted to the Graduate Faculty of
North Carolina State University
in partial fulfillment of the
requirements for the Degree of
Doctor of Philosophy

Nuclear Engineering

Raleigh, North Carolina

2017

APPROVED BY:

_____	_____
Prof. Igor A. Bolotnov Committee Chair	Prof. Nam Dinh
_____	_____
Prof. J. Michael Doster	Prof. Hong Luo Minor Representative
_____	
Dr. Dillon R. Shaver Technical Consultant	

DEDICATION

This dissertation is dedicated to my parents.

BIOGRAPHY

The author, Cameron Brown, grew up in the town of Rockwell, NC and moved to Raleigh, NC in August, 2008 to attend North Carolina State University (NCSU) where he completed a Bachelor of Science in Nuclear Engineering in May of 2012. Also in May of 2012, he began work under his graduate advisor Dr. Igor Bolotnov. During his graduate studies he worked on multiple projects pertaining to multiphase turbulence modeling and presented his research at conferences in Oak Ridge, TN; Chicago, IL; Washington, DC; New Orleans, LA; and Dresden, Germany. From January, 2016 to May, 2016 Cameron was an intern at Idaho National Laboratories in Idaho Falls, ID where he worked on uncertainty quantification and sensitivity analysis for coupled physics simulations of nuclear reactor accident scenarios.

In his personal life, Cameron is an avid wakeboarder, snowboarder, and traveler. He also enjoys spending time with his girlfriend, friends and family, boating, cheering for the Carolina Panthers football team, reading, and the outdoors. As an undergraduate student at NCSU Cameron was active in the Wakeboard & Waterski Club and held club officer positions of Secretary, Vice President, and President. He spent many of his evenings as a graduate student wakeboarding at the cable park. To date, he has wakeboarded at 19 cable parks in 8 different U.S. states including a month spent wakeboarding in Texas. He also enjoys traveling to snowboard, particularly at his favorite resorts of Jackson Hole Mountain Resort in Jackson, WY, Grand Targhee Resort in Alta, WY, and Jay Peak Resort in Jay, VT. He intends to continue wakeboarding and snowboarding for many years to come.

ACKNOWLEDGEMENTS

I would like to thank all of those that have helped to make this degree possible through encouragement, guidance, and support. I would like to thank my parents for their continued insight and helpful advice throughout my studies. I would like to thank my girlfriend, Emylee, for her support and positive attitude that helped me so much along the way. I would also like to thank all of the family and friends that have helped so much – even if it was just to grab a quick supper across from campus – your time and conversation is always appreciated. I would like to thank my colleagues in Dr. Bolotnov's research group that always had an open ear for discussion. I would also like to thank Pedram Ghassemi – we have moved through the NCSU undergraduate and graduate Nuclear Engineering programs together as roommates, officemates, and as friends and I look forward to where our professional careers will send us.

I would like to thank Dr. Igor Bolotnov for the direction and mentorship that he has shown me in my time as a graduate student at NCSU. He has pushed me to improve academically and professionally while teaching me to become a productive researcher. I would like to thank Dr. Jun Fang for all of his help and insight, particularly with the spectral analysis of the subchannel geometry, and for being an excellent travel partner to conferences. I would like to thank Dr. Dillon Shaver for all of his help with NPHASE-CMFD and the productive discussions. I would also like to thank Dr. R.T. Lahey for his continued insight into how to improve the spectral cascade-transport model. I would like to thank Dr. Shigeo Hosokawa for providing me with experimental data.

I would like to thank Hermine Kabbendjian for all of her assistance with all matters pertaining to the department and tying up the loose ends of paper work.

I would like to thank my committee members; Dr. J. Michael Doster, Dr. Nam Dinh, and Dr. Hong Luo for their insight into how to improve my research and this dissertation.

I would also like to acknowledge the support from Consortium for Advanced Simulation of Light Water Reactors (http://www.casl.gov), an Energy Innovation Hub (http://www.energy.gov/hubs) for Modeling and Simulation of Nuclear Reactors under U.S. Department of Energy [grant number DE-AC05-00OR22725].

CONTENTS

LIST OF TABLES

LIST OF FIGURES

LIST OF ABBREVIATIONS

1D	One-dimensional
2D	Two-dimensional
3D	Three-dimensional
BIT	Bubble-induced turbulence
CFD	Computational fluid dynamics
CHF	Critical heat flux
CIPS	Crud-induced power shift
CT	Cascade-transport
DNB	Departure from nucleate boiling
DNS	Direct numerical simulation
FFT	Fast Fourier transform
GPU	Graphics processing unit
HRN	High-Reynolds number
HWA	Hot wire anemometry
LDV	Laser Doppler velocimetry
LES	Large eddy simulation
LETOT	Large eddy turnover time
LHS	Left hand side
LOD	Length over diameter
LRN	Low-Reynolds number
M-CFD	Multiphase computational fluid dynamics
PDE	Partial differential equation
PIV	Particle image velocimetry
PWR	Pressurized water reactor
RANS	Reynolds-averaged Navier Stokes
RHS	Right hand side
SAC	Spectral analysis code
SCTM	Spectral cascade-transport model

TKE	Turbulent kinetic energy

LIST OF COMMON SYMBOLS FOR SCTM

D_m	Diffusion in bin-*m*
$E(\kappa)$	Turbulent kinetic energy spectrum function
ε	Turbulent dissipation
ε_m	Turbulent dissipation in bin-*m*
γ_{m_i}	Spectral weighting factor for bin-*m*, bubble size group-*i*
k	Turbulent kinetic energy
k_m	Turbulent kinetic energy in bin-*m*
κ	Wave number
$\bar{\kappa}_m$	Center of wave number bin-*m*
κ_0	Left boundary (smallest) wave number
κ_N	Right boundary (largest) wave number
N	Number of spectral bins
ν	Kinematic viscosity
ν^T	Turbulent viscosity
ν_m^T	Turbulent viscosity in bin-*m*
P_m	Turbulence production in bin-*m*
ϕ_i	Bubble-induced turbulence source term for bubble size group-*i*
Ψ_m	Total bubble-induced turbulence source term for bin-*m*
ρ	Density
T_m	Spectral transfer in bin-*m*
U	Mean velocity
u_τ	Friction velocity
ξ	Spectral resolution
y^+	Non-dimensional wall-distance

1. INTRODUCTION

Understanding the fundamental physics of multiphase flows is imperative in industries such as nuclear and chemical engineering. Safety and thermal-hydraulic analysis of current and future generations of nuclear reactors can benefit extensively from high fidelity predictive capabilities of multiphase flows. Multiphase computational fluid dynamics (M-CFD) approach allows modeling three-dimensional (3D) distributions of gas/liquid volume fractions as well as mean velocities and turbulent parameters in various geometries. In nuclear reactor related geometries, M-CFD models must account for intricate flow scenarios such as flow around spacer grids, mixing vanes, fuel bundles, etc. M-CFD is more difficult than single-phase turbulence modeling since bubble interactions with the liquid turbulence must be modeled to achieve closure [1].

As computational capabilities continue to increase, direct numerical simulation (DNS) is becoming more affordable for representative nuclear geometries [2] while full-scale reactor modeling with Reynolds-averaged Navier-Stokes (RANS) type turbulence models is on the horizon [3-5]. However, multiphase turbulence interactions must be well understood and the physical models of such processes must be validated in reactor relevant geometries and flow scenarios. DNS provides data to quantify bubble interactions with the liquid turbulence for the development of more physically sound closure terms to be used in the most common turbulence models such as k-ε [6] (or k-ω [7], SST [8], etc.), as well as turbulence models that are being developed specifically for multiphase reactor relevant applications [9-11]. DNS also provides results that can be used to assess existing turbulence modeling approaches as well as to develop more physically-based spectral turbulence models. Spectral turbulence models provide more flow statistics than traditional two-equation models (i.e. the turbulent kinetic energy (TKE) spectrum) and are a desirable choice for M-CFD since bubble source terms can be modeled as contributions to specific turbulence scales. In polydispersed flows, the contributions of bubbles of different physical characteristics such as size and velocity can be quantified separately in terms of their contributions to the TKE spectrum.

In this work, the continued development and improvement of the spectral cascade-transport turbulence model (SCTM) to become a 3D turbulence model available for use in M-CFD codes is presented. The one-dimensional (1D) SCTM formulation was improved and validated against DNS data using a software package for the solution of partial differential equations (PDEs).

The SCTM formulation was extended to 3D and the model was implemented into a powerful M-CFD code. Simulations of turbulent single-phase flow, monodispersed bubbly two-phase flow, and polydispersed bubbly two-phase flow were performed using the SCTM turbulence closure option in the M-CFD code. A supplemental spectral analysis of DNS data in different geometries for single and two-phase bubbly flows was performed to provide SCTM numerical validation data and investigate the TKE spectrum in different geometries for bubbly two-phase flows. A new spectral analysis technique was developed to show that modulation of the TKE spectrum slope in bubbly two-phase flows is due solely to the presence of the bubble wakes.

1.1 Literature Survey

System and subchannel analysis codes have difficulty predicting local heat transfer information [3] as well as complex 3D information about coolant mixing, flow, temperature, and pressure distribution in reactor fuel assemblies [12]. All this information is important for improving nuclear reactor thermal-hydraulic analysis and, as a result of the coupled physics, neutronic and material performance considerations as well. M-CFD analysis of nuclear reactor behavior using the Reynolds-averaged Navier-Stokes equations is an area of active research.

RANS models solve the Reynolds-averaged equations for the mean velocity field, rather than the instantaneous velocity field such as in DNS (or large eddy simulation (LES) at large scale), but capture considerably more flow physics than subchannel analysis type models. The following review of literature will show the mathematical basis for RANS turbulence modeling and how current wall-resolved two-equation turbulence models are formulated (§ 1.1.1). Followed by an overview of the turbulent kinetic energy spectrum and spectral RANS models (§ 1.1.1.1) as well as some discussion on the current state-of-the-art for M-CFD with turbulent viscosity closure models for the RANS equations (§ 1.1.1.2). Finally, some literature is presented on the turbulent kinetic energy spectrum in two-phase bubbly flows along with difficulties in obtaining the spectrum in both experimental and numerical domains due to the passage of the bubble over an experimental or numerical probe (§ 1.1.2).

1.1.1 RANS Models

The Reynolds-averaged equations for the mean velocity field are acquired by time averaging the Navier-Stokes equations. The RANS equations are available abundantly in the open literature with differences in notation. Following the notation of Wilcox [13], the Reynolds-averaged equations for mass and momentum, respectively, are:

$$\frac{\partial U_i}{\partial x_i} = 0 \tag{1.1}$$

$$\rho \frac{\partial U_i}{\partial t} + \rho U_j \frac{\partial U_i}{\partial x_j} = -\frac{\partial P}{\partial x} + \frac{\partial}{\partial x_j}\left(2\mu S_{ji} - \rho\overline{u_j' u_i'}\right) \tag{1.2}$$

where [13]:

U_i = mean velocity vector

x_i = position vector

ρ = density

P = pressure

μ = molecular viscosity

S_{ji} = $\frac{1}{2}\left(\frac{\partial U_i}{\partial x_j} + \frac{\partial U_j}{\partial x_i}\right)$ = strain-rate tensor

u_i' = fluctuating velocity

Equations (1.1) and (1.2) are the RANS equations for the mean flow for incompressible, constant-property flow. These equations are analogous to the Navier-Stokes equations for the instantaneous flow field except for the appearance of the $\overline{u_j' u_i'}$ correlation that represents the time-averaged rate of momentum transfer due to turbulence [13]. The $-\rho\overline{u_j' u_i'}$ term is known as the Reynolds-stress tensor denoted by $-\rho\tau_{ij}$. Therefore, τ_{ij} is the specific Reynolds-stress tensor:

$$\tau_{ij} = -\overline{u_j' u_i'} \tag{1.3}$$

The expansion of the symmetric specific Reynolds-stress tensor ($\tau_{ij} = \tau_{ji}$) is shown in Equation (1.4). Upon inspection of Equation (1.4), Reynolds-averaging the Navier-Stokes equations resulted in six additional unknown tensor terms with no further addition of equations. This defines the closure problem of turbulence: examination of Equations (1.1), (1.2), and (1.4) specifies that the unknown terms are the pressure, three components of mean velocity, and the six Reynolds stress terms for a combined total of ten unknowns. However, only the mass conservation (Equation (1.1)) and

momentum conservation for the three velocity components (Equation (1.2)) exists from Reynolds-averaging. Therefore, the system of ten unknowns and four equations has yet to be closed and additional equations are needed to determine the Reynolds stresses.

$$\tau_{ij} = -\begin{bmatrix} \overline{u_1'u_1'} & \overline{u_1'u_2'} & \overline{u_1'u_3'} \\ \overline{u_2'u_1'} & \overline{u_2'u_2'} & \overline{u_2'u_3'} \\ \overline{u_3'u_1'} & \overline{u_3'u_2'} & \overline{u_3'u_3'} \end{bmatrix} \tag{1.4}$$

The RANS equations are closed by the solution of the Reynolds stresses determined by a turbulence model, either through the turbulent viscosity hypothesis or by modelling the Reynolds stress directly [14]. Turbulent viscosity models use the Boussinesq eddy-viscosity approximation to compute the specific Reynolds stress tensor as the product of an eddy viscosity and the mean strain-rate tensor [13] such that:

$$\tau_{ij} = 2\nu_T S_{ij} - \frac{2}{3}k\delta_{ij} \tag{1.5}$$

where *k* is the TKE defined to be one-half of the trace of the specific Reynold-stress tensor:

$$k = \frac{1}{2}\overline{u_i'u_i'} = \frac{1}{2}\left(\overline{u'^2} + \overline{v'^2} + \overline{w'^2}\right) \tag{1.6}$$

where the repeated index of the Reynolds stress tensor term presumes summation. Note that the diagonal components of the specific Reynolds-stress tensor represent the normal stresses while the off-diagonal components represent the shear stresses [14].

Therefore, given the distribution of turbulent viscosity the RANS equations can be closed by substituting in the Boussinesq definition of the specific Reynolds-stress tensor (Equation (1.7)). This is a convenient closure to the RANS equations since the unknown Reynolds stresses can be related directly to mean flow quantities to close the system.

$$\frac{\partial U_i}{\partial t} + U_j\frac{\partial U_i}{\partial x_j} = \frac{\partial}{\partial x_i}\left[\nu_{eff}S_{ji}\right] - \frac{1}{\rho}\frac{\partial}{\partial x_j}\left(P + \frac{2}{3}\rho k\right) \tag{1.7}$$

where

$$\nu_{eff} = \nu + \nu_T \tag{1.8}$$

Finally, under the assumption that the Boussinesq approximation is valid, all that remains to solve the RANS equations for the mean flow parameters is to determine the appropriate distribution of the turbulent viscosity (sometimes referred to as the eddy viscosity or eddy diffusivity). The turbulent viscosity can be written as the product of a velocity u^* and length scale l^* (Equation (1.9)).

Specifications of the velocity and length scale to determine the turbulent viscosity are the historical basis for the development of the multitude of RANS turbulence models in the literature.

$$\nu_T = u^* l^* \tag{1.9}$$

Early considerations of Prandtl [15] defined the distribution of turbulent viscosity in terms of some mixing length based on the geometry of the flow [14]. Such mixing length models are considered algebraic models where the relationship between the turbulent viscosity and mixing length must be identified in advance. More advanced algebraic models include the Cebeci-Smith model [16] and the Baldwin-Lomax model [17]. Turbulence modeling approaches have evolved with the increased computational power to perform numerical simulations (Figure 1.1). Specifically, one-equation and two-equation models have been developed based on the turbulent kinetic energy transport equation. Complete one-equation models (i.e. the turbulence length scale is determined by model equations) have been proposed by Baldwin and Barth [18] as well as Spalart and Allmaras [19]. Two-equation turbulence models are inherently ***complete*** and constitute the most widely used approach to turbulence modeling in practice today. More specifically, the k-ε [6] and k-ω [7] two-equation models are often used in CFD with the k-ε model being the most common and available in most commercial CFD codes [14]. Pope [14] notes that from the two modeled quantities of turbulent kinetic energy (k) and dissipation rate (ε) a length scale $\left(L = k^{3/2}/\varepsilon\right)$, a time scale $(\tau = k/\varepsilon)$, and a quantity of dimension of the turbulent viscosity (k^2/ε) can be formed. Many two-equation type models have been developed that make use of the TKE transport equation with some other second equation involving the turbulence length scale. For example, the k-ω model of Wilcox [7], the k-τ model of Speziale et al. [20], the k-ζ model of Robinson et al. [21], and the k-kτ model of Zeierman and Wolfshtein [22] to name a few found in the literature.

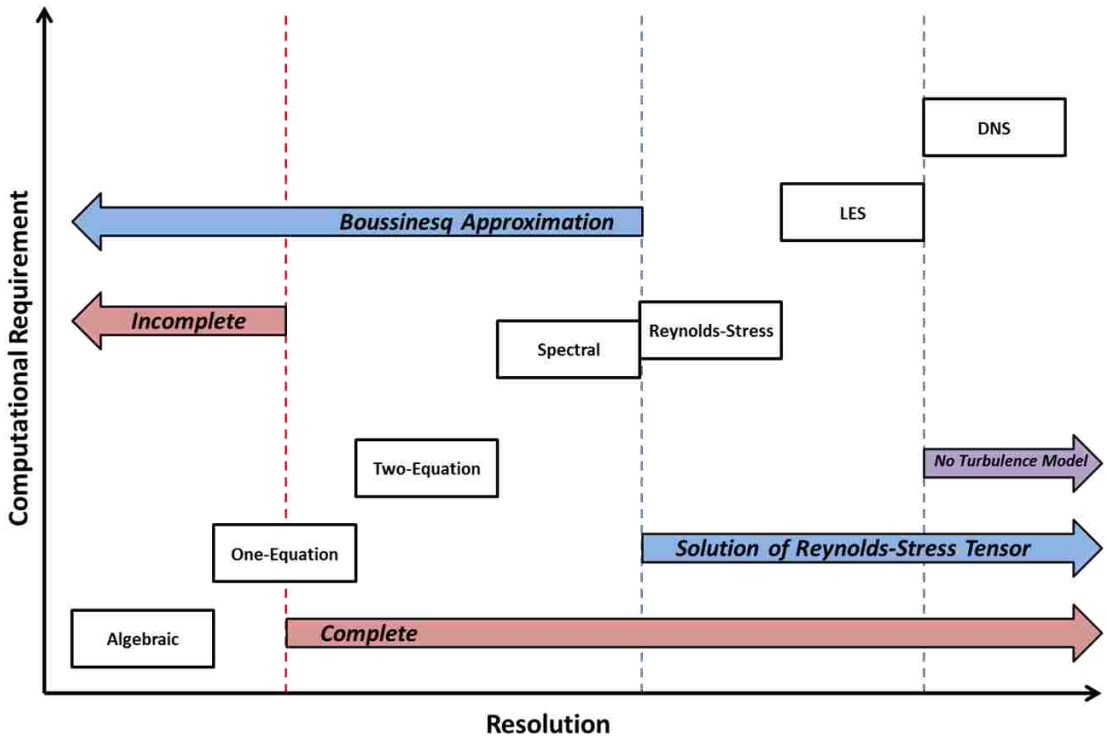

Figure 1.1. Turbulence modeling approaches with increasing computational requirement and resolution. Note that LES still requires a subgrid-scale model that usually employs the Boussinesq approximation.

High-Reynolds number (HRN) turbulence models do not resolve the near-wall turbulent boundary layer and appropriate boundary conditions must be applied to the TKE and turbulent dissipation equations. In most turbulence models for single-phase flow, the logarithmic law of the wall is applied as the boundary condition to define the velocity at some distance from the wall [13]. In general, HRN turbulence models resolve the turbulence down to a dimensionless wall coordinate value (y^+, see Equation (1.14)) of about 30. Low-Reynolds number (LRN) turbulence models resolve the turbulence through the boundary layer all the way to the wall or solid surface of interest. Numerous turbulence models exist for such wall-bounded flows and some examples specific to the k-ε model are those of Jones and Launder [6], Launder and Sharma [23], Lam and Bremhorst [24], and Chien [25]. Wilcox [13] has provided a form of the k-ε equations that are consistent for each of these models such that the only differences arise in model constants and damping functions. The k-ε

equations are shown here as they are given by Wilcox [13] for steady, incompressible boundary layer flows where the *y* direction denotes the direction normal to the solid surface.

$$U\frac{\partial k}{\partial x}+V\frac{\partial k}{\partial y}=\nu_T\left(\frac{\partial U}{\partial y}\right)^2-\varepsilon+\frac{\partial}{\partial y}\left[\left(\nu+\frac{\nu_T}{\sigma_k}\right)\frac{\partial k}{\partial y}\right] \tag{1.10}$$

$$U\frac{\partial \tilde{\varepsilon}}{\partial x}+V\frac{\partial \tilde{\varepsilon}}{\partial y}=C_{\varepsilon 1}f_1\frac{\tilde{\varepsilon}}{k}\nu_T\left(\frac{\partial U}{\partial y}\right)^2-C_{\varepsilon 2}f_2\frac{\tilde{\varepsilon}^2}{k}+E+\frac{\partial}{\partial y}\left[\left(\nu+\frac{\nu_T}{\sigma_\varepsilon}\right)\frac{\partial \varepsilon}{\partial y}\right] \tag{1.11}$$

where dissipation (ε) is related to $\tilde{\varepsilon}$ by:

$$\varepsilon=\varepsilon_o+\tilde{\varepsilon} \tag{1.12}$$

The ε_o term is the value of the dissipation at the wall surface and is defined differently for each of the models. The eddy viscosity formulation is [13]:

$$\nu_T=\frac{C_\mu f_\mu k^2}{\varepsilon} \tag{1.13}$$

thus depending on the modeled *k* and ε to close the RANS system of equations. Note that these models include five empirical damping functions $f_1, f_2, f_\mu, \varepsilon_o,$ and E that depend on the dimensionless parameters [13]:

$$Re_T=\frac{k^2}{\tilde{\varepsilon}\nu},\quad R_y=\frac{k^{1/2}y}{\nu},\quad y^+=\frac{u_\tau y}{\nu} \tag{1.14}$$

For completeness model constants and damping functions for the Chien k-ε model [25] are shown in Equation (1.15).

$$\begin{gathered}f_\mu=1-e^{-0.0115y^+}\\ f_1=1\\ f_2=1-0.22e^{-(Re_T/6)^2}\\ \varepsilon_o=2\nu\frac{k}{y^2}\\ E=-2\nu\frac{\tilde{\varepsilon}}{y^2}e^{-y^+/2}\\ C_{\varepsilon 1}=1.35,\quad C_{\varepsilon 2}=1.80,\quad C_\mu=0.09,\quad \sigma_k=1.0,\quad \sigma_\varepsilon=1.3\end{gathered} \tag{1.15}$$

A few observations should be made concerning the Chien k-ε model in Equations (1.10) – (1.15). First, the right-hand side (RHS) terms in the equation for TKE (Equation (1.10)) are those of turbulent production, turbulent dissipation, and viscous and turbulent diffusion, respectively. Second, the surface boundary conditions are non-intuitive for the empirical dissipation rate transport Equation (1.11). While the no-slip boundary condition at the solid surface indicates that *k*

must vanish at the boundary [13] the value is not so well-defined for the dissipation and some assumption of the dissipation value at the boundary must be made. Third, the near-wall models for *k* and ε are quite empirical and the presence of the solid wall has an effect on the turbulence that must be accounted for through use of damping functions.

1.1.1.1 Spectral RANS Models

Richardson [26] was the first to introduce the energy cascade notion that kinetic energy enters the turbulence due to some production mechanism at the largest scales and is then transferred successively to smaller scales until the energy is removed at the smallest scales due to viscous dissipation [14]. Kolmogorov [27] identified the smallest scales of motion in the flow and the smallest length, time, and velocity scales are justly known as the Kolmogorov scales. Richardson theorized that the turbulence is composed of eddies of various sizes representing some turbulent motion of characteristic length, velocity, and time scales [14]. In terms of the energy cascade, the largest eddies are unstable and break-up, followed by the transfer of energy to smaller eddies. This process is continued to smaller and smaller eddies until the smallest turbulent eddies are removed by viscous effects at the Kolmogorov scales of motion. Therefore, the energy cascade is composed of three distinct regions based on the length scale of the turbulent eddies [14]: the energy containing range where the largest eddies are produced, the inertial subrange where energy is successively transferred to smaller eddies, and the dissipation range where viscous effects dominate. In most turbulence models used for nuclear engineering applications, such as the two-equation models presented in § 1.1.1, the spatial resolution necessary to describe the turbulence is accomplished at the expense of spectral resolution [28]. Spectral models maintain the spatial resolution of turbulence and simultaneously resolve the turbulent kinetic energy spectrum function.

The turbulent kinetic energy spectrum function $E(\kappa)$ in wave number (κ) space is related to the length scale (ℓ) of turbulent motion by Equation (1.16). The relation stipulates that the smallest wave numbers correspond to the largest liquid eddies in the flow. Therefore, as wave number increases the characteristic eddy size decreases and vice versa.

$$\kappa = \frac{2\pi}{\ell} \tag{1.16}$$

Pope [14] indicates that the energy in each wave number range (κ_a, κ_b) can be obtained by integration of the energy spectrum function over the range:

$$k_{(\kappa_a,\kappa_b)} = \int_{\kappa_a}^{\kappa_b} E(\kappa) d\kappa \tag{1.17}$$

While the dissipation rate in homogeneous turbulence in the same range is defined by:

$$\varepsilon_{(\kappa_a,\kappa_b)} = \int_{\kappa_a}^{\kappa_b} 2\nu\kappa^2 E(\kappa) d\kappa \tag{1.18}$$

From Equations (1.17) and (1.18), a general power-law scaling can deduce the slope of the energy spectrum in the inertial subrange and a slope of -5/3 is universally accepted in single-phase flows. Figure 1.2 shows the energy spectrum obtained from DNS of turbulent plane channel flow by Hoyas and Jiminez [29] with some approximate labeling of the energy containing range, inertial subrange, and dissipation range as well as a -5/3 slope. This is a representative spectrum shape for single-phase flows that shows how energy is distributed over the range of eddy sizes in the domain. Note that if Equations (1.17) and (1.18) are integrated over the entire wave number/spectral space (i.e. over all scales from the Kolmogorov length scale to the largest length scale present in the flow) the total turbulent kinetic energy and dissipation rate are obtained.

Spectral RANS turbulence models are formulated on the basis that the interactions between different wave number ranges can be quantified based on mean flow parameters and a turbulent viscosity obtained for closure of Equation (1.7). Spectral models belong to a class of shell models [9, 30] where the turbulent kinetic energy is resolved into a continuous spectrum of scales [28]. Desnyanski and Novikov [31] introduced one of the earliest cascade models where spectral shells are used to model the TKE cascade. In their model, algebraic expressions are used to quantify the transfer of energy between nearest neighboring shells. Following Desnyanski and Novikov, Lewalle and Tavlarides [28] developed the cascade-transport (CT) model and performed calibration and testing with homogeneous uniform shear flow experimental data. In their CT model, energy is exchanged between the nearest modes only, the dissipation term is explicit (without the need for an additional dissipation rate transport equation such as in k-ε type models), and the diffusion and production terms match those in the model TKE equation (Equation (1.10)). Lewalle and Tavlarides [28] used a cumulative spectral eddy viscosity model given by Heisenberg (see Hinze [32]) to formulate the CT model eddy viscosity with a correction factor used outside of the inertial subrange. The CT model achieved good agreement with the experimental results although the authors note that the solution had considerable sensitivity to the form of the turbulent viscosity correction factor.

Lewalle and Tavlarides also note that the added complexity and computation requirements of the CT model are justifiable if multiple length scales are essential to the problem such as in non-equilibrium or two-phase turbulent flows. Note that spectral RANS models provide both spatial and spectral resolution. Therefore, the distribution of turbulent viscosity must be formulated in both spectral and spatial domains to provide the needed closure to the RANS equations.

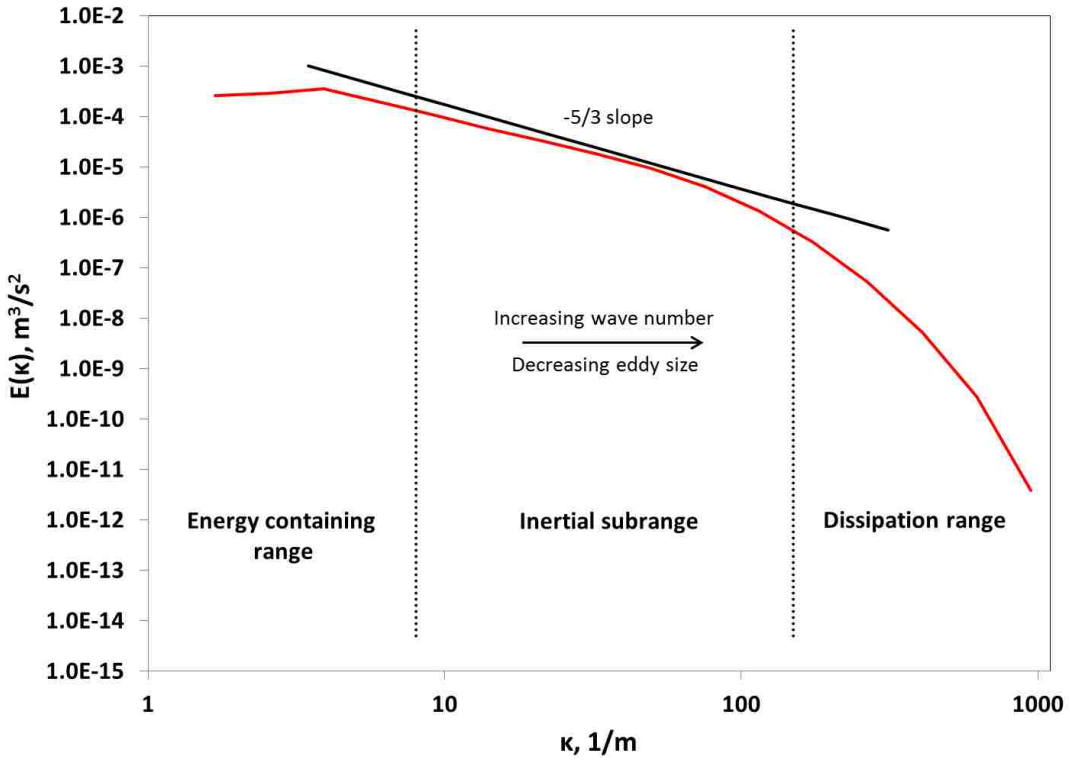

Figure 1.2. Representative energy spectrum. Data from DNS [29] of flat plane channel (Reynolds number based on hydraulic diameter approximately 97,000).

Bolotnov et al. [9-11] have followed the work of Lewalle and Tavlarides [28] to propose the earliest formulations of the spectral cascade-transport model. The SCTM has been developed using a "building block" approach. Specifically, the model has been tested for single-phase and two-phase decay of isotropic turbulence [10], single-phase and two-phase uniform shear flows [9], and single-phase turbulent channel flow without resolving the near-wall boundary layer at a Reynolds number based on friction velocity (Re_τ) of 180 [11]. Each new building block in SCTM development required additional terms to manage the physics in more complex turbulent flows.

1.1.1.2 Multiphase RANS Models

Turbulence modeling for multiphase flow applications must include the effects of additional flow physics to account for the presence of other phases. In nuclear engineering applications, multiphase flow models are essential to improving predictions for a wide range of challenge problems. For example, the prediction of the thermal-hydraulic conditions leading to CRUD formation and ultimately crud-induced power shift (CIPS) [33] or the estimation of critical heat flux (CHF) conditions leading to departure from nucleate boiling (DNB) and fuel rod failure [3]. Although the capabilities to perform DNS of turbulent multiphase flows are advancing a rapid rate [2, 34-38], these simulations are limited to smaller geometries and require considerable computational power. Therefore, M-CFD calculations with RANS approach have emerged as the viable option to improve upon existing 1D subchannel analysis type calculations. M-CFD approach with RANS provides 3D distributions of velocities, gas/liquid volume fractions, as well as turbulent parameters. Current state of the art CFD calculations investigating complex challenge problems for nuclear geometries will benefit tremendously from improved M-CFD turbulence models.

The coupling of averaged Eulerian-Eulerian formulations to RANS turbulence modeling has emerged for use in real-world and system scale calculations [39] as the availability of computational power becomes more prevalent. Lahey [40] has presented a “research roadmap” for the prediction of multiphase flows in nuclear applications to move beyond quasi-multidimensional subchannel models to three-dimensional two-fluid M-CFD models using high quality numerical data from DNS for validation and development. Presently, the literature for nuclear related M-CFD focuses predominately on the modeling of bubbly two-phase flows. In bubbly two-phase flows, there exists a largely continuous liquid fluid with a modest volume fraction of the vapor bubble phase. Lahey [40] presented the four-field, two-fluid (i.e. continuous vapor, continuous liquid, dispersed vapor, and dispersed liquid) conservation equations in addition to the two-phase k-ε model formulation of Lopez de Bertodano et al. [41]. Note that in bubbly flow regimes the conservation equations need only consider the continuous liquid and dispersed vapor fields although the conservation equations can account for other flow regimes of interest such as slug, churn-turbulent, annular, and mist. Rzehak and Krepper [42] state that this two-fluid framework is widely used to model two-phase flows with conservation equations for mass, momentum, and energy of both phases weighted by phasic volume fractions. The exchange of mass, momentum, and energy between the phases are

modeled by interfacial source and sink terms in the conservation equations [42]. There are numerous formulations in the literature for the interfacial momentum exchange terms in the bubbly two-phase flow regime (e.g. drag force, lift force, turbulent dispersion force, wall force, virtual mass force, etc.) as well as models for bubble coalescence and bubble break-up and data from both experiments and DNS continues to improve these closure laws [43-49]. In addition to interfacial closure models, M-CFD using RANS approach requires improved turbulence models that account for the additional flow physics due to the presence of multiple phases.

As recently noted by Colombo and Fairweather [39], the accurate prediction of multiphase turbulence is essential for progress within the M-CFD framework. Many researchers have shown definitively that the presence of bubbles affect the liquid turbulence structure. This can be most easily examined by the modulation of the TKE spectrum due to the presence of bubbles in multiphase flow when compared to single-phase flow. Both experimental results [50-52] and numerical results [53, 54] have found that the slope of the energy spectrum in bubbly two-phase flows differs from the expected -5/3 slope known from Kolmogorov theory. An early approach to account for the presence of bubbles in two-phase bubbly flow was taken by Sato and Sekoguchi [55] who used an analytical approach to split the fluctuations of velocity and pressure in the liquid into those caused by the motion of the bubbles (bubble-induced turbulence or BIT) and those caused by the inherent liquid turbulence independent of the existence of the bubbles. Sato and Sekoguchi [55] developed an additive term for the turbulent viscosity dependent on bubble diameter, void fraction, and the relative velocity of the dispersed vapor phase to the liquid phase to capture the effect of the bubbles on the liquid turbulence. If this method is used without altering a chosen two-equation model it will not provide a direct prediction of TKE and turbulent dissipation [42]. Lee et al. [56] applied a two-phase k-ε model to bubbly flows through use of additional source terms in both the TKE and dissipation equations to account for the effect of the bubbles on the flow. Lopez de Bertodano et al. [41] extended a single-phase k-ε model to a two-phase k-ε model formulation and tested the model for two-phase decay of isotropic turbulence and two-phase bubbly flow in a pipe. Rzehak and Krepper [42] indicate that in addition to BIT terms for either the turbulent viscosity or within a two-equation model it would also be possible to solve separate turbulent transport equations for both the liquid and vapor phases. While this may provide the most physical representation of the problem it also requires more unknown parameters such as phasic interaction

terms and is less applicable at the current time [42]. Therefore, there has been considerable interest in the form of the liquid phase BIT source terms for two-equation RANS modeling.

There exists a substantial number of publications where a various sets of closure relations is compared to a set of multiphase experimental data [57] but almost all use the k-ε, k-ω, or SST turbulence models. In general, BIT source terms can be applied to any turbulence model if dimensional consistency is maintained. There is some discrepancy as to whether consensus has been reached for the BIT source term. Colombo and Fairweather [39] indicate that no generally accepted formulation has emerged while Rzehak et al. [57] indicate that there is general agreement in the literature for the form of the BIT source term in the k-equation. At any rate, it can be agreed that there is no generally accepted form of the BIT source term for the second turbulence model equation (e.g. ε, ω, etc.) due to the need to define a time scale. Rzehak and Krepper [42] compared predictions of the SST turbulence model using BIT source term formulations published by Morel [58], Politano et al. [59], and Troshko and Hassan [60] to results obtained using their own source term as well as to the Sato turbulent viscosity correction for bubbly two-phase flow in a circular pipe. Colombo and Fairweather [39] used a multiphase formulation of the standard k-ε turbulence model [6] and compared the BIT source term predictions of Troshko and Hassan [60], Rzehak and Krepper [42], and a model of their own to bubbly two-phase pipe flow. For each of the aforementioned BIT source term models the k-equation source is expressed as some form of the drag force multiplied by the relative velocity. The only exception is the Morel model [58], which also includes the virtual mass force. Recently, Ma et al. [61] used bubbly two-phase DNS data to develop a new BIT source term based on the drag force, relative velocity, and the bubble Reynolds number. Note that the source terms for the dispersed phase effect on the continuous phase TKE could be implemented into any turbulence model formulation for TKE. For example, Jairazbhoy et al. [62, 63] modeled neutrally buoyant droplets in homogeneous gas turbulence using a two-phase cascade-transport model with an included source term for drop-eddy interactions. Bolotnov et al. [9, 10] added the bubble-induced source term used by Lahey [64] to the spectral cascade-transport model for prediction of two-phase bubbly decay of isotropic turbulence and uniform shear flows.

RANS turbulence modeling of bubbly two-phase flows has, to the author's knowledge, been almost entirely conducted using HRN type two-equation turbulence models where the near-wall boundary layer is not resolved and appropriate boundary conditions must be applied to the TKE and

turbulent dissipation equations. In single-phase flow, the logarithmic law of the wall is well-known and applied as the boundary condition to define the velocity at some distance from the wall [13]. There have been different approaches to the application of boundary conditions in multiphase flows. Politano et al. [59] note that experimental data has shown that the single-phase logarithmic law of the wall is not valid for turbulent two-phase flows. However, some authors have retained the single-phase logarithmic law of the wall as the best estimate for the unknown boundary condition in the modeling of multiphase flows [41, 57]. There have been several attempts to modify the single-phase logarithmic law of the wall to account for the presence of bubbles such as work by Marie et al. [65] and Troshko and Hassan [60, 66]. Politano et al. [59] used a simplified approach to modify the single-phase logarithmic law and demonstrated a good agreement with experimental results. Although, it should be noted that the in their model the height of the gas volume fraction peak was dependent on the first mesh node location close to the wall.

In polydispersed two-phase flow, models must also account for the individual behavior of differently sized bubbles within the flow. Bubbles of distinct size and deformability interact differently with the liquid turbulence. Carrica et al. [67] developed a polydispersed model for bubbly flows. More recently, Krepper et al. [68] have presented the inhomogeneous MUSIG model to distribute bubbles into interacting groups modeled by different velocity fields and appropriate interfacial closure terms. The development of more physically based turbulence closure models should continue to improve predictions of polydispersed bubbly two-phase flow as well as higher void fraction flow regimes encountered in nuclear reactor subchannels. While more complex methods such as Reynolds stress models are a possibility [39], these models also introduce the need to account for anisotropic source terms for the bubble induced turbulence [57]. DNS data has shown that bubbles influence the turbulence anisotropy by improving the isotropy ratios [34]. With the complex challenges of multiphase turbulence modeling considered, spectral turbulence models are excellent candidates to provide better physical representation of multiphase flows. Spectral models allow the contributions from different bubble groups (e.g. bubble groups could be split on bubble size such as in the MUSIG model [68], relative velocity, etc.) to be included as BIT source terms at different turbulence scales.

Lance and Bataille [50] showed experimentally that the bubble-induced turbulence energy exhibits non-linear behavior as void fraction increases. Bolotnov et al. [10] showed that the SCTM

could capture this non-linear behavior when the effect of bubbles is introduced into the correct spectral bin. Simpler two-equation turbulence models are not expected to capture this non-linear behavior [10, 39]. The wall-resolved SCTM is an ideal candidate for polydispersed bubbly two-phase flow predictions since the non-linear influence of bubbles from distinct size groups can be added as TKE source terms at the scales of interest and the turbulence is resolved through the boundary layer to the wall. Modeling the TKE spectrum also provides more statistics for validation with experimental and numerical data. Although the slope of the energy spectrum for multiphase flows is not universally accepted, many authors report a slope close to -3.

1.1.2 Spectral Analysis of the Turbulent Kinetic Energy Spectrum

The spectral analysis of single and multiphase turbulent flows provides not only the turbulent kinetic energy spectrum for validation of spectral turbulence models but is also imperative in developing physically sound closure terms for bubble interactions with the liquid turbulence. The one-dimensional energy spectrum of the velocity fluctuations in the liquid phase is essential in quantifying the bubble/turbulence interactions [69] for development of improved BIT source terms. The one-dimensional energy spectrum of the velocity fluctuations in the frequency domain can be calculated by performing fast Fourier transform (FFT) on the velocity fluctuations in the time domain. Advanced spectral turbulence models such as the SCTM [9-11] have shown that the energy spectrum of multiphase flows can improve turbulence closure terms and provide better predictions of flow characteristics. In single-phase flows, the -5/3 slope of the energy spectrum in the pure inertial subrange is known from Kolmogorov theory. However, the slope of the energy spectrum for multiphase flows is not so well understood and differing values are found in the literature.

Most available data for the evaluation of the slope of the energy spectrum in multiphase flows, both experimental and numerical, exists for purely bubble-induced turbulence. Purely bubble-induced turbulence (pseudo-turbulence) refers to an initially at rest flow that is forced by rising bubbles as the only source of liquid turbulence energy [70]. Lance and Bataille [50] suggested the ratio of bubble-induced kinetic energy to the turbulent kinetic energy in the absence of bubbles as an appropriate parameter to characterize a bubbly flow. Rensen et al. [71] defined this dimensionless quantity as the “bubblance” parameter (*b)* and showed that $b = \infty$ for pure pseudo-turbulence and suggested that the slope of the energy spectrum can be determined from the

bubblance alone. Although the bubblance parameter is useful for characterizing a bubbly flow it has not been successful as the only determinant of the slope of the energy spectrum [69, 72]. Sathe et al. [72] suggested that circulation velocity, bubble size distribution, and lateral variation of mean bubble size in an experimental bubble column greatly affect the energy spectrum.

Experimental techniques such as particle image velocimetry (PIV) and hot wire anemometry (HWA) have been used to evaluate the liquid energy spectrum in pseudo-turbulent bubbly flows. Lance and Bataille [50] found the classical -5/3 power law gradually replaced by a -8/3 slope in the high frequency range as void fraction was increased in bubbly turbulence and these results were reproduced by Wang et al. [1]. Rensen et al. [71] were not able to reproduce these results and instead reported a slope slightly less than -5/3 and attributed their differences to the bubblance parameter. Shawkat et al. [51] experimentally investigated the energy spectrum of air-water flow in a vertical pipe and found slopes ranging from -8/3 to -10/3 dependent on the void fraction. They proposed that the traditional inertial subrange might not be valid for two-phase bubbly flows since there is energy production due to liquid-bubble interactions at the traditional inertial subrange length scales. Bolotnov et al. [10] made similar arguments that bubble contributions to the liquid turbulence occur at length scales on the order of the bubble diameter in their spectral cascade-transport model development. Mercado et al. [73] found a slope of -3.18 for the energy spectrum with no dependency on the void fraction. Mendez-Diaz et al. [52] experimentally analyzed pseudo-turbulent flow for two different bubble sizes and three different viscosity liquids and found a slope close to -3 for all cases. A slope of -5/3 transitioning to -3 at higher wave numbers was reported by Sathe et al. [72].

Numerical experiments are a particularly powerful tool that complement and provide comparisons to experimental results. Sugiyama et al. [74] modeled 800 rising particles as bubbles for pseudo-turbulent flow and also found a -3 slope. Mazzitelli and Lohse [70] simulated 288,000 microbubbles for pseudo-turbulence but did not resolve the bubble wakes. They report a -5/3 slope consistent with their observation that the -3 slope is due to energy deposited by the bubble wake that is then directly dissipated. Roghair et al. [54] reported a slope of -3 in DNS of pseudo-turbulent flow for a converged case with 5% void fraction as well as a -3 slope for a non-fully converged case with 15% void fraction. Riboux et al. [75] also proposed that bubble-induced agitation of the liquid phase mainly results from wake interactions and found a slope of -3. They modeled the bubbles as

fixed momentum sources and reproduced the wake some distance from the bubble to minimize computational cost. Bunner and Tryggvason [53] simulated as many as 216 bubbles with void fractions ranging from 2% to 24% in laminar, low Reynolds number bubbly flow and found a slope of approximately -3.6 for comparisons of different numbers of bubbles as well as different void fractions. Bunner and Tryggvason [53] note that their steeper slope of -3.6 in comparison to Lance and Bataille [50] can be attributed to the very different conditions of the simulations. Santarelli and Froehlich [37, 38] simulated monodispersed bubbly flow and polydispersed bubbly flow with a large and small bubble group for a bulk Reynolds number of 5263. Ma et al. [61] performed spectral analysis of the Santarelli and Froehlich [37, 38] data and found a slope of -3. The increasing capabilities of high performance computing (HPC) continue to expand DNS capabilities by allowing simulations of higher Reynolds numbers, larger domain sizes, and more complex geometries. Bolotnov [34] used a massively parallel code, PHASTA, to fully resolve 60 bubbles in a turbulent flow with a Reynolds number based on friction velocity of 400. Bolotnov et al. [35] also used PHASTA to simulate turbulent single and two-phase bubbly flow in a 200 mm diameter circular pipe. Fang et al. [2] have used the same advanced massively parallel code to simulate turbulent single-phase flow, as well as turbulent bubbly two-phase flow, in reactor subchannel geometry. Analytic considerations have also shown a -3 scaling of the energy spectrum for two-phase bubbly flows (e.g. [10], [50], [76]). Bolotnov et al. [10] derived both -5/3 and -3 slope values in the inertial subrange by assumption of a power-law spectra for the single-phase turbulent kinetic energy spectrum.

Estimating the two-phase energy spectrum has additional challenges since the complexity of two-phase flows results in a time history of mixed velocity signals coming from either the liquid or gas phase. The liquid phase velocity history is discontinuous due to the passage of a bubble over an experimental or numerical probe. There exist several methods of handling the discontinuous liquid velocity signal so that FFT can be applied to calculate the energy spectrum although none of these methods have been shown to be definitive. Ilic et al. [69] compared four different methods of bridging the gap in the liquid velocity signal: (i) the method of Tsuji and Morikawa [77] to replace the defective part of the signal with a linear interpolation, (ii) the method of Gherson and Lykoudis [78] to patch together the successive liquid velocity signal, (iii) the method of Wang et al. [1] to replace the defective parts of the signal with the mean velocity of the liquid phase, and (iv) the method of Panidis and Papailiou [79] to analytically replace the defective part of the signal with

segments having the same statistical properties of the liquid signal. Ilic et al. [69] found the method of replacing the defective parts of the signal with the mean velocity of the liquid phase to be most promising. Shawkat et al. [51] also compared different methods of bridging over the defective parts of the liquid velocity signal and chose to use the linear interpolation method. Mercado et al. [73], Ma et al. [61], and Roghair et al. [54] chose to calculate the energy spectrum using the liquid signal pieces between the passage of bubbles and then average for the energy spectrum. This approach creates issues since the length of each data segment will not be the same. Using data segments of differing lengths required the calculation of a minimum data segment length to be included in the averaging for the energy spectrum. Note that even with a minimum segment length the amount of data will decrease with increasing void fraction and the resolved frequency range will be dissimilar for differing data length segments.

Although pseudo-turbulent flows provide valuable insight into the slope of the energy spectrum in multiphase flows, the conditions of multiphase flow in nuclear reactor subchannels are highly turbulent and M-CFD approach must capture the physics of the multiphase energy spectrum for turbulent conditions. Mercado et al. [73] expressed interest in future investigation of flows where turbulent effects become dominant. Mendez-Diaz et al. [52] recently stated that calculating the energy spectrum in fully turbulent flow could demonstrate whether the spatial inhomogeneity of bubbles or the normal turbulent energy cascade dominates the shape of the energy spectrum.

In addition to highly turbulent flow conditions, single-phase CFD and M-CFD must account for complex geometries within the nuclear reactor core. The presence of spacer grids, mixing vanes, and other structural components within the reactor subchannel geometry combine to create intricate flow scenarios that must be accurately modeled. M-CFD simulations should be validated for these flow situations before being scaled up to reactor conditions. Krepper et al. [80] have examined polydispersed bubbly two-phase flow around an obstacle and expressed the need for more physical bubble breakup and coalescence models. Spectral models based on the bubble/turbulence interactions from high quality numerical data from DNS can improve predictions for such nuclear engineering flow conditions.

2. SPECTRAL ANALYSIS OF DNS

As discussed in § 1.1.2, most existing research efforts pertaining to the slope of the energy spectrum in multiphase flows exists for pseudo-turbulence. However, the increasing availability of multiphase turbulent DNS provides data for the spectral analysis of multiphase turbulent flows. Single and two-phase DNS of fully-developed turbulent flow performed using PHASTA [81-86] in flat plane channel [34], circular pipe [35], and PWR reactor subchannel [2] geometries were spectrally analyzed. Performing a comprehensive spectral analysis of turbulent single and two-phase bubbly flows in different geometries provides high quality data to increase the capabilities of advanced spectral turbulence models such as the SCTM. A comparison of the energy spectra for two-phase bubbly flow in different geometries ensures that the SCTM can be applied to different flow scenarios. Results from spectral analysis can be used for model validation as well as the development of improved BIT source terms. Parameters of interest for the performed DNS are shown in Table 2.1. In the two-phase simulations, PHASTA tracks the liquid/gas interface using a level-set method. The bubbles are monodispersed and retain an essentially spherical shape throughout the simulation time.

2.1 Numerical Method

It is necessary to first provide details on how the PHASTA DNS data (Table 2.1) was recorded. Details about the numerical method and capabilities of the PHASTA code can be found in the literature [2, 34, 48, 81]. During each PHASTA simulation (Figure 2.1), instantaneous flow quantities (i.e. velocity, pressure, etc.) were recorded at specific locations within the computational domain called virtual probes. These virtual probes were placed at planar locations normal to the flow-direction covering different distances from the wall. At each wall distance, virtual probes were also placed in the span-wise direction to increase the statistical sample. For example, Figure 2.2 shows how the virtual probes were arranged for the PWR subchannel simulations performed by Fang et al. [2]. The amount of simulation time considered can be described by the Large Eddy Turn Over Time (LETOT) [87] defined as one-half the hydraulic diameter divided by the friction velocity. Note that DNS is notably expensive to perform, especially for larger bubble counts, unstructured geometries, and higher Reynolds numbers. The Reynolds number for the DNS considered in this

work (Table 2.1) is still rather small in comparison to nuclear reactor conditions although the computational requirement is significant. The inner and outer scale separation for smaller Reynolds numbers limits how well the inertial subrange is resolved. However, the slope of the inertial subrange can still be quantified for the presented Reynolds numbers.

Table 2.1. A summary of the parameters for the spectrally analyzed DNS data [2, 34, 35].

Parameter	**Plane Channel**		**Circular Pipe**			**Subchannel**			
	Single-Phase	**Two-Phase**	**Single-Phase**	**Two-Phase**	**Two-Phase**	**Single-Phase**	**Two-Phase**	**Single-Phase**	**Two-Phase**
Reynolds number based on friction velocity, Re_τ	400	400	1920	1920	1920	400	400	996	996
Reynolds number based on hydraulic diameter	29,079	29,079	77,470	77,470	77,470	29,079	29,079	80,744	80,744
Mesh size, elements	20M	20M	1,900M	240M	1,900M	52M	52M	1,110M	1,110M
Domain length (cm)	6.28	6.28	62.8	62.8	62.8	4.0	4.0	4.0	4.0
Number of bubbles	0	60	0	112	895	0	17	0	262
Void fraction, α	0%	1%	0%	1%	1%	0%	1%	0%	1%
Bubble diameter (wall units), d^+	N/A	81.2	N/A	288	144	N/A	200	N/A	200
Eotvos number, $Eo = \frac{(\rho_l - \rho_g) g d^2}{\sigma}$		0.110		0.560	1.31		0.343		0.250
Morton number, $Mo = \frac{g \mu_l^4 (\rho_l - \rho_g)}{\rho_l^2 \sigma^3}$		1.33×10^{-11}		4.13×10^{-14}	1.25×10^{-12}		5.6×10^{-15}		5.1×10^{-13}
Weber number, $We = \frac{\rho_l u_R^2 d}{\sigma}$		0.367		3.0	4.21		1.68		0.06

Recall that the one-dimensional energy spectrum of the velocity fluctuations in the frequency domain can be calculated by performing fast Fourier transform (FFT) on the velocity fluctuations in the time domain (§ 1.1.2). A spectral analysis code (SAC) was developed as the numerical tool to perform the FFT on the velocity fluctuations in the time domain obtained by PHASTA simulations. The SAC was developed using the Fortran language to read DNS time history data files from the PHASTA code and use the Intel® Math Kernel Library (Intel® MKL) to perform FFT. More details of the SAC are available in Appendix A.

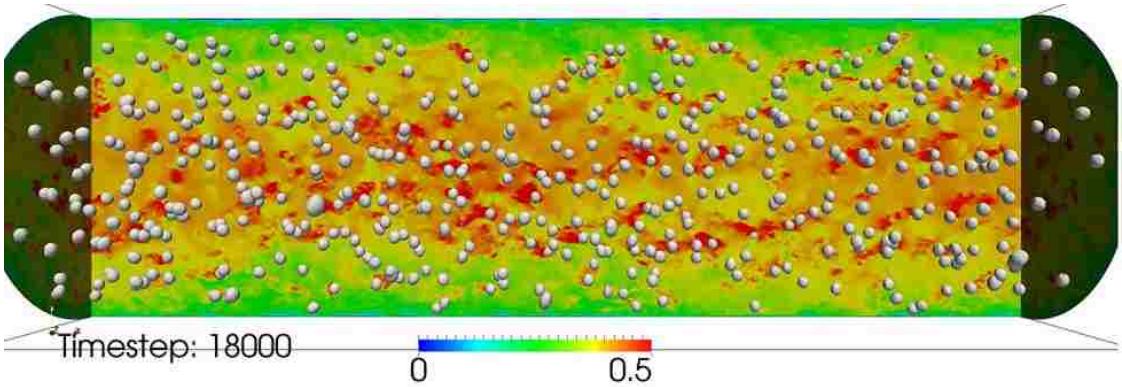

Figure 2.1. Instantaneous velocity distribution of a two-phase circular pipe with 895 bubbles obtained from PHASTA simulation [35].

The recorded instantaneous flow quantities at each time step in a PHASTA simulation results in a discrete time velocity signal characterized by random turbulence induced fluctuations. By applying Reynolds decomposition [14], the instantaneous velocity signal is decomposed into its mean and fluctuating components at each virtual probe location-*i*:

$$u_i(t) = U_i + u_i'(t) \tag{2.1}$$

where u_i is the instantaneous velocity signal (provided by DNS temporal data) and U_i is the mean velocity component calculated by performing the time-average of the instantaneous velocity over the total simulation time T:

$$U_i = \frac{1}{T}\int_t^{t+T} u_i(t')dt' \tag{2.2}$$

The fluctuating velocity component u_i' is then calculated by the SAC for each discrete time in the simulation as the difference in the instantaneous velocity from the mean.

$$u_i'(t) = u_i(t) - U_i \tag{2.3}$$

The velocity fluctuations at each time step are used to compute one half of the single-point velocity correlation (Equation (2.4)) and FFT is then applied, using the Intel® MKL libraries, to calculate the TKE spectrum in the frequency domain using Bartlett's method [88]. In a similar approach to Roghair et al. [54], who averaged the energy spectrum over 27 probes, the energy spectrum was calculated for each of the span-wise virtual probes at a particular distance from the wall and then averaged.

$$R_{ii}(t_j) = u_i'(t_j)u_i'(t_j) \tag{2.4}$$

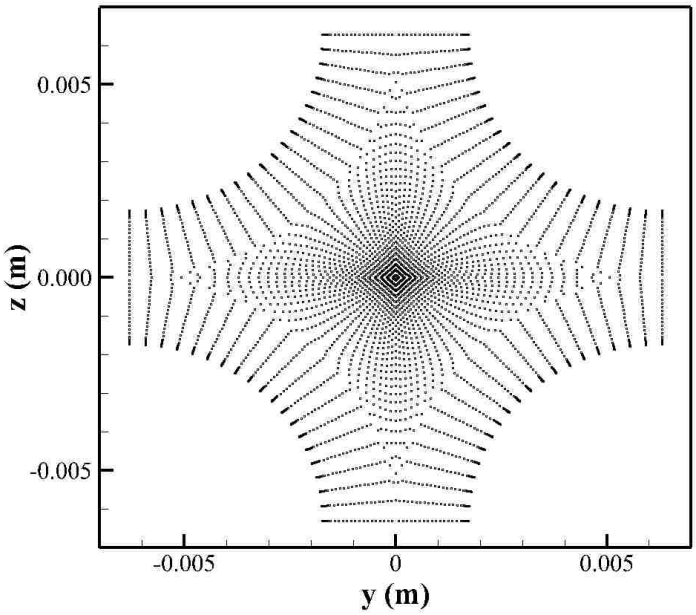

Figure 2.2. Virtual probe locations in the PHASTA simulations performed by Fang et al. [2] of a single PWR reactor subchannel (4.57 mm fuel rod radius, 12.6 mm fuel rod pitch).

For two-phase DNS, the instantaneous velocity signal will be discontinuous due to the passage of a bubble over the virtual probe. The phase indicator function of the level-set method denotes the presence of a bubble at a virtual probe location and thus defines the defective temporal locations of the liquid velocity signal. While numerous methods for bridging the defective portion of the liquid velocity signal exist in the literature (§ 1.1.2), the SAC has been formulated with the capability to either replace the defective portion of the signal with the mean velocity [1], hold the value of the liquid velocity just before the defect [77], or use linear interpolation between the two points of the velocity signal before and after the defect [51, 77]. Figure 2.3 shows fluctuating velocity signals calculated from DNS using the mean insertion, hold value, and linear interpolation methods over a defective portion of the liquid velocity signal defined by a temporal bubble location. Following the findings of Shawkat et al. [51], the linear interpolation technique has been used in the presented research since comparisons with the mean insertion and hold value methods have also shown bias in the spectra at the high frequency range.

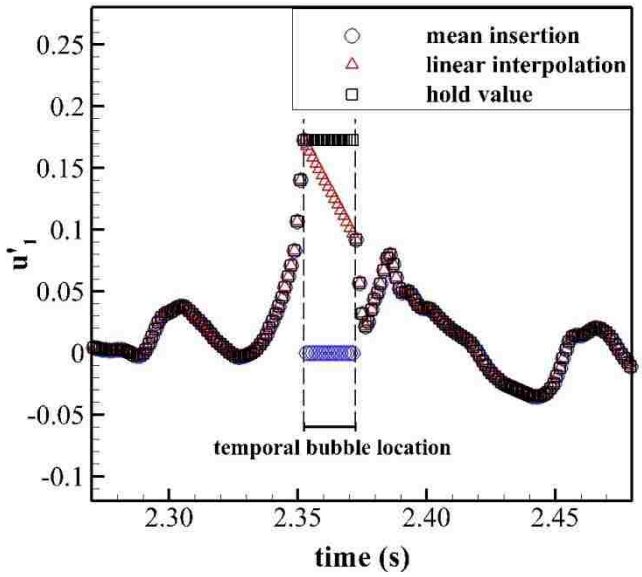

Figure 2.3. The fluctuating velocity signal at a particular span-wise direction for every sixth time step with the defective portions replaced by the mean liquid velocity (blue circles), the value just before the defect (black squares), and a linear interpolation over the defective time (red triangles) for a bubble spanning about 2.35-2.37 seconds.

2.1.1 Pseudo-Void Numerical Experiments

Just as Riboux et al. [75], we believe that bubble effects on the energy spectrum are due to bubble wake interactions with the liquid turbulence. Therefore, pseudo-void numerical experiments were formulated to show that bubble/turbulence interactions change the slope of the energy spectrum only when the bubble wakes are present. Shawkat et al. [51] compared different methods for bridging the gap in the defective two-phase velocity signal by electronically interrupting a single-phase signal with the gas identifier signal from a two-phase signal. Following this approach, pseudo-void simulations were developed where the phase indicator signal from two-phase DNS is overlaid on the velocity signal of single-phase DNS, mimicking the presence of bubbles in the data. The single-phase data is interrupted due to the mimicked gas phase but does not contain the bubble wakes since the velocity signal is not altered outside of the prescribed defective portions. The linear interpolation technique was used to bridge the defective parts of the pseudo-void signal.

Due to the often larger time step in single-phase DNS the temporal bubble location at a numerical probe can be harder to resolve for pseudo-void simulations. For the projection of the

bubble distribution onto the single-phase signal, the single-phase time step can be larger than bubble passage time that was resolved by two-phase DNS in multiple time steps. Therefore, it is important to ensure proper projection of the bubble distribution of the two-phase DNS onto the single-phase data. The “bubble contribution” was developed to measure how well the bubble distribution is reproduced in the pseudo-void simulations, where the bubble contribution is the number of bubbles at a span-wise location normalized by the total bubbles in the simulation.

2.2 Results

2.2.1 Plane Channel

It is necessary to use enough data points in the averaging window when performing FFT to calculate the energy spectrum. Comparisons of the energy spectrum for different numbers of points as integer powers of 2 for the plane channel geometry have shown that using as few as 256 points in the averaging window had minimum deviations from much larger time window widths. The DNS data must be statistically steady-state before being spectrally analyzed and Figure 2.4 shows that the behavior of the single-phase energy spectra is similar for each of the 42 virtual probes in the plane channel case. Similar or better behavior at each of the virtual probes for a particular distance from the wall was observed for all of the cases presented here.

For the two-phase plane channel simulations, 15 averaging windows each with a width of 512 points were used for a total simulation time slightly greater than 4 LETOTs. Figure 2.5 shows the energy spectra for the two-phase plane channel simulations at three different y^+ locations. Note the difference in energy magnitudes since more energy is present in the energy producing region close to the wall. The energy spectra have a slope close to -3 over a frequency range of about 1.5 decades. The flattened profile in the high frequency range is interesting and is due to oversampling the DNS data which causes very high frequency results in the energy spectra at frequencies higher than the Kolmogorov scales of interest. Similar spectral shapes have been shown by Mercado et al. [73] and Roghair et al. [54]. In contrast to the suggestions of Rensen et al. [71], the bubblance was much less than 1 in the turbulent DNS results presented here but the -3 scaling of the slope in the energy spectrum is still observed.

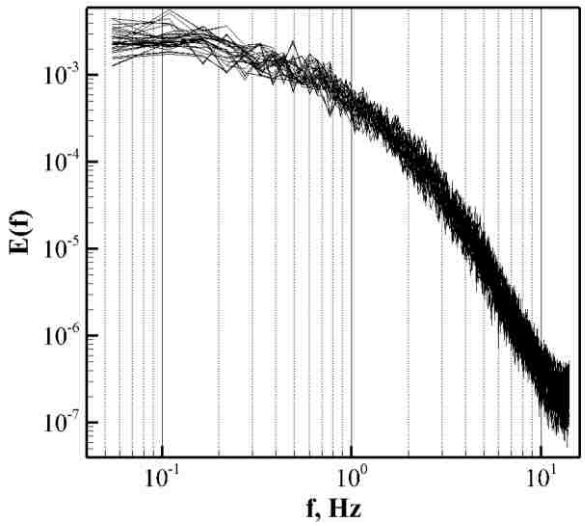

Figure 2.4. The energy spectra for each of the 42 span-wise locations in the single-phase plane channel simulation at $y^+ \approx 15$.

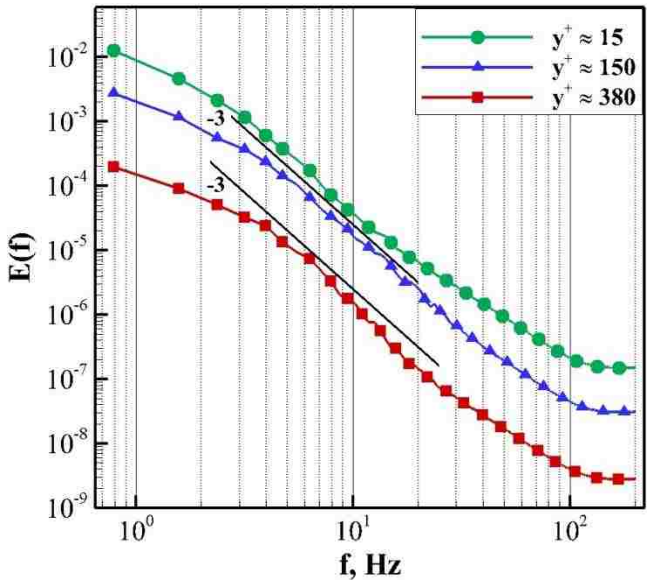

Figure 2.5. Energy spectra for the two-phase plane channel simulations at $y^+ \approx 380$ (red squares), $y^+ \approx 150$ (blue triangles), and $y^+ \approx 15$ (green circles).

Single-phase plane channel simulations were spectrally analyzed with 16 averaging windows each with a width of 512 points for a total simulation time of about 63 LETOTs. The much longer simulation time is a result of the larger time step of the single-phase DNS compared to two-phase

DNS. Therefore, to properly implement the pseudo-void technique the amount of single-phase simulation time used had to be consistent with the overall time of the two-phase record so that bubble locations could be projected onto the single-phase data. Figure 2.6(a) shows how bubbles are distributed at each span-wise location over time at $y^+ \approx 150$ in the two-phase plane channel simulation. A single FFT averaging window with a length of 534 points was used for the pseudo-void spectral analysis so that the time was also about 4 LETOTs. Figure 2.6(b) shows comparisons of bubble contributions at each span-wise location for two-phase and pseudo-void calculations that are in good agreement.

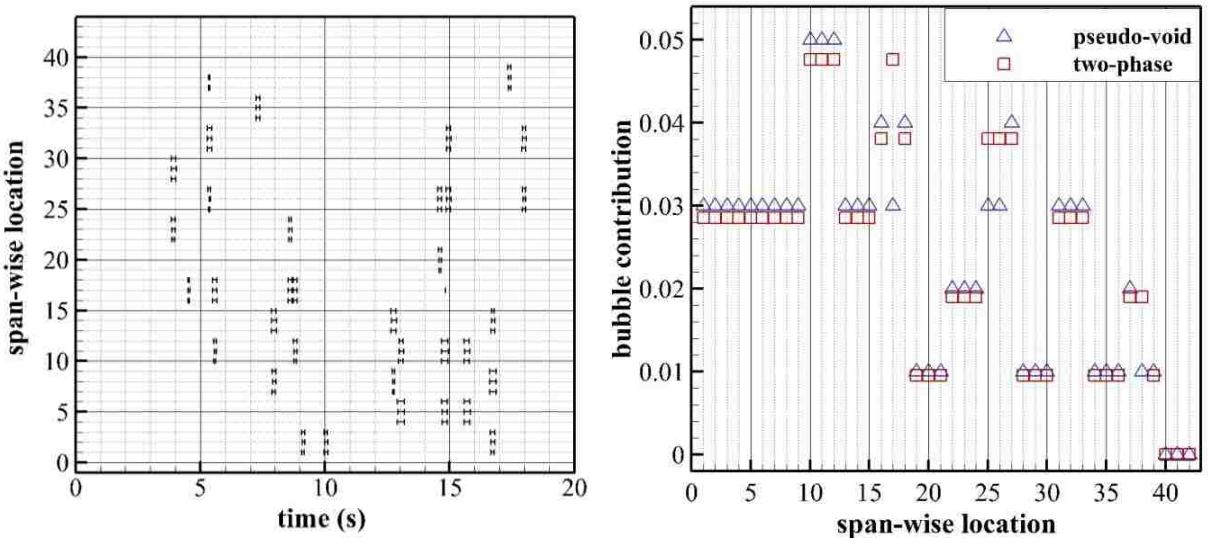

Figure 2.6. (a): Bubble locations (closed-end lines) in time at each of the span-wise virtual probes for the two-phase plane channel case ($y^+ \approx 150$). (b): Bubble contributions from each span-wise location to the overall number of bubbles present in the flow at $y^+ \approx 150$ in the plane channel geometry.

Figure 2.7 shows the single-phase and pseudo-void spectra, as well as a single-phase spectrum for the same time length as the pseudo-void simulation, for three different y^+ locations. The expected -5/3 slope is labeled for each y^+ location and the data is in good agreement although the inertial range is limited at this Reynolds number. The pseudo-void results show no difference from the single-phase data, which demonstrates that the change of the energy spectrum slope in the two-phase simulations is due to bubble wake interactions with the liquid turbulence. The energy

spectra for shorter times (pseudo-void, single-phase with pseudo void time) are not as smooth as the energy spectra for the full single-phase data length since only one FFT averaging window was used.

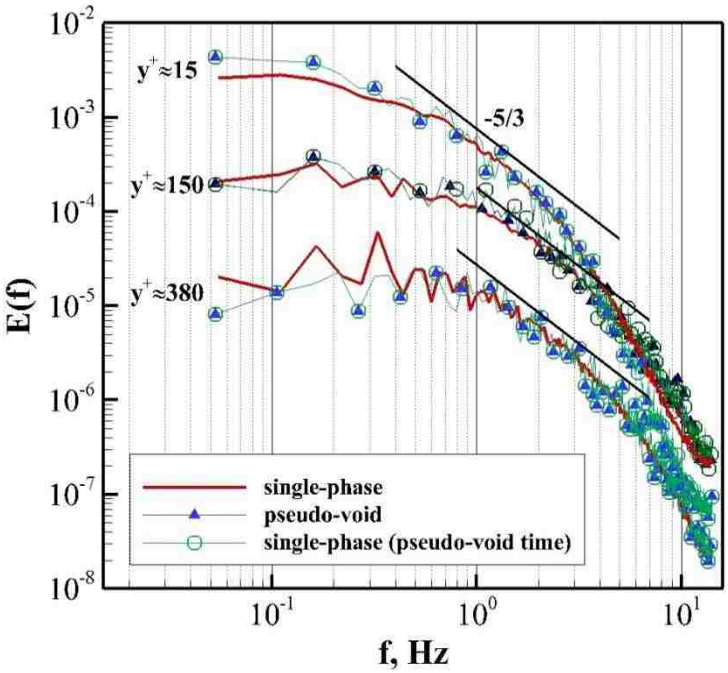

Figure 2.7. Single-phase and pseudo-void energy spectra at $y^+ \approx 380$, $y^+ \approx 150$, and $y^+ \approx 15$ for the plane channel geometry. The full simulation time of about 63 LETOTs is indicated by the thick red line, the pseudo-void simulation is indicated by the triangles, and a single-phase simulation for the same simulation time as the pseudo-void simulation is indicated by the circles.

2.2.2 Circular Pipe

2.2.2.1 One hundred and twelve bubble case

Spectral analysis for the two-phase circular pipe geometry with 112 bubbles was performed with 9 averaging windows of 1024 points each for a total simulation time of about 0.5 LETOT. Due to the much smaller time step of these simulations in comparison to the plane channel geometry more points were required per averaging window. Figure 2.8(a) shows the energy spectra for the two-phase circular pipe simulations at three different y^+ locations. The y^+ locations are formulated such that the pipe centerline value is equal to the Reynolds number based on friction velocity ($Re_\tau = 1920$) and the smaller values represent locations closer to the wall. The two-phase energy spectra in the

circular pipe geometry also exhibit a slope close to -3 over a frequency range of about one decade. The harmonics corresponding to the bubble passage time over the numerical probe are also present in the two-phase spectra. For example, at $y^+ \approx 1620$ a slightly flattened profile is observed at around 40 Hz. Figure 2.8(b) shows a cross-sectional snapshot of the DNS [35] velocity distribution for the circular pipe with 112 bubbles and the wall-peaked void distribution is evident. Similarly, Figure 2.9 shows the velocity distribution as viewed through the pipe and Q-criterion (i.e. $Q = \frac{1}{2}[\Omega^2 - S^2]$ where Ω and S are the vorticity and rate-of-strain tensors, respectively) has been used to visualize the vortical structures induced by the bubbles. The difference in spectra magnitudes is a result of this bubble induced turbulence, as well as the shear induced turbulence, close to the wall. The Q-criterion visualization provides some further illustration into how bubbles interact with the surrounding fluid.

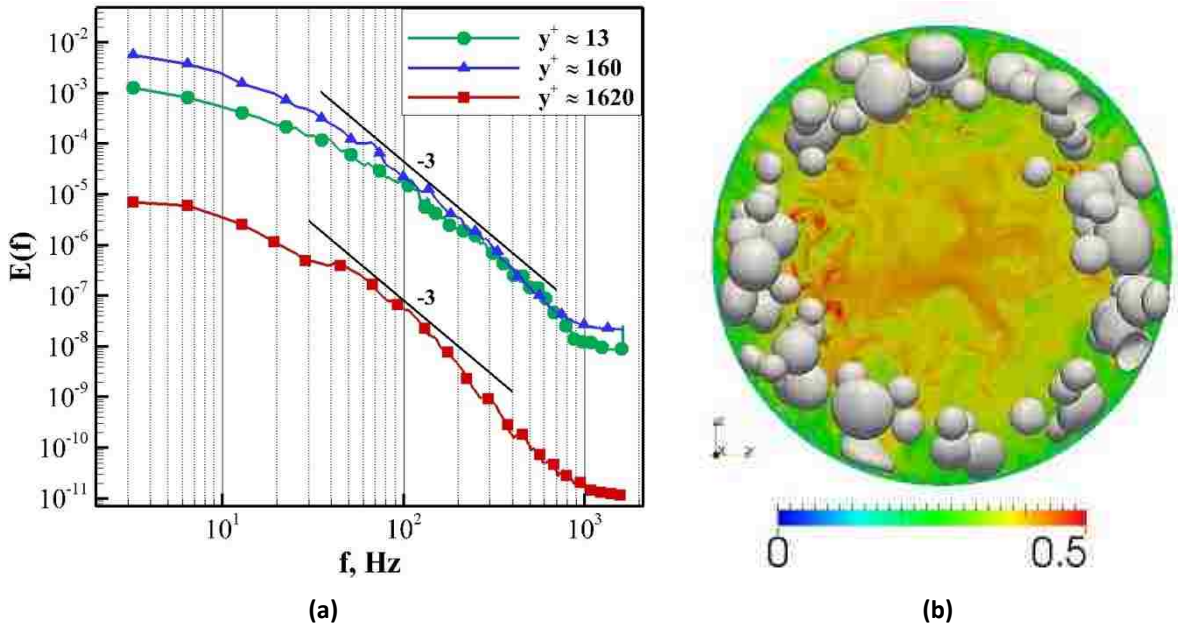

Figure 2.8. (a): Energy spectra for the two-phase circular pipe simulations with 112 bubbles at $y^+ \approx 1620$ (red squares), $y^+ \approx 160$ (blue triangles), and $y^+ \approx 13$ (green circles). (b): Snapshot of the instantaneous velocity distribution for the 112 bubble circular pipe DNS [35].

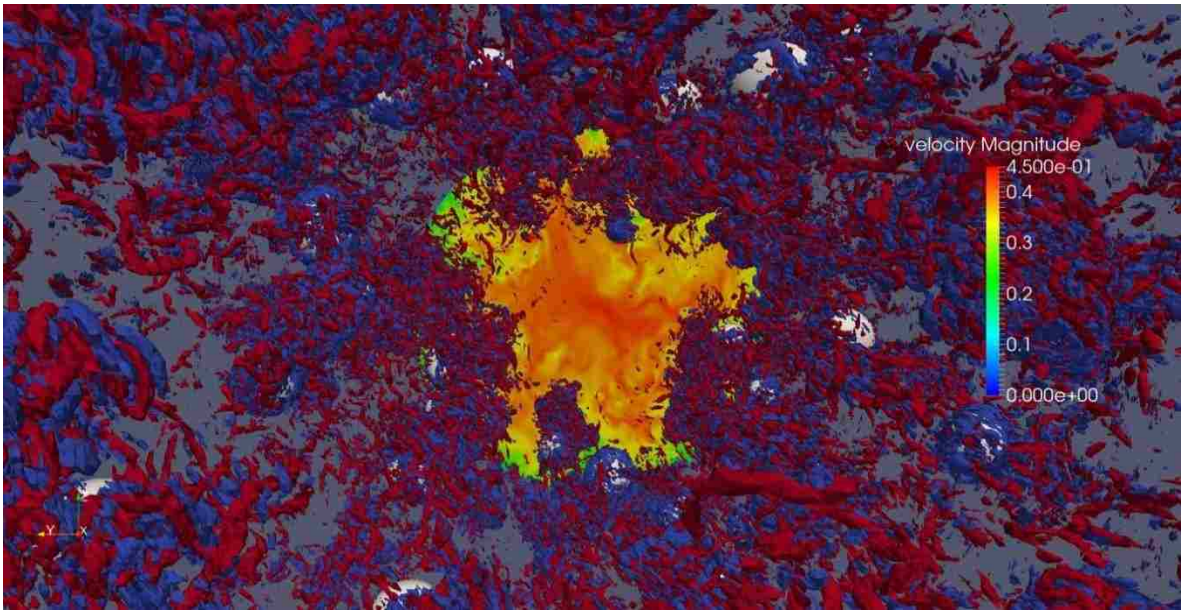

Figure 2.9. The instantaneous velocity distribution for the 112 bubble circular pipe DNS [35] using Q-criterion to visualize the vortical structures (red and blue) induced by the bubbles.

Single-phase and pseudo-void analyses were performed with 9 averaging windows of 1024 points each for a total simulation time of about 0.36 LETOT. Since the time steps were similar for the single-phase and two-phase DNS of the circular pipe the bubble contributions were nearly identical for each span-wise location. In the pipe geometry, span-wise locations are concentric circles of numerical probes that all reside at the same distance from the wall. Figure 2.10 shows the single-phase and pseudo-void energy spectra for the circular pipe geometry and the expected -5/3 slope of the inertial subrange is labeled. The pseudo-void results again show no difference from the single-phase data and demonstrate that the change of the energy spectrum slope in multiphase flows is due to the bubble wake interactions with the liquid turbulence. Note the lower spectrum magnitudes close to the wall for the single-phase simulations (in comparison to two-phase simulations) since the bubble induced vortical structures (Figure 2.9) are absent. A comparison of the fluctuating velocity signal for each of the considered simulations (Figure 2.11) indicates how the turbulence is modulated near the bubble location. In two-phase, the velocity signal is higher in front of the bubble due to the buoyant nature of the rising bubble and high frequency fluctuations are present behind the bubble as the bubble wake. In single-phase versus pseudo-void simulations, the

fluctuating velocity signal is different only across the temporal bubble location where the linear interpolation technique is used to bridge the prescribed discontinuity of the bubble location.

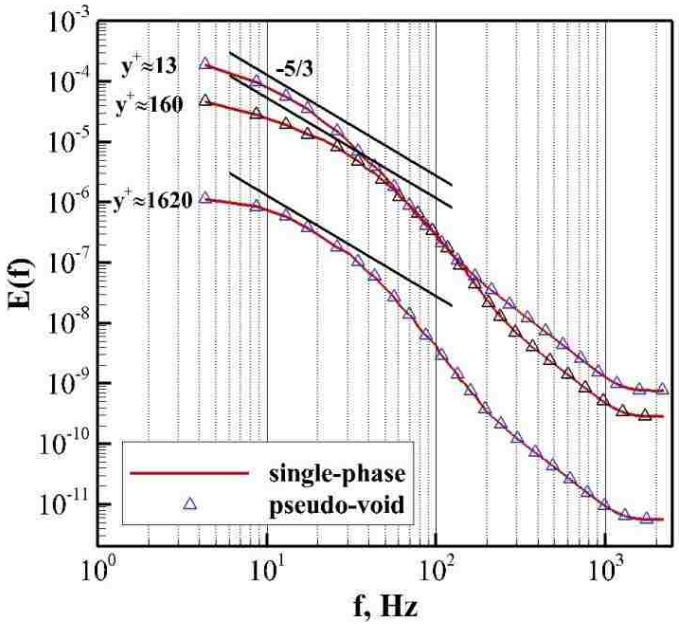

Figure 2.10. Single-phase (solid line) and pseudo-void (triangles) energy spectra for the circular pipe at $y^+ \approx 1620$, $y^+ \approx 160$, and $y^+ \approx 13$.

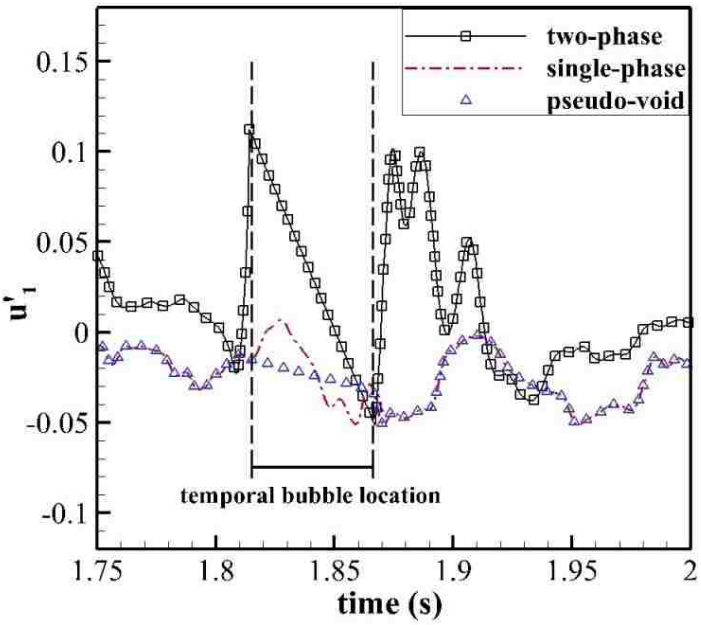

Figure 2.11. Fluctuating velocity signal near a particular bubble location for two-phase (solid black line, squares), single-phase (red dash-dot line), and pseudo-void (blue triangles) DNS.

2.2.2.2 Eight hundred and ninety five bubble case

Two-phase data for the circular pipe geometry with 895 bubbles was spectrally analyzed with 3 averaging windows of 1024 points for a total simulation time of about 0.13 LETOT and results are shown in Figure 2.12. The two-phase data with 895 bubbles indicates a -3 scaling of the energy spectrum for the location closest to the wall and a scaling close to -3 for the other two locations. In this case, the energy spectrum is not higher closer to the wall since the DNS void fraction profile is not wall-peaked (see Figure 2.21(a)) and bubbles present in the center of the pipe induce turbulence as shown by the Q-criterion visualization of the vortical structures induced by the bubbles (Figure 2.13).

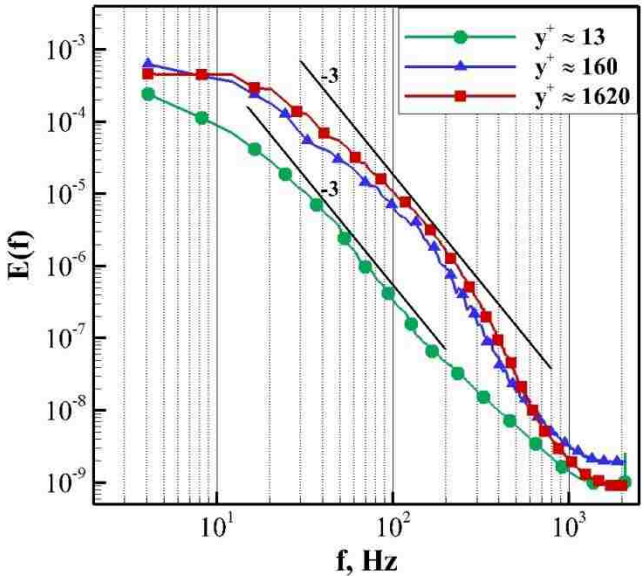

Figure 2.12. Energy spectra for the two-phase circular pipe simulations with 895 bubbles at $y^+ \approx 1620$ (red squares), $y^+ \approx 160$ (blue triangles), and $y^+ \approx 13$ (green circles).

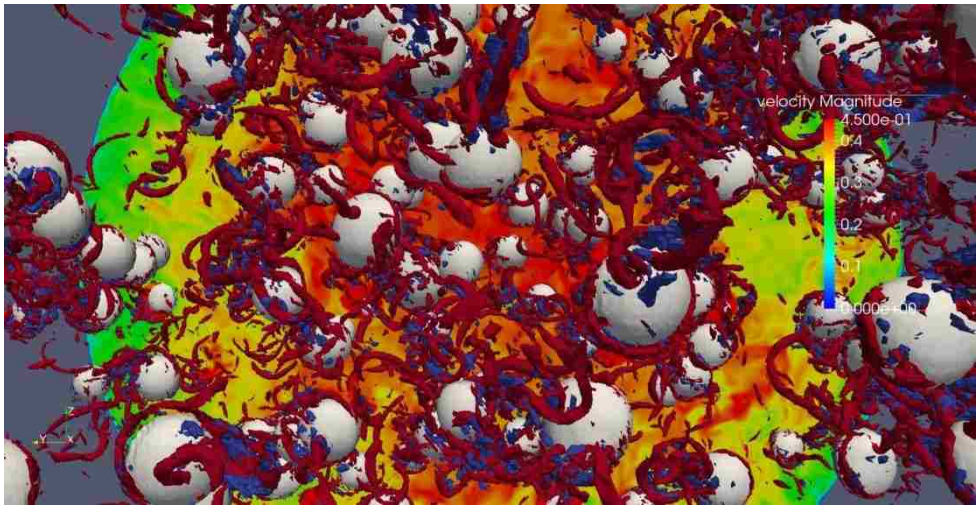

Figure 2.13. The instantaneous velocity distribution for the 895 bubble circular pipe DNS [35] using Q-criterion to visualize the vortical structures (red and blue) induced by the bubbles.

2.2.3 PWR Reactor Subchannel

2.2.3.1 Re_τ = 400

Spectral analysis of the two-phase Re_τ = 400 subchannel was performed using 9 windows of 1024 points for a total data time of about 0.6 LETOT and the results are shown in Figure 2.14(a). A scaling close to -3 is shown for each distance from the wall. The y^+ locations (Figure 2.14(b)) are formulated differently than for traditional channel flow [2] but still represent distance to the wall (the fuel pins in the subchannel case). As with the 895 bubble circular pipe case the spectrum magnitude of the location closest to the wall is not the highest since bubbles present closer to the center of the subchannel induce turbulence.

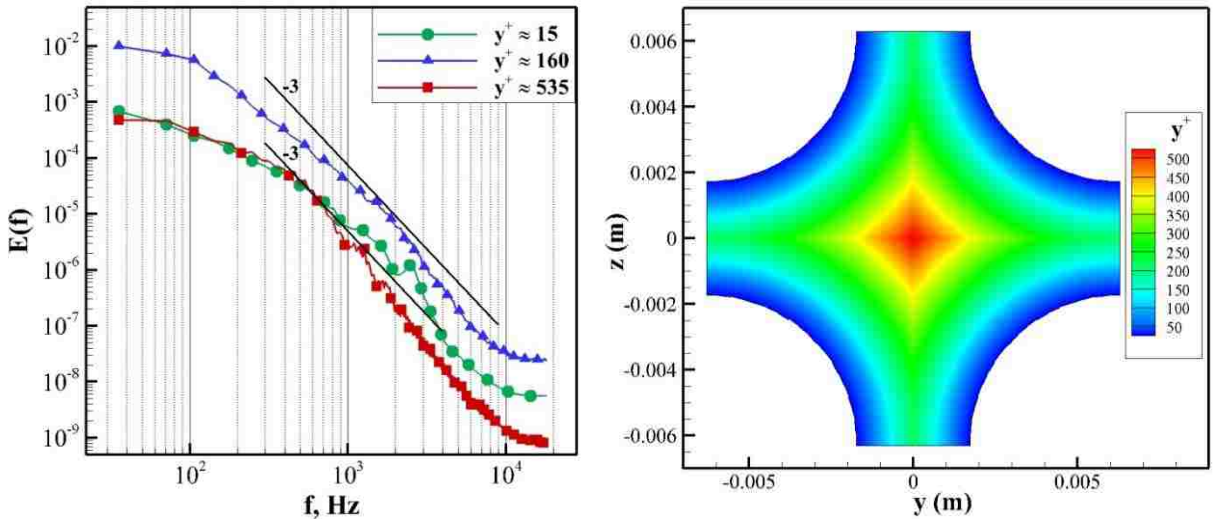

(a) (b)

Figure 2.14. (a): Energy spectra for the two-phase subchannel geometry (Re_τ = 400) at $y^+ \approx 535$ (red squares), $y^+ \approx 160$ (blue triangles), and $y^+ \approx 15$ (green circles). (b): Distribution of y^+ in the Re_τ = 400 nuclear reactor subchannel geometry.

Spectral analysis of the single-phase Re_τ = 400 subchannel was performed using 116 windows of 1024 points for a total data time of about 20 LETOTs. The pseudo-void analysis was performed with 4 windows of 930 points to match the time available from the two-phase data. The energy spectra at different y^+ locations are shown in Figure 2.15 and are in good agreement with the labeled -5/3 scaling in the inertial subrange. The inertial subrange resolution is small for this flow since the separation of turbulent scales is not large for relatively small turbulent Reynolds number. Again the consistent pseudo-void and single-phase results show that only the bubble wakes contribute to the slope modification.

2.2.3.2 Re_τ = 996

The turbulent two-phase bubbly flow DNS for the nuclear reactor subchannel geometry (Re_τ = 996) performed by Fang et al. [2] was spectrally analyzed with 3 averaging windows of 1024 points for about 0.26 LETOT (Figure 2.16(a)). The y^+ locations (Figure 2.16(b)) are formulated in the same way as the Re_τ = 400 case and all the locations shown here demonstrate a -3 scaling quite well.

Spectral analysis of the single-phase Re_τ = 996 subchannel was performed using 11 windows of 1024 points for a total data time of about 5.5 LETOTs (Figure 2.17). The pseudo-void simulation

was performed with one averaging window of 512 points to match the time of the available two-phase DNS data. Again, the single-phase results are consistent with the expected -5/3 slope and the pseudo-void technique shows that bubble wake contributions modify the energy spectrum slope.

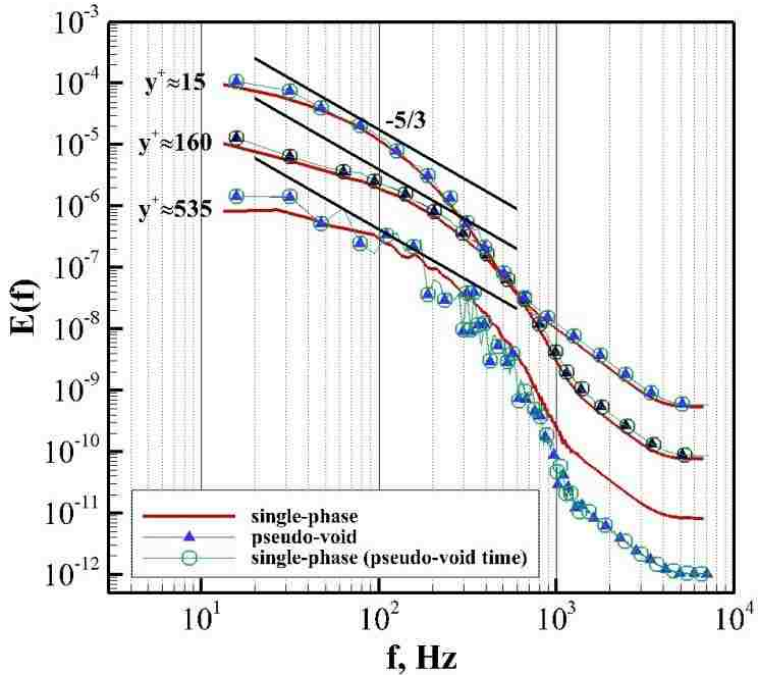

Figure 2.15. Single-phase and pseudo-void energy spectra at $y^+ \approx 535$, $y^+ \approx 160$, and $y^+ \approx 15$ for the subchannel geometry ($Re_\tau = 400$). The full simulation time of about 20 LETOTs is indicated by the thick red line, the pseudo-void simulation is indicated by the triangles, and a single-phase simulation for the same simulation time as the pseudo-void simulation is indicated by the circles.

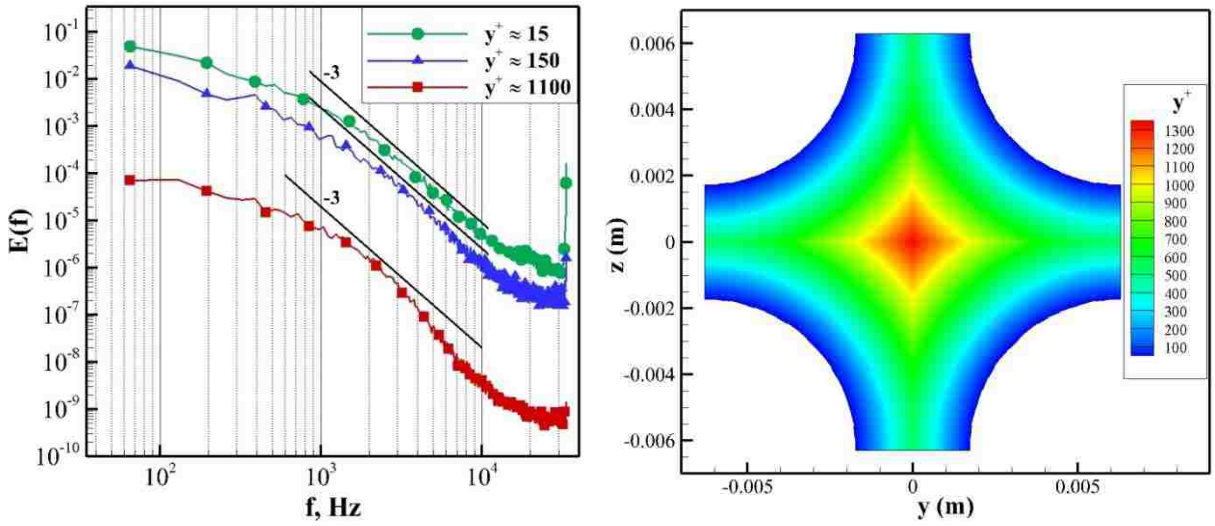

Figure 2.16. (a): Energy spectra for the two-phase subchannel geometry (Re_τ = 996) at y^+ ≈ 1100 (red squares), y^+ ≈ 150 (blue triangles), and y^+ ≈ 15 (green circles). (b): Distribution of y^+ in the Re_τ = 996 nuclear reactor subchannel geometry.

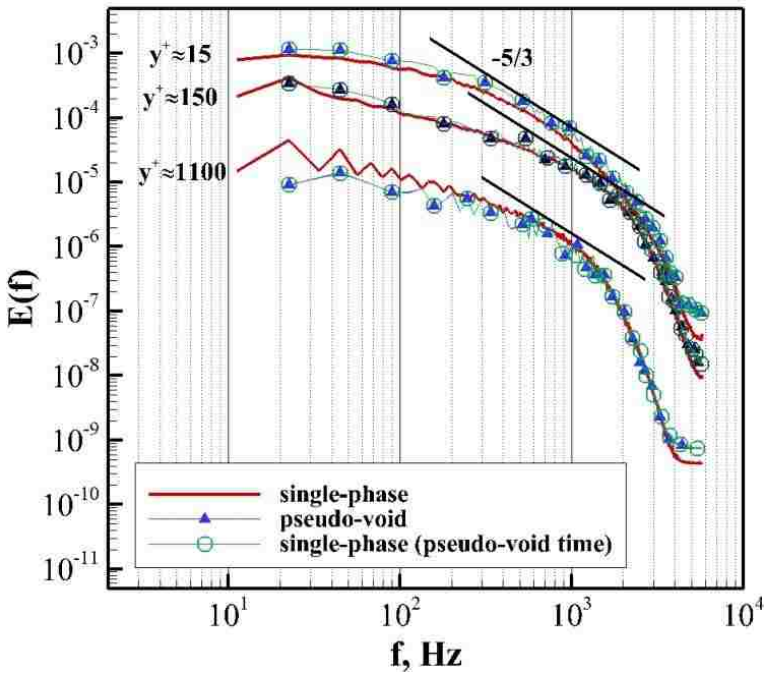

Figure 2.17. Single-phase and pseudo-void energy spectra at y^+ ≈ 1315, y^+ ≈ 150, and y^+ ≈ 15 for the subchannel geometry (Re_τ = 996). The full simulation time of about 5.5 LETOTs is indicated by the thick red line, the pseudo-void simulation is indicated by the triangles, and a single-phase simulation for the same simulation time as the pseudo-void simulation is indicated by the circles.

2.2.4 Comparison of the Flow Geometries

A direct comparison of the two-phase energy spectra for all of the considered geometries in this work is presented for y^+ values of about 15 (Figure 2.18), 150 (Figure 2.19), and near the centerline (Figure 2.20). The energy spectrum for each of the geometries is normalized such that the maximum frequency value is 1 and the magnitudes of each energy spectrum are similar for shape comparison. Consistent shapes, with a power law scaling close to -3, are evident for each of the considered geometries. Figure 2.21(a) shows the void distribution for all geometries scaled as a function of distance measured in bubble diameters from the wall and all the geometries have a void fraction peak close to within the 1.0-2.0 bubble diameter range. The filled symbols indicate the peak locations where the two-phase data was spectrally analyzed (Figure 2.21(b)). The 895 bubble circular pipe geometry has a flatter void fraction profile across the entire channel diameter but, for consistency, we consider the peak location closest to the wall for spectra comparison. The spectra for all the considered geometries at the peak locations (Figure 2.21(b)) also show a similar shape with a power law scaling close to -3.

The slope of the energy spectrum in bubbly two-phase flows is similar for different geometries, including nuclear reactor subchannels, and provides confidence that the SCTM can be universally applied in nuclear reactor core-relevant geometries.

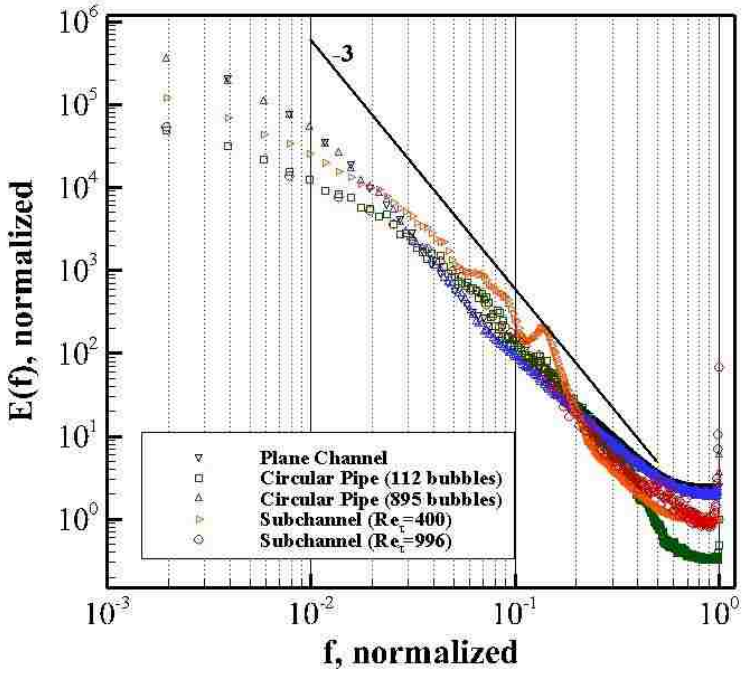

Figure 2.18. Comparison of the energy spectra ($y^+ \approx 15$) for all of the two-phase simulations in each of the geometries considered in the current work.

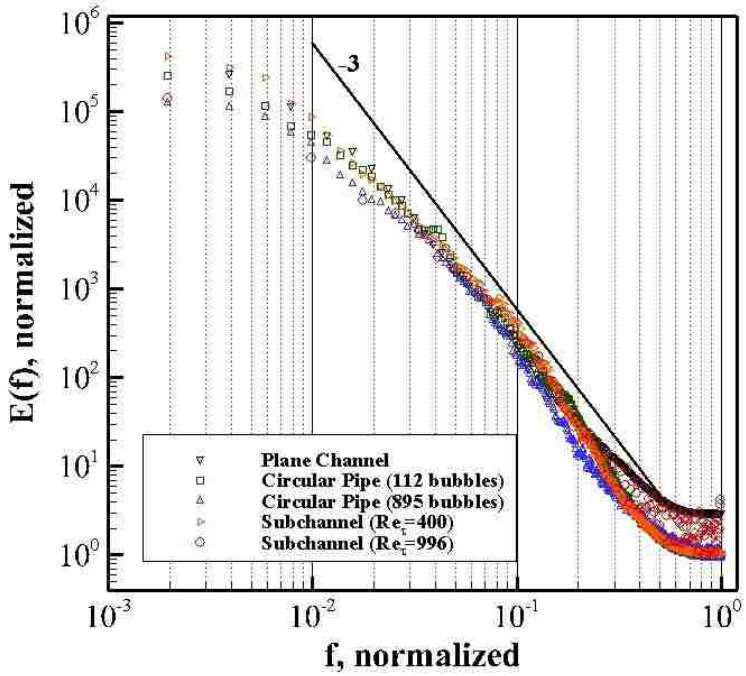

Figure 2.19. Comparison of the energy spectra ($y^+ \approx 150$) for all of the two-phase simulations in each of the geometries considered in the current work.

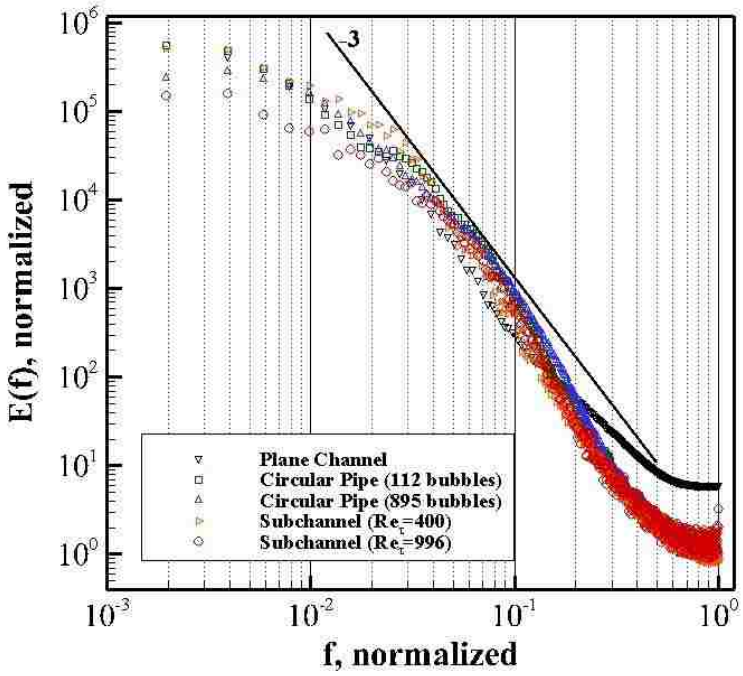

Figure 2.20. Comparison of the energy spectra (y^+ near the centerline) for all of the two-phase simulations in each of the geometries considered in the current work.

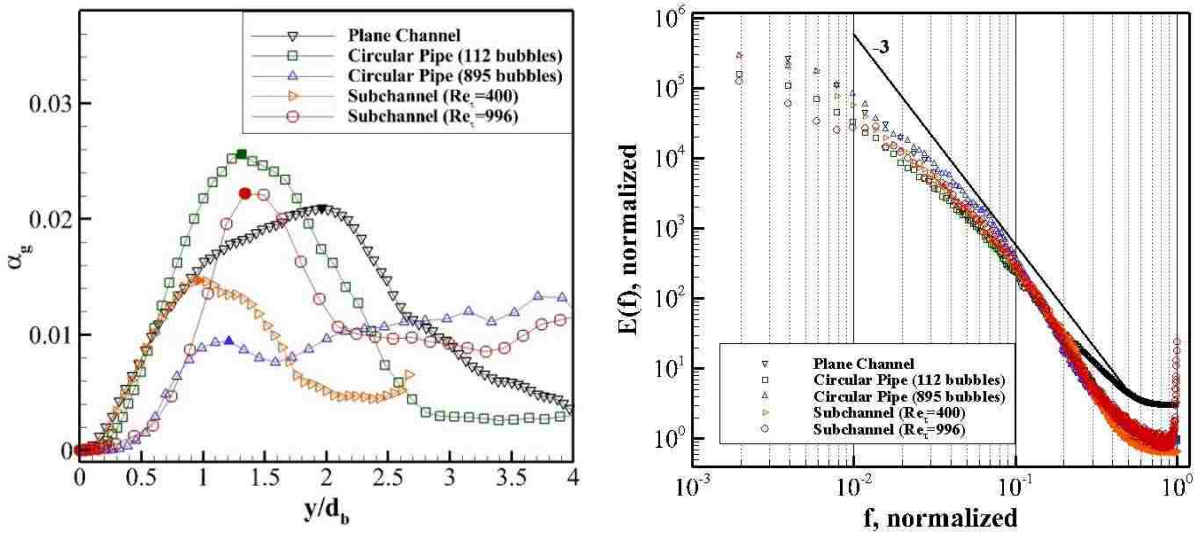

(a) (b)

Figure 2.21. (a): Void fraction distribution as a function of bubble diameter (scaled so that peaks close to the wall are evident). Filled symbols indicate locations of the peaks. (b) Energy spectra calculated at the spatial locations defined by the peaks in (a).

3. ONE-DIMENSIONAL SCTM IMPROVEMENT AND DEVELOPMENT

3.1 SCTM History

Previous development and validation of the SCTM was performed for single and two-phase decay of isotropic turbulence [10], single and two-phase uniform shear flow [9], and a HRN model for single-phase channel flow [11] where wall functions based on the law of the wall boundary condition were used to achieve closure near the wall of the conduit. The previous model formulation [11] required a non-trivial TKE boundary condition at the smallest resolved y^+ value (typically about 30). The previous work by Bolotnov et al. [11] was only applied to a channel flow for a Reynolds number based on friction velocity (Re_τ) of 180. A pure inertial subrange was not observed for such a relatively low Reynolds number and the expected -5/3 slope in the inertial subrange could not be verified.

The authors of the previous research efforts continued SCTM development with some model formulations to extend the model capabilities to resolve the turbulence through the boundary layer all the way to the wall. In this way, SCTM terms utilizing both spatial and spectral damping that accounted for the wall influence were included in the model formulation and the model was tested for Reynolds numbers based on friction velocity of 180, 950, and 2000. Extending the model to a LRN (wall-resolved) type model eliminated the need for *a priori* boundary conditions based on the law of the wall and DNS data. However, the model formulation was not finalized. Figure 3.1 shows some of the results obtained by the previous authors with a wall-resolved formulation. In Figure 3.1(a) the model predictions of the law of the wall demonstrate a non-physical oscillation about the DNS data. Figure 3.1(b) shows some numerical issues with a sawtooth behavior for the model prediction of turbulent viscosity. Figure 3.1(c) and Figure 3.1(d) both show that the numerical predictions do not recover the bin TKE values at the highest wave numbers. These issues were taken into consideration and the present work focused on improving the wall-resolved SCTM formulation and developing an improved model that properly accounts for the wall influence on the turbulence.

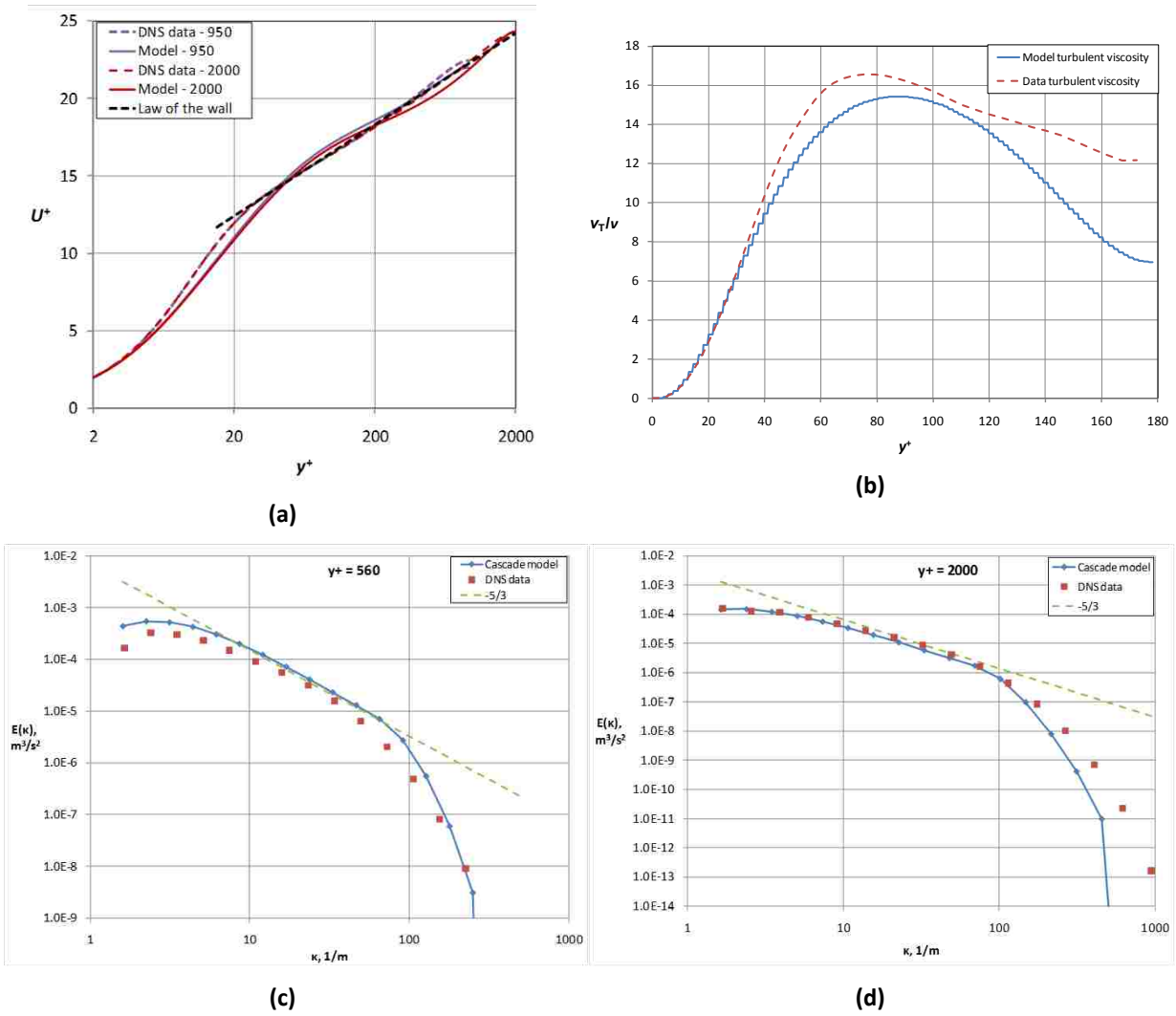

Figure 3.1. Previous results for the wall-resolved SCTM. (a) Law of the wall (Re_τ = 950 and 2000). (b) Turbulent viscosity (Re_τ = 180). (c) – (d) Energy spectrum (Re_τ = 950, Re_τ = 2000).

3.2 One-Dimensional SCTM Formulation

The 1D SCTM formulation is presented here. In this case, 1D refers to the direction across the channel width and normal to the channel wall. The RANS equations (Equation (1.7)) are solved using a turbulent viscosity determined by the SCTM equations where the Boussinesq approximation (Equation (1.5)) requires that turbulent viscosity distribution be modeled to obtain closure.

The SCTM resolves the TKE spectrum by splitting the total TKE into separate wave number bins and solving separate but coupled transport equations for each bin. Recall from § 1.1.1.1 that the energy in each wave number range (κ_a, κ_b) can be obtained by integration of the energy spectrum function over that wave number range (Equation (1.17)) and that the integration of the energy spectrum over all wave numbers results in the total TKE. Therefore, the total TKE can be split into *N* wave number bins corresponding to a separate TKE variable for that particular bin-*m* such that the total TKE is the sum of the spectral energies [10]:

$$k = \sum_{m=1}^{N} k_m \tag{3.1}$$

where k is the total TKE, k_m is the TKE in bin-*m*, and *N* is the total number of wave number bins. The bin TKE values can then be formulated analogous to Equation (1.17):

$$k_m = \int_{\kappa_{m-1}}^{\kappa_m} E(\kappa) d\kappa \tag{3.2}$$

where $E(\kappa)$ is the TKE spectrum introduced in § 1.1.1.1, κ is the wave number (Equation (1.16)), and κ_{m-1} and κ_m are the left and right wave number boundaries for bin-*m*, respectively. Since the entire energy spectrum must be captured with the discrete spectral bins the smallest and largest wave numbers require estimation for a particular problem. Bolotnov et al. [10] have defined the smallest wave number to correspond to the geometry of the problem:

$$\kappa_0 = \frac{2\pi}{\delta} \tag{3.3}$$

where δ is the characteristic length scale of the largest liquid eddies (e.g. the channel half-width in channel flow geometry). They have defined the largest wave number to correspond to the Kolmogorov scale:

$$\kappa_N = \frac{2\pi}{\eta}, \quad \eta = \frac{\nu^{3/4}}{\varepsilon^{1/4}} \tag{3.4}$$

where ν is the kinematic viscosity of the liquid and ε is the turbulent dissipation rate.

The left and right wave number boundary for each of the discrete spectral bins must be defined and the splitting is performed using uniform bin sizes in a logarithmic sense:

$$\kappa_m = \xi \kappa_{m-1} = \xi^m \kappa_0 \tag{3.5}$$

where the parameter ξ is the spectral resolution. Thus, based on the expected scales of a given problem, the number of spectral bins is then a function of the spectral resolution [11]:

$$N = \log_{\xi}\left[\frac{\kappa_N}{\kappa_0}\right] \tag{3.6}$$

where *N* is the number of spectral bins. Lewalle and Tavlarides [28] suggest the spectral resolution be no greater than 2 to properly resolve the non-linear interactions between spectral bins. The minimum number of required spectral bins can then be calculated with ξ = 2. However, enough spectral bins must be utilized so that at the largest scales (smallest wave numbers, Figure 1.2) the numerical results are independent of the number of bins and at the smallest scales (largest wave numbers, Figure 1.2) an accumulation of energy is avoided [28].

The smallest and largest scales of the problem, number of wave number bins, and boundaries of each wave number bin are now defined. Thus, it remains to express the TKE in each bin-*m* and a turbulent viscosity for closure of the RANS equations. The SCTM solves a separate TKE transport equation for each bin-*m.* Bolotnov et al. [9-11] have followed the work of Lewalle and Tavlarides [28] to express the single-phase TKE transport equation for bin-*m* as:

$$\frac{Dk_m}{Dt} = P_m - \varepsilon_m + D_m + T_m \tag{3.7}$$

where P_m, ε_m, D_m, and T_m are the spectral production, dissipation, diffusion, and spectral transfer of the TKE in bin-*m*, respectively. Provided a spectral turbulent viscosity for each bin-*m* can be defined as an additive quantity such that [28]:

$$\nu^T = \sum_{m=1}^{N} \nu_m^T \tag{3.8}$$

the equations can be closed. Each of the terms for bin-*m* will now be discussed separately.

3.2.1 Spectral Transfer

The spectral transfer (i.e. eddy energy cascade) term, T_m, characterizes the non-linear interaction of TKE between wave number bins. Bolotnov et al. [10] followed the assumption that there exists forward transfer of energy from larger to smaller eddies and inverse/backward transfer from smaller to larger eddies. For a particular wave number bin the spectral transfer can then be considered as four distinct terms: the energy inflow through the left boundary, the energy outflow through the right boundary, and the possible outflow through the left boundary and inflow from the right boundary (i.e. inverse cascade):

$$T_m = T_{in}^{left} - T_{out}^{left} + T_{in}^{right} - T_{out}^{right} \tag{3.9}$$

Bolotnov et al. [10, 11] used the donor-cell modeling approach of Kovasznay [32] to represent the inflows and outflows through the left and right wave number boundaries for a particular bin for the four terms. That transfer term is used in the present work and formulated for bin-*m* as:

$$\begin{aligned} T_m = C_1 \sum_{j=-N}^{-1} \beta_j \kappa_{m-1} k_{m+j} \sqrt{E_m \bar{\kappa}_m} - C_1 \sum_{j=1}^{N} \beta_j \kappa_{m-1+j} k_m \sqrt{E_{m+j} \bar{\kappa}_{m+j}} \\ - C_2 \sum_{j=-N}^{-1} \beta_j \kappa_{m+j} k_m \sqrt{E_{m+j} \bar{\kappa}_{m+j}} + C_2 \sum_{j=1}^{N} \beta_j \kappa_m k_{m+j} \sqrt{E_m \bar{\kappa}_m} \end{aligned} \tag{3.10}$$

where $\bar{\kappa} = \frac{\kappa_{m-1} + \kappa_m}{2}$ is the characteristic wave number (center) of bin-*m* and E_m is the TKE density function approximation for bin-*m*. The square root of the energy (E_m) terms in Equation (3.10) effectively represent the spectral "velocity" of the transfer between wave number bins. If the TKE is assumed constant (i.e. Riemann integration) within a spectral bin-*m* then the TKE density function can be approximated as:

$$E_m = \frac{k_m}{\Delta \kappa_m} \tag{3.11}$$

where $\Delta \kappa_m = \kappa_m - \kappa_{m-1}$ is the width of wave number bin-*m*. The C_1 and C_2 are model parameters which quantify the directional transfer rates [11] that have now been further developed using the DNS data of del Alamo et al. [89] and Hoyas and Jiminez [29] to account for the presence of the wall in the low-Reynolds number SCTM:

$$C_1 = 16.0 - 14.8 \left(1 - \exp\left(-\frac{y^+}{40.0}\right)\right)^2, \quad C_2 = 0.3167 C_1 \tag{3.12}$$

where y^+ is the dimensionless distance to the wall (Equation(1.14)). Bolotnov et al. previously found values of C_1 = 1.2 and C_2 = 0.38 for decay of isotropic turbulence [10] and uniform shear flow [9]. Figure 3.2 shows that this near-wall correction term retains these values as distance from the wall is increased.

Equation (3.10) includes weight functions, β_j, that quantify the interaction between wave number bins. The weight functions are formulated such that about 75% of the transfer occurs between bins ranging from half the current bin size to twice the current bin size as suggested by

Domaradzki [90]. Bolotnov et al. [10] quantified the weights by integration of the following distribution over a wave number bin:

$$f(\kappa) = \frac{1}{\hat{\sigma}\sqrt{2\pi}} \exp\left(-\frac{[\log(\kappa) - \log(\bar{\kappa})]^2}{2\hat{\sigma}^2}\right) \tag{3.13}$$

where $\hat{\sigma}$ = 0.225 is the standard deviation and $\bar{\kappa}$ is the left or right boundary of the interacting spectral bin.

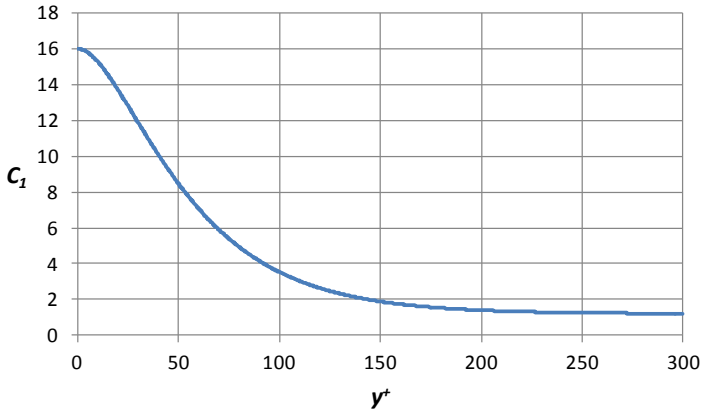

Figure 3.2. Forward transfer coefficient (C_1) dependence upon distance from the wall.

Note that the spectral transfer term has been formulated in such a way as to satisfy the required constraint that the sum of all the spectral components of transfer does not contribute to the total TKE, i.e.:

$$\sum_{m=1}^{N} T_m = 0 \tag{3.14}$$

3.2.2 Dissipation

Bolotnov et al. [11] considered two different contributions to the turbulent dissipation rate in non-homogeneous channel flows. These contributions were the so-called “in-plane” component of dissipation that approaches zero near the wall and the “inter-plane” dissipation component that is non-zero at the wall. Cadiou et al. [91] took a similar approach to decompose the turbulent dissipation into two-components. In the present work, turbulent dissipation is again split into dissipation components that are zero and non-zero at the wall. However, these components are

more succinctly quantified as the terms of the dissipation tensor that are zero at the wall and non-zero at the wall based on an analysis of DNS data (Figure 3.3) and are now named as the homogeneous and inhomogeneous dissipation components, respectively. The homogeneous component follows previous SCTM formulations as a well-known formula [14] for spectral dissipation:

$$\varepsilon_m^p = \int_{\kappa_{m-1}}^{\kappa_m} 2\nu\kappa^2 E(\kappa)d\kappa \cong 2\nu\frac{k_m}{\Delta\kappa_m}\left(\frac{\kappa_m^3}{3} - \frac{\kappa_{m-1}^3}{3}\right) \tag{3.15}$$

where the TKE density function $E(\kappa)$ is again approximated as a constant (Equation (3.11)) in each wave number bin interval (κ_{m-1}, κ_m).

The inhomogeneous dissipation depends on the distance from the wall (*y*) and must be modeled separately for wall-bounded flow. The current work utilizes a new formulation for inhomogeneous dissipation that was based on the previous SCTM formulation [11] but includes new terms and accounts for the wall influence:

$$\varepsilon_m^y = \left[C_{\varepsilon 1}\frac{dU}{dy}u_\tau\nu(\kappa_m - \kappa_{m-1}) + C_{\varepsilon 2}\frac{k_m}{\Delta\kappa_m}u_\tau\left(\frac{\kappa_m^2}{2} - \frac{\kappa_{m-1}^2}{2}\right)\right]\exp(-0.15y^+) \tag{3.16}$$

where $C_{\varepsilon 1}$ = 0.25 and $C_{\varepsilon 2}$ = 0.05 are model constants. This model ensures that the inhomogeneous dissipation is non-zero at the wall and depends on the near wall value of TKE in each bin. The exponential wall-correction term in Equation (3.16) dictates that the inhomogeneous dissipation does not have a significant effect away from the walls, as physically expected. Finally, the total dissipation in bin-*m* (ε_m) is the sum of both contributions:

$$\varepsilon = \sum_{m=1}^{N}\varepsilon_m = \sum_{m=1}^{N}\left(\varepsilon_m^p + \varepsilon_m^y\right) \tag{3.17}$$

where the total dissipation rate is the sum of the dissipation rate for each wave number bin.

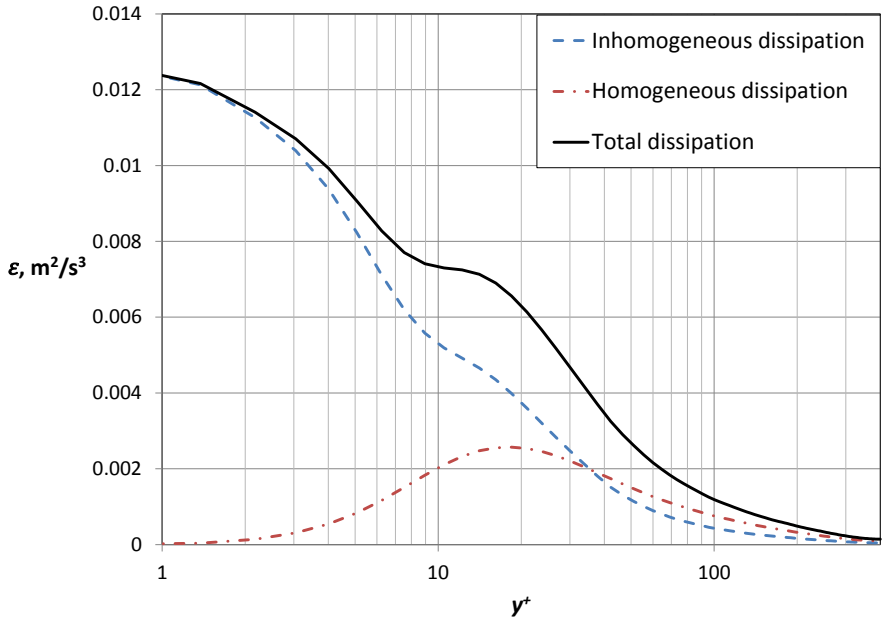

Figure 3.3. Turbulent dissipation components: homogeneous dissipation (dash-dot line) and inhomogeneous dissipation (dashed) line. Based on the DNS results of Bolotnov [34].

3.2.3 Production and Turbulent Viscosity

Lewalle and Tavlarides [28] chose to construct the turbulence production term to correspond to the model TKE equation. The first term on the RHS of the TKE equation for the k-ε model (Equation (1.10)) is the turbulence production term:

$$P = \nu^T \left(\frac{dU}{dy}\right)^2 \tag{3.18}$$

where U is the stream-wise component of mean velocity, y is the direction normal to the wall, and the partial derivative terms have been amended to the total derivative for the 1D SCTM. As shown by Equation (3.8), the SCTM has been formulated under the assumption that the turbulent viscosity is an additive quantity over the spectral wave number bins. Therefore, the turbulence production in bin-*m* is given by:

$$P_m = \nu_m^T \left(\frac{dU}{dy}\right)^2 \tag{3.19}$$

which ensures that the spectral production sums to the proper total in Equation (3.18) [11].

However, the distribution of turbulent viscosity over the spectral space remains to be determined. Bolotnov et al. [9, 11] followed the work of Lewalle and Tavlarides [28] to apply a Heisenberg [32] spectral turbulent viscosity with a correction term outside of the inertial subrange. However, in non-homogeneous wall-resolved flows the wall influence on the turbulence must be considered and Bolotnov et al. [11] provided turbulent viscosity damping functions in the development of the HRN SCTM. They used a spectral wall function to damp the larger eddies close to the wall and a Launder-Sharma [23] near-wall correction term frequently used in k-ε models. Different damping functions are utilized in the present wall-resolved SCTM (much like in low-Reynolds number k-ε models, see Equations (1.10) – (1.15). The turbulent viscosity for bin-*m* is:

$$\nu_m^T = f_\mu f_y f_s \nu_m^T|_{L\&T} = C_H f_\mu f_y f_s \Delta\kappa_m \sqrt{\frac{E(\bar{\kappa}_m)}{\bar{\kappa}_m^3}} \left[E(\bar{\kappa}_m) \bar{\kappa}_m^{5/3} \varepsilon^{-2/3} \right]^{0.75} \tag{3.20}$$

where $f_\mu, f_y,$ and f_s are the damping functions that are multiplied by the Lewalle and Tavlarides (*L&T*) type turbulent viscosity and C_H = 0.40 is a model constant. Although the formulation is different than in the HRN SCTM, f_y is still a spectral wall function that damps the larger eddies close to the wall:

$$f_y = \sqrt{1 - \exp(-1.6 y \bar{\kappa}_m)} \tag{3.21}$$

and $f_\mu$is now the Chien [25] low-Reynolds number near-wall correction (see Equation (1.15)):

$$f_\mu = 1.0 - \exp(\sigma_\mu y^+) \tag{3.22}$$

where for the SCTM σ_μ is dependent upon the Reynolds number based on friction velocity of the flow:

$$\sigma_\mu = -7.38x10^{-3} \exp(-8.53x10^{-4} Re_\tau) \tag{3.23}$$

Finally, a spectral damping function that controls the energy of the largest eddies in the flow is:

$$f_s = 1.0 - \exp\left(-175.0 \frac{\bar{\kappa}_m}{\kappa_N}\right) \tag{3.24}$$

3.2.4 Diffusion

In the previous work of Bolotnov et al. [11] the diffusion term was formulated much like that in k-ε models although the turbulent Schmidt number (σ_k) was dependent on the characteristic wave number of the bin-*m*. In the present work, Lewalle and Tavlarides [28] are more closely

followed and the dissipation term is the same as that used in k-ε models (see the final term in Equation (1.10)):

$$D_m = \frac{\partial}{\partial y}\left[\left(\nu + \frac{\nu_T}{\sigma_k}\right)\frac{\partial k}{\partial y}\right] \tag{3.25}$$

where σ_k = 0.5. This constitutes a more general model that becomes less dependent on the spectral parameters than in previous formulations.

3.2.5 Relationship of the SCTM to Two-Equation k-ε Type Models

Summation of the SCTM TKE transport equations over all wave number bins yields the total TKE as shown in Equation (3.1) on the LHS and total production, dissipation, and viscous and turbulent diffusion terms on the RHS since spectral transfer does not contribute to the overall TKE (Equation (3.14)). Recall from § 1.1.1 that these are the same terms in the TKE equation of standard single-phase k-ε models (Equation (1.10)). However, the exact expression for some of these source terms do not precisely correspond to the empirical results used in the k-ε TKE transport model, rather the expressions for ε and ν^T quantify complicated spectral integrations. However, the spectral cascade-transport turbulence model does not require the use of a transport equation for turbulent dissipation rate as a k-ε model does but is capable of good spatial predictions of the DNS results while also resolving the energy spectrum.

3.3 One-Dimensional SCTM Results from FlexPDE

FlexPDE [92] was used for SCTM calibration and development with comparison to plane channel flow DNS. The domain considered a 1D slice across the channel width in terms of distance from the wall. FlexPDE software is a partial differential equation (PDE) solver that converts a user defined system of PDEs into a finite element model and then chooses an appropriate numerical solution scheme. Validation of the 1D SCTM was performed with FlexPDE so that the primary focus could be on improving the flow physics modeling by taking advantage of a robust numerical treatment to solve the equations, to use the in-situ visualization of FlexPDE for simulation control and improved model development efficiency, and to pose the equations in a natural scripting language.

The SCTM was applied to several Reynolds number flows for validation in 1D FlexPDE. The DNS data (Re_τ = 2000) of Hoyas and Jiminez [29] and (Re_τ = 950) del Alamo et al. [89] allow for validation of not only mean flow parameters, but for model validation of the performance in the spectral domain as well since the DNS information in the spectral domain is available. The SCTM performance has also been assessed for lower Reynolds number turbulent channel flow (Re_τ = 550) using the DNS data of del Alamo and Jiminez [93]. Table 3.1 shows model parameters for all the considered cases.

Although FlexPDE has dynamic time-stepping capabilities, a constant time step of 1.0 was used for each of the presented cases for convergence of the SCTM due to its highly non-linear nature. Spatial mesh resolution across the channel, in the direction normal to the wall (y), was varied using Equation (3.26) to accurately resolve the wall boundary layer. In this way, a finer mesh is utilized closer to the wall and a coarser mesh is utilized closer to the channel centerline. The cubic basis function option for the finite element model in FlexPDE was used for better solution accuracy with some penalty in overall computation time.

$$dy = 0.85\left[1.4 + 25.0\left(\tan^{-1}\left\{y\pi - \frac{\pi}{2}\right\}\right)\frac{\nu}{u_\tau}\right] \tag{3.26}$$

SCTM results from 1D FlexPDE will be shown for the three considered Reynolds numbers (Re_τ = 550, Re_τ = 950, Re_τ = 2000) in comparison to DNS data as well as the low-Reynolds number Chien k-ε model [25]. Overall, predictions of the SCTM are on par with the Chien k-ε model and provide good predictions of the DNS data while also resolving the TKE spectrum. SCTM simulations with perturbed initial conditions were performed and results converged to the same presented solutions.

Table 3.1. SCTM model parameters for each of the considered Reynolds number cases.

Parameter description	Notation	Re_τ = 550	Re_τ = 950	Re_τ = 2000	Units
Friction velocity	u_τ	0.04890	0.04539	0.04130	m/s
Kinematic viscosity	ν	8.945e-5	4.859e-5	2.062e-5	m^2/s
Domain left boundary	y_0^+	0.0	0.0	0.0	-
Domain right boundary	y_1^+	546.70	934.13	2003.15	-
Number of cascade bins	*N*	18	5 - 22	18	-
Spectral resolution parameter	ξ	1.3921	3.361 - 1.317	1.4553	-
Spatial mesh resolution	Δy^+	0.38 – 1.8	0.38 – 3.1	0.34 – 6.7	-
Left boundary of wave number range (largest liquid eddies)	κ_0	1.000	1.333	1.333	1/m
Right boundary of wave number range (smallest liquid eddies)	κ_N	385.7	571.7	1144.0	1/m

3.3.1 Re_τ = 2000

The highest Reynolds number case will be discussed first. As can be seen in Figure 3.4, the SCTM demonstrates good prediction of the mean velocity profile and reasonable agreement for the total TKE profile. Note that a non-dimensional TKE scale $\left(k^+ = {}^{k}/_{u_{\tau^2}}\right)$ was used on the right vertical axis of the plot. Comparisons with the Chien k-ε model show that although TKE is over-predicted by the SCTM, mean velocity is likewise over-predicted by the Chien k-ε.

Figure 3.5 compares SCTM results with the well-known law of the wall:

$$U^+ = \frac{1}{\kappa_0} \ln y^+ + B \tag{3.27}$$

where κ_0 = 0.39 and B = 4.7. The law of the wall indicates that the stream-wise velocity in the flow varies logarithmically with distance from the wall surface [13]. For the SCTM, excellent agreement is shown in the region of applicability of the law of the wall as well as with the DNS data all the way to the wall. The SCTM provides better prediction of the mean velocity than the Chien k-ε model. Unlike in previous spectral cascade-transport models of channel flow [11], a wall function boundary condition is not needed to achieve closure.

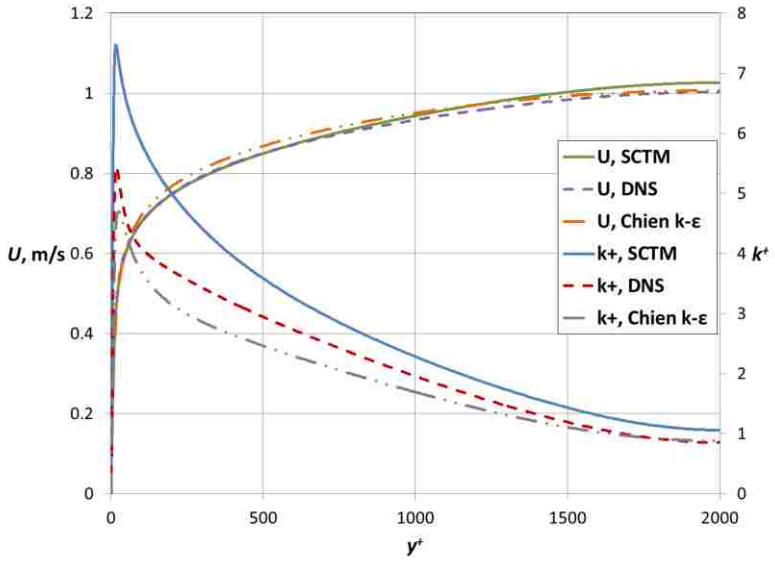

Figure 3.4. Mean velocity and TKE profiles obtained by the SCTM using eighteen (N = 18) wave number bins (solid lines) compared to DNS results (Re_τ = 2000) of Hoyas and Jiminez [29] (dashed lines) and the Chien k-ε model [25] (dashed dot dot lines).

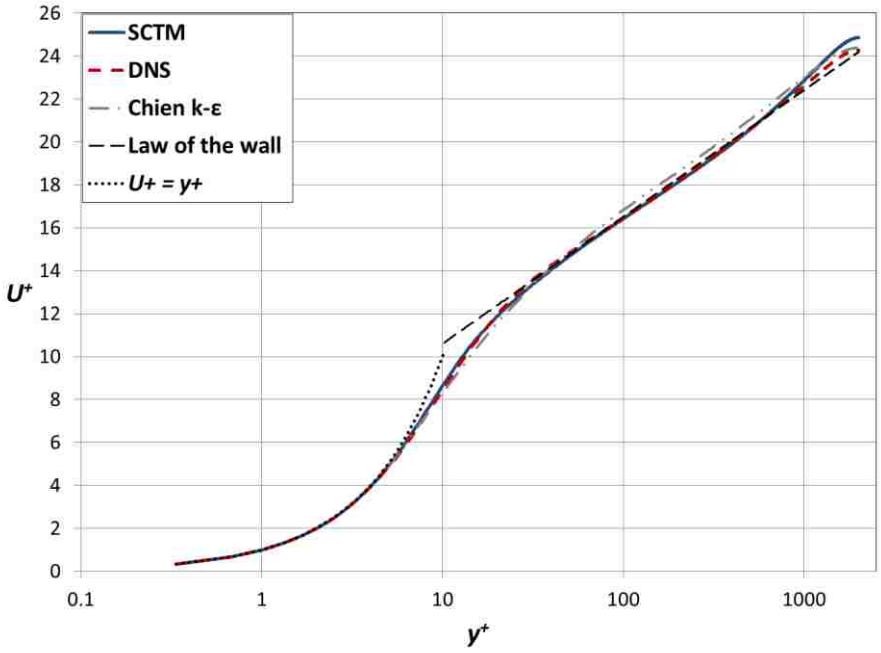

Figure 3.5. Mean velocity profile of the SCTM using eighteen (N = 18, Re_τ = 2000) wave number bins (blue solid line) compared to DNS results of Hoyas and Jiminez [29] (red dashed line), the Chien k-ε model [25] (grey dashed dot dot line), the law of the wall, and $U^+ = y^+$ in the very near wall region.

Spectral energy results can be presented as TKE spectrum at various y^+ locations. Figure 3.6 compares eighteen bin SCTM energy spectrum predictions at four different y^+ locations (y^+ = 2000, y^+ = 1200, y^+ = 400, y^+ = 40) with DNS data [94] and the well-known -5/3 energy spectrum slope for single-phase turbulent flows. Near the channel centerline (Figure 3.6(a)) and through the bulk turbulence region of the flow (Figure 3.6(b), (c)), excellent agreement is observed between the SCTM and the DNS data. However, the model fails to predict the change in energy spectrum slope near the wall (Figure 3.6(d)) where it instead preserves the theoretical -5/3 slope of the inertial subrange. This could be due to slight under-predictions of viscous diffusion and dissipation close to the wall, which will be discussed in accordance with Figure 3.8(d). Applying the SCTM to much higher Reynolds number than were previously examined by Bolotnov et al. [11] for channel flow without resolving the near-wall boundary layer has shown that the model predicts the theoretical -5/3 slope of the inertial subrange. At this particular Reynolds number (Re_τ = 2000), inner and outer scale separation are large enough to observe the inertial subrange and validate model behavior.

The spectral energy results can also be represented as contours in the spectral and spatial domains (Figure 3.7). The peak of TKE is clearly shown very close to the wall and within the smallest wave number range where turbulent liquid eddies are the largest. This follows the spatial and spectral representations of TKE in Figure 3.4 and Figure 3.6, respectively, where the TKE peak was concentrated near the wall and the lowest wave number bins within the energy containing range have values of TKE density many magnitudes larger than values at the dissipation range. Figure 3.7(b) shows the TKE contour zoomed to the peak location to emphasize the concentration of TKE. The characteristic bin number is shown along the horizontal axis and can be matched to the corresponding wave number bin in Table 3.2. The contour plot approach is a convenient way to represent the behavior of the turbulence in both physical and spectral domains and this approach was used in the spectral analysis of DNS data by Bolotnov et al. [94].

Examining SCTM source terms (i.e. the right hand side terms of the single-phase cascade-transport equation (3.7)) in both the spatial and spectral domain indicates that the model behaves as expected in terms of energy production at the lowest wave number bins, energy transfer through the inertial subrange, and the eventual dissipation of the smallest eddies at the highest wave number bins. Figure 3.8(a) shows the SCTM source term balance for bin-5. Eddies in this bin are sized approximately as one-sixth of the channel half width (Table 3.2). Recalling the spectral peak of

TKE from the contour plot in Figure 3.7 it is consistent that eddies in this bin receive energy predominately through the production term (dashed blue line) while energy is removed by the spectral transfer term (red dashed dot dot line) through the energy cascade process. Both the viscous and turbulent diffusion (teal dashed dot line and orange dotted line) terms are considerable in bin-5, where viscous effects are present close to the wall (i.e. y^+ less than about 10) and the change in turbulent diffusion sign occurs to keep the source term balance equal to zero when viscous effects are no longer present. Note that dissipation effects are negligible for eddies of this size.

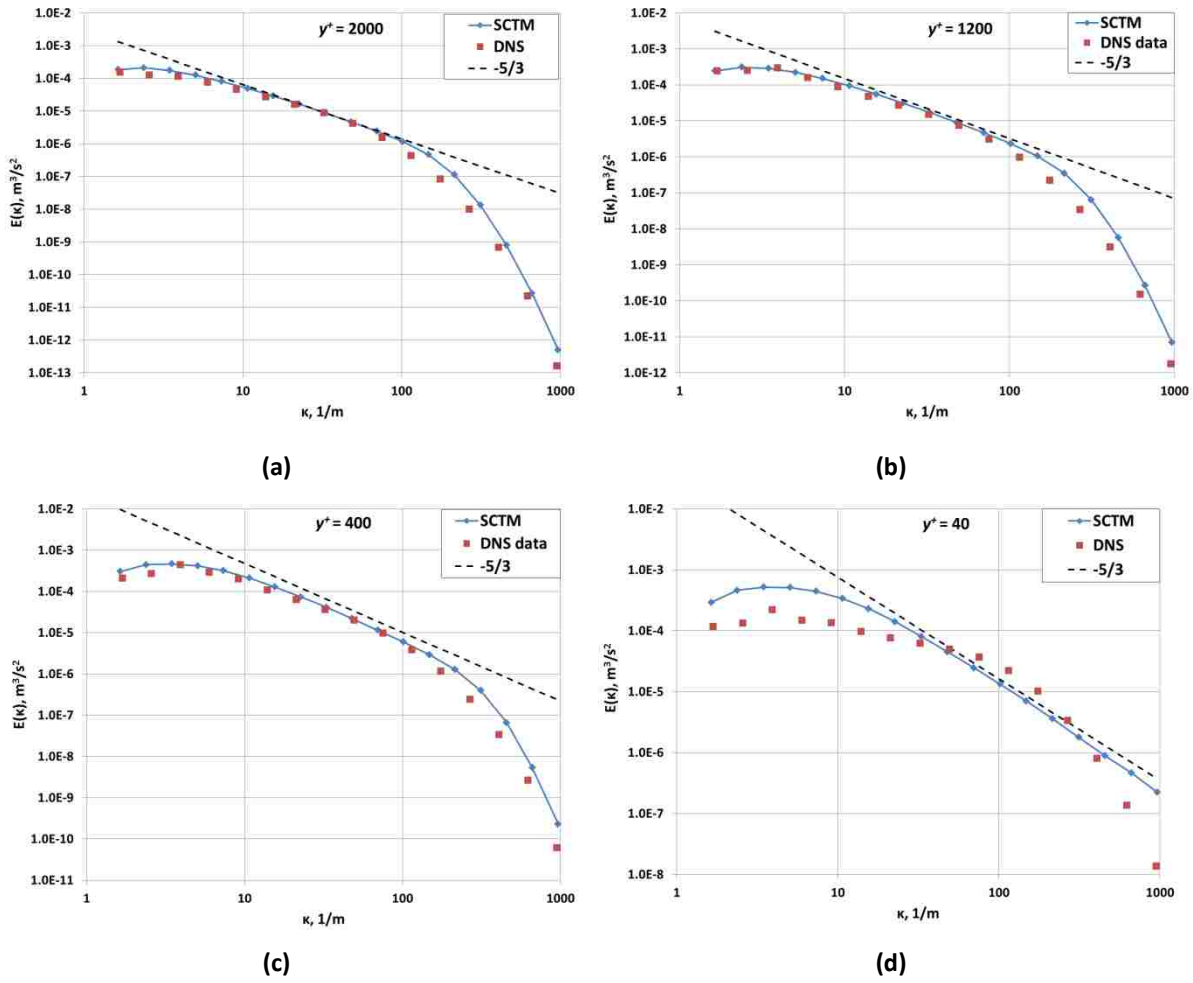

Figure 3.6. SCTM (N = 18, Re_τ = 2000) prediction of the TKE spectrum at four different distances from the wall: (a) y^+ = 2000, (b) y^+ = 1200, (c) y^+ = 400, and (d) y^+ = 40 (blue solid line with diamonds) in comparison to DNS data spectrum (red squares) and -5/3 slope (dashed line).

However, for bin-11 (Figure 3.8(b)) the source terms are distributed much differently. In this bin, eddies are sized as approximately 1/52 of the channel half width. Noting the location of bin-11 in Figure 3.6, this bin resides at the transitional point between the -5/3 slope of the inertial subrange and the steeper slope of the dissipation range. The energy transfer into the bin ($T_{in}^{left} + T_{in}^{right}$) and energy transfer out of the bin ($T_{out}^{left} + T_{out}^{right}$) are printed separately for bin-11 rather than just the net spectral transfer term (Equation (3.9)) and these terms dominate the TKE budget. At the tail of the inertial subrange the energy transfers into and out of the bin are nearly equal and exemplify the interacting spectral shell type model basis for the SCTM. Figure 3.8(b) also shows fully-developed steady state model predictions for bin-11 since the sum of all source terms is essentially zero.

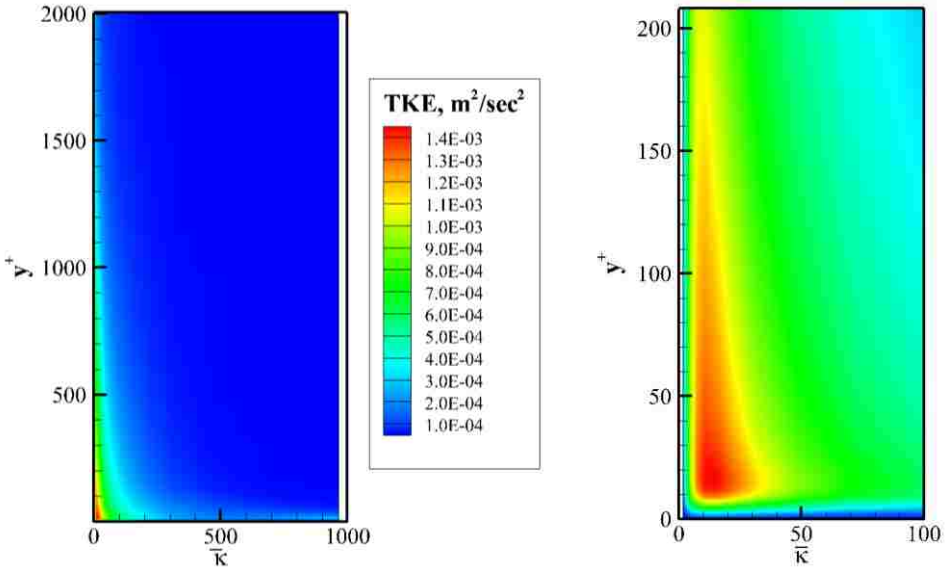

(a) **(b)**

Figure 3.7. SCTM predictions of the TKE contour levels (N = 18, Re_τ = 2000) in the spectral and spatial domains for the full range of y^+ and characteristic wave number values (a) and for a perspective zoomed to the area of interest (b).

Table 3.2. SCTM wave number boundaries for N = 18, Re_τ = 2000 case and the approximate average eddy size in each spectral bin based on the channel half width (δ).

Spectral bin number	Left boundary wave number, 1/m	Right boundary wave number, 1/m	Approximate average eddy size
1	1.333	1.940	4δ/5
2	1.940	2.824	δ/2
3	2.824	4.110	δ/3
4	4.110	5.982	δ/4
5	5.982	8.705	δ/6
6	8.705	12.67	δ/8
7	12.67	18.43	δ/11
8	18.43	26.83	δ/17
9	26.83	39.05	δ/25
10	39.05	56.83	δ/36
11	56.83	82.72	δ/52
12	82.72	120.3	δ/76
13	120.3	175.2	δ/110
14	175.2	254.9	δ/161
15	254.9	371.1	δ/235
16	371.1	540.1	δ/342
17	540.1	786.0	δ/497
18	786.0	1144	δ/724

Figure 3.8(c) shows the SCTM source term distribution for bin-18, or the smallest eddies present in the flow. In this bin, the spectral transfer term transports energy through the left wave number boundary of the bin as energy cascades down from larger eddies. The viscous diffusion term also provides energy in this bin. The homogeneous and inhomogeneous dissipation terms (dashed green line and long-dashed purple line) dominate in removing TKE from the turbulent eddies.

The total source term balance for the SCTM can be obtained by summing the spectral source terms for each bin. The total source term balance for the SCTM (N = 18, Re_τ = 2000) in comparison to the DNS data of Hoyas and Jiminez [29] is shown in Figure 3.8(d). The SCTM predicts these terms quite well, most notably in predicting spatial peak locations, although there is some disagreement in the dissipation and viscous diffusion terms close to the wall. As aforementioned, this disagreement may account for the SCTM failing to predict the slope change of the TKE spectrum close to the wall in Figure 3.6(d). The SCTM spectral transfer term summed over the spectral space is shown in Figure 3.8(d) as well and the term essentially sums to zero.

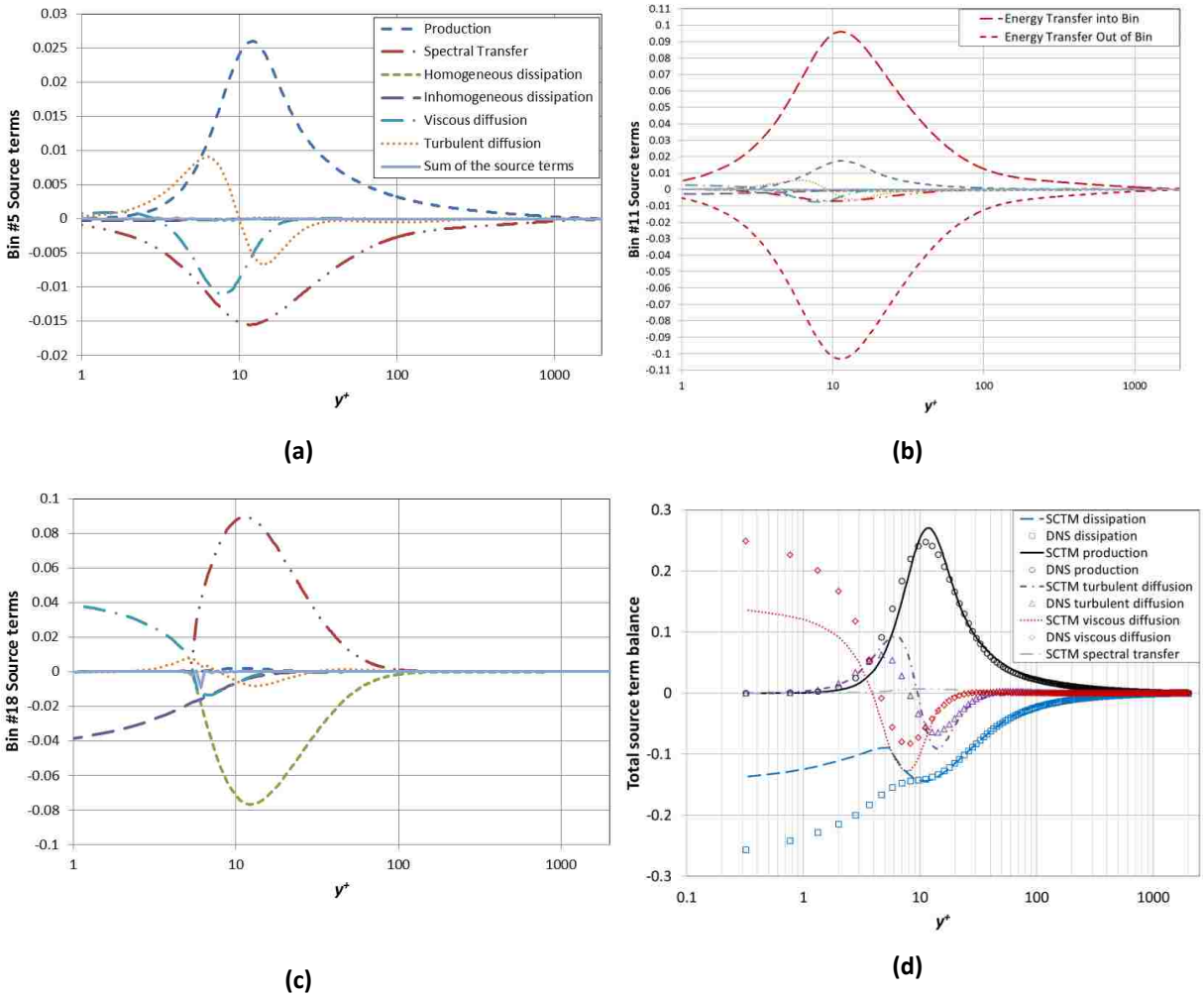

Figure 3.8. (a) - (c): SCTM results for the source term distribution of the cascade-transport equation for bin numbers 5, 11, and 18, respectively (N = 18, Re_τ = 2000). (d): The total source term balance of the SCTM in comparison to the DNS results of Hoyas and Jiminez [29].

Figure 3.9 shows the non-dimensionalized turbulent viscosity prediction of the SCTM (the sum of the bin turbulent viscosities) in comparison to DNS data and the Chien k-ε model. The DNS turbulent viscosity was evaluated using [11]:

$$\nu_T = -\frac{\langle u'v' \rangle}{\frac{dU}{dy}} \tag{3.28}$$

Excellent agreement is observed close to the wall with acceptable agreement for the rest of the flow. Note that the peak location of turbulent viscosity is well predicted by the SCTM and centerline discrepancies are observed for both the SCTM and Chien k-ε.

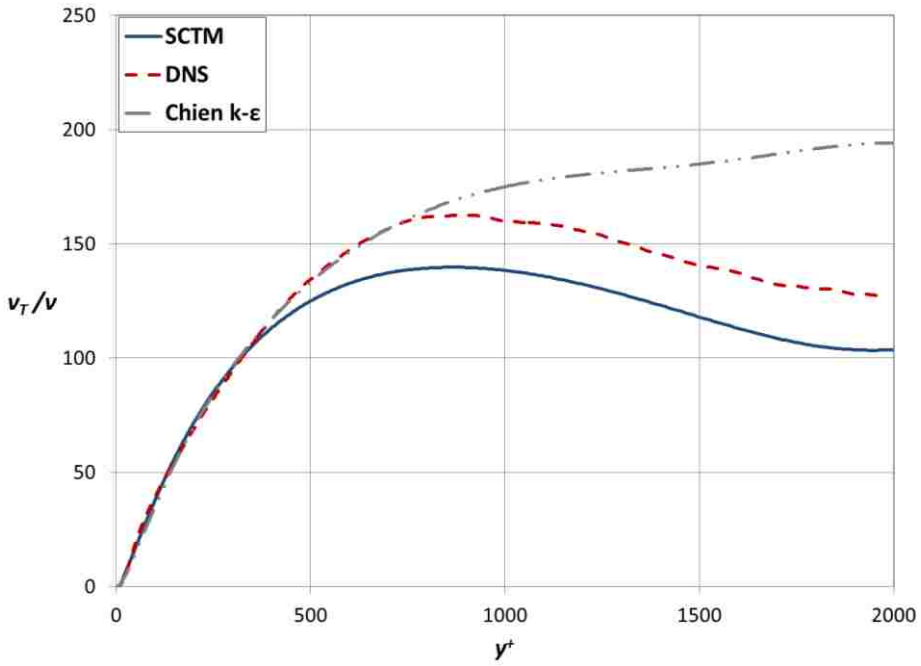

Figure 3.9. Non-dimensional turbulent viscosity distribution of the SCTM (N = 18, Re_τ = 2000; solid blue line) compared with DNS results of Hoyas and Jiminez [29] (dashed red line) and the Chien k-ε model [25] (grey dashed dot dot line).

3.3.2 $Re_\tau = 950$

SCTM predictions for Re_τ = 950 were also performed and compared with DNS data [89] and the Chien k-ε model [25]. Note that for each considered Reynolds number the model formulation remains the same as that in § 3.2 while the wave number ranges (Table 3.1) are different based on the requirements of the SCTM. A spectral resolution study was also performed for this particular case at Re_τ = 950 to ensure that model accuracy does not significantly degrade even when coarser spectral resolution is used.

Figure 3.10(a) shows the mean velocity and TKE profiles calculated by the SCTM in comparison to the DNS data and Chien k-ε model. These mean flow parameters are predicted quite

well. Particularly, the SCTM better predicts the mean velocity behavior than the over-prediction of the Chien k-ε model. However, the SCTM does over-predict the TKE profile further from the wall. The SCTM performs similarly to the Chien k-ε model for the turbulent viscosity (Figure 3.10(b)), where both models over-predict the DNS data at the channel centerline. However, the centerline behavior of the estimated turbulent viscosity has limited influence on model predictive capabilities since the relatively flat velocity profile results in small turbulent production and diffusion. On the other hand, the DNS estimates provided for comparison also have larger uncertainty close to the centerline since this artificial quantity (turbulent viscosity) is computed using the ratio of DNS-estimated turbulent shear stress ($\langle u'v' \rangle$) over DNS-estimated velocity gradient (dU/dy). At the centerline both those quantities are expected to be zero – so turbulent viscosity is not defined using this method. As one approaches the centerline location the uncertainty grows. These two observations explain why away from the wall (where velocity gradients and shear stresses are small) having a disagreement between the model prediction and DNS estimates does not necessarily result in poor model performance (as seen for both Chien and SCTM models).

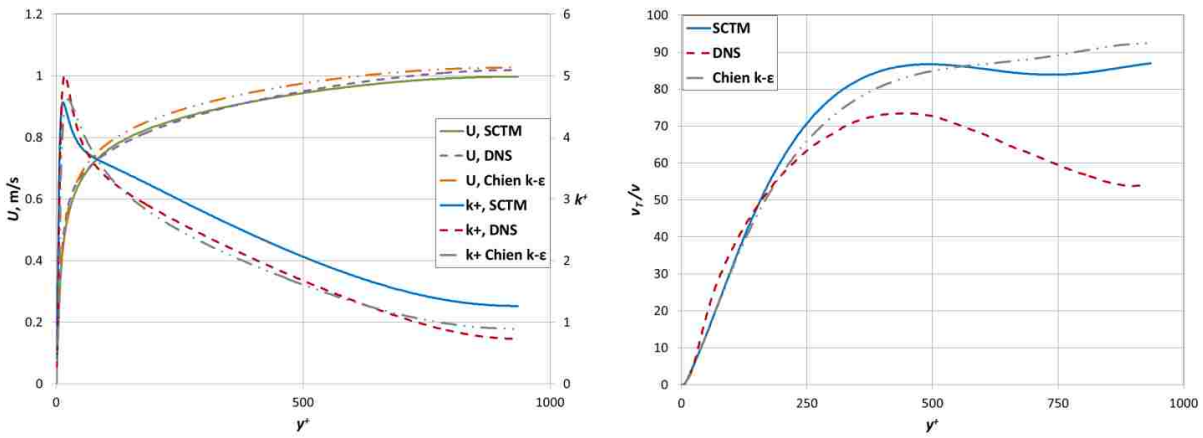

Figure 3.10. Mean velocity and TKE profiles (a) as well as turbulent viscosity profile (b) obtained by the SCTM (N = 18, Re_τ = 950) in comparison to the DNS data of del Alamo et al. [89] and the Chien k-ε model [25].

Figure 3.11 shows how the SCTM mean velocity (N = 18, Re_τ = 950) compares to the well-known law of the wall (Equation (3.27)). The SCTM predicts the law of the wall and the DNS data

quite well, notably achieving the flat velocity profile in the logarithmic region of applicability and well-predicting the DNS data in the very near wall region.

Figure 3.12 shows the total source term balance (the sum over all wave numbers) for the SCTM in comparison with the DNS results of del Alamo et al. [89] for the eighteen bin Re_τ = 950 case. As with the Re_τ = 2000 case (Figure 3.8(d)), good agreement between the SCTM and DNS data is observed with only some notable discrepancy in the dissipation and viscous diffusion estimations close to the wall.

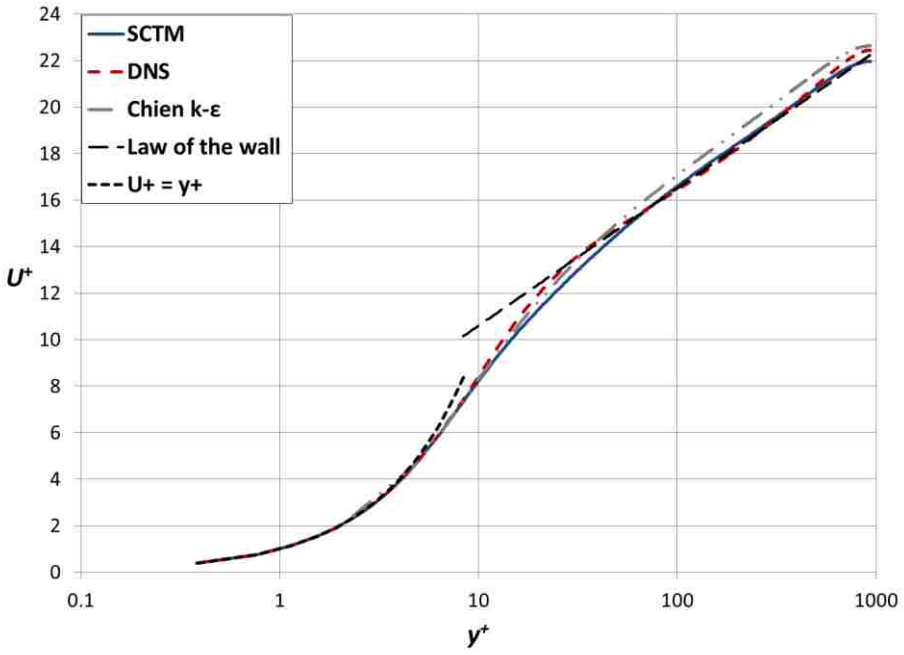

Figure 3.11. Mean velocity profile of the SCTM using eighteen (N = 18, Re_τ = 950) wave number bins (blue solid line) compared to DNS results of del Alamo et al. [89] (red dashed line), the Chien k-ε model [25] (grey dashed dot dot line), the law of the wall, and $U^+ = y^+$ in the very near wall region.

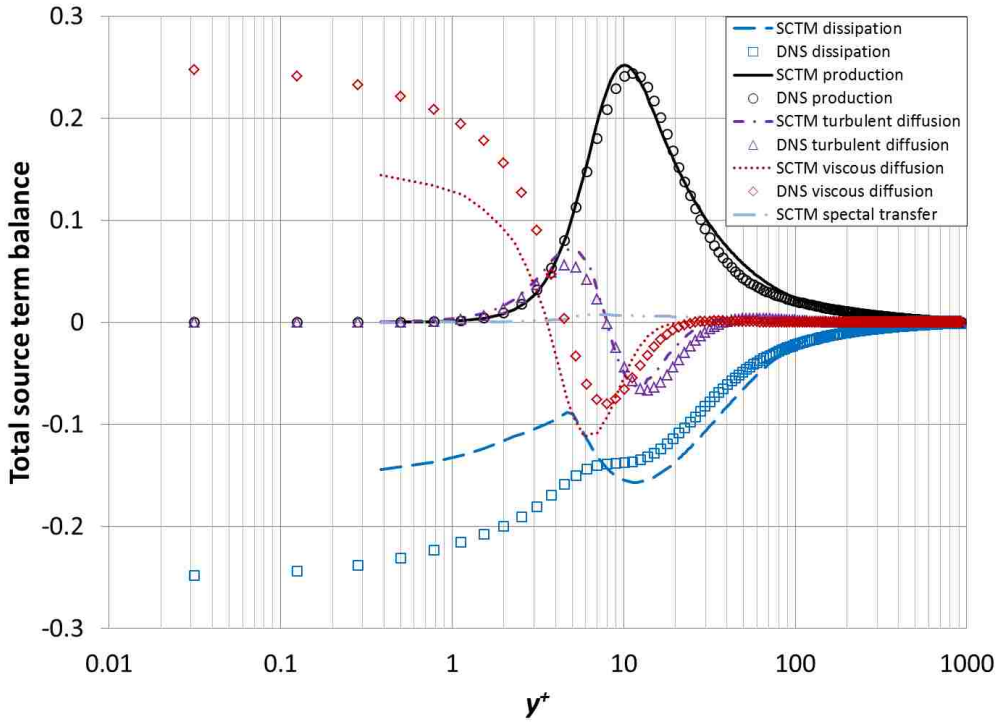

Figure 3.12. Total source term balance for the SCTM (N = 18, Re_τ = 950) in comparison to the DNS results of del Alamo et al. [89].

3.3.2.1 Spectral resolution study

A spectral resolution study was performed for the Re_τ = 950 case where results for N = 5, N = 8, N = 14, N = 18, and N = 22 wave number bins were compared to gauge model performance. The spectral resolution parameter for the different number of wave number bins can be seen in Table 3.3. Clearly, the N = 5 and N = 8 simulations have spectral resolution parameters larger than the suggested maximum value of 2 (§ 3.2) but, as will be shown, acceptable model predictions are still possible. Figure 3.13 displays how turbulent viscosity behaves for the differing number of spectral bins. The N = 5 simulation does show some slightly under-predicted results in comparison to the N = 18 case. However, expected model behavior of convergence to some final solution as the number of bins is increased is observed. Behavior of the remaining mean flow parameters (i.e. mean velocity and TKE) is similar and shown in Figure 3.14.

Table 3.3. Spectral resolution (ξ) values for each of the considered number of bins in the spectral resolution study.

Number of Bins	Spectral Resolution (ξ)
5	3.361
8	2.133
14	1.542
18	1.400
22	1.317

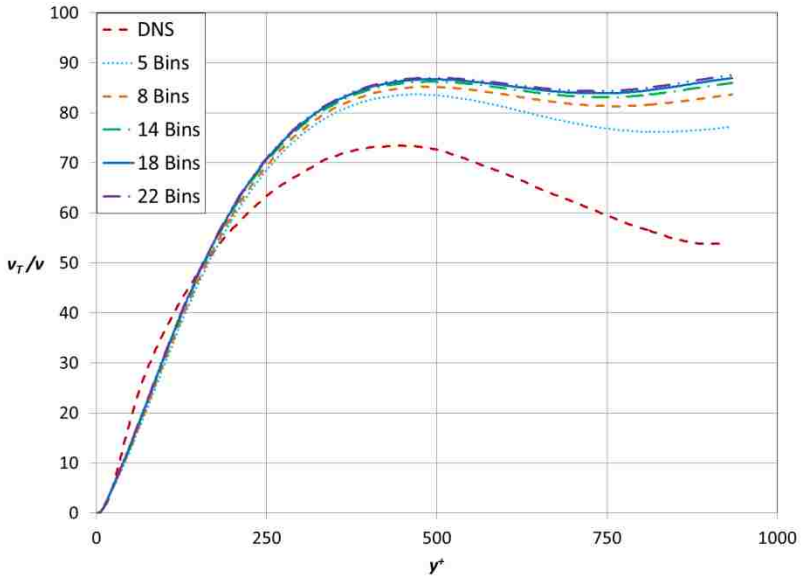

Figure 3.13. SCTM turbulent viscosity (Re_τ = 950) with N = 5 (blue dotted line), N = 8 (orange dashed line), N = 14 (green dashed dot line), N = 18 (solid blue line), and N = 22 (purple dashed dot dot line) wave number bins in comparison to the DNS results of del Alamo et al. [89].

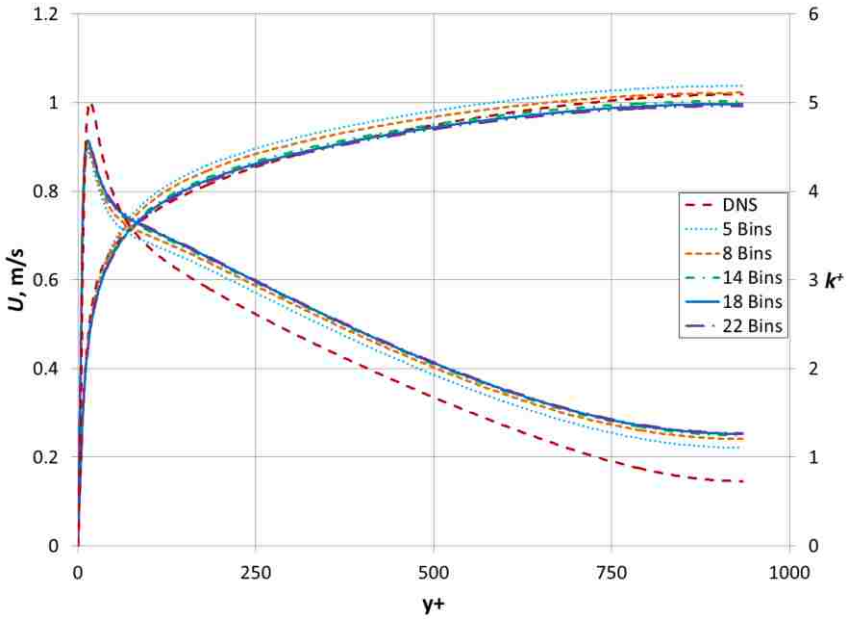

Figure 3.14. SCTM mean velocity and TKE profiles (Re_τ = 950) with N = 5 (blue dotted line), N = 8 (orange dashed line), N = 14 (green dashed dot line), N = 18 (solid blue line), and N = 22 (purple dashed dot dot line) wave number bins in comparison to the DNS results of del Alamo et al. [89].

The TKE spectrum is shown for all of the considered bin numbers in the spectral resolution study at y^+ locations of 930, 560, and 40 in Figure 3.15, Figure 3.16, and Figure 3.17, respectively. Good agreement with the DNS data is observed in the bulk turbulence region away from the wall (y^+ = 930 and y^+ = 560) as well as expected model behavior for different wave number resolutions; namely the higher resolutions (N = 14, N = 18, N = 22) can better predict changes in the slope of the energy spectrum than the lower bin number resolution cases. However, the model is still able to correctly predict the -5/3 slope in the inertial subrange and the changes in energy spectrum behavior even for the very low bin number resolutions of N = 5 and N = 8. Although the smallest allowable spectral resolution for the SCTM has been stated as 2, the presented spectral resolution study has shown that the SCTM is robust since minimal changes are observed even for spectral resolution as high as 3.361 (N = 5). The TKE spectrum in the near wall region (Figure 3.17) fails to predict the change in slope at the transition from the inertial subrange to the dissipation region much like the behavior observed in the Re_τ = 2000 case. Again, this may be due to under-predictions of dissipation and viscous diffusion near the wall. Behavior of the total source term balance was similar for all the different number of bins considered in the spectral resolution study.

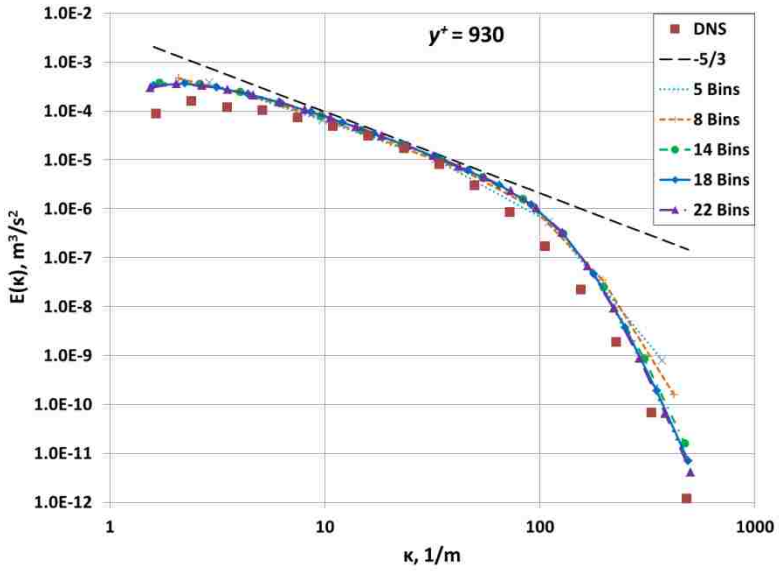

Figure 3.15. SCTM (Re_τ = 950) predictions of the TKE spectrum at y^+ = 930 for 5 (blue "X" symbols), 8 (orange "+" symbols), 14 (green circles), 18 (blue diamonds), and 22 (purple triangles) wave number bins compared to DNS spectrum (red squares) and -5/3 slope (black dashed line).

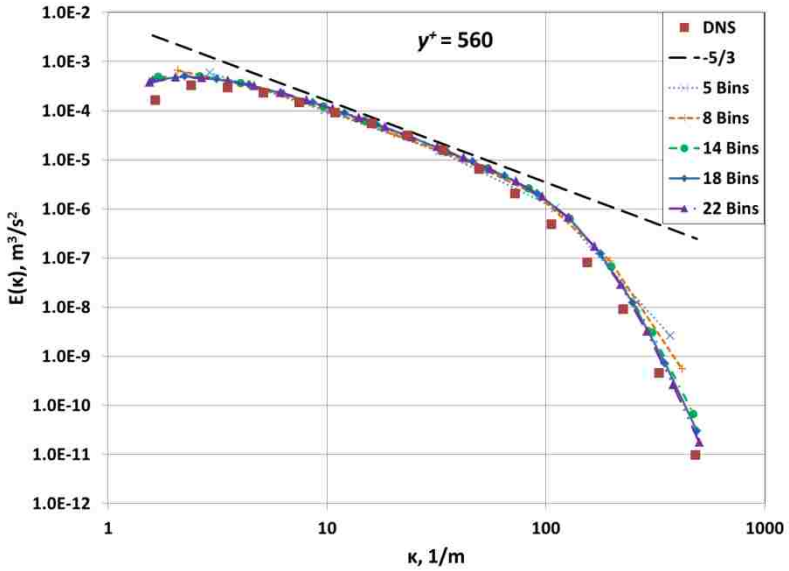

Figure 3.16. SCTM (Re_τ = 950) predictions of the TKE spectrum at y^+ = 560 for 5 (blue "X" symbols), 8 (orange "+" symbols), 14 (green circles), 18 (blue diamonds), and 22 (purple triangles) wave number bins compared to DNS spectrum (red squares) and -5/3 slope (black dashed line).

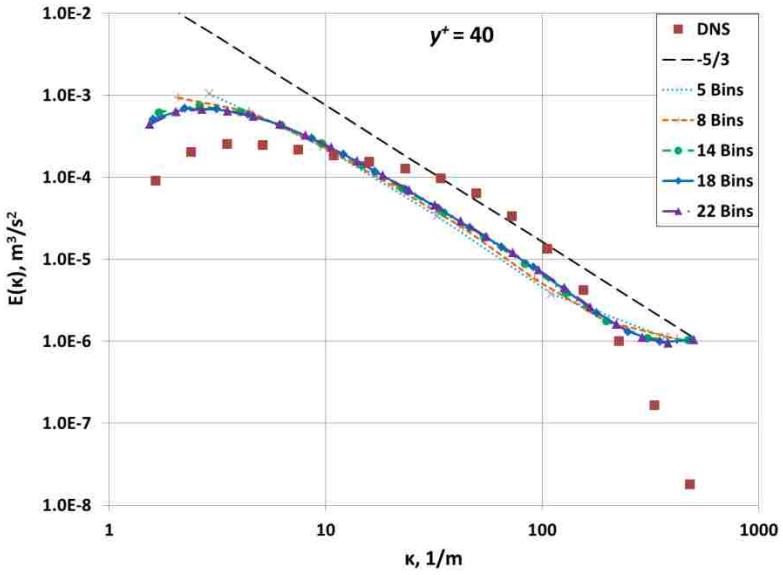

Figure 3.17. SCTM (Re_τ = 950) predictions of the TKE spectrum at y^+ = 40 for 5 (blue "X" symbols), 8 (orange "+" symbols), 14 (green circles), 18 (blue diamonds), and 22 (purple triangles) wave number bins compared to DNS spectrum (red squares) and -5/3 slope (black dashed line).

3.3.3 Re_τ = 550

Figure 3.18 presents a comparison of SCTM (N = 18, Re_τ = 550) mean flow predictions with the DNS data of del Alamo and Jiminez [93] and the Chien k-ε model [25] for the lowest considered Reynolds number used for model calibration and validation. Decent agreement is shown between the SCTM mean velocity and DNS data while acceptable agreement is observed with the TKE magnitude and location. The Chien k-ε model again over-predicts mean velocity in comparison to the SCTM and DNS results. The SCTM missed the prediction of the turbulent viscosity (Figure 3.18(b)) peak. However, the Chien k-ε model predictions are no better than the SCTM and earlier discussion has been given concerning possible reasons for observed disagreement between the DNS results and models. A comparison of the SCTM with the law of the wall (Figure 3.19) shows excellent agreement close to the wall and a flat profile in the applicable logarithmic region although there is some slight under-prediction of mean velocity at moderate y^+ values. Similarly, the Chien k-ε model over-predicts mean velocity behavior in the bulk of the flow.

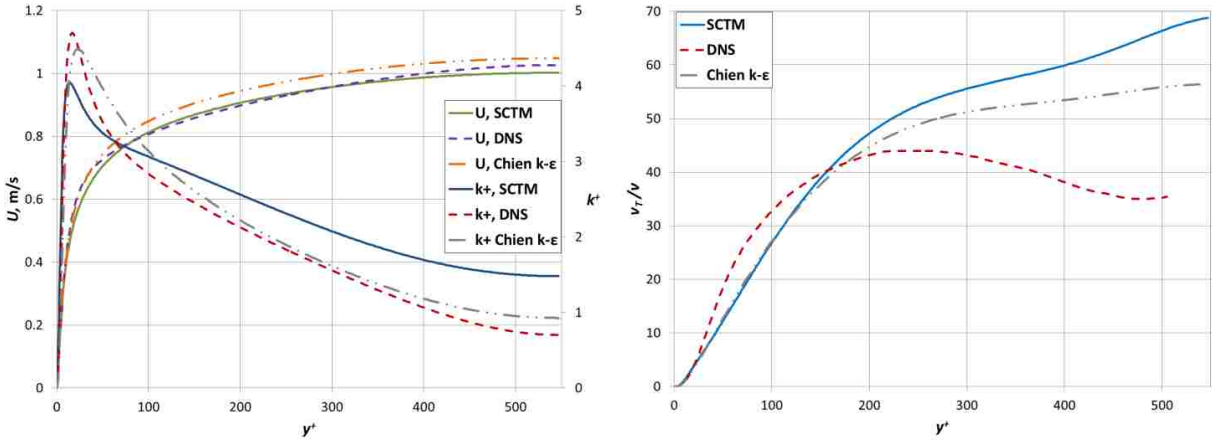

(a) (b)

Figure 3.18. Mean velocity and TKE profiles (a) as well as turbulent viscosity profile (b) obtained by the SCTM (N = 18, Re_τ = 550) in comparison to the DNS data of del Alamo and Jiminez [93] and the Chien k-ε model [25].

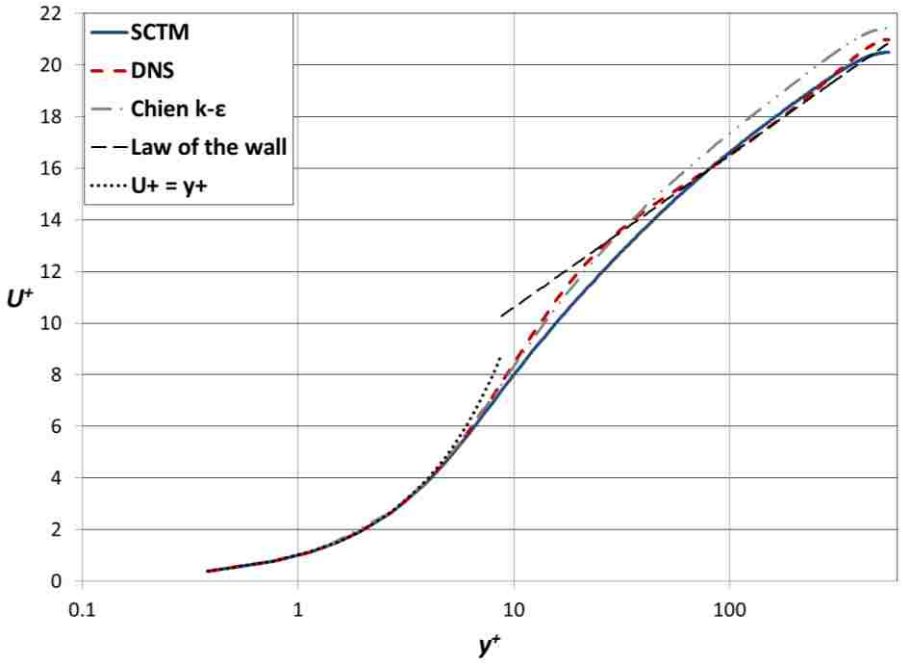

Figure 3.19. Mean velocity profile of the SCTM using eighteen (N = 18, Re_τ = 550) wave number bins (blue solid line) compared to DNS results of del Alamo and Jiminez [93] (red dashed line), the Chien k-ε model [25] (grey dashed dot dot line), the law of the wall, and $U^+ = y^+$ in the very near wall region.

TKE spectrum results for the SCTM (N = 18, Re_τ = 550) are shown in Figure 3.20 in comparison to the theoretical -5/3 slope of the inertial subrange and the overall spectrum shapes are consistent with expectations. Note that at this lower Reynolds number the inner and outer scale separation is reduced but the SCTM can still be validated by the -5/3 slope in the inertial subrange. TKE spectrum results close to the wall for Re_τ = 550 are consistent with results for previous Reynolds numbers and fail to capture the change in slope from the inertial subrange to the dissipation range close to the wall. The total source term balance (Figure 3.21) compares well with DNS results with excellent prediction of peak locations. Consistent with the results at previous Reynolds number, the viscous diffusion and dissipation terms are under-predicted close to the wall.

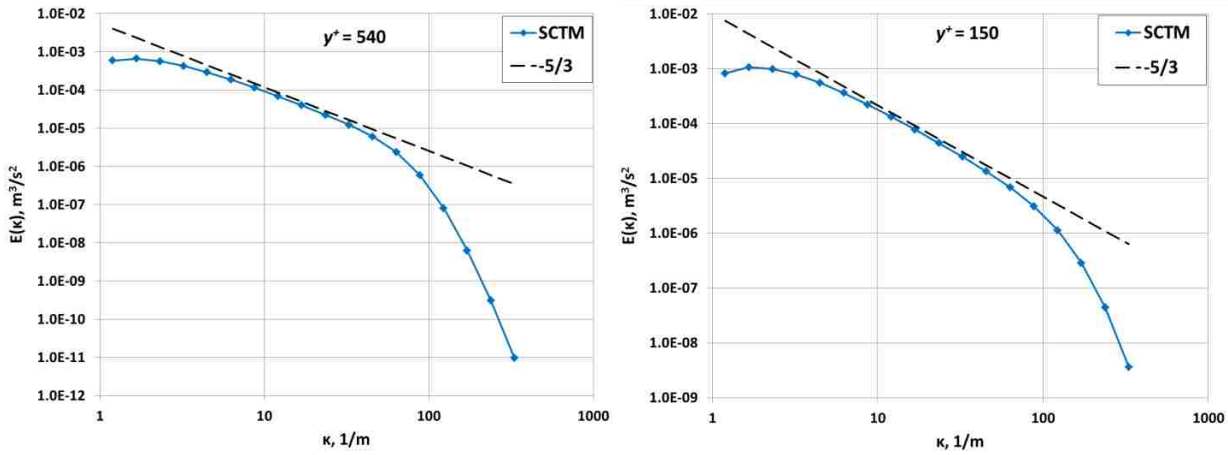

(a) **(b)**

Figure 3.20. SCTM (N = 18, Re_τ = 550) prediction of the TKE spectrum at two different distances from the wall: (a) y^+ = 540 and (b) y^+ = 150 (blue solid line with diamonds) in comparison to the theoretical -5/3 slope (dashed line).

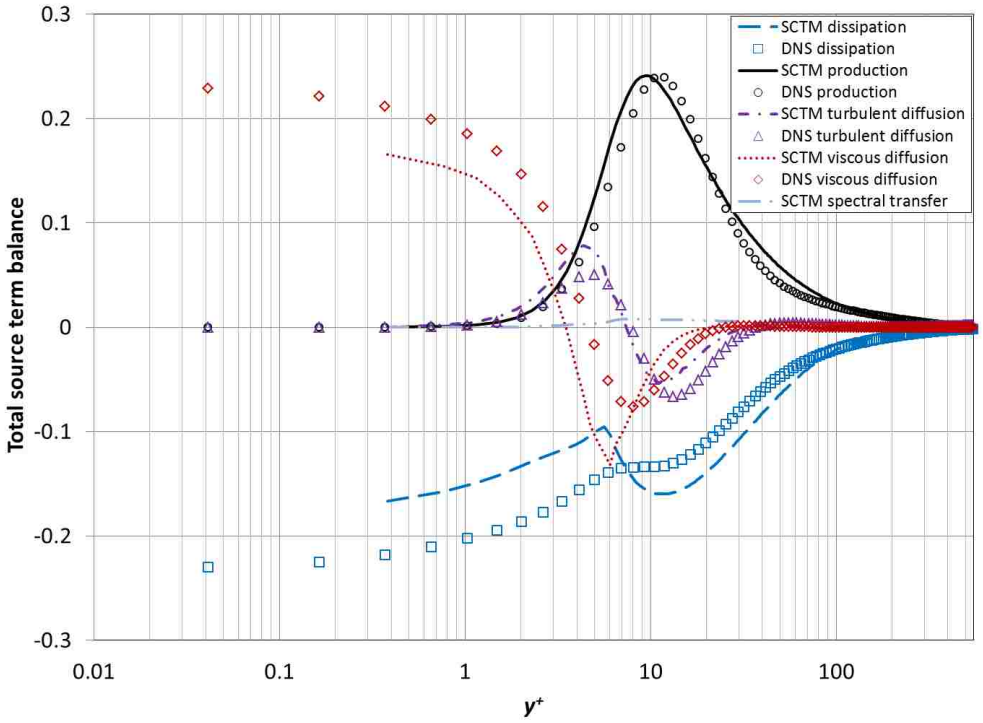

Figure 3.21. Total source term balance for the SCTM (N = 18, Re_τ = 550) in comparison to the DNS results of del Alamo and Jiminez [93].

4. IMPLEMENTATION OF SCTM INTO THREE-DIMENSIONAL M-CFD SOLVER

The completed vision of the SCTM is an advanced multiphase spectral turbulence model for nuclear related applications that provides better flow predictions than current industry standard two-equation models widely used in CFD/M-CFD codes. Therefore, it was a natural step in model development to implement the single-phase SCTM into a 3D M-CFD code and perform model verification and validation with an array of test cases and the existing 1D FlexPDE results.

NPHASE-CMFD is an advanced multiphase computational fluid dynamics code for combined mass, momentum, and energy transfer processes [95] developed by Interphase Dynamics, LLC that was chosen as the 3D M-CFD code for SCTM implementation. NPHASE-CMFD is written in the C programming language with built-in and user defined mechanistic modeling that is integrated with numerics [96]. Highlights of the NPHASE-CMFD code [96] include powerful multiphase capabilities, the use of structured and unstructured grids of arbitrary element type, the ability to model an arbitrary number of fields (fluid components and/or phases), turbulence closure with either low or high Reynolds number k-ε model, parallel processing using the MPI protocol, and the ability to model an arbitrary number of chemical species advected by a chosen field. NPHASE-CMFD has been applied to many challenging multiphase problems. For example, Tiwari et al. [97] used NPHASE-CMFD to perform 3D analyses of single-phase liquid and two-phase dilute particle/liquid flows in U-bend and helical curved conduits. Tselishcheva et al. [98] used NPHASE-CMFD to model two-phase bubbly flow in a horizontal straight pipe and a horizontal pipe with a 90 degree elbow. Behafarid et al. [99] coupled NPHASE-CMFD to the PHASTA DNS code to model fission gas propagation discharged into the coolant channel of a Generation IV sodium fast reactor after a loss-of-flow accident. Waite et al. [100] are continuing to improve dispersed bubbly flow models in NPHASE-CMFD through comparisons of 3D simulations of PWR coolant channels with mixing vanes and spacer grids with the experimental database.

NPHASE-CMFD was chosen for SCTM implementation into a 3D M-CFD code since its capabilities aligned well with the overall model development plan. Implementation into NPHASE-CMFD was important for extending the SCTM to multidimensional problems, taking advantage of high quality meshing software for complex nuclear relevant geometries, using advanced post-processing and visualization tools, using multicore processing, expanding SCTM multiphase

capabilities and numerics, and eventually including the energy equation and heat transfer terms. Implementing the SCTM into NPHASE-CMFD posed challenges, such as the extension from 1D to 3D and numerical convergence that were addressed and are discussed subsequently.

4.1 Repurposing the NPHASE-CMFD Species Transport Equations for the SCTM

NPHASE-CMFD can solve transport equations for an arbitrary number of chemical species, N_s, advected by a chosen field. The species transport equations used in the code assume that the species are well mixed at the molecular level in field-j; sharing the same velocity, pressure, and temperature of the carrier field-j of phase-k [96]. The mass fraction, Y_s, of a particular species-s (s = 1…N_s) describes the mass transfer by convection and diffusion through a conservation transport equation. The conservation transport equation for a particular species-s is defined in Section 4.4 of the NPHASE-CMFD User Manual [96] as:

$$\frac{\partial(\alpha_j \rho_j Y_s)}{\partial t} + \nabla \cdot (\alpha_j \rho_j \overline{v}_j Y_s) = \nabla \cdot \left[\alpha_j \left(\frac{\mu_j}{\sigma_s} + \frac{\mu_j^T}{\sigma_s^T} \right) \nabla Y_s \right] + \Gamma_j''' Y_{sj} + S_s \tag{4.1}$$

where the particular terms are [96]:

Y_s = mass fraction of species-s

μ_j = molecular viscosity for field-j

μ_j^T = turbulent viscosity for field-j

σ_j = laminar species Schmidt number

σ_j^T = turbulent species Schmidt number

Γ_j''' = mass transfer rate due to phase change in field-j and intraphase change from other fields of same phase-k

Y_{sj} = mass fraction of species-s from field-j due to mass transfer

S_s = user implemented species source term

The conservation transport equation is an approximation for the exact species transport mass balance defined in the NPHASE-CMFD User Manual [96] as:

$$\frac{\partial(\alpha_j \rho_j Y_s)}{\partial t} + \nabla \cdot (\alpha_j \rho_j \overline{v}_j Y_s + J_s) = S_s \tag{4.2}$$

where J_s is the mass flux of species-s relative to the mean flow and is modeled by Fick's law of diffusion within NPHASE-CMFD as [96]:

$$J_s = \nabla \cdot \left[\alpha_j \left(\frac{\mu_j}{\sigma_s} + \frac{\mu_j^T}{\sigma_s^T} \right) \nabla Y_s \right] \tag{4.3}$$

The existing numerical framework within NPHASE-CMFD to solve an arbitrary number of species transport equations was an ideal candidate for implementing the SCTM. The conservation transport equation for a particular species-s (Equation (4.1)) is analogous to the SCTM TKE transport equation for a particular bin TKE, k_m, (Equation (3.7)). Therefore, the existing numerical framework can be tailored to solve for bin turbulent kinetic energies rather than species mass fraction by implementing the SCTM source terms on the RHS. Taking the mass transfer rate due to phase change and intraphase change from other fields of same phase-k (Γ_j''') to be zero and substituting in bin TKE (k_m) for species mass fraction (Y_s), the NPHASE-CMFD numerical framework now reads to solve for bin TKE as:

$$\frac{\partial(\alpha_j \rho_j k_m)}{\partial t} + \nabla \cdot (\alpha_j \rho_j \overline{v}_j k_m) = \nabla \cdot \left[\alpha_j \left(\frac{\mu_j}{\sigma_s} + \frac{\mu_j^T}{\sigma_s^T} \right) \nabla k_m \right] + S_m \tag{4.4}$$

where the first term on the RHS is J_s shown in Equation (4.3), or the diffusion term D_m (Equation (3.25)) in the SCTM formulation. The remaining RHS terms of the bin TKE equation (Equation (3.7)) then need to be implemented into NPHASE-CMFD to form the user implemented species source term for bin-*m* such that:

$$S_m = P_m + \varepsilon_m^p + \varepsilon_m^y + T_m \tag{4.5}$$

where the definitions of SCTM bin-*m* production (P_m), homogeneous dissipation (ε_m^p), inhomogeneous dissipation (ε_m^y), and spectral transfer (T_m) were given in § 3.2.

Using the NPHASE-CMFD numerical framework for the species equations tailored to the SCTM provides the bin TKE values that are then fed into the SCTM formulation for turbulent viscosity. The turbulent viscosity is then fed back into the normal code structure for the RANS equations with NPHASE-CMFD (Figure 4.1).

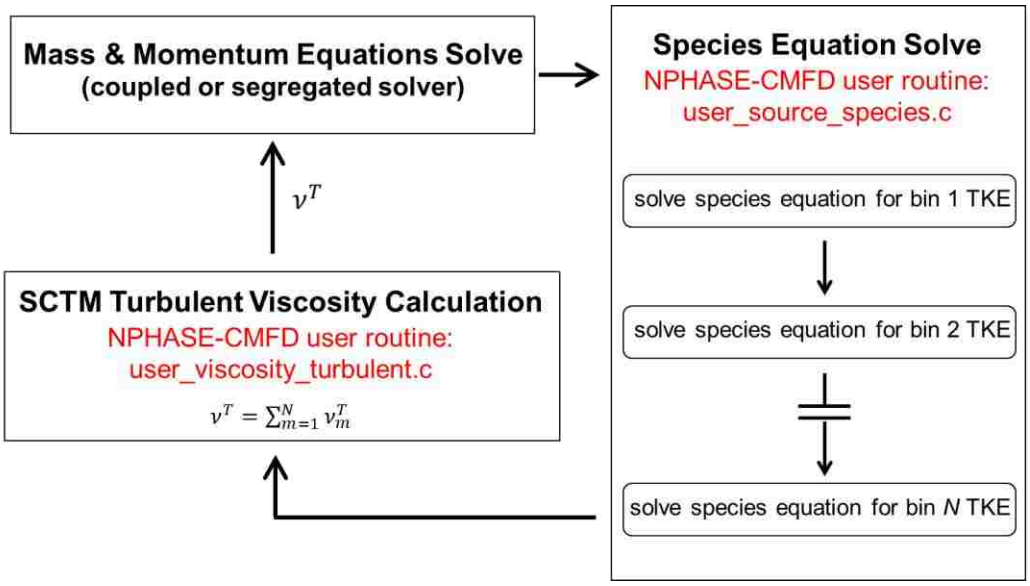

Figure 4.1. NPHASE-CMFD iteration process with species equations tailored to SCTM.

4.2 NPHASE-CMFD Code Structure

NPHASE-CMFD is not an open source code and the user is allowed access to the code internals only through so-called "user routines" that allow for accessing at certain points and performing a given task that alters NPHASE-CMFD equations (e.g. the inclusion of a user source term for the momentum equations or user drag coefficient formulation). The user routines are compiled and linked into the binary executable before program execution [101]. User routines are denoted by the *user_TASK.c* form, where '*TASK*' references some specific coding where the user routine is called from the source code. For example, the *user_viscosity_turbulent.c* and *user_source_species.c* routines that are used by the SCTM (Figure 4.1) are intuitively named for user control of the turbulent viscosity and species source term.

The low-Reynolds number k-ε option must be activated in NPHASE-CMFD to apply the turbulent fluxes near the wall in the momentum equations. Therefore, this option must remain on in the NPHASE-CMFD input so that the SCTM turbulent viscosity is applied in the near-wall region. To eliminate influences of the k-ε equations on the overall simulations in terms of momentum source and computation time the false time step for both k and ε are set to very small values (1.0×10^{-30}) while the solver sweeps for k and ε are both set to zero. This eliminates the k-ε equations while

simultaneously taking advantage of the NPHASE-CMFD use of the turbulent fluxes in the momentum equation.

Some information is required by NPHASE-CMFD to use the SCTM for the calculation of turbulent viscosity. The *user_initialize.c* routine is used for control of the input parameters for the SCTM. In this routine the user can define model constants, wave number boundaries, initial bin TKE values, etc. The calculation of all RHS source terms is controlled from the *user_source_species.c* routine. The overall turbulent viscosity for the NPHASE-CMFD RANS equations is calculated in *user_viscosity_turbulent.c* after calculation of the bin turbulent viscosities. Appendix B provides a more in-depth look at the SCTM numerical implementation into NPHASE-CMFD.

4.3 Verification and Validation

Verification and validation are required to increase confidence in CFD solutions. Simply stated by Roache [102], verification refers to "solving the equations right" and validation refers to "solving the right equations". To expand upon these simple explanations: verification is the process of determining that the programming and computational implementation of the model is correct while validation is the process of determining that the results of the model agree with experimental results and analytic solutions [103]. Verification and validation were both important steps to ensure the SCTM provides acceptable physical results within the framework of NPHASE-CMFD. The NPARC Alliance (a collaboration between NASA Glenn Research Center and Arnold Engineering Development Complex) has outlined six steps for the verification process of a CFD code [103]: (i) examine the computer programming of the code; (ii) examine iterative convergence; (iii) examine consistency; (iv) examine grid convergence; (v) examine temporal convergence; (vi) compare code results to accurate solutions. For example, examining consistency ensures that mass is conserved in flow through a channel. These six steps were taken into account as the SCTM was implemented into NPHASE-CMFD. The SCTM had previously only been evaluated as a 1D formulation with the FlexPDE solver. Therefore, additional issues that arose in the extension to a 3D M-CFD formulation were met with the verification and validation process in mind.

5. SINGLE-PHASE FLOW RESULTS

In this chapter, single-phase results using the SCTM in NPHASE-CMFD are presented for various tests cases. The test cases were chosen for verification of the SCTM implementation and validation of the SCTM performance. Each test case has an abbreviated name and is discussed separately as to why it was performed for verification and validation of the SCTM.

5.1 FT1: Flow Through

The flow through test was quite simple but necessary to evaluate if some initial assumptions about the code behavior were correct. The flow domain was a square channel with symmetry boundary conditions on the top, bottom, left, and right walls; an inlet flow boundary with flow only in the positive-x direction; and an outlet pressure boundary. The species source term and SCTM turbulent viscosity were both artificially set equal to zero. The turbulent kinetic energy and dissipation values for the NPHASE-CMFD k-ε equations were set to equal values and the small false time step and zero solver sweep options were used. The purpose of this test was then a simple check to see that no external source terms act upon the implemented SCTM equations and that the bin TKE values remained constant as advected through the channel. The flow through test also showed that the small false time step and zero solver sweep options can effectively "turn off" the k-ε equations. The results of the flow through tests were as expected.

5.2 DT1: Single-Phase Decay of Isotropic Turbulence

Bolotnov et al. [10] have previously shown that the SCTM performs well for single-phase decay of isotropic turbulence and that in the absence of mean flow gradients the single-phase SCTM equation for TKE in bin-*m* reduces to the spectral transfer and dissipation terms. In the current model formulation for the decay problems, only the homogeneous dissipation term remains such that:

$$\frac{Dk_m}{Dt} = T_m - \varepsilon_m^p \tag{5.1}$$

However, implementation into a 3D M-CFD code, where the initial condition is advected along the flow direction, stipulates a non-zero spatial diffusion term in the flow direction. The DT1 test was

performed to show that the diffusion term can be handled naturally by NPHASE-CMFD (Equation 4.3) and that the spectral transfer and homogeneous dissipation terms were correctly implemented. The DT1 test also showed that the repurposing of the species equations was a suitable method for solving the individual bin TKE values in NPHASE-CMFD.

Kang et al. [104] investigated nearly isotropic turbulence downstream of an active grid at high Reynolds number ($Re_\lambda \approx 720$) and Bolotnov et al. [10] used this data to calibrate the SCTM spectral transfer constants. Kang et al. provided data at four measuring stations downstream of the active grid as well as an analytic formulation to produce the TKE spectrum dependent on flow length scales and dissipation rate. The Kang et al. data was used for validation in the DT1 test.

Square duct geometry with symmetry boundary conditions on all four walls, an inlet boundary condition, and outlet pressure boundary condition was used for the DT1 test. Meshes were first considered with resolution only in the stream-wise (x) direction. One of these meshes (M1 mesh) is shown in Figure 5.1. Air properties at 20 ℃ were used (ρ = 1.2047, μ = 1.821x10^{-5}) to match the kinematic viscosity (ν = 1.511 x10^{-5}) in the experimental data. A constant inflow *x*-direction velocity of 12.0 m/s was prescribed. The data at the first measuring station (x/M = 20 where M is the mesh size of the turbulence-generating grid) was used as the TKE spectrum at the duct inlet.

Figure 5.2 shows the decay of TKE as a function of distance from the inlet for the Kang et al. data and the SCTM. The experimental data is shown at the four downstream measuring stations (non-dimensionalized by the grid size, M) at x/M = 20, x/M = 30, x/M = 40, and x/M = 48. SCTM results for three consecutively refined computational meshes of M1 = 125 elements, M2 = 500 elements, and M3 = 2000 elements are shown. The SCTM simulations were taken to be converged in NPHASE-CMFD when residuals for the species equations reached an order of 10^{-16}. For all the data shown in Figure 5.2 the total TKE was calculated by integrating the energy spectrum. Clearly, the SCTM provides excellent prediction of the spatial TKE decay for each of the considered mesh resolutions.

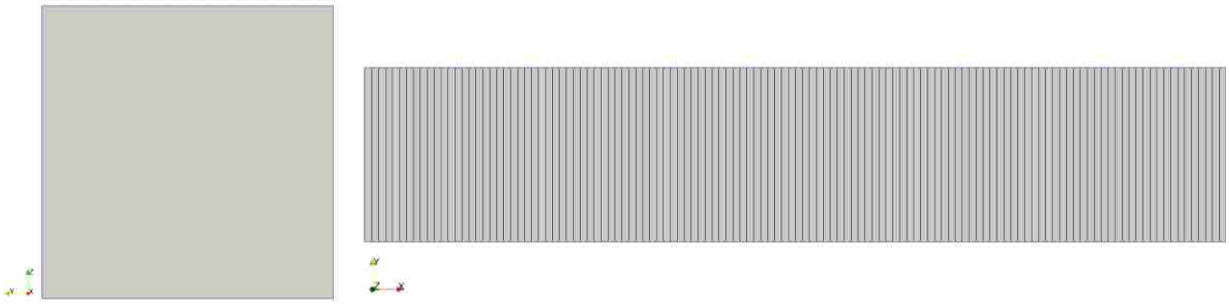

Figure 5.1. M1 mesh with 125 elements in the stream-wise (x) direction.

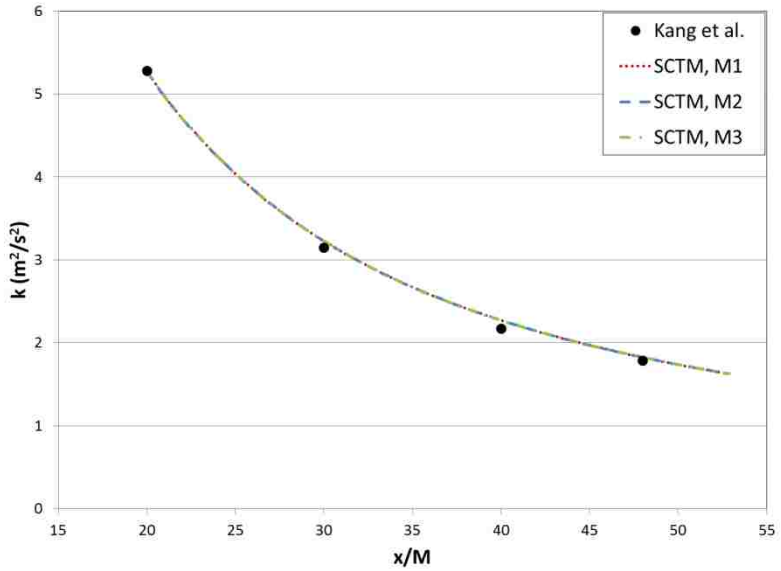

Figure 5.2. SCTM prediction (*N* = 21) of decay of TKE as a function of distance from the inlet (non-dimensionalized by the turbulence-generating grid size, M) for meshes M1, M2, and M3 compared with the experimental data of Kang et al. (symbols).

Spectral results for the SCTM versus the Kang et al. experimental data (Figure 5.3) indicate that the SCTM performs quite well and slightly better at the highest wave numbers for increased mesh resolution. Computational time requirements were considerably increased with increased mesh resolution. The M1 mesh required just 6.9 seconds of total simulation time while the M3 mesh required about 38 minutes. This increase in computational effort is an important realization from the DT1 verification test. Simulations with 14 and 24 wave number bins were also performed (Table 5.1) on the M2 mesh to further assess computational costs of the SCTM (Figure 5.4). These simulations showed that the increase in computational time per iteration scaled exactly linearly with

increased bin resolution. The average times per 100 iterations were 1.81, 2.77, and 3.16 seconds for the 14, 21, and 24 bin simulations, respectively. Figure 5.4 also includes the predictions of the k-ε model available in NPHASE-CMFD and shows that the SCTM better predicts the experimental data. The average cost per 100 iterations using the k-ε model was 0.22 seconds.

Table 5.1. Spatial and spectral representation of performed tests (green) for single-phase decay of isotropic turbulence.

Spectral \ Spatial	M1	M2	M3
$N = 14$			
$N = 21$			
$N = 24$			

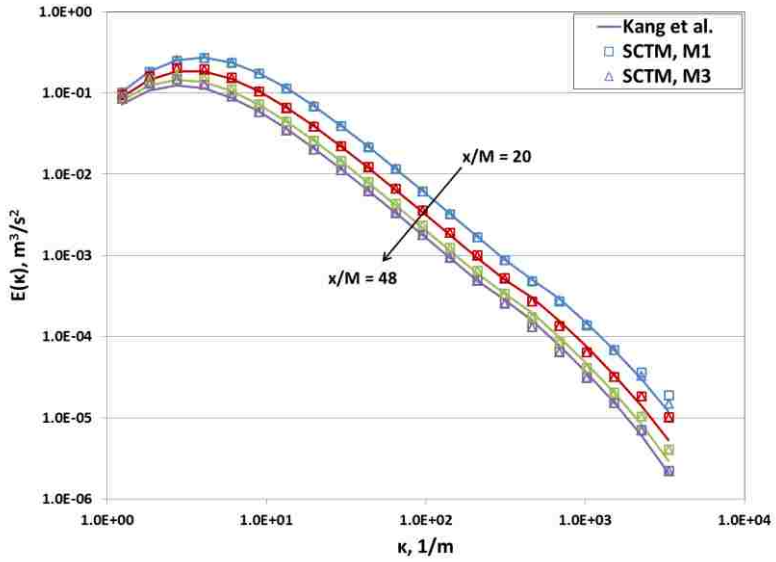

Figure 5.3. Spectral evolution of TKE decay. Shown for the SCTM using M1 (squares) and M3 (triangles) meshes as well as the experimental data of Kang et al.

Thus far, results for the DT1 test were all produced on an essentially 1D mesh such as that shown in Figure 5.1. Simulations were also performed on a mesh with 10 elements each in the *y* and *z* coordinate directions as a simple verification that resolving the mesh in the *y* and *z* directions does not affect the solution. These results were identical to the previously presented results, as expected.

As stated in § 4, implementing the SCTM into a 3D M-CFD code provides the ability to take advantage of high quality post-processing software. Paraview [105] is such software and is able to read the post-processing files from NPHASE-CMFD. Figure 5.5 shows how Paraview can be used to more schematically represent SCTM results from NPHASE-CMFD. The decay of TKE along the duct length is shown for the M3 mesh using 21 wave number bins.

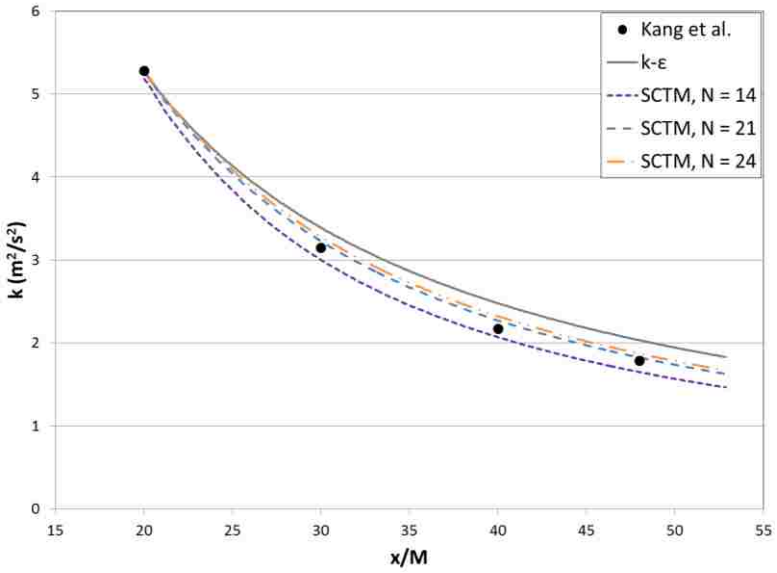

Figure 5.4. SCTM prediction of decay of TKE as a function of distance from the inlet (non-dimensionalized by the grid size, M) using 14, 21, and 24 wave number bins compared with the experimental data of Kang et al. (symbols) and the k-ε model.

The results of the DT1 test showed that the spectral transfer and homogeneous dissipation terms were correctly implemented into NPHASE-CMFD and that the re-purposing of the species equations was an acceptable method of solving for the SCTM bin TKE values. The DT1 test also showed iterative convergence and conservation of total mass through the duct.

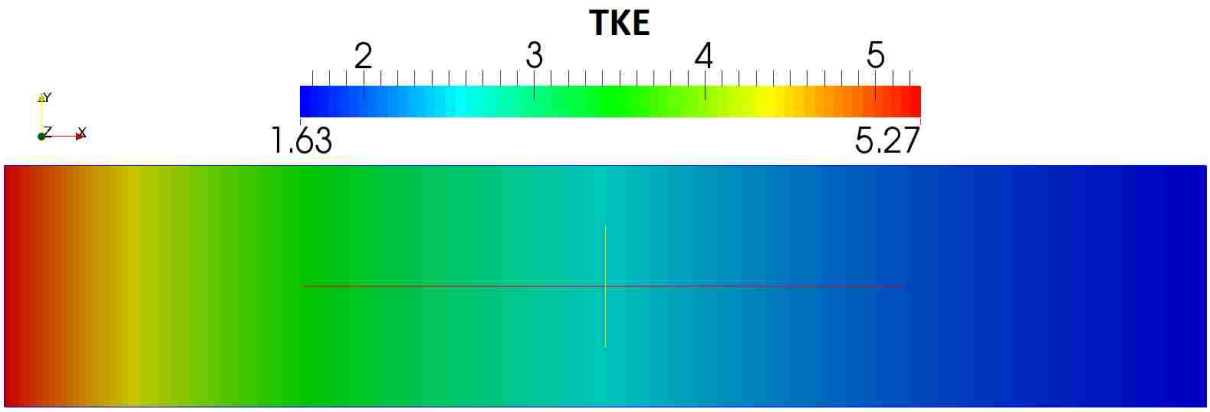

Figure 5.5. SCTM prediction of the TKE decay as a function of spatial position along the duct.

5.3 TCF1: Single-Phase Turbulent Channel Flow

The plane channel flow geometry predicted with the SCTM using FlexPDE (§ 3.3) was an excellent starting point for verification of the wall-resolved SCTM in NPHASE-CMFD. Previous tests (§ 5.1 – 5.2) showed that the k-ε equations could be effectively turned off in NPHASE-CMFD and that repurposing the chemical species equations was an acceptable method for solution of the SCTM TKE transport equations. The DT1 test showed that NPHASE-CMFD handles the diffusion term and that the spectral transfer and homogeneous dissipation terms were correctly implemented. For the single-phase turbulent channel flow test (TCF1) the spectral production and inhomogeneous dissipation terms were implemented as well as the calculation of turbulent viscosity.

Both model performance and numerical convergence are exceedingly important in complex turbulence model development, particularly for highly non-linear models such as the SCTM. The spectral production and inhomogeneous dissipation terms, along with the calculation of turbulent viscosity, were first implemented into NPHASE-CMFD exactly as presented in § 3.2 as used in 1D FlexPDE. Although initial results for the SCTM in NPHASE-CMFD showed that model behavior was converging towards the 1D FlexPDE solution a few conclusions were drawn. The formulation for inhomogeneous dissipation (Equation (3.16)) contained the derivative of mean velocity. This caused numerical issues for predominately two reasons: (i) in CFD calculations the mean velocity on the inflow is generally prescribed as a constant across the manifold which leads to high values of the gradient early in the simulation (due to prescribed no-slip wall boundary conditions) before fully-

developed flow conditions; (ii) NPHASE-CMFD uses the *production destruction clip ratio* [96], or the ratio of turbulent production to turbulent dissipation, to limit the shear-induced turbulence during early iterations and this approach should be used with the SCTM as well. Therefore, if the turbulent dissipation contains the mean flow gradient then limiting turbulent production based on turbulent dissipation rate becomes non-sensible and the calculations become increasingly numerically stiff. As shown previously, SCTM predictions with 1D FlexPDE for the overall energy budget (Figure 3.8(d), Figure 3.12, Figure 3.21) under-predicted the dissipation close to the wall that is controlled by inhomogeneous dissipation. After careful deliberation, the most practical plan of action was then to improve both model behavior and numerical convergence by implementing a modified inhomogeneous dissipation term from that shown previously in Equation (3.16). The improved inhomogeneous dissipation term is shown in § 5.3.1 and a method for improving the convergence behavior and numerical stability of the SCTM in NPHASE-CMFD is shown in § 5.3.2.

5.3.1 Improved Inhomogeneous Dissipation Term

The improved inhomogeneous dissipation term was formulated based on Equation 4.222 presented in Wilcox [13]:

$$k \sim y^2 \;\; and \;\; \frac{\varepsilon}{k} \to \frac{2\nu}{y^2} \;\; as \;\; y \to 0 \tag{5.2}$$

such that the SCTM inhomogeneous dissipation term for bin-*m* is now:

$$\varepsilon_m^y = \frac{2\nu k_m}{y^2} \exp(-0.15 y^+) \tag{5.3}$$

where *y* is the physical distance to the closest wall and the exponential term remains to ensure that the inhomogeneous dissipation term has no effect outside of the near-wall boundary layer. Note that this modified inhomogeneous dissipation term eliminated two model constants $(C_{\varepsilon 1}, C_{\varepsilon 2})$ while simultaneously reducing numerical stiffness and, as will be shown, providing better predictions of the DNS dissipation shape and TKE. Note that this term is similar to the Chien k-ε boundary condition for dissipation close to the wall as shown in Equation (1.15).

The modification of the inhomogeneous dissipation term required that the model constants be altered slightly to account for the difference in SCTM formulation. All the parameters are as

exactly as presented in the 1D formulation (§ 3.2) except the turbulent viscosity damping terms that now have the following forms:

$$\begin{aligned} f_y &= [1-\exp(-1.6y\bar{\kappa}_m)]^{1/4} \\ f_\mu &= 1.0-\exp(-0.007y^+) \\ f_s &= 1.0-\exp\left(-125.0\frac{\bar{\kappa}_m}{\kappa_N}\right) \end{aligned} \tag{5.4}$$

Although the model formulation would ideally remain the same in the transition from the 1D solver to the 3D M-CFD code the need for improved performance and numerical convergence required that it should be modified. It is also important to note that the previous formulation contained a model constant calibrated in the f_μ term (Equation (3.22)) calculated by the Reynolds number based on friction velocity. This is intuitive in the previous 1D work where the friction velocity (u_τ) was known *a priori* but is not so intuitive when the model is extended to flow scenarios where the friction velocity is not known *a priori* and can be more difficult to quantify in a 3D calculation on each iteration. All the SCTM calculations using NPHASE-CMFD in the present work were performed with identical model constants (§ 3.2, Equation (5.4)). It is expected that some model constant adjustment based on mean flow parameters, such as what is done for traditional wall-resolved two-equation models (Equations (1.10) – (1.15)) [13], will be required for future endeavors with the SCTM. However, at this time an adjustable model constant would stand to degrade the physical arguments and the form of these constants will be more suitably determined as more test cases are performed. A survey over the whole results database should be completed with continued model development beyond the current scope. Equation (5.4) contains the model constants expected to need calibration as the SCTM is applied to more turbulent flows. In the future, adjustment of the model constants based on turbulent flow parameters will improve model performance over a wide range of applications.

5.3.2 Variable Relaxation Factors

NPHASE-CMFD uses relaxation factors for flow field variables to improve numerical convergence by the addition of numerical damping [96]. For a given variable, ϕ, the value at the next iteration ($n+1$) is updated by:

$$\phi^{n+1} = \beta\phi^{n+k} + (1-\beta)\phi^n \tag{5.5}$$

where β is the value of the relaxation factor and the $n+k$ index indicates the calculated value of ϕ at the next iteration. Note that a relaxation factor of *zero* would provide no solution advancement and that a value of *one* would provide no numerical damping. The relaxation factors have been altered based on the wave number bins to control numerical convergence with the SCTM. Considering the large difference in time scales between the largest and smallest eddies present in the flow it makes sense that the transport equations for different size eddies have different convergence "speeds". Therefore, an option was included with the SCTM in NPHASE-CMFD to turn on variable relaxation factors. With this option, the relaxation factor for a particular bin TKE equation is defined as:

$$\beta_m = \frac{\beta^{max}}{\sqrt{\bar{\kappa}_m}} \tag{5.6}$$

where β^{max} is the user-defined relaxation factor value. Equation (5.6) specifies that the largest eddy sizes have the largest relaxation factor values and therefore the fastest convergence speed and vice versa. This eliminates some numerical issues at the smallest eddy sizes where the transfer term can dictate negative TKE values when the simulation is far from the solution such as in the initial iterations. Testing has shown that after the solution has evolved the variable relaxation factor can be turned off and the solutions are consistent.

5.3.3 Meshing

The numerical mesh setup used to test the SCTM in the TCF1 case was essentially 1D since boundary lower growth occurs off the lower wall and the other three walls of the duct are assigned symmetry (no-slip) boundary conditions in NPHASE-CMFD. Figure 5.6 shows the cross-sectional view of a numerical mesh with 48 elements in the direction parallel to the solid wall boundary and Figure 5.7 shows how the stream wise velocity and TKE compare for this 48 element mesh with a higher resolution mesh with 199 elements in the direction parallel to the solid wall boundary. Clearly, the predictions are nearly identical. All the following results shown here were simulated on the lower resolution mesh with 48 elements in the direction normal to the solid wall boundary. The length-over-diameter (LOD) of the mesh was equal to 200.

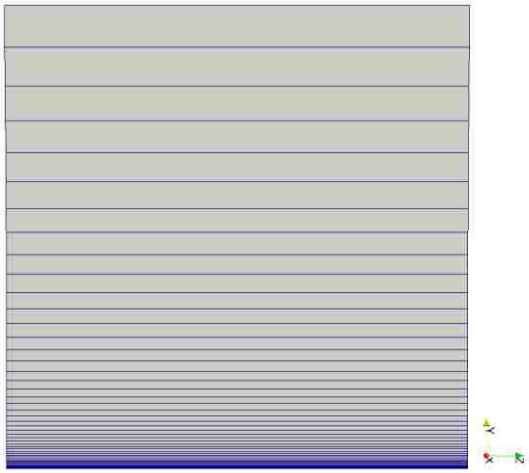

Figure 5.6. Cross-sectional view of a numerical mesh with 48 cells in the direction parallel to the wall boundary.

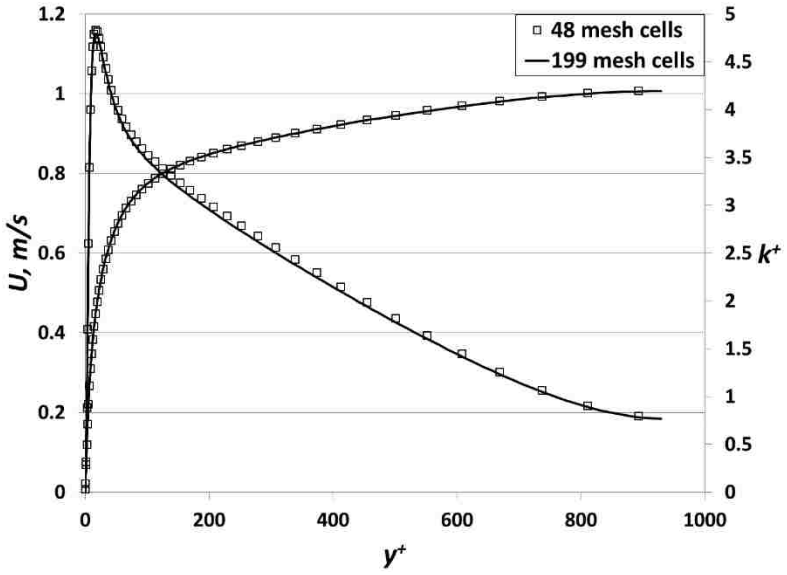

Figure 5.7. Stream-wise velocity (left vertical axis) and non-dimensional TKE (right vertical axis) predicted by SCTM in NPHASE-CMFD using two different mesh resolutions (N = 5, Re_τ = 950).

5.3.4 Re_τ = 2000

SCTM predictions using NPHASE-CMFD for the highest considered Reynolds number case are shown in Figure 5.8 – Figure 5.10 in comparison to previously shown SCTM predictions using

FlexPDE and the DNS data. Most notably, the SCTM with improved inhomogeneous dissipation term implemented into NPHASE-CMFD provides exceedingly better results for the TKE (Figure 5.8(b)). Results for stream-wise velocity (Figure 5.8(a)) and turbulent viscosity (Figure 5.9(a)) differ from the estimates with FlexPDE. The location of the turbulent viscosity peak is not predicted as well with NPHASE-CMFD while the peak magnitude is better captured. The total turbulent dissipation shape (Figure 5.9(b)) is captured better as well and much improved from the previous result with FlexPDE (Figure 3.8(d)). The SCTM is somewhat able to capture the inflection point in the turbulent dissipation shape around y^+= 10. The total spectral transfer term sums to zero as expected and does not contribute to the overall TKE budget. Note that the viscous/turbulent diffusion terms are not included in the total source terms plot (Figure 5.9(b)) since only the turbulence production, homogeneous dissipation, inhomogeneous dissipation, and spectral transfer terms are the user-defined functions supplied to NPHASE-CMFD (see Equation (4.5)).

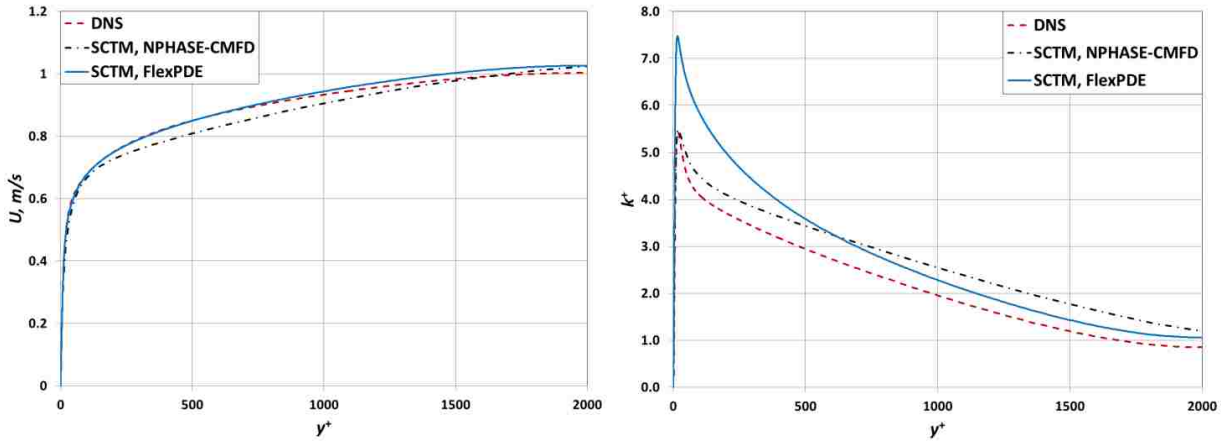

Figure 5.8. SCTM predictions (N = 18, Re_τ = 2000) of stream wise velocity (a) and TKE (b) using NPHASE-CMFD (black dashed dot line) in comparison to SCTM prediction using FlexPDE (solid blue line) and DNS data (red dashed line) of Hoyas and Jiminez [29].

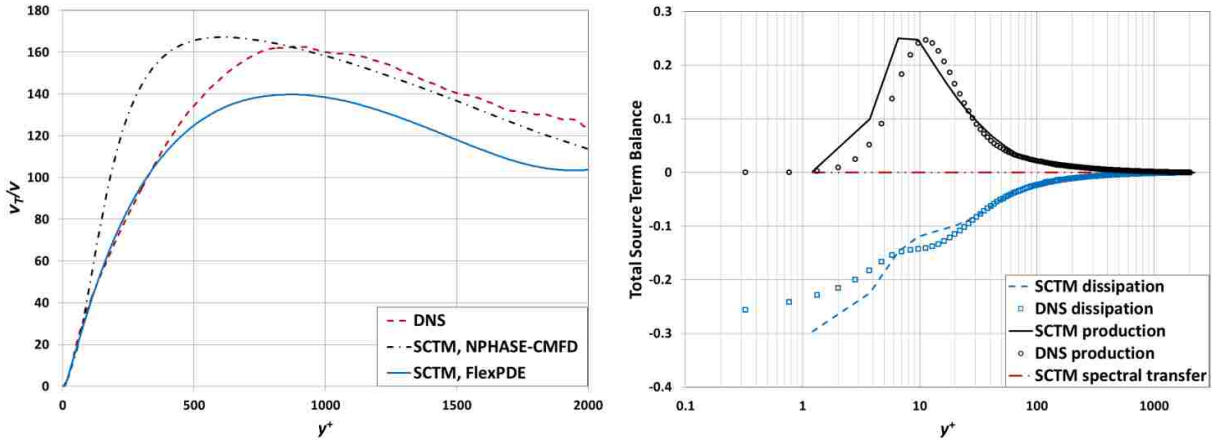

(a) **(b)**

Figure 5.9. (a): SCTM prediction (N = 18, Re_τ = 2000) of turbulent viscosity in comparison to SCTM prediction using FlexPDE (solid blue line) and DNS data (red dashed line) of Hoyas and Jiminez [29]. (b): Total source term balance of SCTM using NPHASE-CMFD in comparison to DNS data of Hoyas and Jiminez [29].

Spectral energy results are shown at two y^+ locations in Figure 5.10 and the SCTM predictions using NPHASE-CMFD are very similar to those from FlexPDE. There is still some discrepancy closer to the wall (Figure 5.10(a)) where there is a build-up of energy in the high wave number range. Although the dissipation shape is much better represented with the new formulation for inhomogeneous dissipation the SCTM still fails to capture the change in energy spectrum slope in the transition from the inertial subrange to the dissipation range for the Re_τ= 2000 case.

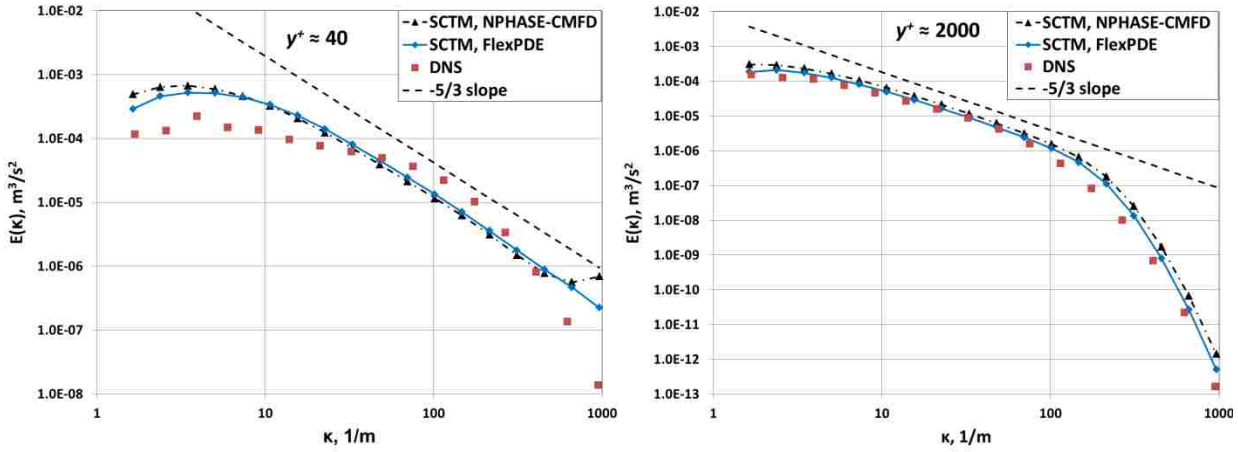

(a) **(b)**

Figure 5.10. SCTM (N = 18, Re_τ = 2000) prediction of the TKE spectrum using NPHASE-CMFD (black triangles) and FlexPDE (blue diamonds) in comparison to the DNS data (red squares) and -5/3 slope (dashed line) at y^+ = 40 (a) and y^+ = 2000 (b).

Results from the Re_τ= 2000 case rendered in Paraview are shown in Figure 5.11 – Figure 5.13. The output capabilities of NPHASE-CMFD allow different bin contributions to the TKE to be viewed over the whole geometry as well as an *x*-axis slice showing behavior normal to the solid wall boundary (Figure 5.11). The stream-wise velocity is shown as an *x*-axis slice at LOD = 180 location (Figure 5.12) as well as over the total channel length (Figure 5.13). Clearly, the uniform velocity at the inlet requires some length to reach fully-developed flow. Comparisons of data at different measuring stations along the channel length have shown that fully developed flow is achieved.

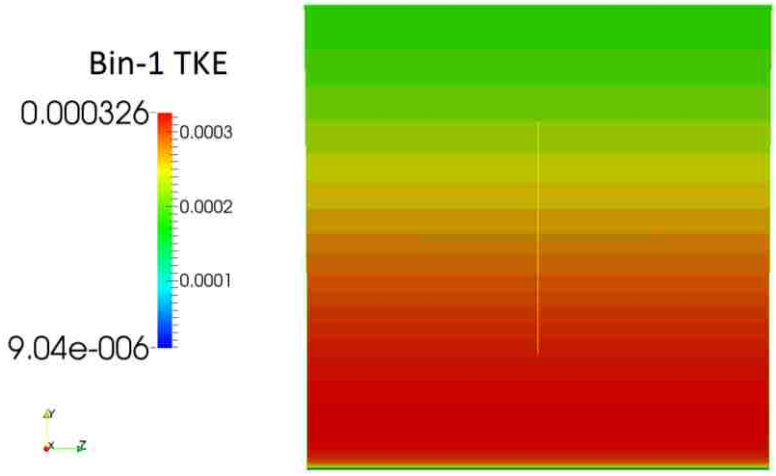

Figure 5.11. SCTM (N = 18, Re_τ = 2000) prediction using NPHASE-CMFD rendered in Paraview for the bin-1 TKE shown at stream-wise location LOD = 180 as a slice along the x-axis.

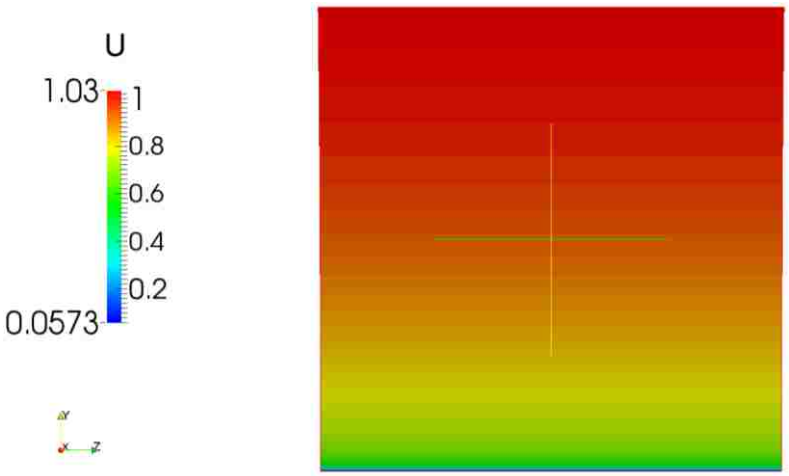

Figure 5.12. SCTM (N = 18, Re_τ = 2000) prediction using NPHASE-CMFD rendered in Paraview for the stream-wise velocity shown at stream-wise location LOD = 180 as a slice along the x-axis.

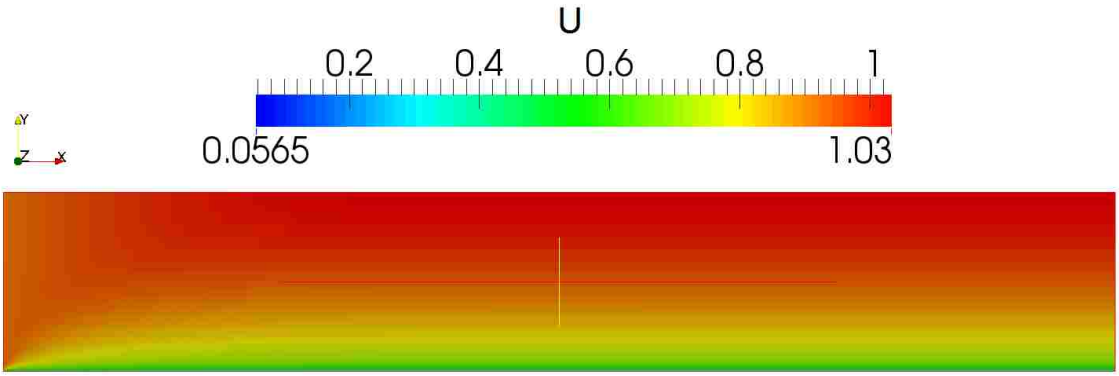

Figure 5.13. SCTM (N = 18, Re_τ = 2000) prediction using NPHASE-CMFD rendered in Paraview for the stream-wise velocity along the channel length. Shown here is a slice stream-wise along the z-axis and scaled to one thirty-second of the total channel length.

5.3.5 Re_τ = 950

SCTM predictions using NPHASE-CMFD are similar to those from FlexPDE for Re_τ= 950 for the stream-wise velocity (Figure 5.14(a)) while the TKE is better predicted (Figure 5.14(b)). Although the turbulent viscosity magnitude prediction is further from the DNS data using NPHASE-CMFD (Figure 5.15(a)) the shape of the DNS curve is better modeled using NPHASE-CMFD. The total source term balance shows (Figure 5.15(b)) that the production peak is slightly closer to the wall than the DNS data. However, as with the higher Reynolds number case discussed previously, the new formulation for inhomogeneous dissipation provides a vastly improved prediction of the overall shape of the turbulence dissipation curve from DNS and again is able to capture the deflection point in the curve around y^+= 10. The overall spectral transfer term sums to zero as expected and does not contribute to the TKE budget.

Spectral energy results at Re_τ= 950 are shown in Figure 5.16 for two different distances from the solid wall boundary. The SCTM results from NPHASE-CMFD are very close to those from FlexPDE. Although the model formulation has been slightly altered between predictions from the two numerical tools the similar behavior is encouraging numerical verification that the SCTM performance in the 3D M-CFD code is as expected.

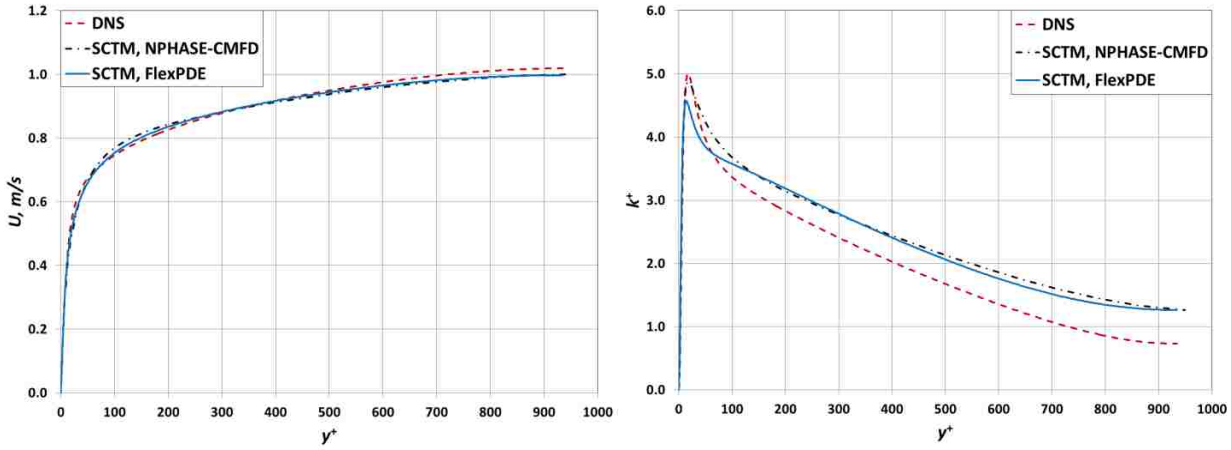

Figure 5.14. SCTM prediction (N = 18, Re_τ = 950) of stream wise velocity (a) and TKE (b) using NPHASE-CMFD (black dashed dot line) in comparison to SCTM prediction using FlexPDE (solid blue line) and DNS data (red dashed line) of del Alamo et al. [89].

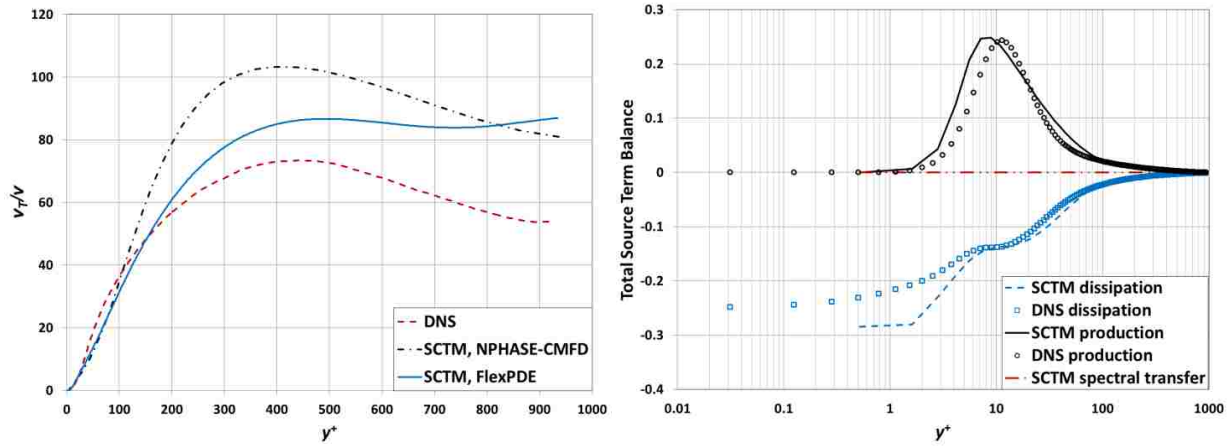

Figure 5.15. (a): SCTM prediction (N = 18, Re_τ = 950) of turbulent viscosity in comparison to SCTM prediction using FlexPDE (solid blue line) and DNS data (red dashed line) of del Alamo et al. [89]. (b): Total source term balance of SCTM using NPHASE-CMFD in comparison to DNS data of del Alamo et al. [89].

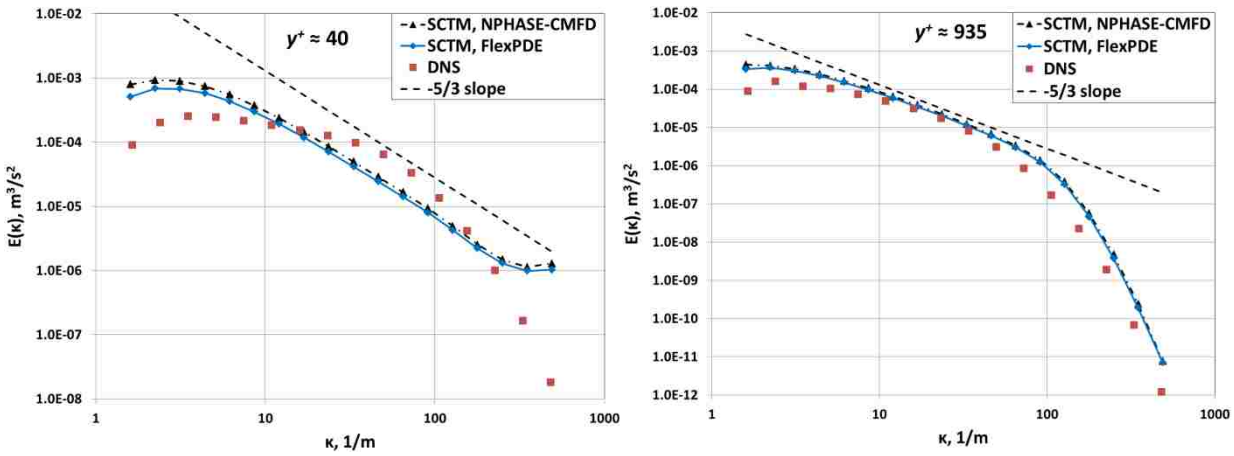

Figure 5.16. SCTM (N = 18, Re_τ = 950) prediction of the TKE spectrum using NPHASE-CMFD (black triangles) and FlexPDE (blue diamonds) in comparison to the DNS data (red squares) and -5/3 slope (dashed line) at y^+ = 40 (a) and y^+ = 935 (b).

5.3.6 Re_τ = 550

The general trends for the higher Reynolds number cases discussed previously are seen for the SCTM predictions using NPHASE-CMFD at Re_τ= 550 (Figure 5.17 – Figure 5.19). Note that at this Reynolds number the TKE peak is well-predicted (Figure 5.17(b)) and turbulence dissipation shape is very well modeled by the SCTM (Figure 5.18(b)). Spectral energy results at two different y^+ locations show very similar results for NPHASE-CMFD and FlexPDE. However, at this Reynolds number the energy build-up in the high wave number range for the location close to the wall is slightly less for the NPHASE-CMFD results than for the FlexPDE results. It is possible that significantly increasing the number of spectral bins could mitigate this build-up of energy in the dissipation range although the spectral resolution for each of these cases is less than the maximum suggested value of 2.

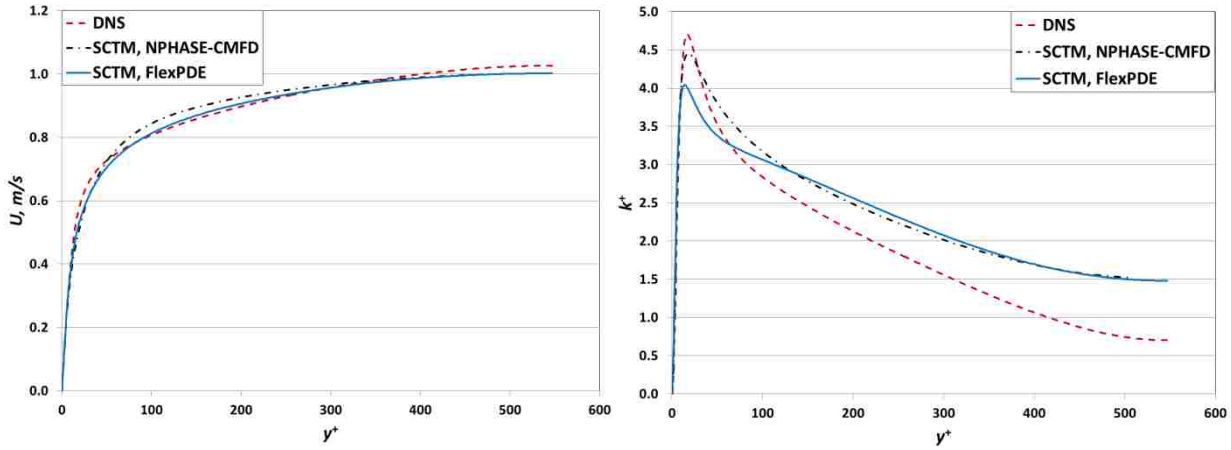

(a) **(b)**

Figure 5.17. SCTM predictions (N = 18, Re_τ = 550) of stream wise velocity (a) and TKE (b) using NPHASE-CMFD (black dashed dot line) in comparison to SCTM prediction using FlexPDE (solid blue line) and DNS data (red dashed line) of del Alamo and Jiminez [93].

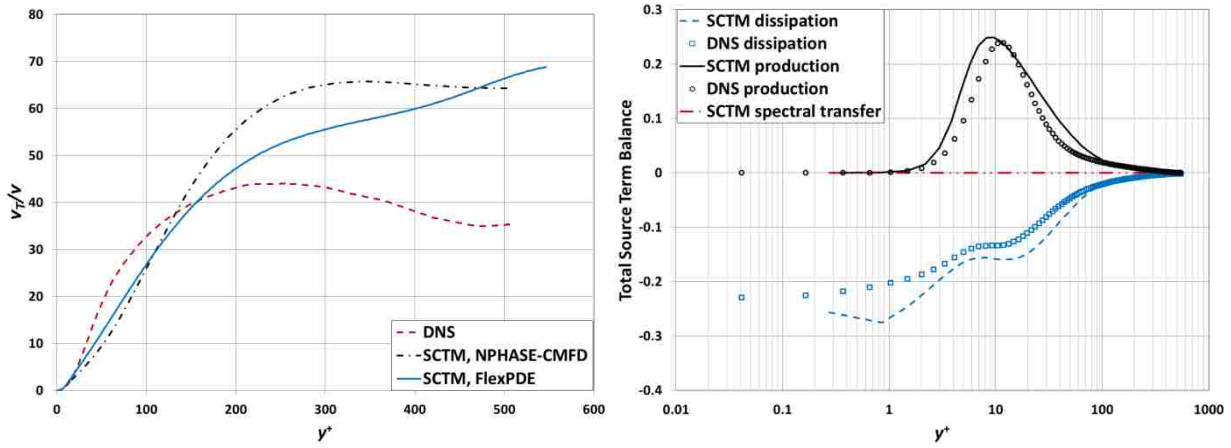

(a) **(b)**

Figure 5.18. SCTM prediction (N = 18, Re_τ = 550) of turbulent viscosity in comparison to SCTM prediction using FlexPDE (solid blue line) and DNS data (red dashed line) of del Alamo and Jiminez [93]. (b): Total source term balance of SCTM using NPHASE-CMFD in comparison to DNS data of del Alamo and Jiminez [93].

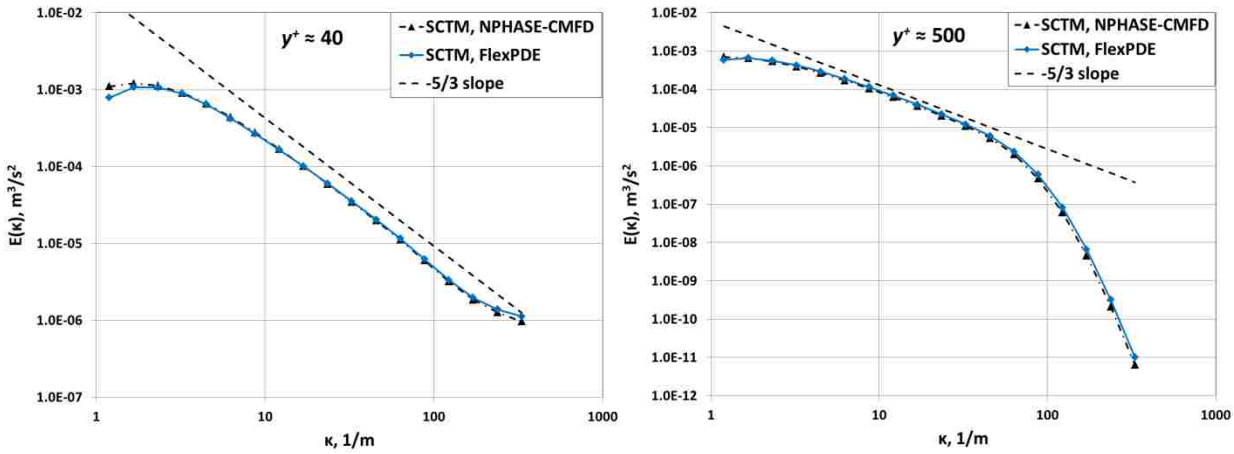

(a) **(b)**

Figure 5.19. SCTM (N = 18, Re_τ = 550) prediction of the TKE spectrum using NPHASE-CMFD (black triangles) and FlexPDE (blue diamonds).

5.4 TPF1: Single-Phase Turbulent Pipe Flow

It is important that the SCTM implementation into NPHASE-CMFD was tested for geometries that are at the very least non-square in nature as a precursor to the overall goal of modeling nuclear reactor subchannels with mixing vanes and spacer grids. Therefore, circular pipe geometry was a good next choice for testing the implementation of the model; particularly testing gradient terms and terms that rely on distance to the wall. NPHASE-CMFD has an R-Z cylindrical coordinate option that can be used for axisymmetric two-dimensional geometries [106]. With this option, Cartesian meshes with a single element in the theta direction can be simulated in cylindrical coordinates. When the length of the single element in the theta direction is equal to 2π the entire pipe geometry is simulated. Figure 5.20 shows how the square geometry translates to the R-Z coordinate system using the NPHASE-CMFD *cylindrical coordinates* option. Note that if the *cylindrical coordinates* option is not used in NPHASE-CMFD and the "Pipe Wall" and "Centerline" boundaries are set to wall boundary conditions this mesh would constitute flow between parallel plates in Cartesian geometry.

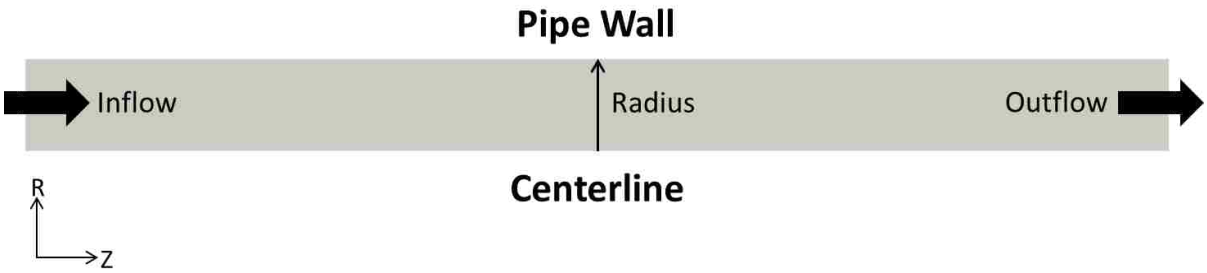

Figure 5.20. Schematic of the flow in axisymmetric pipe with R-Z coordinates in NPHASE-CMFD.

5.4.1 25 mm Diameter Pipe

Circular pipe geometry was considered with an inner diameter of 25 mm. This geometry corresponds to the experimental work of Hosokawa and Tomiyama [107] that used Laser Doppler velocimetry (LDV) image processing techniques to investigate upward single and bubbly two-phase flows with air-water systems at atmospheric conditions. In their work, radial distributions of void fraction, bubble aspect ratio, phasic velocities, liquid TKE, and average bubble diameter were measured. Hosokawa and Tomiyama [107] provided radial profiles of TKE for two single-phase experiments with inlet liquid volumetric flux ($J_L = v_L \alpha_L$) values of 0.5 m/s (Re ≈ 14,000) and 1.0 m/s (Re ≈ 28,000), respectively. Henceforth the J_L = 0.5 m/s case will be referred to as HT11 and the J_L = 1.0 m/s case will be referred to as HT12, where the first numerical index on each case name of "1" indicates single-phase. The working fluid was water at atmospheric conditions (ρ = 997.561 and μ = 8.887x10^{-4}). Three numerical meshes were generated with equidistance spacing in the radial direction of 51, 103, and 207 elements, respectively. A mesh convergence study was performed using the LRN k-ε model and the least resolved mesh with 51 elements across the radial direction was found to be sufficient for LRN turbulence modeling. Furthermore, the average value of turbulent dissipation from the k-ε model result was used to estimate the right wave number boundary (Equation 3.4) for the SCTM in the HT12 case. The left and right wave number boundaries for the HT12 case were κ_0 = 1.0 m^{-1} and κ_N = 7.82x10^4 m^{-1}, respectively. Given the wave number boundaries the minimum number of wave number bins (Equation 3.6) was found to be about N = 16 and N = 18 bins were then used for the simulations. These same values were used for the HT11 case as a conservative estimate.

Predictions of TKE from NPHASE-CMFD using both the SCTM and the k-ε model are shown in comparison to Hosokawa and Tomiyama experimental data in Figure 5.21. In both cases, the k-ε model provides a better prediction of the TKE shape. However, as discussed previously (§ 5.3.1), finalizing SCTM constants over a range of turbulent validation tests beyond the current scope can improve estimates of the TKE shape. The importance of the results shown here is the ability of the SCTM to handle the circular geometry in NPHASE-CMFD using the existing code structure and options for cylindrical geometries.

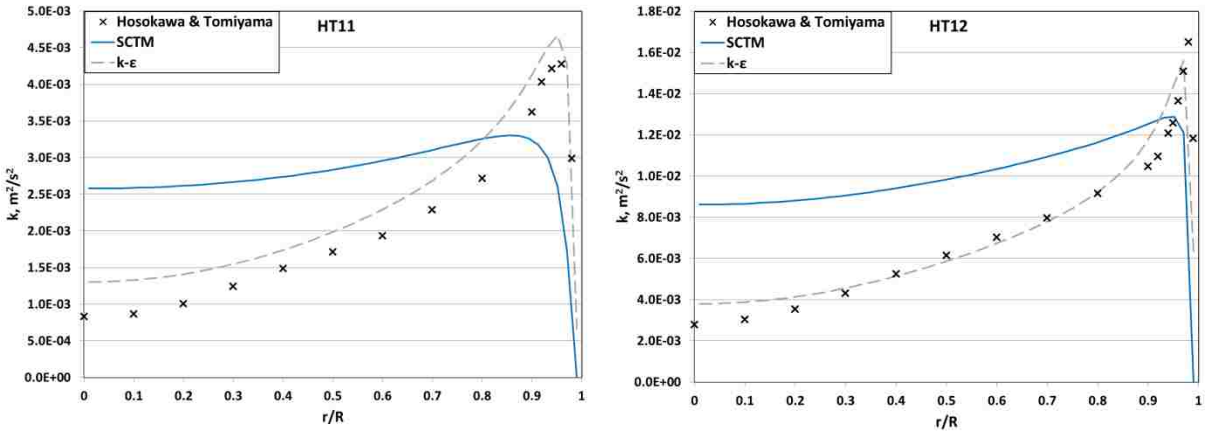

Figure 5.21. Predictions of SCTM (*N* = 18) and k-ε model TKE from NPHASE-CMFD in comparison to Hosokawa and Tomiyama [107] experimental data for case HT11 (a) and HT12 (b). The abscissa is non-dimensional radial distance.

Figure 5.22(a) – (b) shows stream-wise velocity profiles estimated using the SCTM and k-ε model for the HT11 and HT12 cases. The profiles are quite similar, particularly for the higher inlet velocity HT12 case. Although there is no experimental data available for direct comparison the profiles follow the expected shape for pipe flow. Figure 5.22(c) – (d) show the TKE spectra for the HT11 and HT12 cases at various radial distances. Due to the inherent nature of the SCTM to capture the TKE spectrum the -5/3 slope in the inertial subrange is clearly realized. Also, the difference in energy is substantial between radial locations close to the wall and near the centerline. For example, in both the HT11 and HT12 cases the radial location closest to the pipe wall (light blue circles) has an energy density many orders of magnitude higher than at the location closest to the channel

centerline (blue diamonds) at the smallest eddy scales. This is physically sensible considering that the bulk of the smallest eddies in the flow exist close to the solid wall boundary. Note that for both cases the spectral transfer term sums to zero (Figure 5.23) as expected and also indicates SCTM convergence. In both cases, the total production and dissipation terms follow expected physical shapes (Figure 5.23).

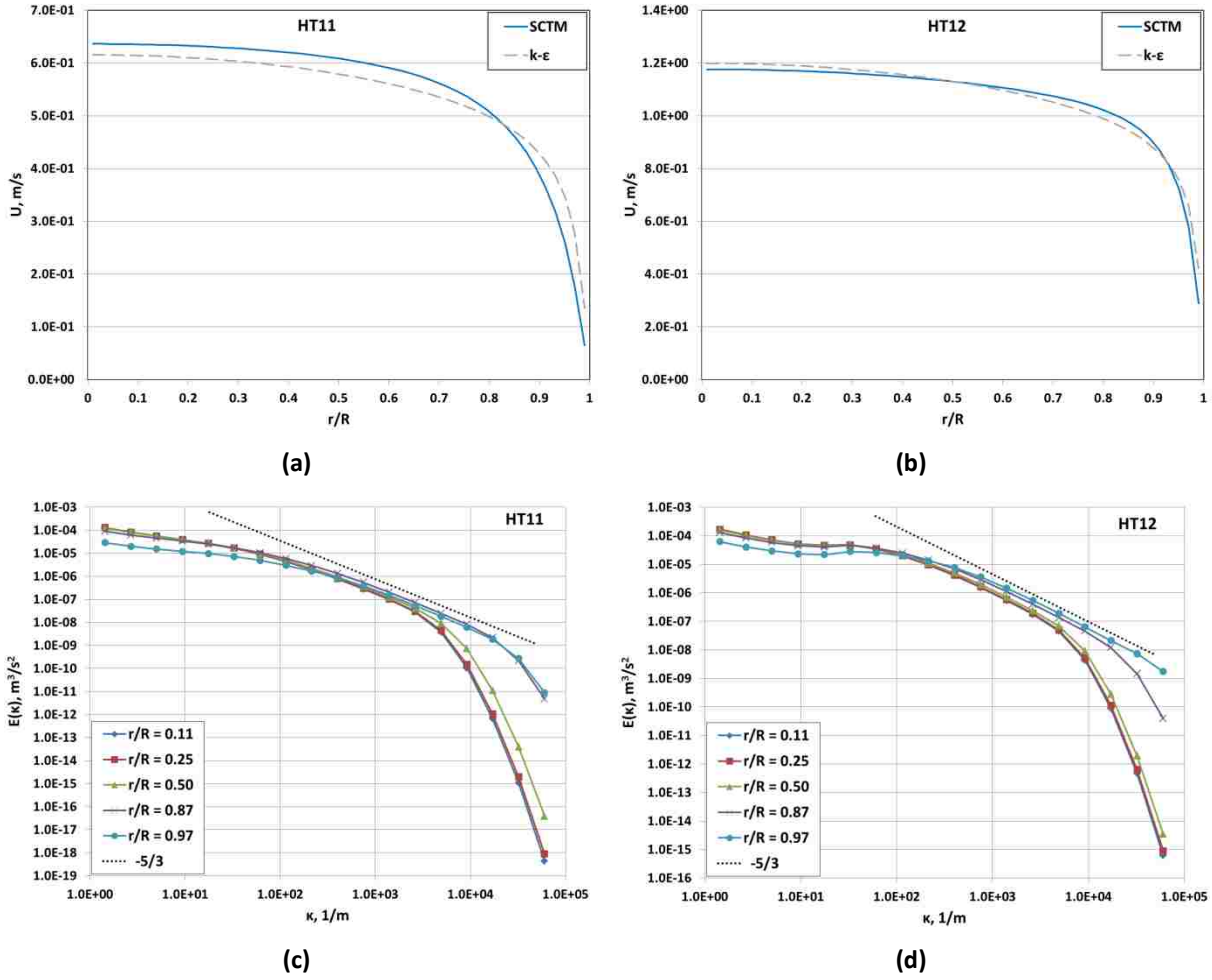

Figure 5.22. Predictions of SCTM (*N* = 18) and k-ε model stream-wise velocity from NPHASE-CMFD for HT11 (a) and HT12 (b). TKE spectra at various radial locations for HT11 (c) and HT12 (d). The abscissa is non-dimensional radial distance.

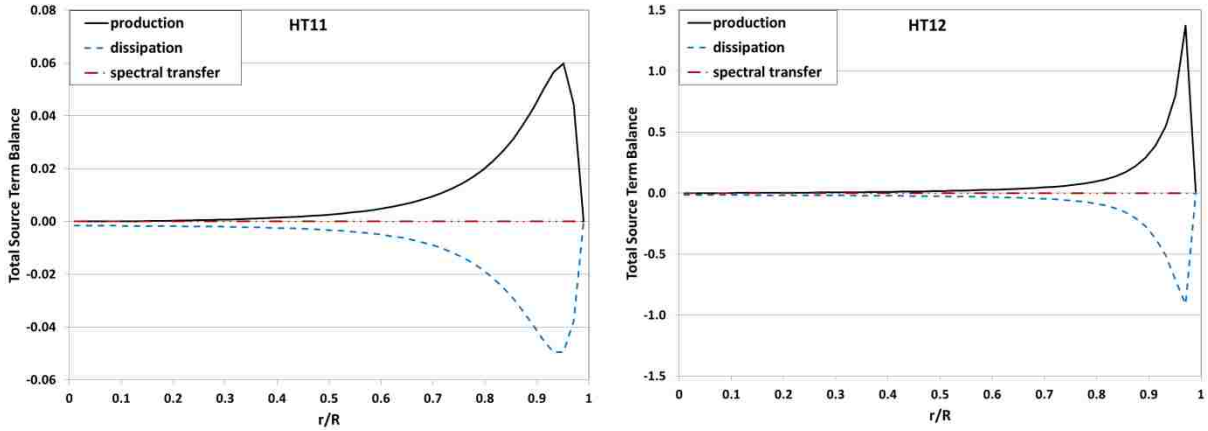

Figure 5.23. Predictions of SCTM (*N* = 18) total source term balance using NPHASE-CMFD for HT11 (a) and HT12 (b). The abscissa is non-dimensional radial distance.

5.4.2 200 mm Diameter Pipe

Circular pipe geometry with an inner diameter of 200 mm was also considered for comparison between the SCTM and k-ε model in NPHASE-CMFD. The cylindrical coordinate option was used in NPHASE-CMFD with an inlet liquid volumetric flux (J_L) of 1.0 m/s corresponding to a Reynolds number of about 224,500 for water at atmospheric conditions (ρ = 997.561 and μ = 8.887x10^{-4}). Two R-Z numerical meshes were generated with equidistant spacing of 325 and 650 elements in the radial direction, respectively. A mesh convergence study with the k-ε model showed that the mesh with 325 elements across the radial direction was sufficient for LRN turbulence modeling. As with the 25 mm diameter pipe (§ 5.4.1), the k-ε prediction of turbulent dissipation was used to estimate the right wave number boundary for the SCTM. The left and right wave number boundaries were κ_0 = 1.0 m^{-1} and κ_N = 7.32x10^4 m^{-1}, respectively. The minimum number of bins (Equation 3.6) was then found to be about *N* = 16 and *N* = 18 bins were then used for the simulations.

Predictions of stream-wise velocity and TKE (Figure 5.24) are similar for the SCTM and k-ε model although the SCTM TKE peak is considerably wider than the k-ε model. As mentioned previously, the peak shape will be slightly modified as SCTM constants are improved. The predictions shown here are for higher Reynolds number than any previously considered tests of the

SCTM and results are within adequate engineering error when measured alongside the k-ε model. The result for the turbulent viscosity distribution (Figure 5.25) exhibits an acceptable physical shape.

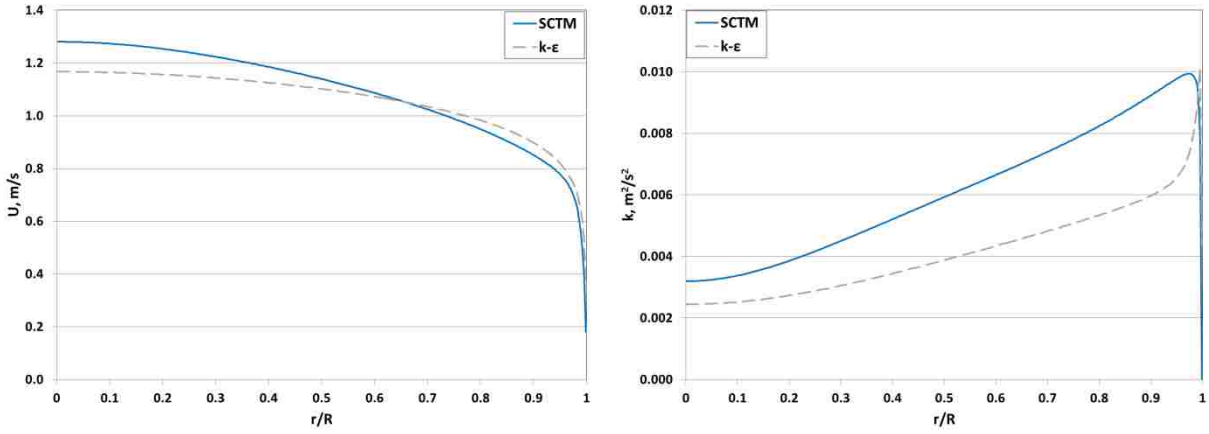

Figure 5.24. Predictions of SCTM (*N* = 18) and k-ε model stream-wise velocity (a) and TKE (b) from NPHASE-CMFD for 200 mm pipe. The abscissa is non-dimensional radial distance.

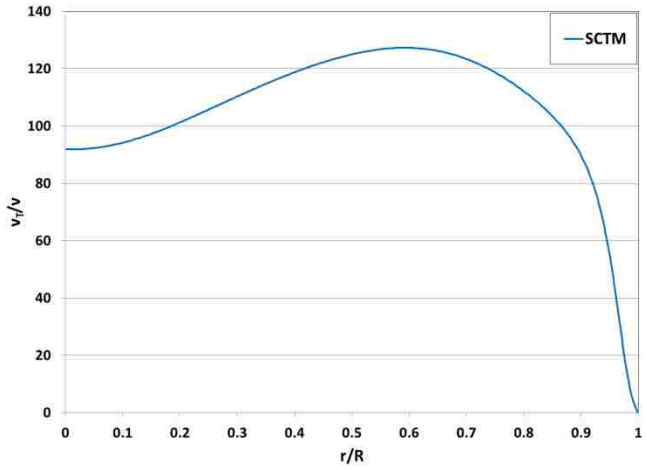

Figure 5.25. SCTM prediction of non-dimensional turbulent viscosity as a function of non-dimensional radial distance for 200 mm pipe.

The TKE spectra are shown at nine radial locations (Figure 5.26) ranging from near the pipe wall to near the pipe centerline. The spectra exhibit the expected -5/3 slope of the inertial subrange and the considerable Reynolds number of the flow allows for sufficient separation of the largest and

smallest scales and thus an appreciable spectral transfer region. The energy at the smallest scales is decreased as moving towards the channel centerline as discussed in accordance with Figure 5.22 for the 25 mm pipe. Even at this higher Reynolds number there are no noticeable tails as a continuation the -5/3 slope of the inertial subrange and therefore it is concluded that the modification of the inhomogeneous dissipation term (§ 5.3.1) did improve the near-wall behavior of the SCTM.

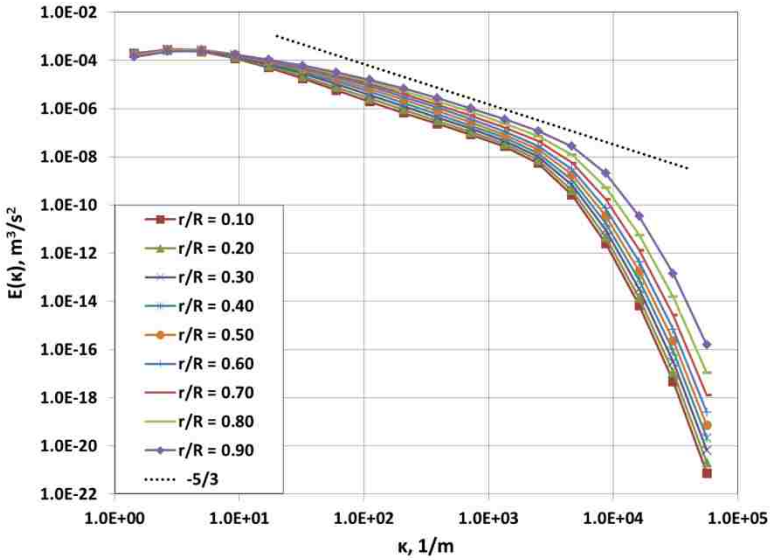

Figure 5.26. TKE spectra at nine radial locations in 200 mm pipe ranging from near the pipe wall to the pipe centerline.

The 200 mm diameter pipe was used to demonstrate the full 3D capabilities of the SCTM implemented into NPHASE-CMFD. The ability to model 3D geometries with M-CFD inherently increases reactor safety and performance calculations and the increasing availability of computational resources allows 3D M-CFD to be a viable option in the nuclear industry. As with the previous computational meshes, the mesh generation software Pointwise [108] was used to generate the 3D 200 mm diameter pipe mesh shown in Figure 5.27 with O-H topology. The 3D 200 mm mesh contains 107,205 mesh elements and has a LOD = 100. To improve convergence for the 3D mesh pseudo-periodic inflow/outflow conditions were used. This type of pseudo-periodic boundary condition has been used with NPHASE-CMFD before but the routines were modified to include the NPHASE-CMFD species equations as well so that SCTM bin TKE values could be recorded.

To use the pseudo-periodic conditions, simulations nodal values are recorded at a stream-wise location (usually around 90 % – 95 % of the total channel length to avoid any effects at the channel outflow) into a binary output file. This binary output file can then be used as an input file on the next set of simulation iterations such that either the mesh inflow is set to the recorded nodal values or the entire mesh is set to the recorded nodal values. This type of pseudo-periodic boundary condition was used for some of the single-element width simulations shown previously but can aid more tremendously in 3D simulations that require substantial wall-clock time.

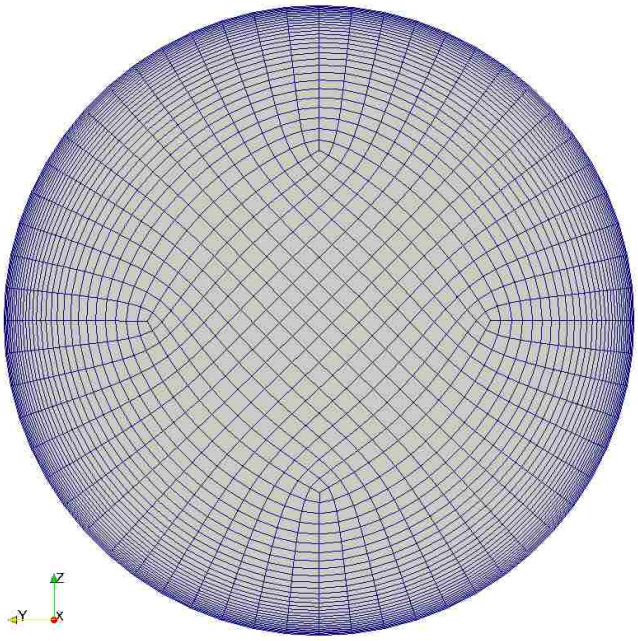

Figure 5.27. Slice across the stream-wise (*x*) axis of the 3D 200 mm diameter pipe mesh.

The 3D results shown here are not comprehensive in terms of mesh resolution but are presented as verification for the SCTM implementation into NPHASE-CMFD. A radial slice across the *x*-axis taken at 95 % of the total pipe length from the pipe inlet was taken in Paraview to view simulation results. The distribution of stream-wise velocities using the k-ε model and the SCTM are shown in Figure 5.28(a) – (b). The distribution of mean velocity as the values on the mesh elements is shown as a line plot across the *y*-axis and through the pipe center for both turbulence models in Figure 5.28(c) – (d). Clearly, the 3D predictions using the SCTM are symmetric and provide an

excellent verification for the SCTM implementation. Figure 5.29 provides additional verification where mean velocity and TKE results are plotted from the pipe wall to the pipe centerline for both the k-ε model and SCTM using the R-Z mesh and the 3D mesh. The predictions using the R-Z mesh and the 3D mesh are consistent. The differences arise due to the coarse nature of the 3D mesh and the use of the values on the mesh elements to plot the data rather than the smoother nodal data for higher resolved R-Z mesh.

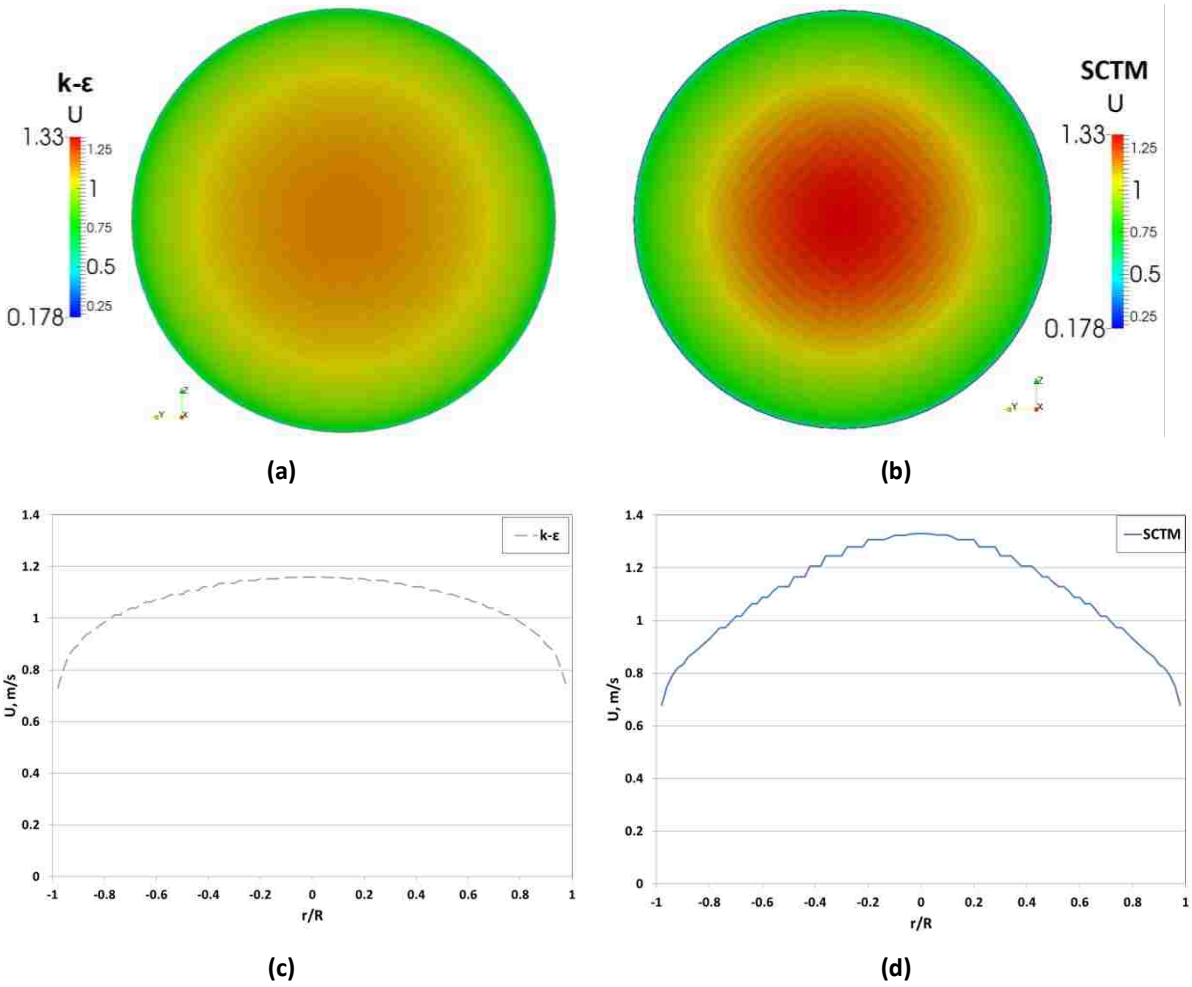

Figure 5.28. Stream-wise velocity in 200 mm diameter pipe using 3D mesh shown as radial slice across the stream-wise *x*-axis for k-ε (a) and SCTM (b) turbulence models and for k-ε (c) and SCTM (d) turbulence models as a line plot across the *y*-axis of the radial slice through the pipe center.

To further demonstrate how the coarse numerical mesh affects the solution the TKE prediction from SCTM is shown without (Figure 5.30(a)) and with (Figure 5.30(b)) the numerical mesh overlaid on a radial slice. Clearly, some mesh effects are evident since the solution is not absolutely smooth and mirrors the shape of the numerical elements. The mesh effects are more dominant approaching the pipe center from the pipe wall since this is the direction of boundary layer growth off the solid wall boundary. However, as discussed above, the 3D test case was an excellent verification test for the SCTM implementation into NPHASE-CMFD.

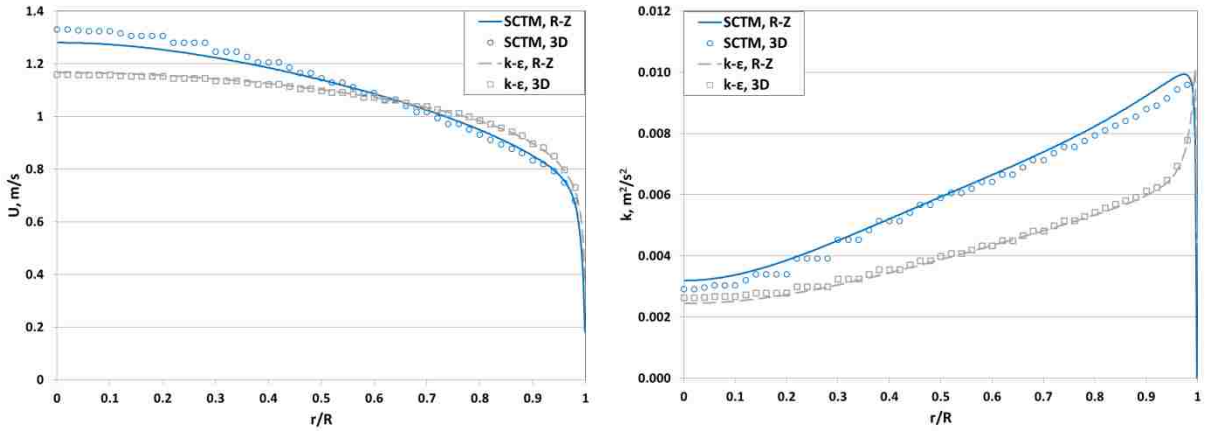

(a) **(b)**

Figure 5.29. A comparison of the R-Z and 3D mesh results in 200 mm diameter pipe for the stream-wise velocity (a) and TKE (b) using k-ε and SCTM turbulence models.

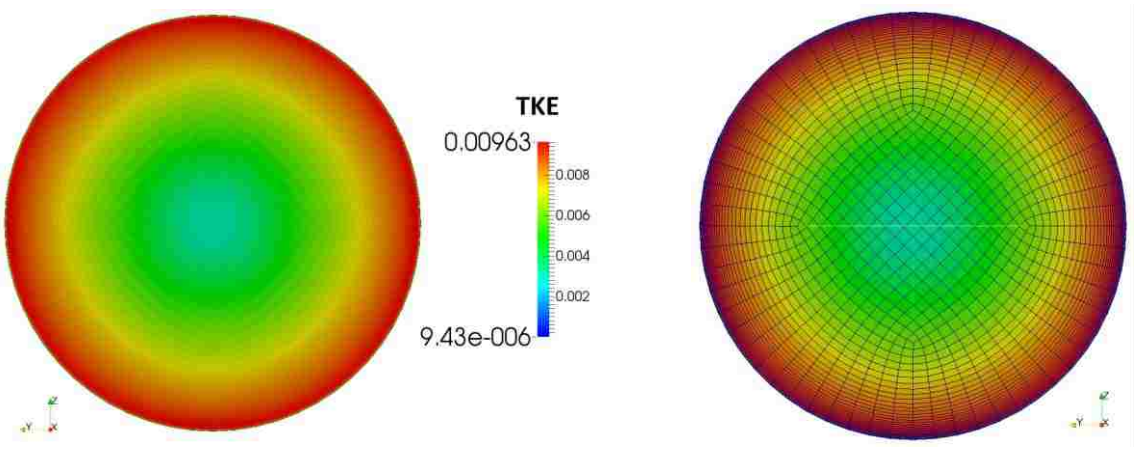

(a) **(b)**

Figure 5.30. TKE prediction in 200 mm diameter pipe using SCTM without mesh overlay (a) and with mesh overlay (b).

5.5 TPLF1: Single-Phase Turbulent Flow between Parallel Plates

Single-phase flow between parallel plates was considered with a plate spacing of 100 mm. This flow scenario is similar to the TCF1 (§ 5.3) test case. However, both plane walls were considered and parameters were dimensional with adiabatic water conditions (ρ = 997.561 and μ = 8.887x10^{-4}). The numerical mesh (Figure 5.31) was generated using Pointwise [108] with 200 equidistant elements in the direction normal to the duct walls resulting in a dimensional mesh spacing of 0.5 mm. Although the near-wall y^+ resolution of this mesh was found to be somewhat coarse in post-processing a mesh resolution study using meshes with 400 and 1600 equidistant elements showed mesh convergence of the mean velocity and nearly identical profiles of TKE. An inlet liquid volumetric flux (J_L) of 1.0 m/s corresponding to a Reynolds number of about 112,250 was prescribed. As with pipe flow cases (§ 5.4), the k-ε prediction of turbulent dissipation was used to estimate the right wave number boundary for the SCTM. The left and right wave number boundaries were κ_0 = 1.0 m^{-1} and κ_N = 8.6x10^4 m^{-1}, respectively. The minimum number of bins (Equation 3.6) was then found to be about N = 16. A bin resolution study was performed for this geometry as well as an examination of expected physical behavior.

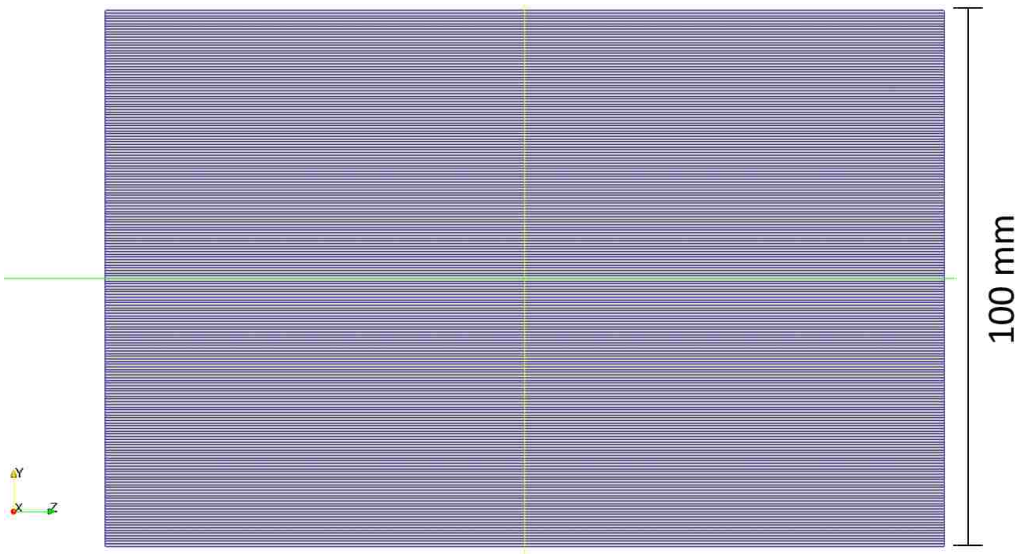

Figure 5.31. 100 mm parallel plate mesh with 200 elements in the (*y*) direction normal to the duct walls. The *z*-axis single element width has been scaled down from the full 2π length for enhanced viewing.

The SCTM calculations of stream-wise liquid velocity using N = 10 (ξ = 3.115), N = 18 (ξ = 1.880), and N = 22 (ξ = 1.676) wave number bins were all similar to the stream-wise liquid velocity estimated using the k-ε model (Figure 5.32). The results of both stream-wise velocity (Figure 5.32) and TKE (Figure 5.33) show wave number bin convergence for the SCTM. The simulations with N = 10 wave number bins results in a spectral resolution parameter (ξ) of 3.115 that is considerably higher than the maximum allowable value of 2.0 (Equation 3.6) but still provides excellent agreement with the higher bin number simulations for stream-wise velocity. The N = 10 wave number simulation slightly underestimates the TKE in comparison to simulations with higher wave number but all the simulations provide a physically expected result where the TKE profile is wall-peaked and depressed in the duct center.

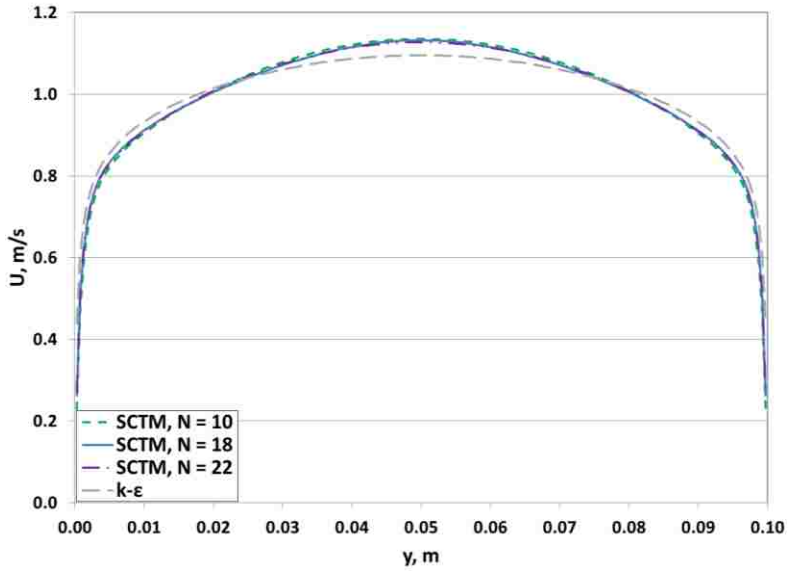

Figure 5.32. Stream-wise velocity using SCTM with N = 10 (ξ = 3.115), N = 18 (ξ = 1.880), and N = 22 (ξ = 1.676) wave number bins in comparison to k-ε model for parallel plate geometry with 100 mm spacing.

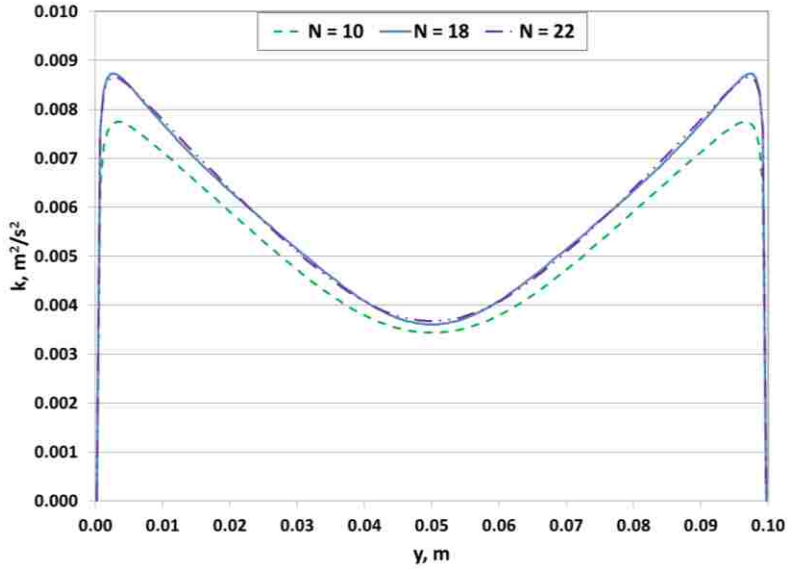

Figure 5.33. TKE prediction using SCTM with N = 10 (ξ = 3.115), N = 18 (ξ = 1.880), and N = 22 (ξ = 1.676) wave number bins for parallel plate geometry with 100 mm spacing.

The parallel plate geometry provides an excellent opportunity for verification of the SCTM implementation into NPHASE-CMFD. Since two solid wall boundaries are present, the SCTM

implementation should naturally apply the terms dependent on wall distance, mean flow gradients, etc. In terms of the statistical average, the turbulence on either side of the duct centerline should be identical. Therefore, profiles of velocity, TKE, etc. should be identical as well when considered on either side of the duct centerline. To demonstrate the correct behavior of the SCTM in this geometry the TKE is plotted as a function of non-dimensional wall distance from -1 to 1 with 0 as the duct centerline (Figure 5.34(a)). If the total duct width (100 mm) is taken as L, then the locations on either side of the duct centerline can be described non-dimensionally as $y/L_{0.5}$. In Figure 5.34(b), locations of equal distance from the duct centerline are chosen for examining TKE spectra. The positive/negative locations on either side of the duct centerline show that the predictions of TKE are identical, as expected. The TKE is highest at the smallest scales for the spatial location closest to the duct walls ($y/L_{0.5}$ = $\pm$ 0.925). This same physical behavior was shown for the circular pipe geometry and discussed in accordance with Figure 5.22 and Figure 5.26. The inner and outer scale separation at this Reynolds number is high enough to confirm the -5/3 slope of the inertial subrange.

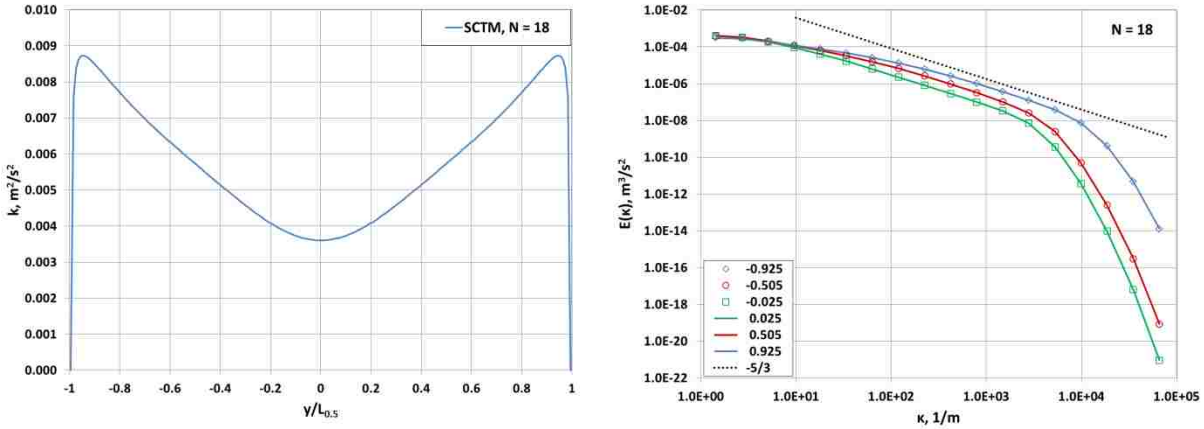

(a) **(b)**

Figure 5.34. (a) SCTM (*N* = 18) TKE plotted as a function of non-dimensional wall distance with zero at duct centerline. (b) TKE spectra at six different spatial locations ($y/L_{0.5}$ = $\pm$ 0.925, $y/L_{0.5}$ = $\pm$ 0.505, $y/L_{0.5}$ = $\pm$ 0.025).

TKE spectrum results for SCTM simulations with *N* = 10 (ξ = 3.115), *N* = 18 (ξ = 1.880), and *N* = 22 (ξ = 1.676) wave number bins are shown for a spatial location near the duct centerline (Figure 5.35(a)) and a spatial location close to the duct wall (Figure 5.35(b)). Spectra at both locations

exhibit the -5/3 slope of the inertial subrange and excellent wave number bin convergence although more distinct characteristics of the TKE spectrum are captured as the number of bins is increased. However, as was shown in a previous bin resolution study (§ 3.3.2.1), the SCTM is robust and is able to capture the TKE spectrum even for spectral resolution parameters significantly greater than the recommended value of 2.0.

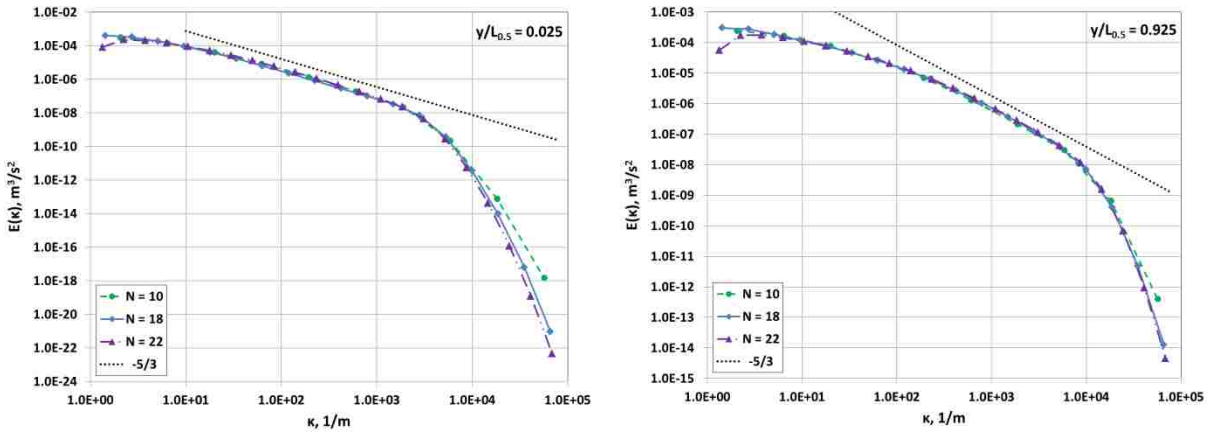

(a) **(b)**

Figure 5.35. TKE spectrum at two different spatial locations, (a) $y/L_{0.5}$ = 0.025 and (b) $y/L_{0.5}$ = 0.925, for SCTM simulations with N = 10 (ξ = 3.115), N = 18 (ξ = 1.880), and N = 22 (ξ = 1.676) wave number bins for parallel plate geometry with 100 mm spacing.

The total source term balance from NPHASE-CMFD using the SCTM with N = 18 wave number bins is shown in Figure 5.36. The wall-peaked profiles of production and dissipation are physically expected and symmetrical. Comparison of the total source term balance from simulations of different wave number bins showed wave number bin convergence. The total spectral transfer term is zero and does not contribute to the overall TKE and indicates SCTM convergence.

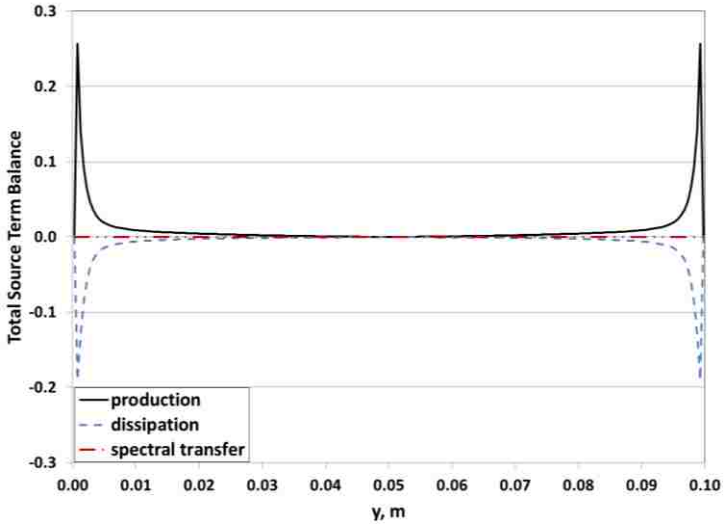

Figure 5.36. Total source term balance using the SCTM (N = 18) in NPHASE-CMFD for the parallel plate geometry with 100 mm spacing.

Paraview [105] software is used to view the simulation results as a more physical representation of the geometry. Figure 5.37 and Figure 5.38 were both taken as a slice perpendicular to the x-axis at a stream-wise location 95 % of the overall duct length from the duct inlet and the z-axis has been scaled shorter for enhanced viewing. Figure 5.37 and Figure 5.38 show the TKE and stream-wise velocity distributions between the parallel plates, respectively. Viewing simulation output from a 3D M-CFD code such as NPHASE-CMFD with Paraview (or similar post-processing software) provides a more qualitative approach to post-processing analysis and can be an additional asset in interpretation of turbulence modeling results.

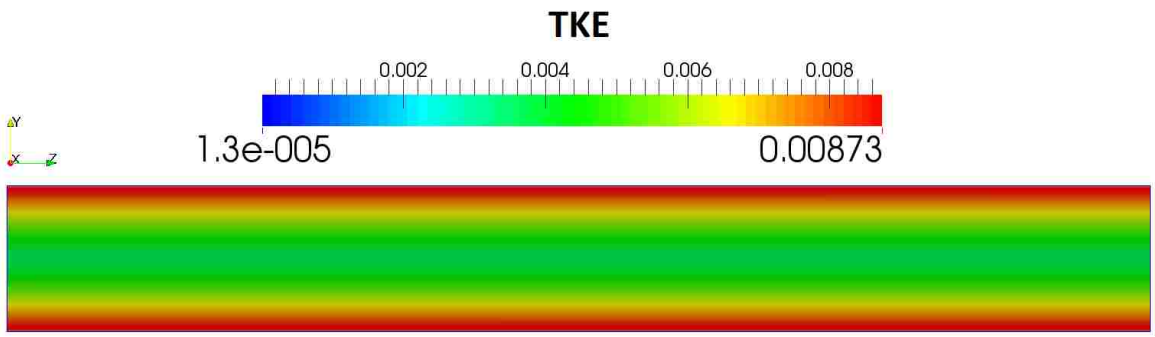

Figure 5.37. TKE distribution between parallel plates with 100 mm spacing (*y* direction is normal to duct walls). *X*-axis cut taken at a stream-wise location 95 % of the distance from the duct inlet. The *z*-axis has been scaled shorter for enhanced viewing.

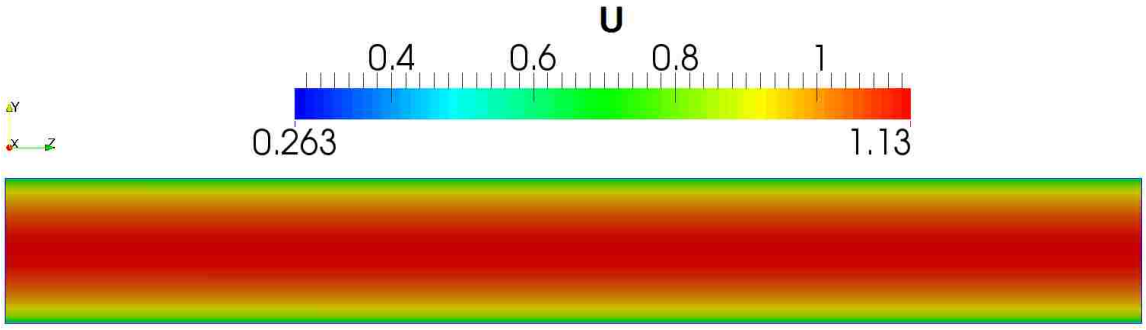

Figure 5.38. Stream-wise velocity (*U*) distribution between parallel plates with 100 mm spacing (*y* direction is normal to duct walls). *X*-axis cut taken at a stream-wise location 95 % of the distance from the duct inlet. The *z*-axis has been scaled shorter for enhanced viewing.

6. TWO-PHASE FLOW RESULTS

In this chapter, two-phase flow results for monodispersed and polydispersed bubbly flows using the SCTM implemented in NPHASE-CMFD are presented for various tests cases. The presented test cases were chosen for verification of the correct physical behavior of the SCTM in NPHASE-CMFD and for validation of the LRN SCTM for two-phase flows in a 3D M-CFD package.

As discussed in § 1.1.1.2, the Eulerian-Eulerian approach has been widely applied to bubbly two-phase flows and continues to be an active area of research. The Eulerian-Eulerian approach solves a set of conservation equations for each phase. In the case of adiabatic flow with no bubble coalescence, bubble break-up, or mass transfer between phases only the mass and momentum equations are required and the phases are treated as incompressible with constant properties:

$$\frac{\partial}{\partial t}\left(\alpha_j \rho_j\right) + \nabla \cdot \left(\alpha_j \rho_j \bar{v}_j\right) = 0 \tag{6.1}$$

$$\frac{\partial}{\partial t}\left(\alpha_j \rho_j \bar{v}_j\right) + \nabla \cdot \left(\alpha_j \rho_j \bar{v}_j \bar{v}_j\right) = -\alpha_j \nabla p_j + \nabla \cdot \left[\alpha_j \left(\bar{\bar{\tau}}_j + \bar{\bar{\tau}}_j^t\right)\right] + \alpha_j \rho_j \bar{g} + \bar{M}_j \tag{6.2}$$

where α_j represents the volume fraction of phase *j*, ρ is the density, $\bar{v}$ is the velocity, p is the pressure, $\bar{g}$ is the gravitational acceleration, $\bar{\bar{\tau}}_j$ and $\bar{\bar{\tau}}_j^t$ are the fluid and Reynolds stress tensors, respectively, and $\bar{M}_j$ represents the interfacial momentum transfer between the phases. In the present work, drag force, virtual mass force, turbulent dispersion force, and a modified lift force that accounts for the presence of the solid wall boundary are utilized such that:

$$\bar{M}_j = M_j^D + M_j^{VM} + M_j^{TD} + M_j^L \tag{6.3}$$

where M_j^D represents the drag force, M_j^{VM} represents the virtual mass force, M_j^{TD} represents the turbulent dispersion force, and M_j^L represents the lift force. NPHASE-CMFD has been designed to perform such Eulerian-Eulerian calculations and solves the mass and momentum conservation equations for each designated phase with user-inputted routines for the interfacial closure terms. Since the focus of the present work is the development and implementation of the M-CFD SCTM, interfacial force terms were implemented following the work of Shaver and Podowski [109] where essentially "off-the-shelf" models were used with little modification for the drag, virtual mass, and turbulent dispersion forces. Shaver and Podowski [109] used a HRN k-ε model and presented a modified lift force coefficient to account for the presence of the solid wall boundary. Since the current work uses the LRN SCTM a new lift coefficient modification that accounts for the solid wall

boundary is used. In addition, this new lift coefficient modification acts as a wall repellent force and eliminates the need for a separate wall force to be included in the interfacial force balance. Existing user routines for each of the interfacial force terms were used with the SCTM and each term is discussed separately in § 6.1.

6.1 Interfacial Forces

6.1.1 Drag Force

The drag force is given as [109]:

$$M_g^D = -\frac{3}{4} C_D \frac{\alpha_d}{D_d} \rho_c (\bar{v}_d - \bar{v}_c) |\bar{v}_d - \bar{v}_c| \tag{6.4}$$

where the subscripts *c* and *d* refer to the continuous (liquid) and dispersed (gas) phases. Note that Equation (6.4) is written for the continuous gas phase and that the drag force for the continuous liquid phase would be equal but opposite (i.e. $M_g^D = -M_l^D$). The drag coefficient is given by [109]:

$$C_D = \frac{24}{Re_b} \left(1 + 0.092 Re_b^{0.78}\right) \tag{6.5}$$

which is slightly modified from a well-accepted relationship for bubbly flow [49, 109].

6.1.2 Virtual Mass Force

The virtual mass force can be significant for developing flows. Although the present work deals with steady-state the virtual mass force is included here for completeness since it will be important in future works with the SCTM in nuclear thermal-hydraulic calculations. Following Shaver and Podowski [109] the form proposed by Drew [44] is used with a constant virtual mass coefficient of $C_{VM} = 0.5$:

$$M_g^{VM} = -C_{VM} \alpha_d \rho_C \left(\frac{D\bar{v}_d}{Dt} - \frac{D\bar{v}_c}{Dt}\right) \tag{6.6}$$

where the operator D/Dt is the material derivative.

6.1.3 Turbulent Dispersion

The turbulent dispersion force follows the work of Podowski [110] and is given as [109]:

$$M_g^{TD} = -C_{TD}\alpha_d\rho_c k_c \nabla\alpha_d \tag{6.7}$$

where C_{TD} = 2/3. Note that for an existing NPHASE-CMFD turbulent dispersion user routine the overall TKE of the continuous phase (k_c) had to be altered to represent the overall TKE calculated by the SCTM.

6.1.4 Lift Force

The lift force formulation is given by Zun [45] as:

$$M_g^L = -C_L\alpha_d\rho_c(\bar{v}_d - \bar{v}_c) \times (\nabla \times \bar{v}_c) \tag{6.8}$$

where C_L is the lift coefficient and active research continues to develop expressions for the lift coefficient dependent on bubble size, deformation, etc. Both experimental [111] and numerical data [48] have shown a change in the sign of the lift coefficient dependent on bubble diameter and that for bubble diameters larger than about 5-6 mm the lift coefficient becomes negative. Recent DNS simulations have suggested that the lift coefficient also becomes negative close to the wall [47]. Therefore, to account for the wall presence in the LRN SCTM a lift coefficient modification was developed and is shown in Figure 6.1. This lift coefficient modification behaves such that it linearly increases from the negative value of the nominal lift coefficient ($C_{L,0}$) at the wall to the positive value of the nominal lift coefficient at one bubble diameter away from the wall and then remains constant. The modification indicates that the lift coefficient is zero at the distance of one bubble radius away from the wall. Mathematically, the lift coefficient is defined as:

$$C_L = \begin{cases} C_{L,0}\left(\dfrac{2y}{D_d} - 1\right) & 0 \le \dfrac{y}{D_d} \le 1 \\ C_{L,0} & 1 < \dfrac{y}{D_d} \end{cases} \tag{6.9}$$

where y indicates the distance to the wall.

In this work, a value of $C_{L,0}$ = 0.03 was used for the monodispersed bubbly flow cases with small bubbles. This value is consistent with previous modeling using NPHASE-CMFD [109, 112]. If larger bubbles are considered and the nominal lift coefficient is negative the lift force modification is not used. Note that Colombo and Fairweather [39] report that lift coefficient values ranging from 0.01 to 0.5 have been used in the literature resulting in good agreement with experimental data.

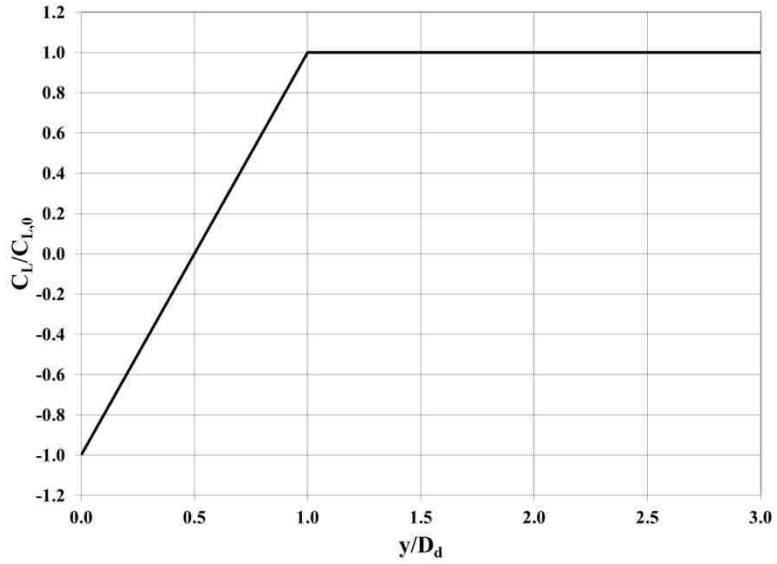

Figure 6.1. Modified lift coefficient as a function of distance from the wall.

6.2 Multiphase Turbulence Closure with the SCTM

Bolotnov et al. [9, 10] showed that the SCTM could be extended to bubbly two-phase decay of isotropic turbulence and homogeneous shear flows with the addition of a BIT source term that accounts for the influence of the dispersed phase on the continuous liquid phase TKE. The BIT source term can be added to the overall TKE balance for a particular bin-*m* (Equation (3.7)):

$$\frac{D\alpha_c k_m}{Dt} = \alpha_c[P_m - \varepsilon_m + D_m + T_m + \Psi_m] \tag{6.10}$$

where Ψ_m is the BIT source term for bin-*m* and the remaining terms are unchanged from their previous definitions. Since bubbly two-phase flows are considered here Ψ_m is considered the BIT source term but physically represents the dispersed phase source term if situations of higher void fraction were to be considered such as slug or churn-turbulent flow. The TKE transport equation is weighted by the continuous liquid phase volume fraction [42, 96]. NPHASE-CMFD solves conservation equations for each phase in the simulation but the turbulence closure option is only used for the continuous liquid phase. The additional BIT source term (Ψ_m) was added to the RHS calculation of the user implemented species source term for bin-*m* in NPHASE-CMFD (Equation (4.5)) and will only be used when a multiphase simulation is initiated. Although only monodispersed

flows were considered in the work of Bolotnov et al. [9, 10] a definition for the form of the BIT source term was provided for polydispersed flow with no bubble coalescence or break-up that assumed bubbles can be split into N_s size groups. These size groups each have a set of specific characteristics such as the volume fraction, the mean diameter, and/or the relative velocity of bubbles in that group [10]. The advantage of spectral turbulence modeling is that each size group can be modeled to modify the TKE spectrum differently. It was assumed that linear superposition can be used to include the influence of all the different size groups on the TKE spectrum [10] such that the total bubble-induced source term for bin-*m*:

$$\Psi_m = \sum_{i=1}^{N_s} \gamma_{m_i} \phi_i \tag{6.11}$$

is the sum of the bubble-induced source terms for each size group (ϕ_i). Note that for a particular bin-*m* the bubble-induced source term is multiplied by a spectral weighting factor (γ_{m_i}) that indicates the contribution for a bubble in size group-*i* to the TKE spectrum in bin-*m*. These weighting factors are distributed to be equal to one for each size group when summed over all spectral bins (e.g. $\sum_{m=1}^{N} \gamma_{m_i} = 1$). The spectral weighting factors for all the results shown here were formulated such that the maximum contribution of the dispersed phase is applied to the wave number bin characteristic of the bubble diameter (e.g. $\kappa_{left} \leq 1/D_i \leq \kappa_{right}$). A Gaussian distribution was used to define the weighting factor for wave numbers smaller than the characteristic bin while a decaying slope ($\kappa^{-1/4}$) was used for wave numbers larger than the characteristic bin. An example spectral weighting factor distribution is shown in Figure 6.2 where the horizontal axis is multiplied by the bubble diameter. This weighting factor distribution corresponds to a simulation with κ_0 = 1.0 m^{-1}, κ_N = 7.82x10^4 m^{-1}, *N* = 18, and a bubble diameter of 3.21 mm (e.g. case HT21, Table 6.2). The boundaries of the wave number bins are shown as vertical dotted lines and the weighting factor is labeled by bin number for each bin. The peak of the weighting factor contribution is applied in bin-10 where the length scale is on the order of the bubble diameter (i.e. κD_d = 1.0). Note that this shape assumes some eddies larger than the characteristic wave number, which is defined by the bubble diameter; receive energy from the bubbles since the contributions to bin-8 and bin-9 are significant.

Bolotnov et al. [10] adjusted the spectral weighting factors to ensure consistency with the experimental TKE spectra that were used for comparison. In the present work, the spectral

weighting factors are estimated based on the physical argument that the majority of energy transferred to the liquid from the dispersed phase occurs at length scales on the order of the bubble diameter. The previous work [10] modified the decaying slope used to define the spectral weighting factors from $\kappa^{-1/4}$ to κ^{-1} at the transition from the inertial subrange to the dissipation range. However, for the SCTM to be a complete turbulence closure model the spectral weighting factors must be assigned before the simulation with no knowledge of the wave number ranges for the transition from the inertial subrange to the dissipation range. The estimation of a Gaussian distribution for wave numbers smaller than the characteristic bin and a $\kappa^{-1/4}$ decaying slope for wave numbers larger than the characteristic bin are then a best estimate of the spectral weighting factor shape. The spectral weighting factors are calculated for each bubble size group when the NPHASE-CMFD simulation is initialized. In the future, if simulations are considered where the bubble size can change due to heat transfer, bubble coalescence, bubble breakup, etc. the calculation of the spectral weighting factors for each bubble size group could easily be reassigned to within the SCTM/NPHASE-CMFD iteration process (Figure 4.1).

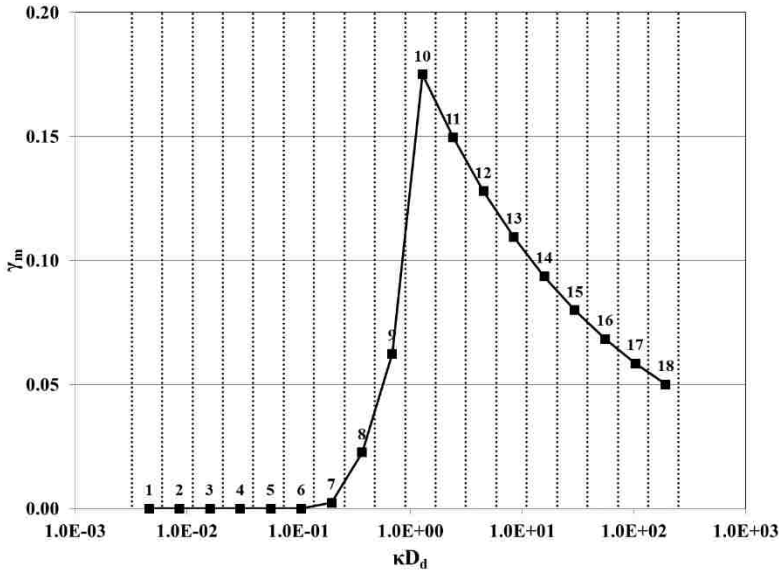

Figure 6.2. Example spectral weighting factor (γ_m) for bubble-induced source term.

Two bubble-induced turbulent source term models have been implemented as options for use with the SCTM in NPHASE-CMFD. The first is that used by Bolotnov et al. [9, 10] and proposed by Lahey [40]:

$$\phi_i = C_{p_i}\left(1 + C_{D_i}^{4/3}\right)\alpha_i V_{R_i}^3 / D_i \tag{6.12}$$

where for size group-*i*: the drag coefficient (C_{D_i}) is given in Equation (6.5), α_i is the local void fraction, V_{R_i} is the relative velocity, D_i is the bubble diameter, and $C_{p_i} = 1/2\, C_{VM_i}$ [10]. The second bubble-induced source option is that proposed by Rzehak and Krepper [42]:

$$\phi_i = \frac{3}{4} C_{D_i} \alpha_i V_{R_i}^3 / D_i \tag{6.13}$$

where the terms are defined the same as in Equation (6.12).

The SCTM has been applied to upward monodispersed and polydispersed adiabatic air-water flows in different geometries.

6.3 Comparison of High- and Low-Reynolds Number Turbulence Closures

This work is the first time a LRN turbulence modeling approach has been used for multiphase flow modeling in NPHASE-CMFD. Therefore, a first test was conducted using the code's native k-ε model to compare the HRN and LRN turbulence closure options where the new lift coefficient modification (Figure 6.1) was used for the LRN model. This test was performed using simple parallel plate flow geometry with constant air-water properties at atmospheric conditions (Table 6.1). The spacing between the plates was 20.25 mm, the Reynolds number was approximately 30,000, the liquid and gas superficial velocities were 1.216 and 0.075, respectively, and bubbles maintained a constant diameter of 2.0 mm. The results in Figure 6.3 show satisfactory agreement for the HRN and LRN model comparison. The predictions are quite similar although the LRN model captures the TKE peak close to the wall. Clearly, the LRN model predicts the correct zero void fraction boundary condition close to the solid wall boundary.

Table 6.1. Material properties for atmospheric air/water conditions. Note these values are similar to those used by Rzehak et al. [57].

Property	Description	Value	Units
ρ_c	Continuous phase (water) density	997.561	$kg \cdot m^{-3}$
μ_c	Continuous phase (water) molecular viscosity	8.887×10^{-4}	$kg \cdot m^{-1} \cdot s^{-1}$
ρ_d	Dispersed phase (air) density	1.204	$kg \cdot m^{-3}$
μ_d	Dispersed phase (air) molecular viscosity	1.725×10^{-5}	$kg \cdot m^{-1} \cdot s^{-1}$
σ	Surface Tension	0.0728	$N \cdot m^{-1}$

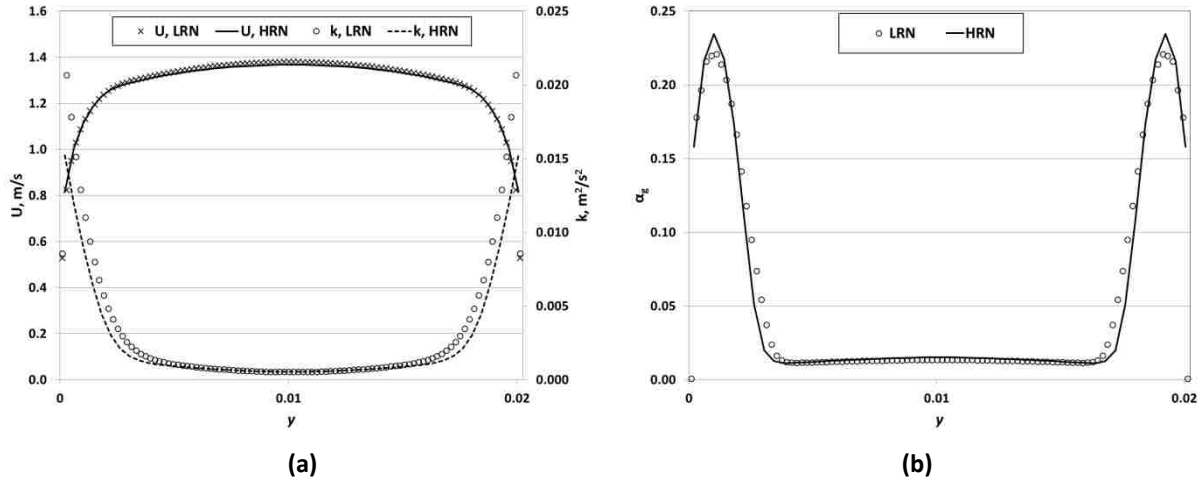

(a) (b)

Figure 6.3. Comparison of HRN and LRN k-ε results for parallel plate geometry. (a) Stream-wise liquid velocity (left vertical axis) and TKE (right vertical axis). (b) Void fraction.

6.4 TPF2: Two-Phase Turbulent Pipe Flow

Circular pipe geometry using the NPHASE-CMFD R-Z cylindrical coordinate option is again an excellent test for the SCTM (see § 5.4). Much of the experimental data available in the literature for bubbly two-phase flow exists for upward circular pipe flow and the SCTM was compared against existing monodispersed experimental data in 25 mm diameter pipe. The SCTM was also used to model polydispersed bubbly two-phase flow in 25 mm diameter pipe and monodispersed bubbly two-phase flow in 200 mm diameter pipe on a 3D numerical mesh.

6.4.1 25 mm Diameter Pipe

6.4.1.1 Monodispersed Bubbly Two-Phase Flow

The experimental data of Hosokawa and Tomiyama [107] was chosen as the first assessment of the wall-resolved SCTM for turbulent bubbly two-phase flows. As discussed previously (§ 5.4.1), Hosokawa and Tomiyama [107] used LDV image processing techniques to investigate upward single and bubbly two-phase flows with air-water systems at atmospheric conditions. Table 6.2 gives the average parameters of interest for four test cases. As with the single-phase simulations (§ 5.4.1), the left and right wave number boundaries were κ_0 = 1.0 m^{-1} and κ_N = 7.82x10^4 m^{-1}, respectively and the minimum number of wave number bins was calculated to be N = 16. For all the results shown here N = 18 wave number bins were used unless explicitly noted to use N = 16 wave number bins.

Table 6.2. Parameters for experimental data of Hosokawa and Tomiyama [107].

Case	J_c (m/s)	J_d (m/s)	α_d	D_d (mm)
HT21	0.5	0.018	0.0231	3.21
HT22	0.5	0.025	0.0399	4.25
HT23	1.0	0.02	0.0146	3.52
HT24	1.0	0.036	0.0330	3.66

Predictions of mean liquid velocity in the stream-wise direction are shown for the SCTM and k-ε model in comparison to the experimental data for each test case in Figure 6.4. For case HT21, results for both of the bubble-induced turbulent source terms implemented into the SCTM are shown, where "L" denotes the Lahey term (Equation (6.12)) and "RK" denotes the Rzehak and Krepper term (Equation (6.13)). For the k-ε results, the NPHASE-CMFD turbulence model is used with no additional turbulent source terms as well as with the Lahey term user-implemented. Note that for the k-ε model the turbulent dissipation equation source had to be included as well (as defined by Lahey [40]). The predictions of mean liquid velocity are in good agreement with the experimental data for each test case except for the k-ε result with the Lahey source term that is depressed in the pipe center. In each of the cases both the SCTM and k-ε model predict velocity profiles near the pipe center that are flatter than the profile measured experimentally. In case HT21,

both bubble-induced source term models provide an identical result along with the prediction using the minimum N = 16 wave number bins rather than N = 18 wave number bins.

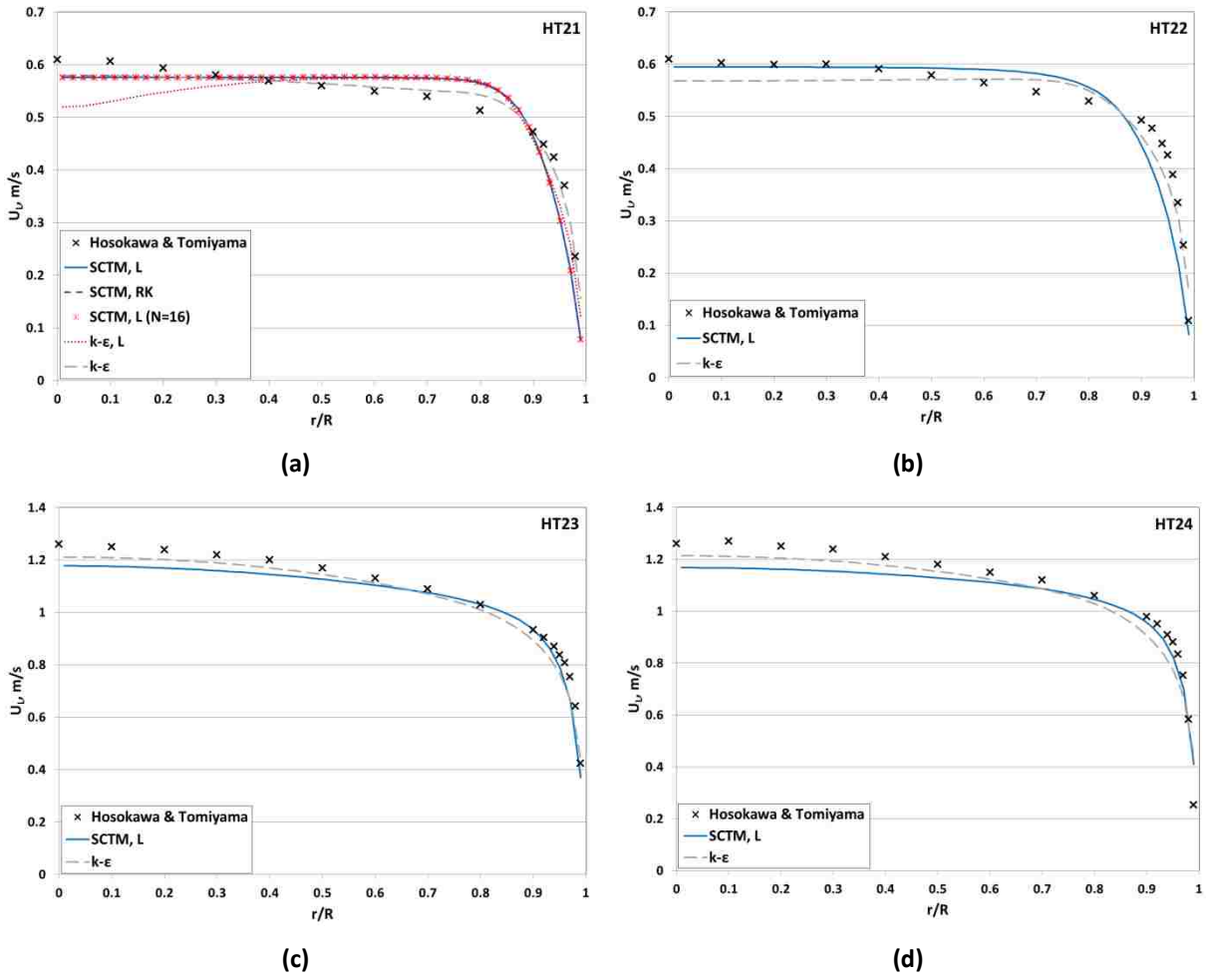

Figure 6.4. SCTM and k-ε predictions of mean stream-wise liquid velocity in comparison to experimental data of Hosokawa & Tomiyama [107].

SCTM and k-ε predictions of TKE are shown in comparison to the Hosokawa and Tomiyama experimental data in Figure 6.5. The predictions of TKE for both turbulence models are in much larger disagreement with the experimental data than the mean velocity across all four cases. Similar difficulties in predicting TKE profiles of bubbly two-phase flows with eddy viscosity turbulence models have been shown in the literature [39, 42]. Similar to the single-phase prediction in 25 mm pipe (Figure 5.21), the SCTM results show a wider TKE peak than the k-ε model. However, both

turbulence models fail to predict the TKE magnitude although for the higher Reynolds number HT23 and HT24 cases (Figure 6.5(c), Figure 6.5(d)) the k-ε model does show slightly better predictions. In lower Reynolds number cases HT21 and HT22 (Figure 6.5(a), Figure 6.5(b)) the k-ε prediction near the pipe centerline is very low although, for the HT22 case, the SCTM prediction is equally as disagreeable albeit the estimate is much higher than the experimental data. Notably, the SCTM predictions using either bubble-induced source term in the HT21 case are nearly identical. As discussed previously (§ 1.1.1.2), issues with the form of the bubble-induced source term are most predominant when determining the timescale of the source term for the dissipation rate equation. Since the SCTM does not use an empirical dissipation rate transport equation, such as that used in two-equation models, the need to determine this controversial timescale is eliminated. The HT21 simulation with the minimum N = 16 wave number bins is essentially identical to the N = 18 wave number bins simulation and indicates bin convergence of the SCTM.

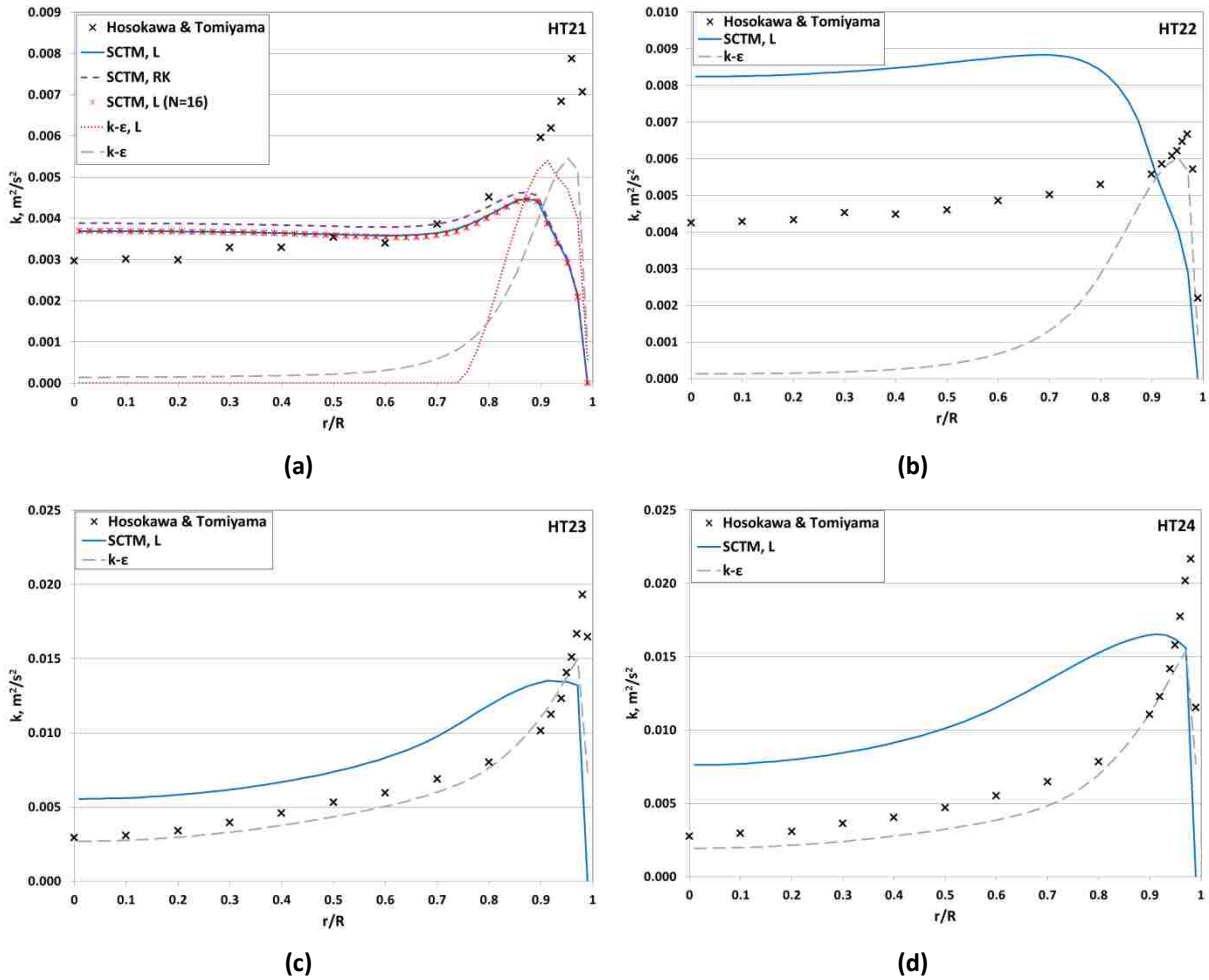

Figure 6.5. SCTM and k-ε predictions of liquid TKE in comparison to experimental data of Hosokawa & Tomiyama [107].

NPHASE-CMFD simulation results for gas volume fraction with the SCTM and k-ε model are shown in comparison to the experimental data in Figure 6.6 for all four cases. As with the mean velocity and TKE predictions the influence of bubble-induced source terms is negligible for the SCTM and bin convergence is shown for the N = 16 wave number bins HT21 simulation. It is interesting to note the experimental data profiles are rather flat for the lower Reynolds number cases HT21 and HT22 (Figure 6.6(a), Figure 6.6(b)) but both turbulence models predict a more wall-peaked void fraction profile. For the higher Reynolds number HT23 and HT24 cases (Figure 6.6(c), Figure 6.6(d)) the experimental data shows a wall-peaked void fraction distribution that both turbulence models better estimate. At higher Reynolds number, the SCTM predicts the peak location, peak magnitude,

and overall shape of the gas volume fraction distribution quite well. This improvement over the HT21 and HT22 cases could partially be due to the higher shear-induced turbulence in this case and therefore higher velocity gradient. This creates a stronger lift force that pushes the volume fraction towards the wall and follows the experimental result of a more pronounced wall-peaked profile. There is some numerical checkerboarding behavior in estimates of the void fraction from both the k-ε model and the SCTM, particularly for the HT23 case. However, the general trend of void fraction shape should still be accepted.

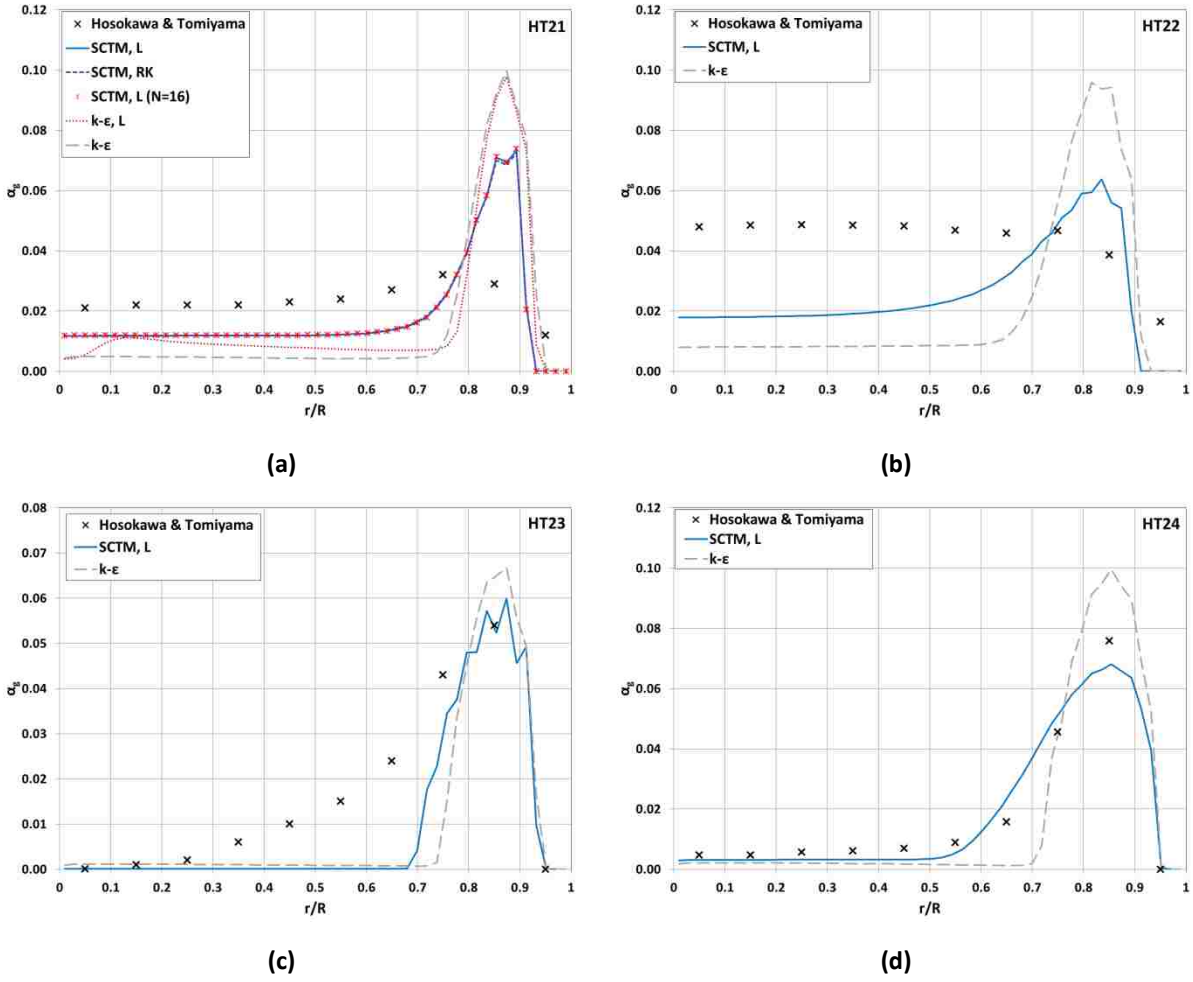

Figure 6.6. SCTM and k-ε predictions of dispersed phase volume fraction in comparison to experimental data of Hosokawa & Tomiyama [107].

SCTM predictions of the TKE spectrum ($E(\kappa) = k_m/\Delta\kappa_m$) are shown for a radial spatial location near the pipe centerline (Figure 6.7(a)) and near the pipe wall (Figure 6.7(b)) for case HT21.

Near the pipe centerline the void fraction profile is essentially flat (Figure 6.6(a)) resulting in homogeneous turbulent bubbly flow. At this location, the TKE spectrum for the two-phase results shows the -5/3 slope of the inertial subrange transitioning to a less-steep slope than that shown in single-phase flow with the same liquid volumetric flux (case HT11). This transition to a less steep slope in homogeneous turbulent bubbly flow has been presented in the literature [50] and shown in previous work with the SCTM [10] and a value close to -11/3 is reasonable. However, near the pipe wall (Figure 6.7(b)) the difference in TKE spectrum behavior is not as pronounced in the dissipation range. The influence of the bubble-induced source term can be seen around bin-8 where the two-phase spectra magnitudes become higher than the single-phase. However, the shapes of the spectra remain consistent through the inertial subrange and dissipation range. One possible explanation is that this location is close to the peak of TKE and the shear-induced TKE of the liquid therefore dominates throughout the energy cascade process.

Spectral analysis of turbulent bubbly two-phase DNS data showed (§ 2) that modulation of the spectrum slope occurs even in flows where the shear-induced turbulence is significantly greater than the bubble-induced turbulence although it is possible that the modulation close to wall boundaries differs than in the essentially homogeneous bubbly two-phase turbulence region in the bulk of the flow. Appendix C provides a more detailed comparison of the single-phase and two-phase spectra as a function of spatial location in the 25 mm diameter pipe. The results in Appendix C show that the single-phase and two-phase spectra become more similar in the high wave number range as distance from the pipe centerline increases. The results for 16 wave number bins in comparison to 18 wave number bins show that the SCTM achieves independence from spectral resolution. TKE spectrum results again show that the difference in the Lahey and Rzehak and Krepper source terms is negligible for the SCTM. The TKE spectrum results for the HT22 case were similar to those from the HT21 case.

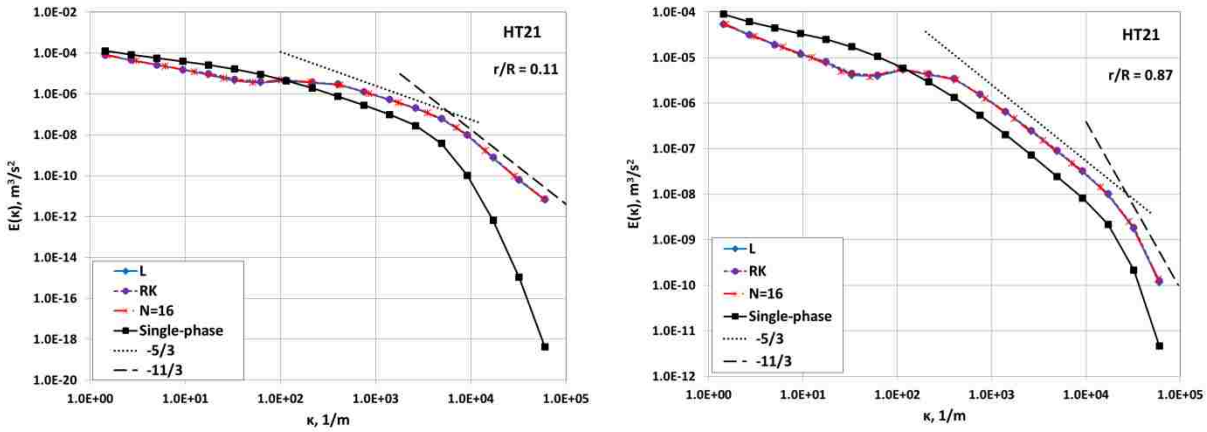

(a) **(b)**

Figure 6.7. SCTM TKE spectrum at two spatial locations (HT21) compared to single-phase result.

Interestingly, TKE spectrum comparisons between the HT24 case and a single-phase case with the same liquid volumetric flux (case HT12) only show moderate differences (Figure 6.8). The discussion pertaining to Figure 6.7 still holds true between locations in the bulk of the flow and in the near-wall region. However, the spectrum is only slightly less steep in the dissipation range for the radial location in the bulk of the flow. Due to the overall under-prediction of the TKE in the HT21, HT23, and HT24 cases it is possible that the bubble-induced source term needs to have a stronger effect on the overall TKE if the HT22 case is considered an outlier. A more distinct difference in spectrum results may then be realized for this HT24 case. TKE spectrum results for the HT23 case are similar to those shown for the HT24 case. When considering all these cases it should be reiterated that *no model constants have been adjusted* for the SCTM.

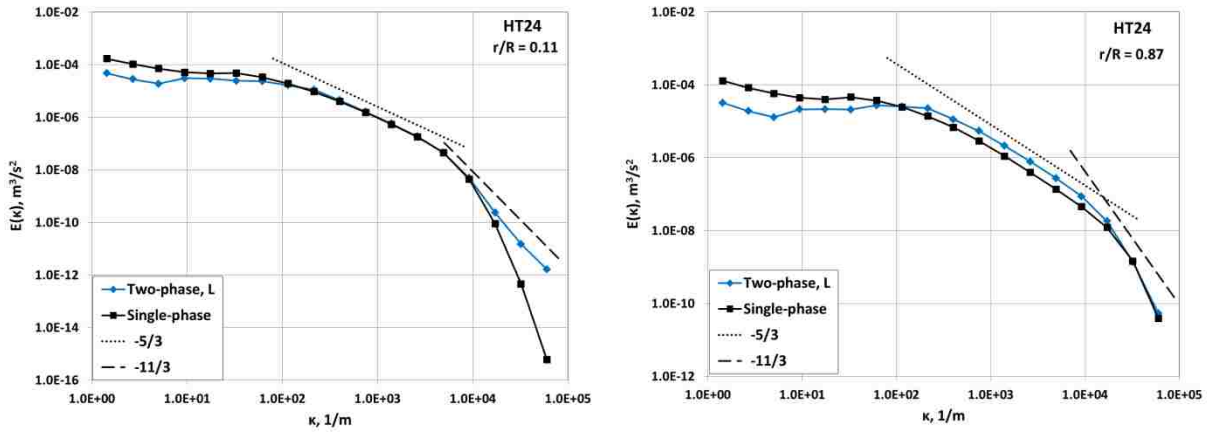

(a) (b)

Figure 6.8. SCTM TKE spectrum at two spatial locations (HT24) compared to single-phase result.

6.4.1.2 Polydispersed Bubbly Two-Phase Flow

A polydispersed test case was formulated to demonstrate the physical behavior of the SCTM when different bubble size groups are present. A small bubble size group and large bubble size group were modeled using the SCTM with the Lahey bubble-induced source term following Equation (6.12) to formulate the overall source term for bin-*m*. NPHASE-CMFD solves a separate set of mass and momentum equations for the liquid field, the first bubble size group, and the second bubble size group. The interfacial force terms were kept identical to those presented in § 6.1 with the exception of the lift coefficient for the large bubble group which was changed to a value of -0.015. For comparison, a monodispersed case was also considered where the bubble size was found to provide the same amount of gas volume occupied within the domain (see Appendix D for equivalent bubble diameter calculation details). The parameters for these cases are shown in Table 6.3. The gas volume fraction distributions for both of these cases are shown in Figure 6.9. The overall gas volume fraction of the polydispersed case is very similar to that of the equivalent monodispersed case. However, when considered separately, the correct physical behavior of the small and large bubble size groups is realized. The small bubbles are pushed towards the wall and the large bubbles are pushed towards the pipe centerline for a core-peaked profile. Although this behavior can be predominately controlled through the interfacial force definition, using the SCTM allows bubble size groups to retain their own influence on the liquid turbulence. Also, in more complex scenarios

where bubble break-up and coalescence are important the equations for both can be included separately for each bubble size group.

Table 6.3. Parameters for polydispersed case in 25 mm diameter pipe geometry.

Case	J_c (m/s)	J_{d1} (m/s)	J_{d2} (m/s)	α_{d1}	α_{d2}	D_{d1} (mm)	D_{d2} (mm)
Polydispersed	0.475	0.028	0.007	0.04	0.01	3.00	6.00
Monodispersed	0.475	0.035	-	0.05	-	3.25	-

It is interesting to investigate the influence of the bubbles on the liquid turbulence through the TKE spectrum (Figure 6.10). Two radial locations are considered where Figure 6.10(a) is within the bulk of the flow and the void fraction profile is essentially flat and Figure 6.10(b) is near the pipe wall and the void fraction peak. The change in energy spectrum slope in comparison to single-phase case with the same liquid volumetric flux is in accordance with the previous observations for Figure 6.7. In this case, the interesting physics of the different bubble sizes is captured in the spectrum and differences are seen between the polydispersed and equivalent monodispersed case. The influence of the large bubble group as an additional energy source is shown as an increase in the spectrum magnitude in the polydispersed case around bin-6 – bin-9. Interestingly, the spectrum magnitude is decreased for the polydispersed case in the first two wave number bins. It is possible that the presence of the gas phase in the center of the channel in the form of the larger bubbles suppresses the liquid turbulence at the largest eddy scale or limits the allowable size of the largest eddies in the flow.

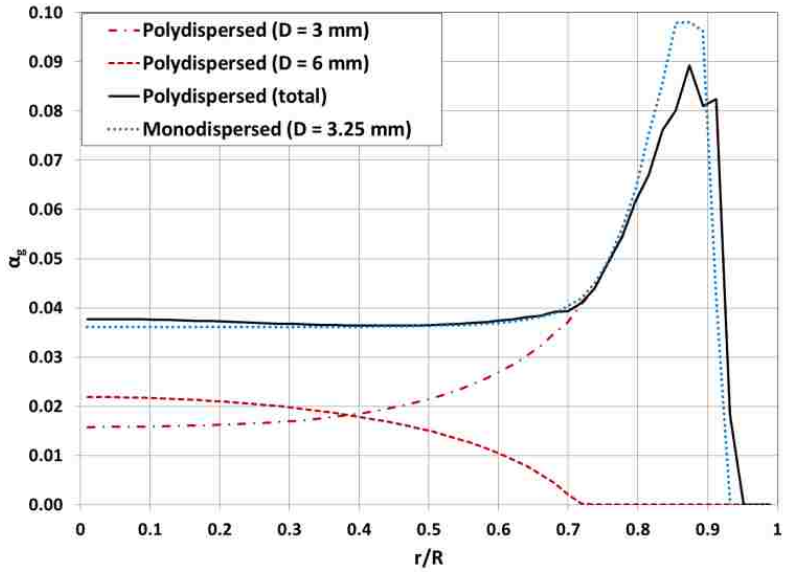

Figure 6.9. Gas volume fraction distribution for polydispersed and equivalent monodispersed cases in 25 mm diameter pipe geometry ("D" indicates bubble diameter).

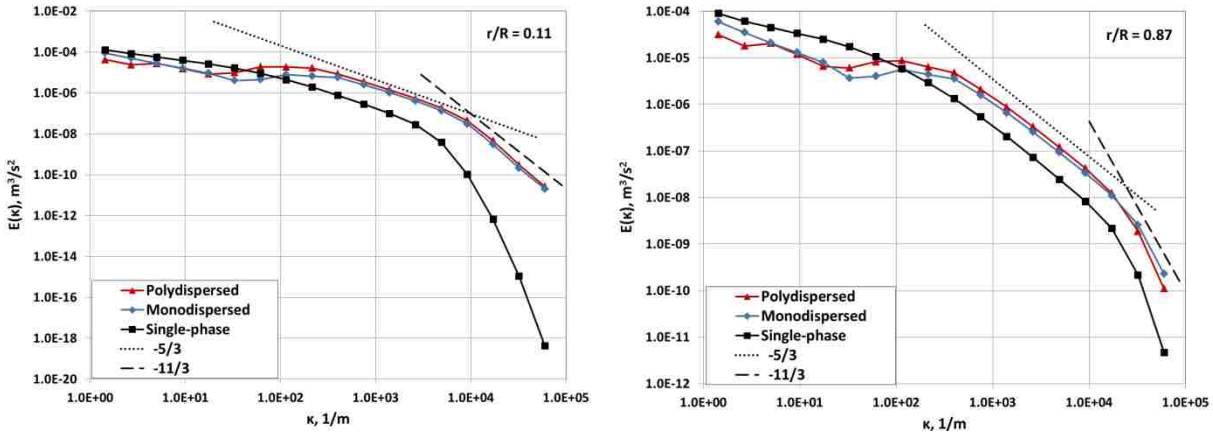

Figure 6.10. SCTM TKE spectrum results at two different spatial locations for polydispersed and equivalent monodispersed cases in 25 mm diameter pipe geometry.

The comparison to the Hosokawa and Tomiyama experimental data was an encouraging first test of the SCTM behavior for monodispersed and polydispersed wall-bounded bubbly two-phase flow. The results for mean flow parameters are similar to those from the k-ε model and within the engineering uncertainty generally shown in the literature for M-CFD using RANS approach. The TKE

spectrum predictions shown here are reasonable and resolving the TKE spectrum allows bubble groups with distinctively different characteristics to influence the liquid turbulence on their own accord. Using NPHASE-CMFD, each bubble group has a separate set of mass and momentum equations so that extension to more complex flows with phasic interaction is readily possible.

6.4.2 200 mm Diameter Pipe

The 200 mm diameter pipe geometry was chosen to qualitatively demonstrate SCTM two-phase capabilities in NPHASE-CMFD for a 3D geometry. The 3D 200 mm diameter pipe mesh shown in Figure 5.27 was again used although, as previously discussed (§ 5.4.2), this mesh was quite coarse in terms of required resolution for LRN turbulence modeling. However, the objective of the results shown here are verification of the ability for the SCTM to be used in NPHASE-CMFD for 3D multiphase simulations.

The inlet conditions for this two-phase case were a prescribed inlet velocity of 1.0 m/s for both the liquid and gaseous phases and inlet volume fractions of 98 % and 2 % for the liquid and gas phases, respectively. The liquid volumetric flux (J_c) was then 0.98 and the gas volumetric flux (J_d) was then 0.02. The bubble size (D_d) was 4.0 mm. The left and right wave number boundaries were identical to the single-phase case and set as κ_0 = 1.0 m^{-1} and κ_N = 7.32x10^4 m^{-1}, respectively. As with the single-phase case, the minimum number of spectral bins was calculated to be *N* = 16 and *N* = 18 bins were used for the simulation. The liquid and gas properties were taken to be water and air at atmospheric conditions (Table 6.1). These inlet conditions correspond to a bulk Reynolds number of about 224,500. The spectral weighting factors were calculated as shown in § 6.2 and used with the Lahey BIT source term (Equation (6.12)).

Figure 6.11(a) – (b) shows the stream-wise liquid and gas phase velocities taken as a slice perpendicular to the *x*-axis at a stream-wise location 95 % of the overall pipe length from the pipe inlet. Figure 6.11(c) – (d) shows the stream-wise liquid and gas phase velocities as a line plot across the *y*-axis of the radial slice through the pipe center where the values for the line plots were obtained from Paraview as values on the mesh elements across the *y*-axis. The stream-wise velocities verify the behavior of the SCTM for two-phase behavior in 3D geometry. The simulation was not executed to total convergence but the correct trends are exemplified. The shapes of the

velocity profiles are reasonable and a relative velocity of the gas phase to the liquid phase has developed due to the buoyant nature of the rising bubbles.

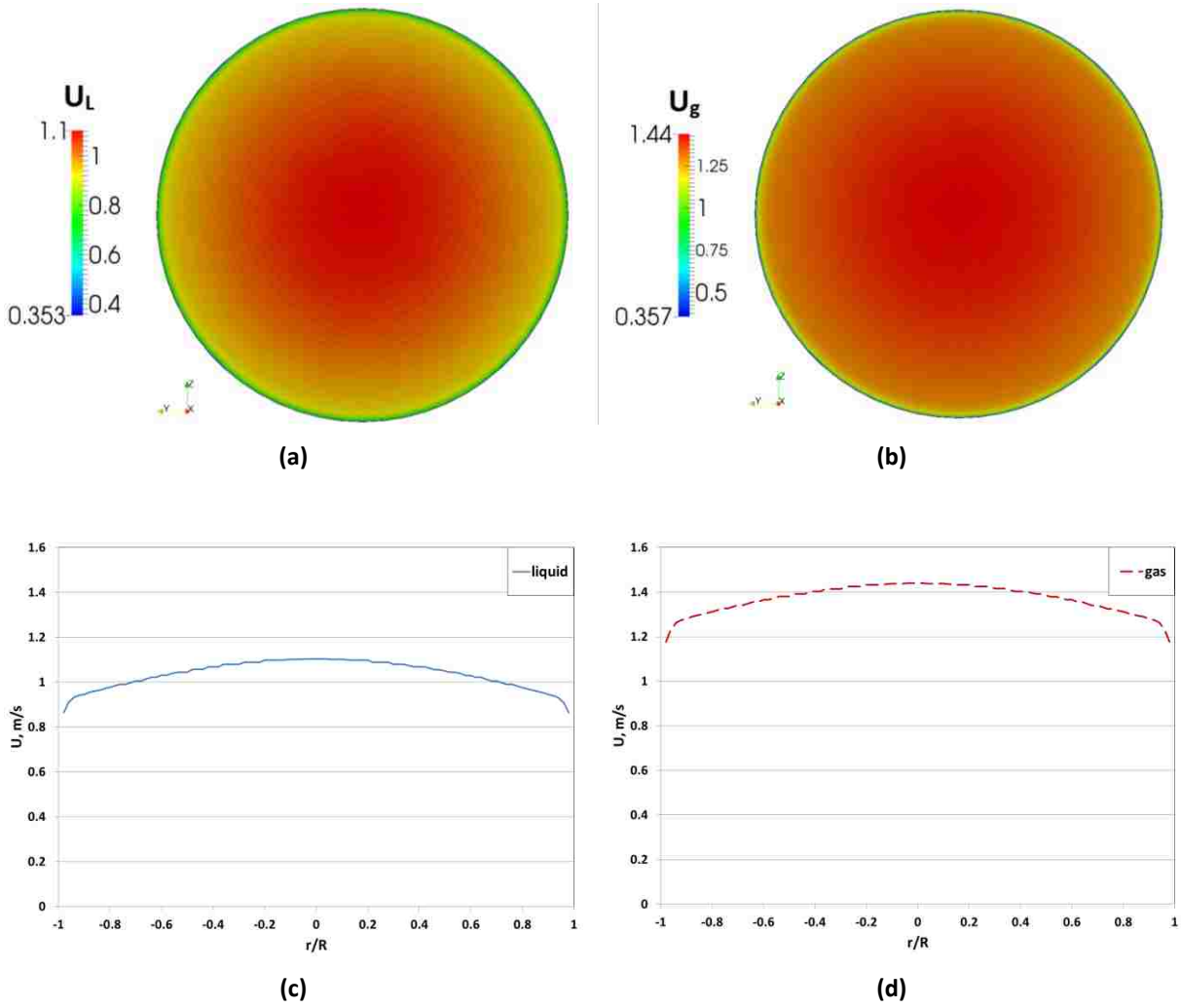

Figure 6.11. Stream-wise liquid and gas velocity distributions. (a) – (b): shown as a slice across the stream-wise (*x*) axis of the pipe at an axial position 95 % of the total pipe length from the inlet. (c) – (d): shown as a line plot across the radial slice.

Likewise, the volume fraction predictions shown as a slice across the stream-wise (*x*) axis of the pipe at an axial position 95 % of the total pipe length from the inlet and the line plots of volume fractions across the *y*-axis of the slice (Figure 6.12) also exemplify the expected trends. The gas phase volume fraction is wall-peaked and the effect of the lift force with wall-repellent coefficient is

seen as the dark blue ring very close to the wall (Figure 6.12(b)). The simulation results shown here are reasonable even though the numerical mesh is coarse. Some mesh effects are evident in the 3D distributions of volume fraction as areas of discoloration due to coarseness of the mesh. The 3D 200 mm diameter pipe results shown here are an excellent verification of the SCTM behavior in NPHASE-CMFD.

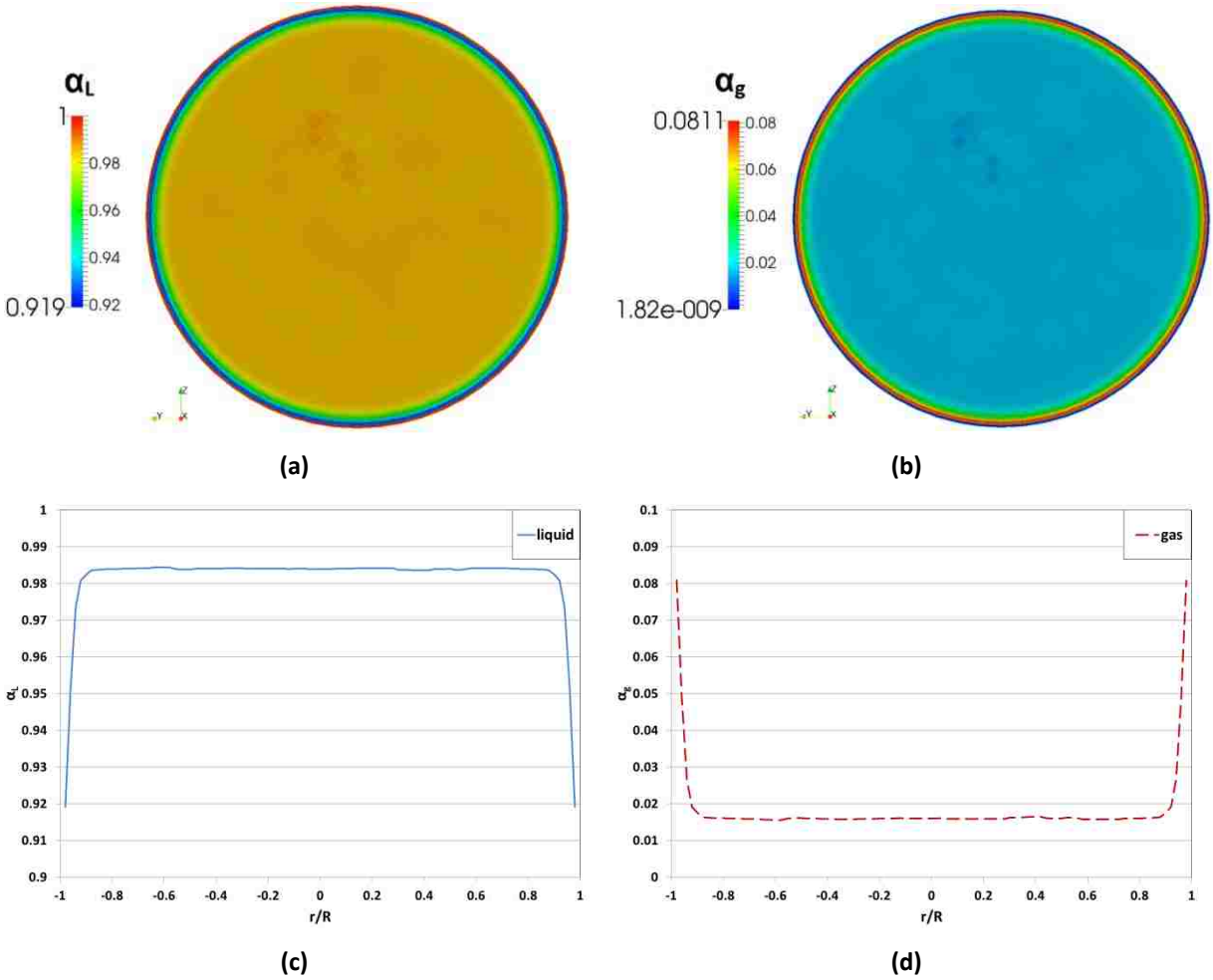

Figure 6.12. Liquid and gas phase volume fraction distributions. (a) – (b): shown as a slice across the stream-wise (*x*) axis of the pipe at an axial position 95 % of the total pipe length from the inlet. (c) – (d): shown as a line plot across the radial slice.

6.5 TPLF2: Two-phase Turbulent Flow between Parallel Plates

The parallel plate geometry with 100 mm spacing between the plates (§ 5.5) was used for simulation of monodispersed and polydispersed bubbly two-phase flow. The working fluids were water and air at atmospheric conditions (Table 6.1). The numerical mesh with 200 equidistant elements in the direction normal to the duct walls with a dimensional mesh spacing of 0.5 mm was used just as with the single-phase case. The left and right wave number boundaries were identical to the single-phase case and set as κ_0 = 1.0 m^{-1} and κ_N = 8.6x10^4 m^{-1}, respectively. The results for the single-phase case showed that *N* = 18 and *N* = 22 spectral bins converged to nearly identical solutions and *N* = 18 spectral bins are used for the two-phase simulations. For both the monodispersed and polydispersed cases the Lahey BIT source term was used.

6.5.1 Monodispersed Bubbly Two-Phase Flow

The inlet conditions for monodispersed bubbly two-phase flow are shown in Table 6.4 below and correspond to a bulk Reynolds number of about 112,250.

Table 6.4. Inlet conditions for monodispersed two-phase simulation in parallel plate geometry.

Phase	Velocity (m/s)	Volume Fraction	Volumetric Flux (m/s)	Bubble Diameter (mm)
Liquid (water)	1.0	0.98	0.980	-
Gas (air)	1.1	0.02	0.022	4.0

Velocity distributions for the liquid and gas phases are shown in Figure 6.13 as a line plot across the duct in the direction normal to the walls and in Figure 6.14 as a slice perpendicular to the *x*-axis at a stream-wise location 95 % of the overall duct length from the duct inlet where the *z*-axis has been scaled shorter for enhanced viewing. The difference in gas and liquid velocity shows that a relative velocity of about 0.33 m/s develops between the phases due to the buoyant nature of the rising bubbles. In comparison to the liquid velocity profile from the single-phase simulation (Figure 5.32), the velocity profiles are much flatter across the duct with the only appreciable gradient occurring very close to the walls. This same type of velocity profile flattening between single-phase and two-phase simulations was seen for the 25 mm pipe simulations as well (Figure 5.22 vs. Figure 6.4).

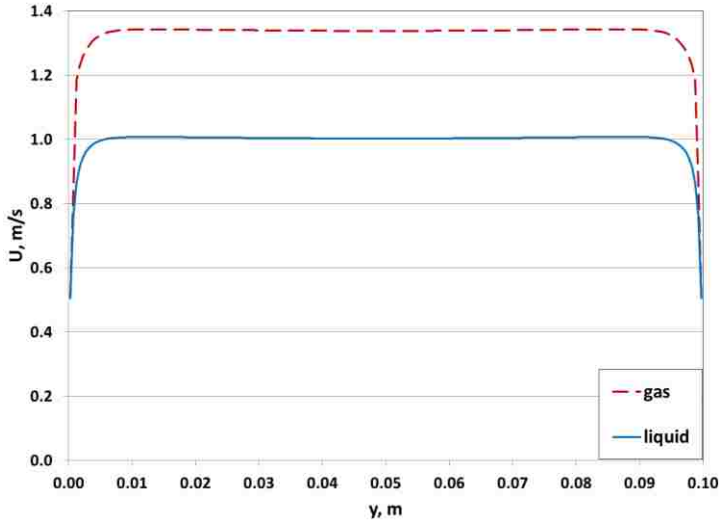

Figure 6.13. Prediction of liquid and gas velocities in the stream-wise direction.

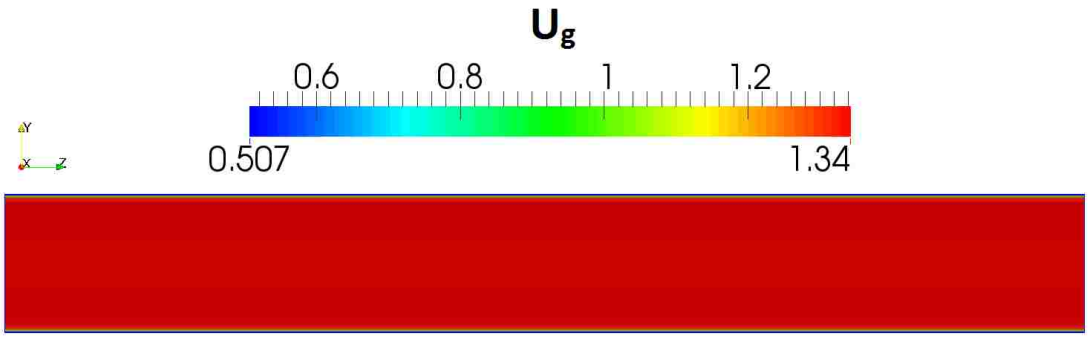

(a)

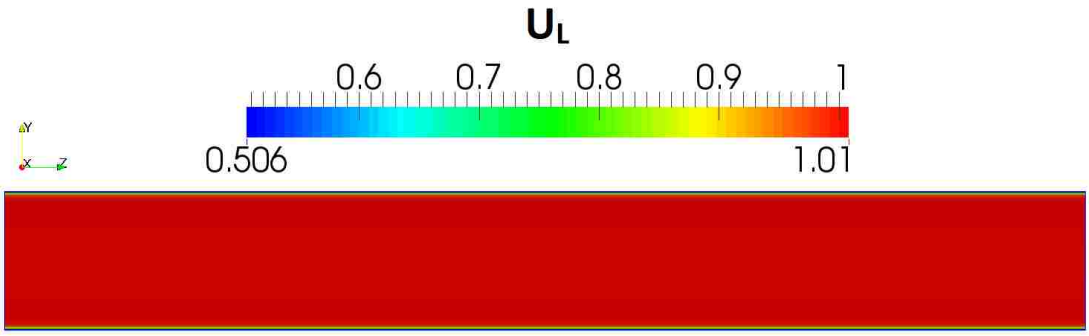

(b)

Figure 6.14. Stream-wise liquid (U_L) and gas (U_g) velocity distributions between parallel plates with 100 mm spacing (y direction is normal to duct walls). The z-axis has been scaled shorter for enhanced viewing.

Prediction of the void fraction distribution (Figure 6.15) shows the expected wall-peaked behavior for small bubbles where the lift forces acts to push the bubbles towards the duct walls. Due to the presence of the solid wall boundaries void fraction value peaks at slightly greater than 7 % even though the inlet average void fraction was 2 %. With the LRN SCTM and the modified lift coefficient (Equation (6.9)) the area of zero void fraction within one bubble diameter of the wall is evident in Figure 6.15(a) and as the solid blue region very close to the duct walls in Figure 6.15(b). Considering the sharp gradients of mean velocities and volume fractions close to the walls, LRN turbulence modeling can enhance predictions of multiphase flow since the near-wall boundary layer is resolved rather than estimated as a boundary condition with controversial two-phase law of the wall formulations.

The TKE distribution for both single-phase (§ 5.5, J_L = 1.0 m/s) and two-phase simulations in parallel plate geometry is shown in Figure 6.16(a). The two-phase results show the expected wall-peaked TKE profile with a more pronounced peak than the single-phase results. The two-phase results are also of higher magnitude than single-phase results. This increase in magnitude can be realized in the TKE spectra. Figure 6.16(b) – Figure 6.16(d) show the TKE spectra at three different spatial locations. The spatial locations for the TKE spectra are denoted on the TKE distribution in Figure 6.16(a) as the red star symbols. In each of the spectra, the low wave number/large-eddy end of the spectra has a distinctly different shape and less energy than the single-phase data. Conversely, the energy spectra all exhibit higher energy content in the high wave number/small-eddy end of the spectra. Although the small wave number range has considerably less energy in two-phase flow the contribution of BIT is still sufficient enough to increase the overall TKE. Also, the two-phase spectra exhibit the -5/3 slope of the inertial subrange transitioning to a slope less steep than comparable single-phase data as has been shown previously with the spectral analysis of DNS data and in the 25 mm diameter pipe geometry calculations with the SCTM and NPHASE-CMFD. Similar to the 25 mm diameter pipe geometry, the difference in energy in the high wave number range increases as spatial distance from the solid wall boundary increases. In light of the much flatter TKE profile in the bulk of the flow for two-phase data in comparison to single-phase data (Figure 6.16(a)), this difference in the high wave number end of the spectra could be due to the continuous influence of BIT in the essentially homogeneous two-phase flow region near the duct

centerline. The peak of the spectral weighting factor (γ_m) for this case occurred in bin-9 and the increase of TKE density in bin-9 is evident for each of the spatial locations.

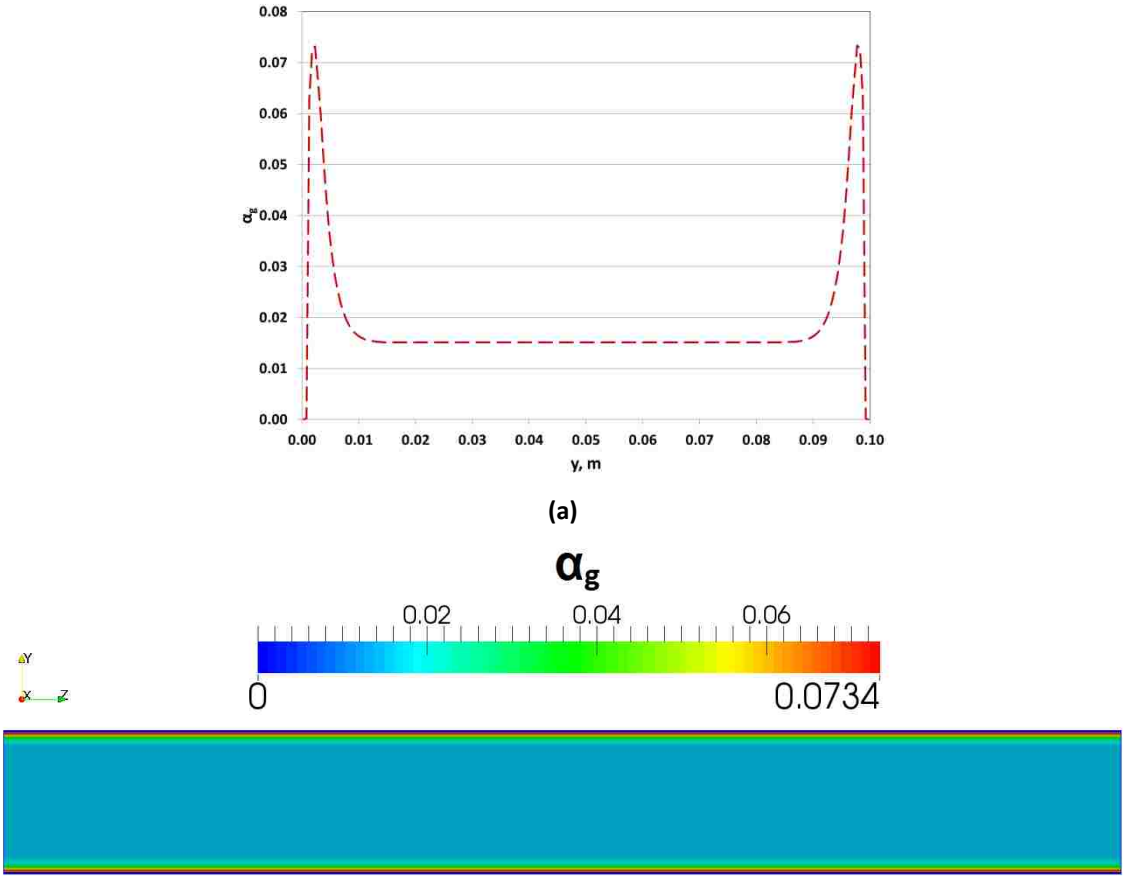

Figure 6.15. Gas volume fraction as a line plot across the duct width (a) and as a slice across the stream-wise direction (*y* direction is normal to duct walls) with the *z*-axis has been scaled shorter for enhanced viewing (b).

In terms of SCTM verification within the NPHASE-CMFD code, the mean velocity, void fraction, and TKE distributions are all symmetric about the duct centerline as expected. This indicates that in two-phase simulations where multiple wall boundary conditions are present the SCTM correctly calculates gradients, wall-distances, etc. as required by the model formulation. This provides increased confidence that the SCTM has been correctly implemented into NPHASE-CMFD.

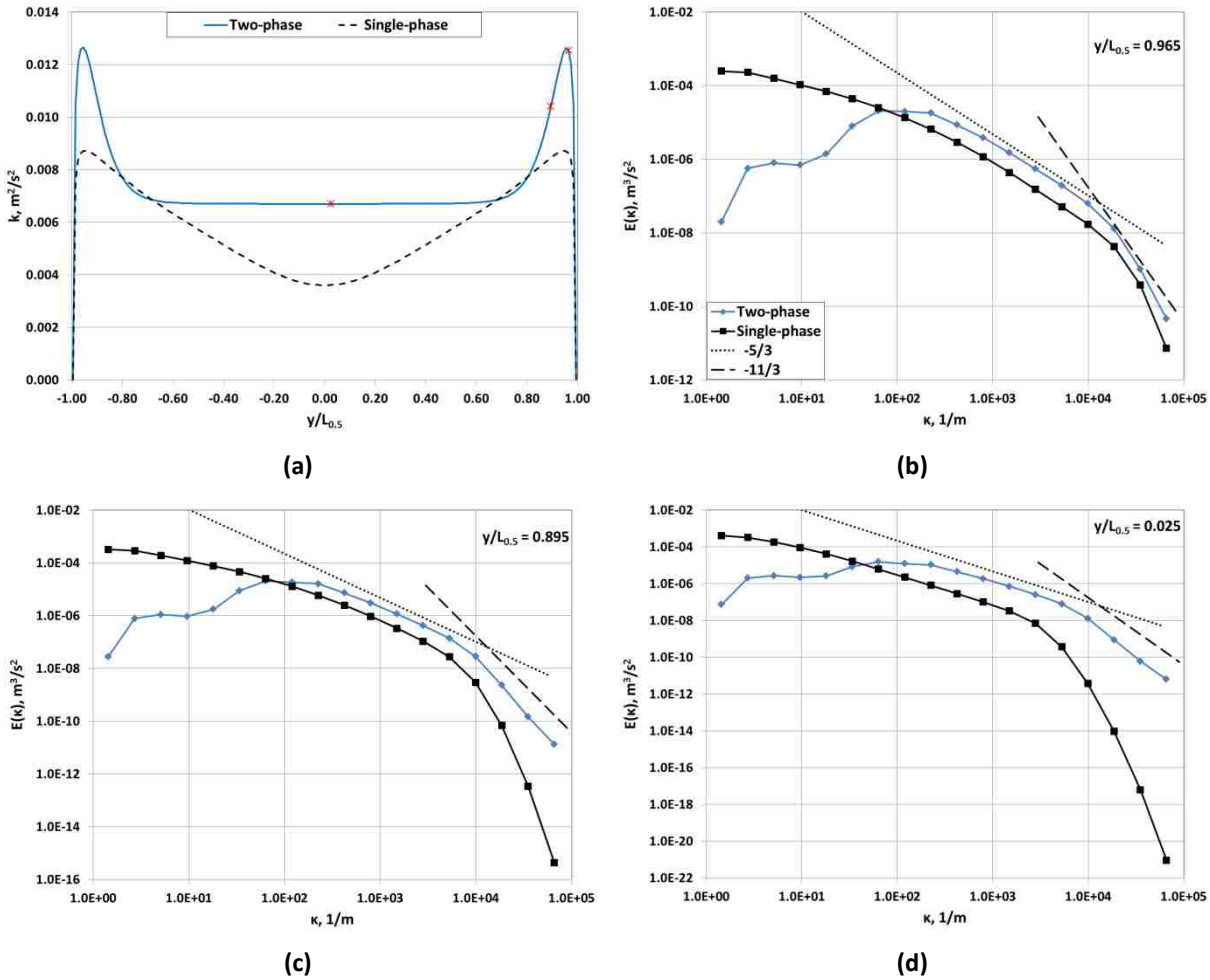

Figure 6.16. (a): Single-phase and two-phase SCTM TKE as a function of non-dimensional wall distance with zero at duct centerline. (b) – (d): TKE spectra at three spatial locations ($y/L_{0.5}$ = 0.965, 0.895, 0.025) denoted by star symbol on TKE distribution in (a).

The total source term balance is shown in Figure 6.17 and, with the exception of the diffusion term since it is handled internally by NPHASE-CMFD, constitutes the RHS of Equation (6.10) and includes the production, spectral transfer, dissipation, and BIT/dispersed phase source terms. The shapes of the production and dissipation terms are similar to those for single-phase flow (Figure 5.36) albeit the peak magnitudes are higher in two-phase flow. The increase in peak magnitudes is physically sound due the sharp gradients of velocity close to the duct walls in two-phase flow. The BIT source term mirrors the shape of the void fraction distribution and peaks close to the duct walls with the influence of the modified lift coefficient apparent as the region equal to zero BIT source

very close to the walls. The total spectral transfer term indicates that spectral transfer does not contribute to the overall TKE.

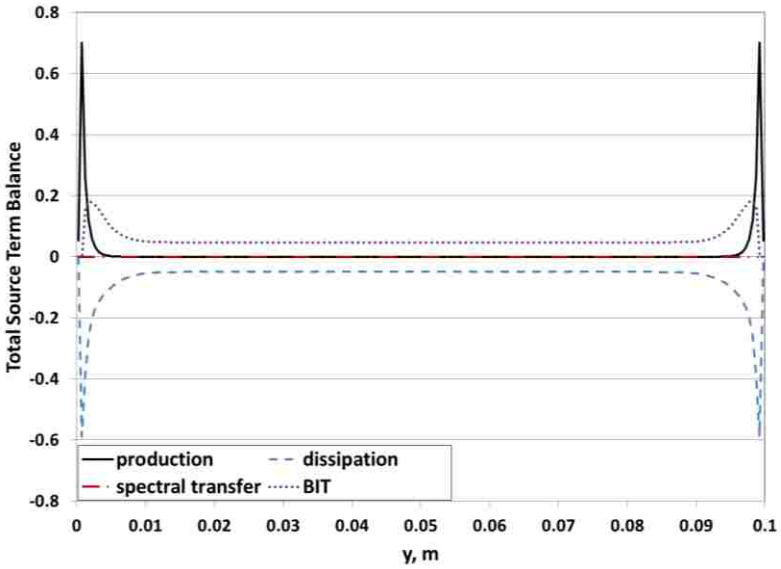

Figure 6.17. Total source term balance using the SCTM in NPHASE-CMFD for two-phase simulation in the parallel plate geometry with 100 mm spacing.

While Figure 6.17 shows the distribution of the BIT source term in the spatial domain, Figure 6.18 displays how the BIT source term is distributed in the spectral domain. In Figure 6.18 the spectral weighting factor (γ_m) is plotted as a function of the bin characteristic wave number ($\bar{\kappa}_m$) multiplied by the bubble diameter. For this particular case, the peak of the spectral weighing factor, where the wave number is on the order of the bubble diameter, occurs in wave number bin-9. Recall that discussion on how the spectral weighting factors are determined at the initialization of a two-phase simulation with the SCTM in NPHASE-CMFD was provided in § 6.2.

It is interesting to view the bin BIT source terms as a contour in both the spectral and spatial domains (Figure 6.19). The distribution of the BIT source term is shown to be peaked (concentrated area colored as red) in bin-9 and close to the duct walls. The contour plot is a schematic way to combine Figure 6.17 and Figure 6.18 and view the BIT source term in both spatial and spectral space. The advantage of the SCTM for two-phase flow simulations is the ability to define the BIT source term across the spatial and spectral domain; i.e. anywhere within the space mapped by

Figure 6.19. The non-dimensional spatial distance ($y/L_{0.5}$) and logarithm of wave number (log[κ]) were chosen as the *y*-axis and *x*-axis, respectively, simply for feasibility of viewing the contour plot.

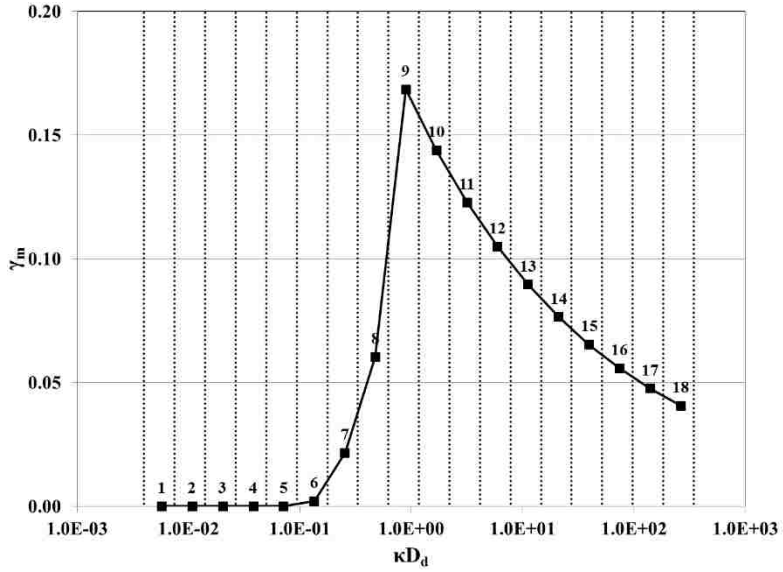

Figure 6.18. Spectral weighting factor (γ_m) of the BIT source term in two-phase parallel plate geometry simulation. The wave number bin boundaries are shown as vertical dotted lines.

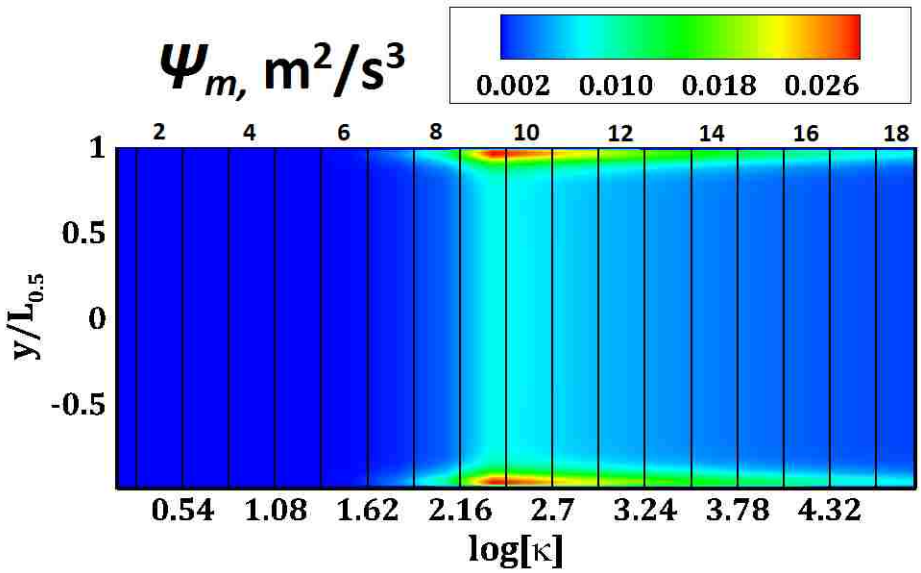

Figure 6.19. Contour levels of the bin BIT source terms in the spatial and spectral domains for the two-phase simulation in parallel plate geometry. The vertical lines represent wave number boundaries that are defined along the top of the plot.

The distribution of non-dimensional turbulent viscosity (ν_T/ν) predicted by the SCTM for monodispersed two-phase flow in the parallel plate geometry is shown in Figure 6.20. The capability of the SCTM to reasonably estimate the distribution of turbulent viscosity within the bulk of the flow and through the boundary layer to the wall and return that estimation to NPHASE-CMFD has been verified.

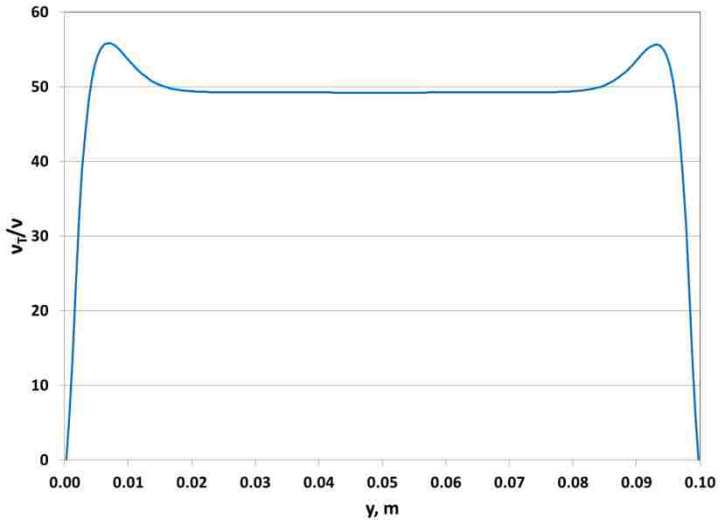

Figure 6.20. Distribution of turbulent viscosity, non-dimensonalized by kinematic viscosity, determined by the SCTM for two-phase flow in parallel plate geometry.

6.5.2 Polydispersed Bubbly Two-Phase Flow

The inlet conditions for polydispersed bubbly two-phase flow with a small and large bubble group are shown in Table 6.5 below and correspond to a bulk Reynolds number of about 112,250. The nominal lift coefficient for the large bubble group was $C_{L,0}$ = -0.015 as was done for the large bubble group in the polydispersed two-phase flow simulations in 25 mm diameter pipe geometry (§ 6.4.1.2).

Prediction of the gas volume fraction (Figure 6.21(a)) shows the different behavior of the small and large diameter bubble groups. The small bubbles are pushed towards the duct walls for a wall-peaked void fraction distribution and the large bubbles are pushed towards the channel center for a core-peaked void fraction distribution. There is a region of essentially zero total void fraction on either side of the large bubble group volume fraction peak that could be due to the interaction of

velocity, void fraction, and the lift force calculation. This region corresponds to counter-acting lift forces for the small and large bubble size groups. Improved lift force closure, particularly for the large bubble size group, could improve void fraction behavior in the future. Each bubble group has an individual set of mass and momentum equations that are solved within the NPHASE-CMFD framework. Figure 6.21(b) – (c) shows how stream-wise liquid velocity and TKE are influenced by the existence of the large bubble group. For monodispersed two-phase flow both of these quantities had a flat profile within the free stream region of the duct away from the influence of the walls. However, the presence of the large bubble group concentration within the duct center accelerates the liquid velocity in this region. The BIT source term of the large bubble group also imparts an increase of TKE that is seen to almost mirror the shape of the large bubble group void fraction distribution in the duct center. Additional figures showing these mean flow quantities are included in Appendix E.

Table 6.5. Inlet conditions for polydispersed two-phase simulation in parallel plate geometry.

Phase	Velocity (m/s)	Volume Fraction	Volumetric Flux (m/s)	Bubble Diameter (mm)
Liquid (water)	1.0	0.97	0.970	-
Gas (air) – small bubble group	1.2	0.02	0.024	3.0
Gas (air) – large bubble group	1.4	0.01	0.014	6.0

The influence of the large bubble group is also seen in the total source term balance (Figure 6.21(d)) where production, dissipation, and the BIT source term all differ from the predictions for monodispersed flow in Figure 6.17. The production term has two peaks on either side of the duct center due to the gradient of the liquid phase velocity caused by the large bubble group. In the duct center the inhomogeneous dissipation (Equation (5.3)) is negligible since the distance from the wall is substantial. However, the homogeneous dissipation (Equation (3.15)) is dependent on TKE and creates the dissipation peak in the duct center due to the added TKE of the large bubble group. The influence of the large bubble group on the total source balance is captured through the BIT source term.

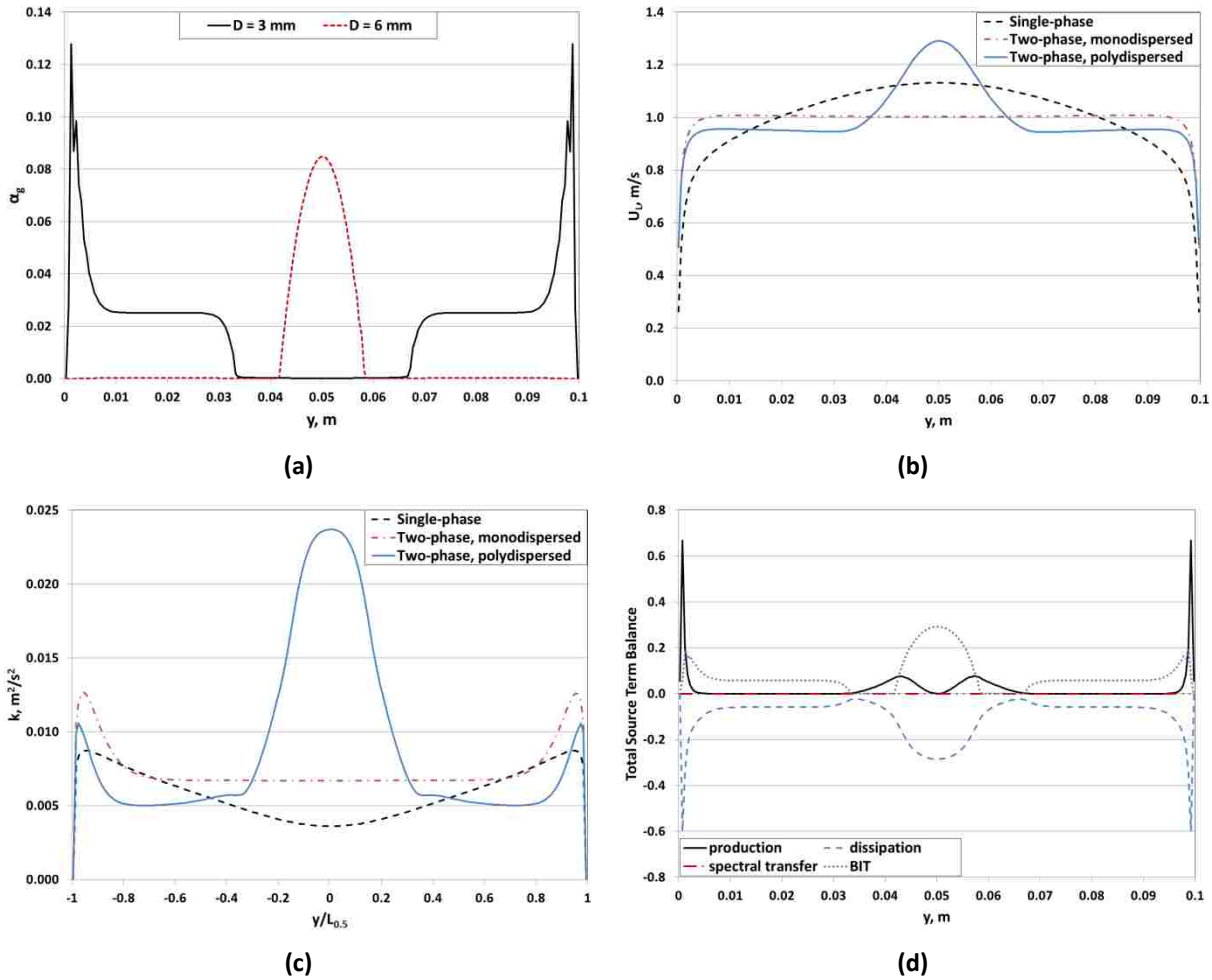

Figure 6.21. (a): Gas volume fraction of 3 mm (solid black line) and 6 mm (dashed red line) bubble groups.. (b): Stream-wise liquid velocity distribution. (c): TKE as a function of non-dimensional wall distance with zero at duct centerline. (d): Total source term balance.

The TKE spectra show the -5/3 slope of the inertial subrange transitioning to a slope close to -11/3 (Figure 6.22) as has been shown for other predictions of bubbly two-phase flow with the SCTM. The polydispersed spectra show some resemblance at the smallest wave numbers to the monodispersed spectra. There is an increase in spectra magnitude around bin-9 and bin-10 where the peak of the spectral weighting factor occurs for the large and small bubble groups, respectively. Interestingly, spectra shapes for spatial locations near the void fraction peak of the large bubble group (e.g. $y/L_{0.5}$ = 0.005) and small bubble group (e.g. $y/L_{0.5}$ = 0.975) exhibit a similar shape and

have magnitudes at the highest wave numbers that are larger than locations where the void fraction is essentially flat (e.g. $y/L_{0.5}$ = 0.295).

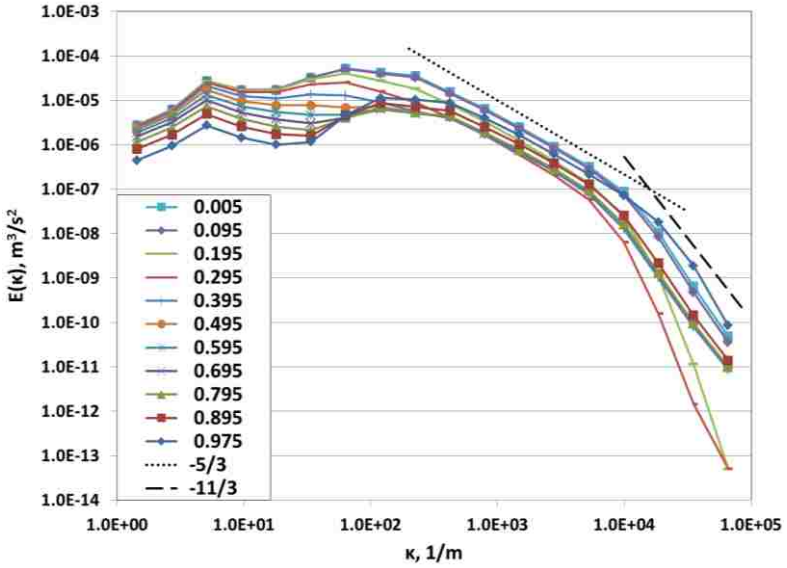

Figure 6.22. TKE spectra at different spatial locations (legend shows $y/L_{0.5}$ locations).

Recall from Equation (6.11) that the total BIT source term (Ψ_m) for bin-*m* is the sum of the source terms for each considered bubble size group. In this two bubble size group case, the total BIT source term for bin-*m* is then:

$$\Psi_m = \gamma_{m_1}\phi_1 + \gamma_{m_2}\phi_2 \tag{6.14}$$

where subscripts "1" and "2" indicate the small and large bubble size groups, respectively. The first and second terms on the RHS of Equation (6.14) are shown as contours in the spectral and spatial domain in Figure 6.23 (see also Appendix E). The non-dimensional spatial distance ($y/L_{0.5}$) and logarithm of wave number (log[κ]) were chosen as the *y*-axis and *x*-axis, respectively, simply for feasibility of viewing the contour plot. In Figure 6.23(a), the peak of the BIT source term for the small bubble group occurs in bin-10 and very close to the walls. In Figure 6.23(b), the peak of the BIT source term for the large bubble group occurs in bin-9 and within the center of the duct. The ability to resolve contributions of different bubble size groups to the liquid turbulence in both the spectral and spatial domains is the inherent capability of the SCTM that will increase the fidelity of RANS M-CFD.

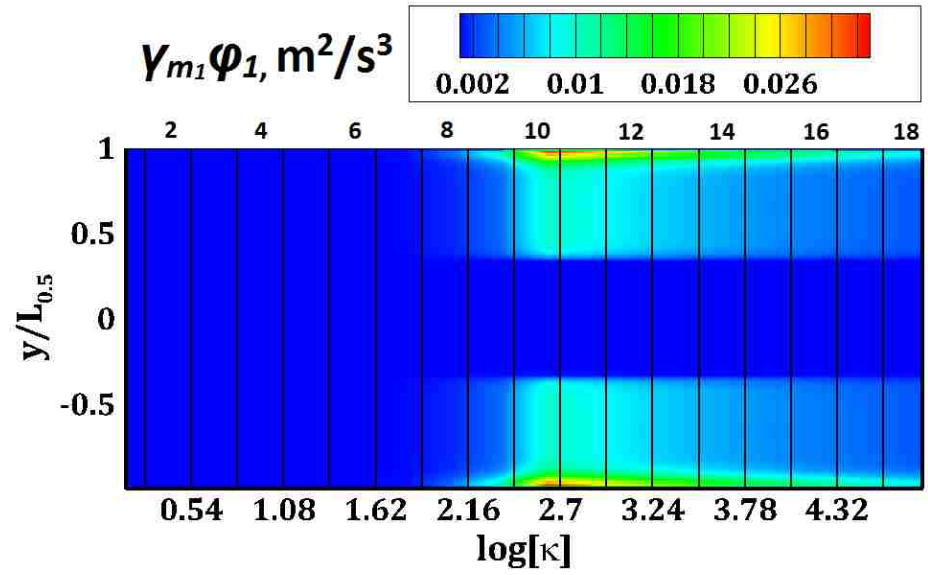

(a)

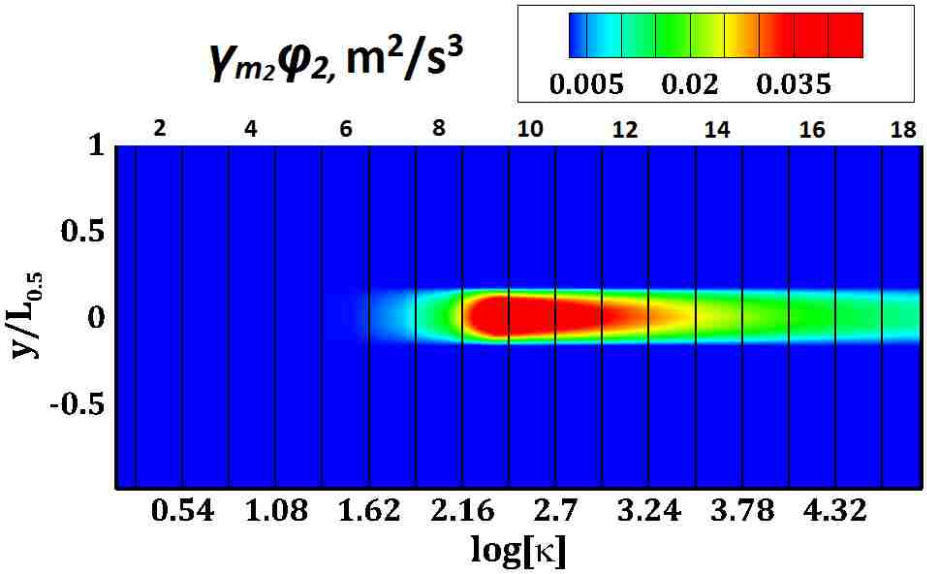

(b)

Figure 6.23. Contour levels of the bin BIT source terms in the spatial and spectral domains for the small (a) and large (b) bubble group in polydispersed two-phase simulation in parallel plate geometry. The vertical lines represent wave number boundaries that are defined along the top of the plot.

7. CONCLUSIONS

The SCTM has been further developed and tested as a RANS turbulence closure option in M-CFD codes for polydispersed two-phase flows. High-fidelity predictions of polydispersed two-phase flows are essential to improving safety and thermal-hydraulic analyses of current and future generations of nuclear reactors. M-CFD simulations with advanced spectral turbulence models such as the SCTM are becoming viable options for nuclear reactor analysis as available computational power continues to increase. M-CFD with RANS turbulence modeling captures 3D distributions of velocity, volume fraction, TKE, etc. that are not resolved with the current industry standard 1D thermal-hydraulic analysis techniques. Simulations of two-phase flows are more difficult than single-phase flows since bubble interactions with the liquid turbulence must be quantified and included in the modeling approach. The development of high-fidelity multiphase turbulence models specifically for nuclear reactor applications will improve reactor safety calculations and allow nuclear power plant operation closer to the margin with higher confidence levels.

DNS data has emerged as an excellent tool for improving turbulence model formulations since characteristics that are generally hard to capture in experiments are recorded in DNS. The expansive data that is obtained from DNS can be used for validation as well as undergo data mining techniques to reveal additional information. The spectral analysis of single-phase and two-phase DNS to provide the TKE spectrum provides further data about the bubble interactions with the liquid turbulence.

In this work, spectral analysis of turbulent single-phase and bubbly two-phase DNS data in different geometries was performed to investigate the modulation of the TKE spectrum slope due to the presence of bubbles. A novel technique called pseudo-void was developed to show that the bubble wake interaction with the liquid turbulence is the contributing factor to the modification of the energy spectrum slope in two-phase flows from the expected -5/3 slope of the inertial subrange in single-phase flows. The spectral analysis was performed in different geometries and at different bulk Reynolds numbers to show that the slope of the energy spectrum in bubbly two-phase flows is similar regardless of these factors and that spectral turbulence models such as the SCTM can be universally applied to bubbly two-phase flow modeling.

An existing spectral turbulence model was adopted for model improvement and development. The existing model had been used in 1D to model single and two-phase decay of isotropic turbulence, single and two-phase uniform shear flow, and single-phase channel flow without resolving the near-wall boundary layer for a relatively low bulk Reynolds number. In this work, the SCTM was first improved for 1D and extended to a LRN type model in simple plane channel flow and validated for Reynolds numbers up to 2000 based on friction velocity. The SCTM was compared with DNS data for mean flow parameters as well as the TKE spectrum and TKE budget. The SCTM was then extended to a 3D model and implemented into the M-CFD code NPHASE-CMFD as a wall-resolved LRN turbulence closure option that resolves the turbulence in the spectral and spatial domains. Numerical considerations in NPHASE-CMFD required that the model be formulated slightly differently than the 1D formulation. The SCTM was then tested extensively in NPHASE-CMFD and compared with predictions from 1D FlexPDE, the k-ε model, DNS data, and experimental data. The SCTM has been tested in NPHASE-CMFD for various geometries using 2D and 3D numerical meshes.

A BIT source term was included in the SCTM for use with the existing code structure of NPHASE-CMFD so that different dispersed phase groups can influence the TKE separately in the spectral and spatial domains. The two-phase LRN SCTM in NPHASE-CMFD was tested for various geometries and compared with experimental data. The SCTM provides estimations of experimental data that are within the engineering uncertainty of the k-ε model while simultaneously providing more flow physics. The SCTM also provides physically expected results when applied to polydispersed bubbly two-phase flow scenarios.

In conclusion, the SCTM has been developed for use in 3D M-CFD codes and the accomplished work includes:

i. Performing spectral analysis of turbulent single and two-phase bubbly DNS data in different geometries to show that that the two-phase spectra are similar in different geometries and using a novel method to show that bubble wakes modulate the TKE spectrum.
ii. Improving and developing the 1D SCTM as a LRN type turbulence model and testing the SCTM in 1D FlexPDE with validation data from DNS.

iii. Formulating the SCTM as a 3D turbulence closure option to be used in 3D M-CFD codes and implementing the model into NPHASE-CMFD.

iv. Performing verification and validation testing of the SCTM in NPHASE-CMFD for single and two-phase flow scenarios.

8. RECOMMENDATIONS FOR FUTURE WORK

The presented spectral analysis and development of the SCTM for two-phase flows provides a foundation for the use of DNS data to improve turbulence modeling approaches and the continued use of the SCTM in M-CFD code packages. A discussion of recommendations for future work is provided with regards to both spectral analysis and the SCTM.

8.1 Future Work Recommendations for Spectral Analysis

The archive of DNS data will continue to be expanded as computational capabilities allow simulation of larger geometries, higher Reynolds numbers, higher void fractions, etc. The spectral analysis of these simulations can be performed with the presented spectral analysis technique to provide the TKE spectrum and comparisons of the spectra should be completed as a function of these different simulation parameters. However, future work with DNS datasets could focus on data mining to provide more exact terms for use with the SCTM. For example, it could be possible to deduce further information on how bubbles influence the liquid turbulence to improve the formulation of the spectral weighting factor. An analysis toolkit could be formulated for SCTM validation where DNS is performed and spectrally analyzed in a way that provides data for exact comparison with the simulation from the SCTM in a RANS M-CFD package. In this way, the SCTM could be validated with DNS data not only through mean flow parameters, the TKE spectrum, and the TKE budget but also through more advanced statistics such as the BIT source term in the spectral and spatial domains.

8.2 Future Work Recommendations for the SCTM

The presented work has developed the SCTM as a turbulence closure option that can be used in M-CFD codes for simulation of turbulent single and two-phase bubbly flows. In particular, the SCTM can model an arbitrary number of dispersed phase groups and, when coupled to a code such as NPHASE-CMFD, separate mass and momentum equations are solved for each dispersed phase group. This flexibility allows the SCTM to be used as an advanced spectral turbulence model moving forward for high-fidelity RANS simulations of monodispersed and polydispersed two-phase flows that is expected to be valid for higher void fraction distributions than can be captured with

traditional two-equation turbulence models. The SCTM is a LRN turbulence model and therefore eliminates the need for unknown two-phase law of the wall type boundary conditions. Future work with the SCTM could focus on a few areas for improvement including:

i. Finalizing the constants in the model formulation as a more extensive library of test cases is produced. The results shown here are acceptable and have been produced with no modification of model constants but could possibly be improved if model constants are dependent on mean flow parameters such as what is traditionally done with LRN two-equation turbulence models. An extensive sensitivity analysis to model constants could accompany this endeavor.
ii. Take advantage of state-of-the-art computing capabilities to decrease the computational time required for SCTM simulations. Multithreading of the SCTM is possible since the solution of the bin TKE values can be performed simultaneously. With the emerging use of graphics processing units (GPUs) for computation the SCTM could be highly scalable where, at each iteration, the bin TKE values could be solved across an array of GPUs.
iii. Perform more validation tests with experimental and DNS data. Turbulence models are improved as more users of the model provide feedback of model performance in numerous flow scenarios. The SCTM could be compared with various experimental tests and DNS data to gauge model performance. For example, the SCTM could be tested in classical complex turbulence model validation tests such as flow over backwards facing step as well as more nuclear focused validation tests such as polydispersed bubbly two-phase flow around an obstacle.

The recommendations for future work provide an avenue for the SCTM to become a widely validated turbulence closure option for improved multiphase flow predictions when compared to traditional two-equation RANS turbulence models. The recommendations also indicate how data analysis of large DNS datasets can improve lower fidelity simulations such as those with RANS turbulence models. A schematic roadmap for the development is presented in Figure 8.1 with recommendations for future work shown in red. The presented work has developed the SCTM so that it can be used in M-CFD code packages with physical predictions of two-phase flow.

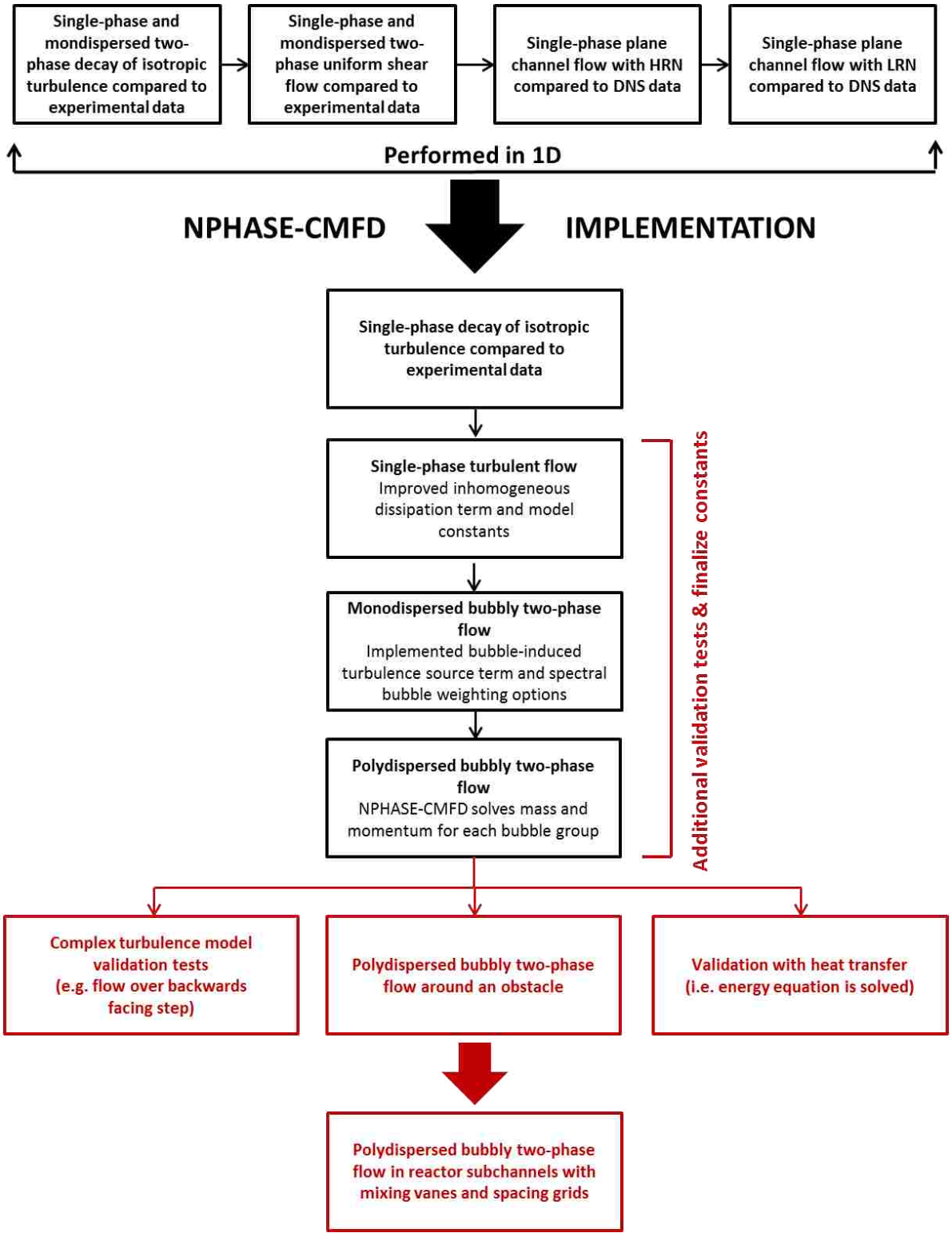

Figure 8.1. Roadmap for SCTM development. Future work recommendations are shown in red.

9. REFERENCES

1. Wang, S. K., Lee, S. J., Jones, O. C. & Lahey, R. T. Statistical-Analysis of Turbulent 2-Phase Pipe-Flow. *Journal of Fluids Engineering-Transactions of the Asme* **112**, 89-95 (1990).
2. Fang, J., Rasquin, M. & Bolotnov, I. A. Interface tracking simulations of bubbly flows in PWR relevant geometries. *Nuclear Engineering and Design* (2016).
3. Kang, S. K. & Hassan, Y. A. Computational fluid dynamics (CFD) round robin benchmark for a pressurized water reactor (PWR) rod bundle. *Nucl. Eng. Des.* **301**, 204-231 (2016).
4. Jeong, J., Song, M. & Lee, K. RANS based CFD methodology for a real scale 217-pin wire-wrapped fuel assembly of KAERI PGSFR. *Nucl. Eng. Des.* **313**, 470-485 (2017).
5. Laviéville, J., Mérigoux, N., Guingo, M., Baudry, C. & Mimouni, S. A Generalized turbulent dispersion model for bubbly flow numerical simulation in NEPTUNE_CFD. *Nucl. Eng. Des.* **312**, 284-293 (2017).
6. Jones, W. & Launder, B. Prediction of Laminarization with a 2-Equation Model of Turbulence. *Int. J. Heat Mass Transfer* **15**, 301-& (1972).
7. Wilcox, D. Reassessment of the Scale-Determining Equation for Advanced Turbulence Models. *AIAA J.* **26**, 1299-1310 (1988).
8. Menter, F. 2-Equation Eddy-Viscosity Turbulence Models for Engineering Applications. *AIAA J.* **32**, 1598-1605 (1994).
9. Bolotnov, I. A., Lahey, R. T.,Jr., Drew, D. A., Jansen, K. E. & Oberai, A. A. A spectral turbulent cascade model for single- and two-phase uniform shear flows. *Journal of Turbulence* **9**, 1-18 (2008).
10. Bolotnov, I. A., Lahey, R. T.,Jr., Drew, D. A. & Jansen, K. E. Turbulent cascade modeling of single and bubbly two-phase turbulent flows. *Int. J. Multiphase Flow* **34**, 1142-1151 (2008).
11. Bolotnov, I. A., Lahey, R. T., Drew, D. A., Jansen, K. E. & Oberai, A. A. Spectral cascade modeling of turbulent flow in a channel. *Japanese Journal of Multiphase Flow* **23**, 190-204 (2009).
12. Cheng, J., Yan, L. & Li, F. CFD simulation of a four-loop PWR at asymmetric operation conditions. *Nucl. Eng. Des.* **300**, 591-600 (2016).
13. Wilcox, D. in *Turbulence Modeling for CFD* (DCW Industries, La Canada, CA, 2002).
14. Pope, S. B. in *Turbulent flows* (Cambridge University Press, Cambridge ;New York, 2000).

15. Prandtl, L. A report on testing for built-up turbulence. *Z. Angew. Math. Mech.* **5**, 136-139 (1925).
16. Smith, A. M. O. & Cebeci, T. Numerical solution of the turbulent boundary layer equations. *Douglas Aircraft Division Report DAC 33735* (1967).
17. Baldwin, B. S. & Lomax, H. Thin-layer approximation and algebraic model for separated turbulent flows. *AIAA Paper*, 78-257 (1978).
18. Baldwin, B. S. & Barth, T. J. A one-equation turbulence transport model for high reynolds number wall-bounded flows. *NASA ™-102847* (1990).
19. Spalart, P. R. & Allmaras, S. R. A one-equation turbulence model for aerodynamic flows. *AIAA Paper, Reno, NV*, 92-439 (1992).
20. Speziale, C. G., Abid, R. & Anderson, E. C. A critical evaluation of two-equation models for near wall turbulence. *AIAA Paper, Seattle, WA*, 90-1481 (1990).
21. Robinson, D., Harris, J. & Hassan, H. Unified Turbulence Closure-Model for Axisymmetrical and Planar Free Shear Flows. *AIAA J.* **33**, 2325-2331 (1995).
22. Zeierman, S. & Wolfshtein, M. Turbulent Time Scale for Turbulent-Flow Calculations. *AIAA J.* **24**, 1606-1610 (1986).
23. Launder, B. & Sharma, B. I. Application of the energy dissipation model of turbulence to the calculation of flow near a spinning disc. *Letters in Heat and Mass Transfer* **1**, 131-138 (1974).
24. Lam, C. & Bremhorst, K. A Modified Form of the K-Epsilon Model for Predicting Wall Turbulence. *J. Fluids Eng. -Trans. ASME* **103**, 456-460 (1981).
25. Chien, K. Predictions of Channel and Boundary-Layer Flows with a Low-Reynolds-Number Turbulence Model. *AIAA J.* **20**, 33-38 (1982).
26. Richardson, L. F. in *Weather Prediction by Numerical Process* (Cambridge University Press, Cambridge, 1922).
27. Kolmogorov, A. The Local-Structure of Turbulence in Incompressible Viscous-Fluid for very Large Reynolds-Numbers. *Proc. R. Soc. London Ser. A-Math. Phys. Eng. Sci.* **434**, 9-13 (1991).
28. Lewalle, J. & Tavlarides, L. A Cascade-Transport Model for Turbulent Sheer Flows. *Phys. Fluids* **6**, 3109-3115 (1994).
29. Hoyas, S. & Jimenez, J. Scaling of the velocity fluctuations in turbulent channels up to Re-tau=2003. *Phys. Fluids* **18**, 011702 (2006).

30. Bohr, T., Jensen, M. H., Paladin, G. & Vulpine, A. in *A dynamical systems approach to turbulence* (Cambridge University Press, 1998).
31. Desnyanski, V. N. & Novikov, E. A. Simulation of cascade process in turbulent flows. *Journal of Applied Mathematics and Mechanics* **38**, 216 (1974).
32. Hinze, J. O. in *Turbulence* (McGraw-Hill, New York, 1975).
33. Petrov, V., Kendrick, B. K., Walter, D., Manera, A. & Secker, J. Prediction of CRUD deposition on PWR fuel using a state-of-the-art CFD-based multi-physics computational tool. *Nucl. Eng. Des.* **299**, 95-104 (2016).
34. Bolotnov, I. A. Influence of Bubbles on the Turbulence Anisotropy. *Journal of Fluids Engineering-Transactions of the Asme* **135**, 051301 (2013).
35. Bolotnov, I. A. &Fang, J. *Interface tracking simulations as an engineering tool for two-phase flow model development*, Japan-U.S. Seminar on Two-Phase Flow Dynamics, West Lafayette, IN, USA, 2015).
36. Lu, J. & Tryggvason, G. Dynamics of nearly spherical bubbles in a turbulent channel upflow. *J. Fluid Mech.* **732**, 166-189 (2013).
37. Santarelli, C. & Froehlich, J. Direct Numerical Simulations of spherical bubbles in vertical turbulent channel flow. Influence of bubble size and bidispersity. *Int. J. Multiphase Flow* **81**, 27-45 (2016).
38. Santarelli, C. & Froehlich, J. Direct Numerical Simulations of spherical bubbles in vertical turbulent channel flow. *Int. J. Multiphase Flow* **75**, 174-193 (2015).
39. Colombo, M. & Fairweather, M. Multiphase turbulence in bubbly flows: RANS simulations. *Int. J. Multiphase Flow* **77**, 222-243 (2015).
40. Lahey, R. The simulation of multidimensional multiphase flows. *Nucl. Eng. Des.* **235**, 1043-1060 (2005).
41. Debertodano, M., Lahey, R. & Jones, O. Development of a K-Epsilon Model for Bubbly 2-Phase Flow. *J. Fluids Eng. -Trans. ASME* **116**, 128-134 (1994).
42. Rzehak, R. & Krepper, E. CFD modeling of bubble-induced turbulence. *Int. J. Multiphase Flow* **55**, 138-155 (2013).
43. Santarelli, C., Roussel, J. & Froehlich, J. Budget analysis of the turbulent kinetic energy for bubbly flow in a vertical channel. *Chem. Eng. Sci.* **141**, 46-62 (2016).

44. Drew, D. & Lahey, R. Application of General Constitutive Principles to the Derivation of Multidimensional 2-Phase Flow Equations. *Int. J. Multiphase Flow* **5**, 243-264 (1979).
45. Zun, I. The Transverse Migration of Bubbles Influenced by Walls in Vertical Bubbly Flow. *Int. J. Multiphase Flow* **6**, 583-588 (1980).
46. Hibiki, T. & Ishii, M. Lift force in bubbly flow systems. *Chem. Eng. Sci.* **62**, 6457-6474 (2007).
47. Thomas, A. M., Fang, J., Feng, J. & Bolotnov, I. A. Estimation of Shear-Induced Lift Force in Laminar and Turbulent Flows. *Nucl Technol* **190**, 274-291 (2015).
48. Feng, J. & Bolotnov, I. A. Interfacial force study on a single bubble in laminar and turbulent flows. *Nucl. Eng. Des.* **313**, 345-360 (2017).
49. Ishii, M. & Zuber, N. Drag Coefficient and Relative Velocity in Bubbly, Droplet Or Particulate Flows. *AIChE J.* **25**, 843-855 (1979).
50. Lance, M. & Bataille, J. Turbulence in the Liquid-Phase of a Uniform Bubbly Air Water-Flow. *J. Fluid Mech.* **222**, 95-118 (1991).
51. Shawkat, M. E., Ching, C. Y. & Shoukri, M. On the liquid turbulence energy spectra in two-phase bubbly flow in a large diameter vertical pipe. *Int. J. Multiphase Flow* **33**, 300-316 (2007).
52. Mendez-Diaz, S., Serrano-Garcia, J. C., Zenit, R. & Hernandez-Cordero, J. A. Power spectral distributions of pseudo-turbulent bubbly flows. *Phys. Fluids* **25**, 043303 (2013).
53. Bunner, B. & Tryggvason, G. Dynamics of homogeneous bubbly flows Part 2. Velocity fluctuations. *JOURNAL OF FLUID MECHANICS}* **466}**, 53-84} (2002}).
54. Roghair, I. *et al*. Energy spectra and bubble velocity distributions in pseudo-turbulence: Numerical simulations vs. experiments. *Int. J. Multiphase Flow* **37**, 1093-1098 (2011).
55. Sato, Y. & Sekoguchi, K. Liquid velocity distribution in two-phase bubble flow. *Int. J. Multiphase Flow* **2**, 79-95 (1975).
56. Lee, S. J., Lahey, R. T. & Jones, O. C. The prediction of two-phase turbulence and phase distribution using a k-ε model. *Japanese Journal of Multiphase Flow* **3**, 335-368 (1989).
57. Rzehak, R., Ziegenhein, T., Kriebitzsch, S., Krepper, E. & Lucas, D. Unified modeling of bubbly flows in pipes, bubble columns, and airlift columns. *Chem. Eng. Sci.* **157**, 147-158 (2017).
58. Morel, C. Turbulence Modeling and First Numerical Simulations in Turbulent Two-Phase Flows. *CEA* (1997).

59. Politano, M., Carrica, P. & Converti, J. A model for turbulent polydisperse two-phase flow in vertical channels. *Int. J. Multiphase Flow* **29**, 1153-1182 (2003).

60. Troshko, A. & Hassan, Y. A two-equation turbulence model of turbulent bubbly flows. *Int. J. Multiphase Flow* **27**, 1965-2000 (2001).

61. Ma, T., Santarelli, C., Ziegenhein, T., Lucas, D. & Froehlich, J. Direct numerical simulation-based Reynolds-averaged closure for bubble-induced turbulence. *Phys. Rev. Fluids* **2**, 034301 (2017).

62. Jairazbhoy, V., Tavlardies, L. & Lewalle, J. A Cascade Model for Neutrally Buoyant Dispersed 2-Phase Homogeneous Turbulence .1. Model Formulation. *Int. J. Multiphase Flow* **21**, 467-483 (1995).

63. Jairazbhoy, V. & Tavlarides, L. A Cascade Model for Neutrally Buoyant Dispersed 2-Phase Homogeneous Turbulence .2. Numerical-Solution and Results. *Int. J. Multiphase Flow* **21**, 485-500 (1995).

64. Lahey, R. T., Jr. On the Computation of Multiphase Flows. *Nucl Technol* **167**, 29-45 (2009).

65. Marie, J., Moursali, E. & TranCong, S. Similarity law and turbulence intensity profiles in a bubbly boundary layer at low void fractions. *Int. J. Multiphase Flow* **23**, 227-247 (1997).

66. Troshko, A. & Hassan, Y. in *Law of the wall for two-phase turbulent boundary layers* (ed Lee, J.) 145 (TAYLOR & FRANCIS LTD, LONDON; 11 NEW FETTER LANE, LONDON EC4P 4EE, ENGLAND, 1998).

67. Carrica, P., Drew, D., Bonetto, F. & Lahey, R. A polydisperse model for bubbly two-phase flow around surface ship. *Int. J. Multiphase Flow* **25**, 257-305 (1999).

68. Krepper, E., Lucas, D., Frank, T., Prasser, H. & Zwart, P. J. The inhomogeneous MUSIG model for the simulation of polydispersed flows. *Nucl. Eng. Des.* **238**, 1690-1702 (2008).

69. Ilic, M., Worner, M. & Cacuci, D. G. *Evaluation of energy spectra in bubble driven liquid flows from direct numerical simulations* (6th International Conference on Multiphase Flow, ICMF 2007, Leipzig, Germany, 2007).

70. Mazzitelli, I. M. & Lohse, D. Evolution of energy in flow driven by rising bubbles. *Physical Review E* **79** (2009).

71. Rensen, J., Luther, S. & Lohse, D. The effect of bubbles on developed turbulence. *J. Fluid Mech.* **538**, 153-187 (2005).

72. Sathe, M., Joshi, J. & Evans, G. Characterization of turbulence in rectangular bubble column. *Chemical Engineering Science* **100**, 52-68 (2013).

73. Mercado, J. M., Gomez, D. C., Van Gils, D., Sun, C. & Lohse, D. On bubble clustering and energy spectra in pseudo-turbulence. *J. Fluid Mech.* **650**, 287-306 (2010).

74. Sugiyama, K., Takagi, S. & Matsumoto, Y. Multi-scale analysis of bubbly flows. *Comput. Methods Appl. Mech. Eng.* **191**, 689-704 (2001).

75. Riboux, G., Legendre, D. & Risso, F. A model of bubble-induced turbulence based on large-scale wake interactions. *J. Fluid Mech.* **719**, 362-387 (2013).

76. Risso, F. Theoretical model for k(-3) spectra in dispersed multiphase flows. *Phys. Fluids* **23**, 011701 (2011).

77. Tsuji, Y. & Morikawa, Y. Ldv Measurements of an Air Solid 2-Phase Flow in a Horizontal Pipe. *J. Fluid Mech.* **120**, 385-409 (1982).

78. Gherson, P. & Lykoudis, P. S. Local Measurements in 2-Phase Liquid-Metal Magneto-Fluid-Mechanic Flow. *J. Fluid Mech.* **147**, 81-104 (1984).

79. Panidis, T. & Papailiou, D. D. The structure of two-phase grid turbulence in a rectangular channel: an experimental study. *Int. J. Multiphase Flow* **26**, 1369-1400 (2000).

80. Krepper, E., Beyer, M., Frank, T., Lucas, D. & Prasser, H. CFD modelling of polydispersed bubbly two-phase flow around an obstacle. *Nucl. Eng. Des.* **239**, 2372-2381 (2009).

81. Jansen, K. A stabilized finite element method for computing turbulence. *Comput. Methods Appl. Mech. Eng.* **174**, 299-317 (1999).

82. Whiting, C. & Jansen, K. A stabilized finite element method for the incompressible Navier-Stokes equations using a hierarchical basis. *Int. J. Numer. Methods Fluids* **35**, 93-116 (2001).

83. Tejada-Martinez, A. & Jansen, K. A parameter-free dynamic subgrid-scale model for large-eddy simulation. *Comput. Methods Appl. Mech. Eng.* **195**, 2919-2938 (2006).

84. Nagrath, S., Jansen, K., Lahey, R. & Akhatov, I. Hydrodynamic simulation of air bubble implosion using a level set approach. *J. Comput. Phys.* **215**, 98-132 (2006).

85. Rasquin, M. *et al*. Scalable Implicit Flow Solver for Realistic Wing Simulations with Flow Control. *Comput. Sci. Eng.* **16**, 13-21 (2014).

86. Bolotnov, I. A. *et al*. Detached direct numerical simulations of turbulent two-phase bubbly channel flow. *Int. J. Multiphase Flow* **37**, 647-659 (2011).

87. Di Liberto, M. & Ciofalo, M. A study of turbulent heat transfer in curved pipes by numerical simulation. *Int. J. Heat Mass Transfer* **59**, 112-125 (2013).

88. Proakis, J. G. in *Digital signal processing : principles, algorithms, and applications* (ed Manolakis, D. G.) (Prentice Hall, Englewood Cliffs, NJ., 1996).

89. Del Alamo, J. C., Jimenez, J., Zandonade, P. & Moser, R. D. Scaling of the energy spectra of turbulent channels. *J. Fluid Mech.* **500**, 135-144 (2004).

90. Domaradzki, J. & Rogallo, R. Local Energy-Transfer and Nonlocal Interactions in Homogeneous, Isotropic Turbulence. *Physics of Fluids A-Fluid Dynamics* **2**, 413-426 (1990).

91. Cadiou, A., Hanjalic, K. & Stawiarski, K. A two-scale second-moment turbulence closure based on weighted spectrum integration. *Theor. Comput. Fluid Dyn.* **18**, 1-26 (2004).

92. PDE Solutions Inc. FlexPDE. Finite element analysis software package. www.pdesolutions.com.

93. Del Alamo, J. & Jimenez, J. Spectra of the very large anisotropic scales in turbulent channels. *Phys. Fluids* **15**, L41-L44 (2003).

94. Bolotnov, I. A., Lahey, R. T., Jr., Drew, D. A., Jansen, K. E. & Oberai, A. A. Spectral analysis of turbulence based on the DNS of a channel flow. *Comput. Fluids* **39**, 640-655 (2010).

95. Antal, S. P., Ettorre, S. M., Kunz, R. F. & Podowski, M. Z. *Development of a next generation computer code for the prediction of multicomponent multiphase flows* (Int. Meeting on Trends in Num. and Phys. Modeling for Ind. Multiphase Flow, 2000).

96. Interphase Dynamics, L. NPHASE-CMFD User Manual. (2002).

97. Tiwari, P., Antal, S. & Podowski, M. Three-dimensional fluid mechanics of particulate two-phase flows in U-bend and helical conduits. *Phys. Fluids* **18**, 043304 (2006).

98. Tselishcheva, E. A., Antal, S. P. & Podowski, M. Z. Mechanistic multidimensional analysis of horizontal two-phase flows. *Nucl. Eng. Des.* **240**, 405-415 (2010).

99. Behafarid, F. *et al*. Coupled Dns/rans Simulation of Fission Gas Discharge during Loss-Of-Flow Accident in Generation Iv Sodium Fast Reactor. *Nucl Technol* **181**, 44-55 (2013).

100. Waite, B. M., Shaver, D. R. & Podowski, M. Z. *Multidimensional Modeling of Two-Phase Flow in PWRs with Mixing Vane Spacer Grids* (ANS Winter Meeting, 2015).

101. Interphase Dynamics, L. NPHASE-CMFD Program Manual. (2002).

102. Roache, P. J. in *Verification and validation in computational science and engineering* (Hermosapublishers, Albuquerque, N.M., 1998).

103. http://www.grc.nasa.gov/WWW/wind/valid/homepage.html.
104. Kang, H., Chester, S. & Meneveau, C. Decaying turbulence in an active-grid-generated flow and comparisons with large-eddy simulation. *J. Fluid Mech.* **480**, 129-160 (2003).
105. Squillacote, A. H. The ParaView Guide: A Parallel Visualization Application. (2007).
106. Interphase Dynamics, L. NPHASE-CMFD Example Manual. (2002).
107. Hosokawa, S. & Tomiyama, A. Multi-fluid simulation of turbulent bubbly pipe flows. *Chem. Eng. Sci.* **64**, 5308-5318 (2009).
108. Pointwise, I. Pointwise V17.3 Release 3. (2015).
109. Shaver, D. R. &Podowski, M. Z. *Modeling of Interfacial Forces for Bubbly Flows in Subcooled Boiling Conditions* (Transactions of the American Nuclear Society Ser. 113, 2015).
110. Podowski, M. Z. On the consistency of mechanistic multidimensional modeling of gas/liquid two-phase flows. *Nucl. Eng. Des.* **239**, 933-940 (2009).
111. Tomiyama, A., Tamai, H., Zun, I. & Hosokawa, S. Transverse migration of single bubbles in simple shear flows. *Chemical Engineering Science* **57**, 1849-1858 (2002).
112. Jiao, H. &Podowski, M. Z. *An Analysis of Multidimensional Models of Gas/Liquid Flows* (Transactions Vol. 107 American Nuclear Society Annual Winter Meeting Ser. 107, 2012).

10. APPENDICES

10.1 Appendix A

Selected algorithms from the spectral analysis Fortran program are presented.

10.1.1 Handling the Defective Two-Phase Signal

The algorithm for handling the defective two-phase signal based on user input is presented here:

```
509     do ir=1,Nrun
510     do ih=1,Nhom
511     do j=1,Ntime
512      if(phase(m,j-1,ih,ir).gt.0.5.and.phase(m,j,ih,ir).lt.0.5) then
513       startj= j
514      else if(phase(m,j,ih,ir).lt.0.5.and.phase(m,j+1,ih,ir).gt.0.5) then
515       endj= j
516       jcount= endj-startj
517       k=0
518       do while(k.lt.jcount+1)
519        if(defectflag.eq.1) then
520        !mean insert
521        uinst(m,startj+k,ih,ir)= umean(m)
522        vinst(m,startj+k,ih,ir)= vmean(m)
523        winst(m,startj+k,ih,ir)= wmean(m)
524        else if(defectflag.eq.2) then
525        !interpolation
526        uinst(m,startj+k,ih,ir)= uinst(m,startj-1,ih,ir) +
(uinst(m,endj+1,ih,ir)-uinst(m,startj-1,ih,ir))*  &
527         ((Ctime(startj+k) - Ctime(startj-1))/(Ctime(endj+1) - Ctime(startj-1)))
528        vinst(m,startj+k,ih,ir)= vinst(m,startj-1,ih,ir) +
(vinst(m,endj+1,ih,ir)-vinst(m,startj-1,ih,ir))*  &
529         ((Ctime(startj+k) - Ctime(startj-1))/(Ctime(endj+1) - Ctime(startj-1)))
530        winst(m,startj+k,ih,ir)= winst(m,startj-1,ih,ir) +
(winst(m,endj+1,ih,ir)-winst(m,startj-1,ih,ir))*  &
531         ((Ctime(startj+k) - Ctime(startj-1))/(Ctime(endj+1) - Ctime(startj-1)))
532        else if(defectflag.eq.3) then
533        !hold value before defect
534        uinst(m,startj+k,ih,ir)= uinst(m,startj-1,ih,ir)
535        vinst(m,startj+k,ih,ir)= vinst(m,startj-1,ih,ir)
536        winst(m,startj+k,ih,ir)= winst(m,startj-1,ih,ir)
537        end if !defectflag
538        k=k+1
539       end do
540
541      end if
542     end do
543     end do
544     end do
```

10.1.2 FFT

The algorithm for computing the FFT and the resulting energy spectrum in each segment used for Bartlett's method is presented here:

```
551     !calculate the fluctuating velocities and TKE
552     write(*,*) 'Calculating flucutating velocities and TKE for yplus:',
yplus(ypoint(m)) !yplusfrac(m)
553      do ir=1,Nrun
554       do j=1,Ntime
555        do ih= 1,Nhom
556
557         !handling the defect is taken care of above with choice in input file
558         uprime(m,j,ih,ir)= uinst(m,j,ih,ir) - umean(m)         !x direction
fluctuating velocity
559         vprime(m,j,ih,ir)= vinst(m,j,ih,ir) - vmean(m)         !y direction
fluctuating velocity
560         wprime(m,j,ih,ir)= winst(m,j,ih,ir) - wmean(m)         !z direction
fluctuating velocity
561
562         !TKE for the whole data sequence
563         TKE(m,j,ih,ir)= 0.5D0*(uprime(m,j,ih,ir)*uprime(m,j,ih,ir) +
vprime(m,j,ih,ir)*vprime(m,j,ih,ir)    &
564          + wprime(m,j,ih,ir)*wprime(m,j,ih,ir))
565
566
567
568        end do !ih
569       end do !j
570      end do !ir
571
572     !ASSEMBLING THE PERIODOGRAM AND FINDING ENERGY SPECTRUM
573     !split up the whole data sequence into the segments of equal length before
performing FFT
574      do ir=1,Nrun
575       do ih=1,Nhom
576        do k=1,segments
577         do mseg=1,lsegment
578
579          pxx(m,k,mseg,ih,ir)= TKE(m,(mseg+(k-1)*lsegment),ih,ir)
580
581         end do !mseg
582        end do !k
583       end do !ih
584      end do !ir
585
586
587     !perform the FFT at the different j locations for each segment
588     write(*,*) 'Performing FFT for yplus value:', m
589     FFTlength= lsegment
590      do ir=1,Nrun
591       do ih=1,Nhom
592        do k=1,segments
593
594         status = DftiCreateDescriptor(MYFFT,DFTI_DOUBLE,DFTI_REAL,1,FFTlength)
595         status = DftiCommitDescriptor(MYFFT)
```

```
596         status = DftiComputeForward(MYFFT,pxx(m,k,:,ih,ir))
597         status = DftiFreeDescriptor(MYFFT)
598
599        end do !k
600       end do !ih
601      end do !ir
602
603      !square the periodogram at each point and divide by segment length
604      do ir=1,Nrun
605       do ih=1,Nhom
606        do k=1,segments
607         do mseg=1,lsegment+2
608
609          pxx(m,k,mseg,ih,ir)= (pxx(m,k,mseg,ih,ir)**2.0D0)/real(lsegment)
610
611         end do !mseg
612        end do !k
613       end do !ih
614      end do !ir
615
616      !average over the number of segments
617      do ir=1,Nrun
618       do ih=1,Nhom
619        do mseg=1,lsegment+2
620        pbart(m,mseg,ih,ir)= 0.0D0
621         do k=1,segments
622
623          !sum over the segments
624          pbart(m,mseg,ih,ir)= pbart(m,mseg,ih,ir) + pxx(m,k,mseg,ih,ir)
625
626         end do !k
627        end do !mseg
628       end do !ih
629      end do !ir
630
631      do ir=1,Nrun
632       do ih=1,Nhom
633        do mseg=1,lsegment+2
634
635          !divide out the number of segments
636          pbart(m,mseg,ih,ir)= pbart(m,mseg,ih,ir)/real(segments)
637
638        end do !mseg
639       end do !ih
640      end do !ir
641
642     !get the magnitude of the energy spectrum from real and imag parts of FFT
643     do ir=1,Nrun
644      do ih=1,Nhom
645       do mseg=1,lsegment/2
646        re= pbart(m,2*mseg+1,ih,ir)                              !real part of
FFT
647        im= pbart(m,2*mseg+2,ih,ir)                              !imaginary part
of FFT
648        magrun(m,mseg,ih,ir)= sqrt(re*re + im*im)        !FFT magnitude
649       end do !mseg
650      end do !ih
651     end do !ir
652
```

```
653     !sum over the run number and divide it out
654     do ih=1,Nhom
655      do mseg=1,lsegment/2
656      maghom(m,mseg,ih)= 0.0D0
657       do ir=1,Nrun
658        maghom(m,mseg,ih)= maghom(m,mseg,ih) + magrun(m,mseg,ih,ir)
659       end do !ir
660        maghom(m,mseg,ih)= maghom(m,mseg,ih)/real(Nrun)
661      end do !mseg
662     end do !ih
663
664     !sum over the homogeneous direction and divide it out
665     do mseg=1,lsegment/2
666     mag(m,mseg)= 0.0D0
667      do ih=1,Nhom
668       mag(m,mseg)= mag(m,mseg) + maghom(m,mseg,ih)
669      end do
670       mag(m,mseg)= mag(m,mseg)/real(Nhom)
671     end do
```

10.2 Appendix B

The NPHASE-CMFD iteration process with the SCTM is shown in more detail in Figure 10.1 with the user routines detailed in red. More extensive routines to handle the SCTM are called from the standard user routines where access is permitted to the NPHASE-CMFD code and those routines are discussed throughout the remainder of Appendix B.

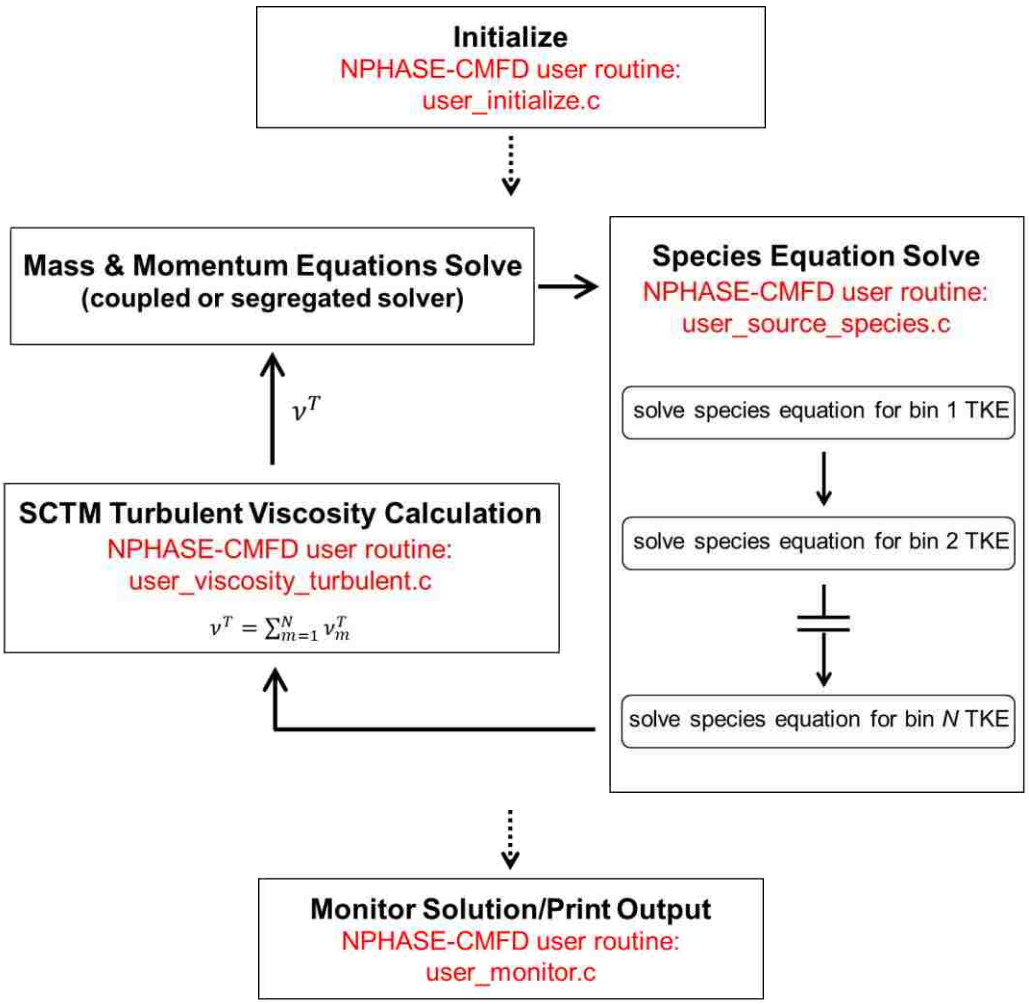

Figure 10.1. NPHASE-CMFD iteration process with SCTM implemented.

10.2.1 NPHASE-CMFD Routine – user_initialize.c

Table 10.1 provides further information on the NPHASE-CMFD routine user_initialize.c. Note that the routines for mean flow gradients, wall coordinates, homogeneous dissipation,

inhomogeneous dissipation, and the bin eddy viscosities are called from this routine only for numerical stability purposes on the first iteration but will be discussed further in § 10.2.2.

Table 10.1. Information for NPHASE-CMFD routine user_initialize.c.

Routine	user_initialize.c
Purpose	SCTM constants and parameters are input by the user and data storage arrays are defined.
Calls Routines	beta_transfer bin_boundaries eddy_viscosity homogeneous_dissipation inhomogeneous_dissipation mean_gradients set_inflow set_tke_IC spectral_bubble_weight wall_coordinates

The entire user_initialize.c routine is shown here. For routines called from user_initialize.c only relevant algorithms will be shown.

```
001 #include <stdlib.h>
002 #include "nphase_struct.h"
003 #include <math.h>
004 #include "definitioans.h"
005 #include <stdio.h>
006
007 extern struct data var;
008 extern struct boundary_patch partition ;
009
010 //requested outputs
011 // 1 = print | 0 = quiet
012 int     print_mvy= 1 ;              //mean velocity files (y)
013 int     print_mvx= 0 ;              //mean velocity files (x)
014 int     print_ek = 1 ;              //TKE density files
015 int     print_ba = 1 ;              //beta-j transfer weights
016 int     print_ka = 1 ;              //bin boundary information
017 int     print_kb = 0 ;              //TKE in each bin
018 int     print_su = 0 ;              //bin source terms
019 int     print_st = 1 ;              //total source terms
020 int     print_gb = 1 ;              //spectral bubble weights (bin
distribution)
021 int     print_ds = 1 ;              //dispersed TKE source terms
022
023 //flags
024 int iSCTMlowhigh  = 0 ;             //hi(1)/lo(0) Re option   | (right now no
wall functions)
025 int variablerelax = 1 ;             //option to use the variable relaxation
factor based on wave number
```

```
026 double  rfsmax    = 0.9 ;           //maximum value for variable relaxation
factor
027
028 //SCTM model constants defined here
029 int     kcntltot ;                        //total number of k controlled nodes
030 double *Species_Node_Old;
031
032 //wavenumber boundaries
033 double wnleft =  1.0 ;              //left wavenumber boundary
034 double wnright = 7.32e4 ;           //right wavenumber boundary
035 double *kappa ;                     //bin boundary
036 double *kappa_center ;              //center of wavenumber bin
037 double *kappa_width  ;              //width of wavenumber bin
038
039 //homogeneous dissipation
040 double *homogeneous_dissipation_node ;     //homogeneous dissipation pointer
041
042 //inhomogeneous dissipation constants
043 double c_inhom = 0.15   ;                        //constant in exponential
damping term
044 double *inhomogeneous_dissipation_node;    //inhomogeneous dissipation pointer
045 double *total_tds_node ;                        //total dissipation for use
in eddy_viscosity.c
046
047 //transfer term constants
048 double sigma_transfer = 40.0 ;  //sigma constant in transfer weight
049 double sigma0 = 0.225 ;              //transfer spectral width
050 double *betaj ;                      //beta transfer weight
051 double *transfer_node ;              //transfer for bin-m on node pointer
052
053 //production term and turbulent viscosity constants
054 double CH = 0.40 ;                  //nu_T multiplier
055 double betanu = 0.75 ;              //Heisenberg beta in nu_T calculation
056 double NCM = -1.6 ;                 //NCM in f_y damping function
057 double SCM = -125.0 ;               //SCM in f_s damping function
058 double *production_node ;       //production for bin-m on node pointer
059 double *turbulent_viscosity ;   //turbulent viscosity for bin-m on node pointer
060 int    cliptotal ;                        //total nodes where turbulence has
been clipped
061
062 //gradient storage
063 double *gradient_u ;                //x-direction velocity gradient
064 double *gradient_v ;                //y-direction velocity gradient
065 double *gradient_w ;                //z-direction velocity gradient
066
067 //wall coordinate storage
068 double *u_tau ;                      //friction velocity
069 double *y_p ;                       //y plus
070
071 //multiphase storage
072 int    bubble_source_model = 1  ;          //bubble model 1) LAHEY;  2) RK
073 int    wm = 4 ;                                   //weighting model
074 double *gamma_bubble ;                     //spectral bubble weight function
per group
075 double *phi_bubble   ;                           //total bubble source term
076 double *bubble_source_node ;               //bubble source term on node (Psi_m)
077
078  int user_initialize()
079 {
```

```
080 /*--------------------------------------------------
081     routine to initialize variables and set boundary conditions
082
083     called from:
084     initialize
085
086 --------------------------------------------------*/
087
088     int *nspecies= var.nspecies ;
089     int *nnode= var.nnode ;
090     int *iter=var.iter ;
091     int *nfield=var.nfield ;
092
093     real *tds=var.tds ;
094     real *rfs=var.rfs ;
095     real *walldistance=var.walldistance ;
096     real *wallshearappor=var.wallshearappor ;
097
098     int inode ;
099     int ibf ;
100     int bin ;
101     int carrier_field ;
102     int nstridebintds ;
103     int j ;
104     int nstridebin_cntl ;
105     int nstridebin ;
106
107     double wd ;
108
109     entered("user_initialize") ;
110
111     //calculate the bin boundaries
112     kappa=             (double *)malloc((*nspecies + 1)*sizeof(double)) ;
//allocate space for kappa
113     kappa_center=      (double *)malloc((*nspecies + 1)*sizeof(double)) ;
//allocate space for center of bin
114     kappa_width=       (double *)malloc((*nspecies + 1)*sizeof(double)) ;
//allocate space for width of bin
115     bin_boundaries() ;                                                    //call
bin boundary function
116
117     //set the SCTM bin initial conditions
118         //OVERRIDES THE INPUT FILE
119         if(*iter == 0) set_tke_IC() ;
120
121     //set the inflow with the file
122         // 0 - set the inflow
123         // 1 - set the inflow and initialize everywhere
124         set_inflow(1) ;
125
126     //calculate the beta transfer weights
127     betaj=      (double *)malloc(*nspecies *sizeof(double)) ;   //allocate
space for betaj
128     beta_transfer()  ;                                          //calculate
betaj in function
129
130     //allocate the global pointers
131     homogeneous_dissipation_node=       (double *)malloc(*nnode*
*nspecies*sizeof(double)) ;
```

```
132     inhomogeneous_dissipation_node=    (double *)malloc(*nnode*
*nspecies*sizeof(double)) ;
133     transfer_node=                              (double *)malloc(*nnode*
*nspecies*sizeof(double)) ;
134     production_node=                            (double *)malloc(*nnode*
*nspecies*sizeof(double)) ;
135     turbulent_viscosity=                        (double *)malloc(*nnode*
*nspecies*sizeof(double)) ;
136     total_tds_node=                             (double *)malloc(*nnode*
          sizeof(double)) ;
137     Species_Node_Old=                           (double *)malloc(*nnode*
*nspecies*sizeof(double)) ;
138     gradient_u=                                 (double *)malloc(*nnode* 3*
          sizeof(double)) ;
139     gradient_v=                                 (double *)malloc(*nnode* 3*
          sizeof(double)) ;
140     gradient_w=                                 (double *)malloc(*nnode* 3*
sizeof(double)) ;
141     u_tau=                                      (double *)malloc(*nnode*
sizeof(double)) ;
142     y_p=                                        (double *)malloc(*nnode*
sizeof(double)) ;
143     gamma_bubble=                               (double *)malloc((*nfield-1)*
(*nspecies)*sizeof(double)) ;
144     phi_bubble=                                 (double *)malloc(*nnode*
(*nfield-1)*sizeof(double)) ;
145     bubble_source_node=                   (double *)malloc(*nnode* (*nfield-
1)* *nspecies*sizeof(double));
146
147
148     //multiphase - choose a model for bubble weight contribution to bins
149         //  1)  contribution to single bin at bubble length scale
150         //  2)  2*beta-j (normal) distribution to wave numbers >= bubble length
scale
151         //  3)  kappa^slope for wave numbers >= bubble length scale
152         //  4)  beta-j*kappa^slope for kappa > bubble length scale <=
kappa^slope
153         if(*nfield>1){
154          spectral_bubble_weight(wm) ;
155         }
156
157
158     //intialize the total tds
159     carrier_field=1 ;
160     if(*iter == 0){
161         for(inode=0; inode<=*nnode-1; ++inode){
162         LaminarViscosity_InternalNode(inode,carrier_field)=
InputFileViscosity(carrier_field) ;
163         Density_InternalNode(inode,carrier_field)=
InputFileDensity(carrier_field) ;
164              *(total_tds_node+inode)= 0.0 ;
165          for(bin=1; bin<=*nspecies; ++bin){
166           nstridebin= (*nnode)*(bin-1) ;
167           *(inhomogeneous_dissipation_node +inode+nstridebin)= 0.0 ;
168           *(homogeneous_dissipation_node   +inode+nstridebin)= 0.0 ;
169           *(transfer_node                        +inode+nstridebin)= 0.0 ;
170           *(production_node                      +inode+nstridebin)= 0.0 ;
171           *(turbulent_viscosity                         +inode+nstridebin)= 0.0
;
```

```
172           *(u_tau                                          +inode           )= 0.0
;
173           *(y_p                                            +inode           )= 0.0
;
174          }
175         }
176     }
177
178     //initialize mean gradients and wall coordinates
179     mean_gradients(carrier_field) ;
180     wall_coordinates(carrier_field) ;
181
182     for(bin=1; bin<=*nspecies; ++bin){
183      homogeneous_dissipation(carrier_field,bin) ;
184      inhomogeneous_dissipation(bin+8,carrier_field,bin) ;
185     }
186
187      //get total tds based off initialization
188          for(inode=0; inode<= *nnode-1; ++inode){
189           *(total_tds_node+inode)= 0.0 ;
190           for(j=1; j<=*nspecies; ++j){
191            nstridebintds= (*nnode)*(j-1) ;
192    *(total_tds_node+inode) +=
*(homogeneous_dissipation_node+inode+nstridebintds)+
*(inhomogeneous_dissipation_node+inode+nstridebintds) ;
193           } //j loop
194          } // inode loop
195
196     //initialize the bin eddy viscosities
197     for(bin=1; bin<=*nspecies; ++bin){
198      eddy_viscosity(carrier_field,bin) ;
199     }
200
201     //initiate the old species values as the initial
202      for(j=1; j<=*nspecies; ++j){
203       nstridebin_cntl= (*nnode)*(j-1) ;
204       for(inode=0; inode<= *nnode-1; ++inode){
205        *(Species_Node_Old+inode+nstridebin_cntl)= Species_InternalNode(inode,j)
;
206       } //inode
207      } //j
208
209     exiting("user_initialize") ;
210
211     return 0 ;
212
213 }
```

10.2.1.1 Routine – beta_transfer.c

Relevant algorithms from beta_transfer.c routine to calculate the transfer weights.

```
35      entered("beta_transfer") ;
36
37      betaprime = tempralloc(*nspecies) ;
38
39      //calculate beta for m>j, stores betaj from bin(1) to bin(N-1)
40      for(jbin=1; jbin<= *nspecies - 1 ; ++jbin) {
41       *(betaprime+jbin) = 0.5*(1.0/(sigma0*sqrt(2.0*pi)))*
```

```
42       (exp(-(pow((log10(kappa[*nspecies-1])-
log10(kappa[jbin])),2.0)/(2.0*sigma0*sigma0))) +
43       (exp(-(pow((log10(kappa[*nspecies])-
log10(kappa[jbin])),2.0)/(2.0*sigma0*sigma0)))))*
44       (log10(kappa[*nspecies-jbin]) - log10(kappa[*nspecies-jbin-1]))   ;
45      }
46
47      //NOTE**** not storing the negative of beta-j since it is equal
48
49      //set up global beta so it is consistent with number of bins away from bin-
m
50      for(jbin=1; jbin<= *nspecies - 1; ++jbin){
51       *(betaj + jbin)= *(betaprime+*nspecies - jbin) ;
52      }
53
54      temprdealloc(betaprime);
55
56      exiting("beta_transfer") ;
```

10.2.1.2 Routine – bin_boundaries.c

Relevant algorithms from bin_boundaries.c routine to calculate the wave number boundaries.

```
31      entered("bin_boundaries") ;
32
33      ////////////////////////////////////////////////////////////////////
34      //          wavenumber boundary calculations
//
35      ////////////////////////////////////////////////////////////////////
36
37      //calculate the spectral resolution
38      lambda=  exp((log(wnright)-log(wnleft))/ (double)*nspecies) ;
      //spectral resolution, lambda
39
40      //loop over the number of bins to get boundaries
41      for(iwn=0 ; iwn<= *nspecies ; ++iwn) {
42          *(kappa + iwn)= wnleft*pow(lambda,(double)iwn) ;
43      }
44
45      //loop to find bin widths and centers
46      for(iwn=1; iwn<= *nspecies  ; ++iwn) {
47          *(kappa_center + iwn)= 0.5*(*(kappa+iwn) + *(kappa+iwn-1)) ; //bin
centers
48          *(kappa_width + iwn)= *(kappa+iwn) - *(kappa+iwn-1) ;
      //bin widths
49      }
50
51      ////////////////////////////////////////////////////////////////////
52
53      exiting("bin_boundaries") ;
```

10.2.1.3 Routine – set_inflow.c

The details of this routine are not included since the set_inflow.c routine existed from previous use with NPHASE-CMFD. A simple alteration of the existing routine was performed to provide output for the chemical species equations storage from NPHASE-CMFD.

10.2.1.4 Routine – spectral_bubble_weight.c

Relevant algorithms from spectral_bubble_weight.c routine to calculate the spectral bubble weighting factor (γ_{m_i}) using the model chosen from user_initialize.c.

```
042     entered("spectral_bubble_weight") ;
043
044     //print an output message
045     printf("\n") ;
046     printf("*****************************************************************\n")
;
047     printf("Multiphase run! setting bubble contributions using \n") ;
048     printf(" bubble weight model # \t%i\n",wm) ;
049     printf("*****************************************************************\n")
;
050     printf("\n") ;
051
052     slope = -1.0/4.0 ;
053
054     //loop over the dispersed fields - bubble groups
055     for(ifield=1; ifield<=*nfield-1; ++ifield){
056      bubble_group    = ifield ;
057      dispersed_phase = ifield + 1 ;
058      db              = BubbleDiameter_InternalNode(10,dispersed_phase) ;
059      kappa_bubble    = 1.0/db ;
060      nstride         = *nspecies* (bubble_group-1) ;
061
062
063      //find characteristic bin for current bubble size
064      for(j=1; j<= *nspecies; ++j){
065       if(kappa_bubble >= *(kappa+j-1) && kappa_bubble <= *(kappa+j) ) {
066        dbbin = j ;
067       }
068      }//j
069
070
//+++++++++++++++++++++++++++++++++++++++++++++++++++++++++++++++++++++++++++++++/
/
071       //                BUBBLE WEIGHTING MODEL #1
                             //
072
//+++++++++++++++++++++++++++++++++++++++++++++++++++++++++++++++++++++++++++++++/
/
073       if(wm == 1){
074        for(j=1; j<= *nspecies; ++j){
075         if(j==dbbin){
076          *(gamma_bubble + nstride + j) = 1.0  ;
077         }
```

```
078         else{
079          *(gamma_bubble + nstride + j) = 0.0 ;
080         }
081        }//j
082       }//wm = 1
083
//+++++++++++++++++++++++++++++++++++++++++++++++++++++++++++++++++++++++++++++++++++++++/
/
084
085
//+++++++++++++++++++++++++++++++++++++++++++++++++++++++++++++++++++++++++++++++++++++++/
/
086       //                              BUBBLE WEIGHTING MODEL #2
                              //
087
//+++++++++++++++++++++++++++++++++++++++++++++++++++++++++++++++++++++++++++++++++++++++/
/
088       else if(wm == 2){
089        for(j=1; j<= *nspecies; ++j){
090         if(j<dbbin){
091          *(gamma_bubble + nstride + j) = 0.0 ;
092         }
093         else if(j>=dbbin){
094          *(gamma_bubble + nstride + j) = 2.0* *(betaj+j-dbbin+1) ;
095         }
096        }//j
097       }//wm = 2
098
//+++++++++++++++++++++++++++++++++++++++++++++++++++++++++++++++++++++++++++++++++++++++/
/
099
100
//+++++++++++++++++++++++++++++++++++++++++++++++++++++++++++++++++++++++++++++++++++++++/
/
101      //                              BUBBLE WEIGHTING MODEL #3
                             //
102
//+++++++++++++++++++++++++++++++++++++++++++++++++++++++++++++++++++++++++++++++++++++++/
/
103      else if(wm == 3){
104        sum = 0.0 ;
105            for(j=1; j<= *nspecies; ++j){
106             if(j<dbbin){
107              *(gamma_bubble + nstride + j) = 0.0 ;
108             }
109             else if(j>=dbbin){
110              *(gamma_bubble + nstride + j) = pow(*(kappa_center+j),slope) ;
111             }
112         sum += *(gamma_bubble + nstride + j) ;
113            }//j
114
115            for(j=1; j<= *nspecies; ++j){
116         *(gamma_bubble + nstride + j) /= sum ;
117        }//j
118      }//wm = 3
119
//+++++++++++++++++++++++++++++++++++++++++++++++++++++++++++++++++++++++++++++++++++++++/
/
120
```

```
121
//+++++++++++++++++++++++++++++++++++++++++++++++++++++++++++++++++++++++++++++++/
/
122      //                              BUBBLE WEIGHTING MODEL #4
                              //
123
//+++++++++++++++++++++++++++++++++++++++++++++++++++++++++++++++++++++++++++++++/
/
124      else if(wm == 4){
125       sum = 0.0 ;
126           for(j=1; j<= *nspecies; ++j){
127            if(j<dbbin){
128         *(gamma_bubble + nstride + j) = *(betaj+dbbin-j) *
pow(*(kappa_center+dbbin),slope) ;
129        }//j<dbbin
130        else if(j>=dbbin){
131         *(gamma_bubble + nstride + j) = pow(*(kappa_center+j),slope) ;
132        }//j>=dbbin
133        sum += *(gamma_bubble + nstride + j) ;
134       }//j
135
136           for(j=1; j<= *nspecies; ++j){
137            *(gamma_bubble + nstride + j) /= sum ;
138           }//j
139      }//wm=4
140
//+++++++++++++++++++++++++++++++++++++++++++++++++++++++++++++++++++++++++++++++/
/
141
142     } //ifield
143
144     exiting("spectral_bubble_weight") ;
```

10.2.2 NPHASE-CMFD Routine – user_source_species.c

Table 10.2. provides further information on the NPHASE-CMFD routine user_source_species.c. Note that some routines such as the calculation of the mean flow gradients and the wall coordinates are only called during the first bin TKE solve to eliminate computational overhead since mean flow gradients are not altered during the iteration on NPHASE-CMFD chemical species equations.

Table 10.2. Information for NPHASE-CMFD routine user_source_species.c.

Routine	user_source_species.c
Purpose	Calculate the RHS of each bin TKE equation and set boundary conditions.
Calls Routines	bubble_model (if *m* = 1 and multiphase simulation) bubble_source (if multiphase simulation) eddy_viscosity homogeneous_dissipation inhomogeneous_dissipation mean_gradients (if *m* = 1) prod transfer wall_coordinates (if *m* = 1)

The entire user_source_species.c routine is shown here. For routines called from user_source_species.c only relevant algorithms will be shown.

```
001 #include "nphase_struct.h"
002 #include <math.h>
003 #include "definitions.h"
004 #include <stdio.h>
005 extern struct data var;
006 extern struct boundary_patch partition ;
007 extern struct boundary_patch wall ;
008
009 //global definitions
010 extern double *homogeneous_dissipation_node ;
011 extern double *inhomogeneous_dissipation_node ;
012 extern double *transfer_node ;
013 extern double *turbulent_viscosity ;
014 extern double *production_node ;
015 extern double *kappa_center ;
016 extern double *total_tds_node ;
017 extern double *Species_Node_Old ;
018 extern double *bubble_source_node ;
019 extern int    variablerelax ;
020 extern double rfsmax ;
021
022 int user_source_species(int ivar)
023 {
024 /*-------------------------------------------------
025     user routine for species source/sink terms
026
027     tailored to the SCTM transport model
028     begin work: April, 2015
029
030     called from:
031     species
032 -------------------------------------------------*/
033
034     int *nspecies=var.nspecies ;          //number of species (i.e. k) eqns
035     int *nnode=var.nnode ;
036     int *nfield=var.nfield ;
037
038     real *tke=var.tke ;
```

```
039     real *tds=var.tds ;
040     real *small=var.small ;
041     real *large=var.large ;
042     real *diff=var.diff ;
043     real *walldistance=var.walldistance ;
044     real *rfs=var.rfs ;
045
046     int inode ;
047     int bin ;                               //current bin number
048     int carrier_field ;
049     int j ;
050     int nstridebin ;
051     int nstridebintds ;
052     int nstridebin_old ;
053     int nstridebubble ;
054     int ibf ;
055     int ifield ;
056
057     double gamma ;
058     double wallarea ;
059     double wd ;
060
061     double *tempralloc(),*temprdealloc() ;
062     double *dispersed_source ;
063
064     entered("user_source_species") ;
065
066     dispersed_source = tempralloc(*nnode) ;
067
068     // species number
069     bin = ivar - 8;
070     carrier_field = 1 ;
071     nstridebin= (*nnode)*(bin-1) ;
072     if(bin == 1) {
073         mean_gradients(carrier_field) ;
074         wall_coordinates(carrier_field) ;
075         if(*nfield > 1){
076          for(ifield=1; ifield<= *nfield-1; ++ifield){
077           bubble_model(ifield) ;
078          } //ifield
079         } //if nfield>1
080     }
081
082     LaminarPrandtlNumber(ivar,1)   = 1.0 ;
083     TurbulentPrandtlNumber(ivar,1) = 0.5 ;
084
085     //variable relaxation factor
086     if(variablerelax == 1) {
087      *(rfs+bin-1) = rfsmax/ sqrt( *(kappa_center+bin) ) ;
088     }
089
090     //*************************************************************************
091     //  SOURCE TERMS CALL
                                    *
092     //*************************************************************************
093
094     //transfer routine
095     transfer(carrier_field,bin) ;
096
```

```
097     //inhomogeneous dissipation routine
098     inhomogeneous_dissipation(ivar,carrier_field,bin) ;
099
100     //homogeneous dissipation routine
101     homogeneous_dissipation(carrier_field,bin) ;
102
103     //update total dissipation
104     for(inode=0; inode<= *nnode-1; ++inode){
105      *(total_tds_node+inode)= 0.0 ;
106      for(j=1; j<=*nspecies; ++j){
107       nstridebintds= (*nnode)*(j-1) ;
108       *(total_tds_node+inode) +=
*(homogeneous_dissipation_node+inode+nstridebintds)
109         + *(inhomogeneous_dissipation_node+inode+nstridebintds) ;
110      } //j loop
111     }//inode loop
112
113     //eddy viscosity routine
114     eddy_viscosity(carrier_field,bin) ;
115
116     //production routine
117     prod(ivar,carrier_field,bin) ;
118
119     //bubble source term
120     if(*nfield>1){
121      for(ifield=1; ifield<= *nfield-1; ++ifield){
122       bubble_source(ifield,bin) ;
123      }//ifield
124     }
125
126     //formulate the species source term
127     for(inode=0; inode<= *nnode-1; ++inode){
128
129      if(*nfield>1){
130       *(dispersed_source + inode) = 0.0 ;
131       for(ifield=1;ifield<= *nfield-1; ++ifield){
132        nstridebubble = *nnode*(bin-1) + *nnode* *nspecies* (ifield-1) ;
133        *(dispersed_source + inode) += *(bubble_source_node + nstridebubble +
inode) ;
134        // *(dispersed_source + inode) += 0.0 ;
135       }//ifield
136      }//nfield>1
137
138     if(*nfield ==1 ){
139          SourceTerm_Species(inode,carrier_field) =
140           - *(inhomogeneous_dissipation_node     +inode+nstridebin)
141           - *(homogeneous_dissipation_node       +inode+nstridebin)
142           + *(transfer_node                             +inode+nstridebin)
143           + *(production_node                           +inode+nstridebin) ;
144      }
145      else{
146      SourceTerm_Species(inode,carrier_field) =
147      - *(inhomogeneous_dissipation_node+inode+nstridebin)
    *VolumeFraction_InternalNode(inode,carrier_field)
148       - *(homogeneous_dissipation_node  +inode+nstridebin)

*VolumeFraction_InternalNode(inode,carrier_field)
149       + *(transfer_node                    +inode+nstridebin)
*VolumeFraction_InternalNode(inode,carrier_field)
```

```
150       + *(production_node           +inode+nstridebin)
*VolumeFraction_InternalNode(inode,carrier_field)
151       + *(dispersed_source          +inode           )
*VolumeFraction_InternalNode(inode,carrier_field) ;
152      }
153
154      SourceTerm_Species(inode,carrier_field) *= NodeVolume_InternalNode(inode)*

Density_InternalNode(inode,carrier_field) ;
155
156      //store the old species value
157      if(bin == 1){
158       for(j=1;j<=*nspecies; ++j){
159        nstridebin_old = (*nnode)*(j-1) ;
160        *(Species_Node_Old+inode+nstridebin_old)= Species_InternalNode(inode,j)
;
161       }
162      }
163
164     } //end loop over nodes
165
166     //*************************************************************************
167     //  Dirichlet boundary conditions for species // wall boundary BCs
                    *
168     //*************************************************************************
169     for(ibf=0; ibf<=NumberFaces_WallBoundary-1; ++ibf){
170         TurbulentKineticEnergy_WallBoundary(ibf,carrier_field)       = 0.0 ;
171         UVelocity_WallBoundary(ibf,carrier_field)                          =
0.0 ;
172         VVelocity_WallBoundary(ibf,carrier_field)                    = 0.0 ;
173         WVelocity_WallBoundary(ibf,carrier_field)                    = 0.0 ;
174         Species_WallBoundary(ibf,bin)                                = 0.0 ;
175         inode=  AdjacentNodeNumber_WallBoundary(ibf) ;
176         wallarea=   Area_WallBoundary(ibf) ;
177         wd=         *(walldistance+inode);
178
179      //note the hardcode of Schmidt numbers
180      gamma= (LaminarViscosity_InternalNode(inode,carrier_field) / 1.0 )
             + ( *(turbulent_viscosity+inode+nstridebin) / 0.5 ) ;
181      NodeCoefficientMatrix_Species(inode,carrier_field) -=
Density_InternalNode(inode,carrier_field)*gamma*wallarea/wd ;
182     } //end of ibf loop
183
184     temprdealloc(dispersed_source) ;
185
186     exiting("user_source_species") ;
187
188     return 0 ;
189 }
```

10.2.2.1 Routine – bubble_model.c

Relevant algorithms from bubble_model.c routine to calculate BIT source term in each bin with the form of the BIT source term defined in user_initialize.c.

```
043     entered("bubble_model") ;
044
045
```

```
046     //get current fields
047     continuous_phase = 1 ;
048     dispersed_phase  = ifield + 1 ;
049     nstride = (ifield-1)* *nnode ;
050
051     //virtual mass coefficient & cp
052     cvm = 0.5 ;
053     cp  = 0.5*cvm ;
054
055
056
057 if(bubble_source_model == 1){
058
059     //-------------------------------------------------------------------------
-------------------------------------
060     //                        LAHEY MODEL
061     //-------------------------------------------------------------------------
-------------------------------------
062     for(inode=0; inode<= *nnode-1; ++inode){
063
064      //calculate relative velocities and magnitudes
065      urel = UVelocity_InternalNode(inode,dispersed_phase) -
UVelocity_InternalNode(inode,continuous_phase) ;
066      vrel = VVelocity_InternalNode(inode,dispersed_phase) -
VVelocity_InternalNode(inode,continuous_phase) ;
067      wrel = WVelocity_InternalNode(inode,dispersed_phase) -
WVelocity_InternalNode(inode,continuous_phase) ;
068
069      velrelmag = sqrt( urel*urel + vrel*vrel + wrel*wrel ) ;
070      Re_rel=velrelmag*Density_InternalNode(inode,continuous_phase)*
BubbleDiameter_InternalNode(inode,dispersed_phase)
071                        /LaminarViscosity_InternalNode(inode,continuous_phase);
072
073      //drag coefficient
074      cd=24.0/Re_rel*(1.+0.092*pow(Re_rel,0.78));
075      cd=max(cd,0.4);
076
077      //volume fractions
078      ag = VolumeFraction_InternalNode(inode,dispersed_phase) ;
079
080      //bubble diameter
081      db = BubbleDiameter_InternalNode(inode,dispersed_phase) ;
082
083      //nodal phi value
084      *(phi_bubble + nstride + inode) = cp* (1.0 + pow(cd,4.0/3.0))* ag*
pow(velrelmag,3.0) / db ;
085
086     } //inode
087
088     //-------------------------------------------------------------------------
-------------------------------------
089     //                          END LAHEY MODEL
090     //-------------------------------------------------------------------------
-------------------------------------
091
092 }//bubble_source_model = 1
093
094
095
```

```
096 else if(bubble_source_model == 2){
097
098     //-------------------------------------------------------------------------
-------------------------------------
099     //                       RK MODEL (RZEHAK & KREPPER, IJMF, 2013)
100     //-------------------------------------------------------------------------
-------------------------------------
101     for(inode=0; inode<= *nnode-1; ++inode){
102
103      //calculate relative velocities and magnitudes
104      urel = UVelocity_InternalNode(inode,dispersed_phase) -
UVelocity_InternalNode(inode,continuous_phase) ;
105      vrel = VVelocity_InternalNode(inode,dispersed_phase) -
VVelocity_InternalNode(inode,continuous_phase) ;
106      wrel = WVelocity_InternalNode(inode,dispersed_phase) -
WVelocity_InternalNode(inode,continuous_phase) ;
107
108      velrelmag = sqrt( urel*urel + vrel*vrel + wrel*wrel ) ;
109      Re_rel=velrelmag*Density_InternalNode(inode,continuous_phase)*
BubbleDiameter_InternalNode(inode,dispersed_phase)
110                       /LaminarViscosity_InternalNode(inode,continuous_phase);
111
112      //drag coefficient
113      cd=24.0/Re_rel*(1.+0.092*pow(Re_rel,0.78));
114      cd=max(cd,0.4);
115
116      //volume fractions
117      ag = VolumeFraction_InternalNode(inode,dispersed_phase) ;
118
119      //bubble diameter
120      db = BubbleDiameter_InternalNode(inode,dispersed_phase) ;
121
122      //nodal phi value
123      *(phi_bubble + nstride + inode) = 0.75*cd*ag*pow(velrelmag,3.0) / db ;
124
125     } //inode
126
127     //-------------------------------------------------------------------------
-------------------------------------
128     //                                                  END RK MODEL
129     //-------------------------------------------------------------------------
-------------------------------------
130
131 }//bubble_source_model = 2
132
133     exiting("bubble_model") ;
```

10.2.2.2 Routine – bubble_source.c

Relevant algorithms from bubble_source.c routine to calculate the BIT source for each wave number bin (e.g. $\gamma_{m_i}\phi_i$).

```
39      entered("bubble_source") ;
40
41      bubble_group    = ifield ;
42      dispersed_phase = ifield + 1 ;
43      nstridegamma    = *nspecies* (bubble_group-1) ;
44      nstridephi      = *nnode*    (bubble_group-1) ;
```

```
45      nstride     = *nnode*(bin-1) + *nnode* *nspecies* (bubble_group-1) ;
46
47      //bubble_source_node
48      gamma = *(gamma_bubble + nstridegamma + bin) ;
49
50      for(inode=0;inode<=*nnode-1;++inode){
51       phi = *(phi_bubble + nstridephi + inode) ;
52
53       *(bubble_source_node + nstride + inode) = gamma*phi ;
54
55      } //inode
56
57      exiting("bubble_source") ;
```

10.2.2.3 Routine – eddy_viscosity.c

Relevant algorithms from eddy_viscosity.c routine to calculate the turbulent viscosity in each wave number bin.

```
065     entered("eddy_viscosity") ;
066
067     m= bin ;
068     nstride= 0 ;
069     nstridebin= (*nnode)*(m-1) ;
070
071     //loop over the nodes to calculate the damping functions and turbulent
viscosity
072     for(inode=0; inode<= *nnode-1; ++inode){
073
074      if(iSCTMlowhigh == 0 ){
075      //fs damping function
076      fs= 1.0 - exp(SCM*kappa_center[m]/kappa[*nspecies]) ;
077
078      //fmu damping function
079      wd=*(   walldistance+inode);
080      pd=*(porwalldistance+inode);
081      mind=MIN(wd,pd);
082      CCM= -0.007 ;
083      fmu= 1.0 - exp(CCM* *(y_p+inode)) ;
084
085      //fy damping function
086      fy= pow((1.0 - exp(NCM*mind*kappa_center[m])),0.25);
087      }
088      else if(iSCTMlowhigh == 1){
089      fs  = 1.0 ;
090      fmu = 1.0 ;
091      fy  = 1.0 ;
092      }
093
094      //calculate turbulent viscosity
095      Em    = Species_InternalNode(inode,m)/ *(kappa_width+m) ;
096      term1 = sqrt(Em/pow(*(kappa_center+m),3.0)) ;
097      term2 = pow(Em* pow(*(kappa_center+m),(5.0/3.0))
          * pow(*(total_tds_node+inode),(-2.0/3.0)),betanu) ;
098      nunode= CH*fs*fmu*fy* *(kappa_width+m)*term1*term2 ;
099      *(turbulent_viscosity+inode+nstridebin)= nunode ;
100
101     } //end loop over the nodes
```

```
102
103     exiting("eddy_viscosity") ;
```

10.2.2.4 Routine – homogeneous_dissipation.c

Relevant algorithms from homogeneous_dissipation.c routine to calculate the homogeneous dissipation in each wave number bin.

```
37      entered("homogeneous_dissipation") ;
38
39      m= bin ;
40      nstridebin= (*nnode)*(m-1) ;
41
42      // homogeneous dissipation on node for the current bin m
43      for(inode=0 ; inode<= *nnode-1 ; ++inode) {
44       *(homogeneous_dissipation_node+inode+nstridebin) =
45
2.0*LaminarViscosity_InternalNode(inode,carrier_field)/Density_InternalNode(inode,c
arrier_field)
46        *(Species_InternalNode(inode,m)/kappa_width[m])
47        *(pow(kappa[m],3.0)/3.0 - pow(kappa[m-1],3.0)/3.0) ;
48      } //end loop over nodes
49
50      exiting("homogeneous_dissipation") ;
```

10.2.2.5 Routine – inhomogeneous_dissipation.c

Relevant algorithms from inhomogeneous_dissipation.c routine to calculate the inhomogeneous dissipation in each wave number bin.

```
50      entered("inhomogeneous_dissipation") ;
51
52      m= bin ;
53      nstride= 0 ;
54      nstridebin= (*nnode)*(m-1) ;
55
56      // inhomogeneous dissipation
57      for(inode=0 ; inode<=*nnode-1 ; ++inode) {
58
59       wd=*(   walldistance+inode);
60       pd=*(porwalldistance+inode);
61       mind=MIN(wd,pd);
62
63       *(inhomogeneous_dissipation_node+inode+nstridebin)=
64              exp(-c_inhom* *(y_p+inode))*
65              2.0* Species_InternalNode(inode,m)*
66              (*(vism+inode+nstride)/ *(rho+inode+nstride)) / (wd*wd) ;
67
68      } //end loop over nodes
69
70      exiting("inhomogeneous_dissipation") ;
```

10.2.2.6 Routine – mean_gradients.c

Relevant algorithms from mean_gradients.c routine to calculate the mean flow gradients. This routine is only called from user_source_species.c when bin-*m* = 1 to reduce computational overhead.

```
28      entered("mean_gradients") ;
29
30      //calculate gradients
31      gradient(u,gradient_u,1,carrier_field) ;
32      gradient(v,gradient_v,2,carrier_field) ;
33      gradient(w,gradient_w,3,carrier_field) ;
34
35      exiting("mean_gradients") ;
```

10.2.2.7 Routine – prod.c

Relevant algorithms from prod.c routine to calculate the turbulence production in bin-*m*. Note on line 073 that a preexisting mean strain rate algorithm was used.

```
058     entered("prod") ;
059
060     m= bin ;
061     nstridebin= (*nnode)*(m-1) ;
062     clipcount= 0 ;
063     if(m==1){
064       cliptotal= 0 ;
065     }
066
067     nstride = 0 ;
068     stride1 = *nnode ;
069     stride2 = 2* *nnode ;
070
071     //production term for bin m
072     for(inode=0; inode<=*nnode-1; ++inode){
073      //use mean strain rate generation routine from Igor Bolotnov TURBULENCE
ROUTINES (01/13/2017)
074      term1 = *(gradient_u        +inode)* *(gradient_u        +inode)
075            + *(gradient_v+stride1+inode)* *(gradient_v+stride1+inode)
076            + *(gradient_w+stride2+inode)* *(gradient_w+stride2+inode);
077                     + *lcyl* *(v+nstride+inode)* *(v+nstride+inode)/
078                         (*(yc+inode)+ *small)/ (*(yc+inode)+ *small);
079      term2 = *(gradient_u+stride1+inode) + *(gradient_v        +inode) ;
080      term3 = *(gradient_u+stride2+inode) + *(gradient_w        +inode) ;
081      term4 = *(gradient_v+stride2+inode) + *(gradient_w+stride1+inode) ;
082
083
084      production= *(turbulent_viscosity+inode+nstridebin) *
    (2.*term1 + term2*term2 + term3*term3 + term4*term4 ) ;
085
086      dest= ABS( *(inhomogeneous_dissipation_node+inode+nstridebin) +
 *(homogeneous_dissipation_node+inode+nstridebin)) ;
087      clippedprod= *prodclip*dest ;
088
089      *(production_node+inode+nstridebin)= MIN(clippedprod,production) ;
```

```
090
091      if(clippedprod<=production) clipcount+=1 ;
092
093     }
094
095     cliptotal+=clipcount ;
096         if(m == *nspecies && cliptotal>0 ) printf("total clip %i\n",cliptotal)
;
097
098     exiting("prod") ;
```

10.2.2.8 Routine – transfer.c

Relevant algorithms from transfer.c routine to calculate the spectral transfer between wave number bins for a particular wave number bin-*m*.

```
049     entered("transfer") ;
050
051     m= bin ;
052
053     nstride= 0 ;
054     nstridebin= (*nnode)*(m-1) ;    //correct location in array for current bin
055
056     //check for a negative k value to avoid non-real numbers
057     kcntl= 0 ;
058     if(bin==1) kcntltot= 0 ;
059
060     for(j=1; j<=*nspecies; ++j){
061      nstridebin_cntl= (*nnode)*(j-1) ;
062      for(inode=0; inode<= *nnode-1; ++inode){
063           if(Species_InternalNode(inode,j)<=0.0) {
064            Species_InternalNode(inode,j)=
*(Species_Node_Old+inode+nstridebin_cntl) *0.90 ;
065        kcntl+= 1 ;
066           } //end if k<0
067          } //end loop over nodes (inode)
068     } //end loop over bins (j)
069     kcntltot+= kcntl ;
070     if(bin==*nspecies && kcntltot>0) printf("Total number of nodes where k
values have been controlled:\t%i\n",kcntltot) ;
071
072
073
074  //loop over the nodes
075  for(inode=0; inode<= *nnode - 1; ++inode){
076   //initialize for each node
077   TC1= 0.0 ;
078   TC2= 0.0 ;
079   TC3= 0.0 ;
080   TC4= 0.0 ;
081
082   //loop over the bins before current bin m
083     if(m > 1){
084      for(j=1; j<= m-1; ++j){
085
086       TC1 += betaj[j]*kappa[m-1]*Species_InternalNode(inode,m-j)*
087        sqrt(Species_InternalNode(inode,m)*kappa_center[m]/kappa_width[m]) ;
088
```

```
089       TC3 += betaj[j]*kappa[m-j]*Species_InternalNode(inode,m)*
090            sqrt(Species_InternalNode(inode,m-j)*kappa_center[m-
j]/kappa_width[m-j]) ;
091
092       } //end of loop over bins before m
093     } //end of if m>1
094
095
096   //loop over the bins after the current bin m
097     if(m < *nspecies){
098      for(j=1; j<= *nspecies - m; ++j){
099
100       TC2 += betaj[j]*kappa[m-1+j]*Species_InternalNode(inode,m)*
101
sqrt(Species_InternalNode(inode,m+j)*kappa_center[m+j]/kappa_width[m+j]) ;
102
103           TC4 += betaj[j]*kappa[m]*Species_InternalNode(inode,m+j)*
104            sqrt(Species_InternalNode(inode,m)*kappa_center[m]/kappa_width[m]) ;
105
106      } //end of loop over bins after m
107     } //end of if m<N
108
109
110  //get C1 & C2 at the current node (y+ dependent)
111  if(iSCTMlowhigh == 0){
112   C1= 16.0 - 14.8*pow((1.0-exp(- *(y_p+inode)/sigma_transfer)),2.0) ;
113   C2= 0.3167*C1 ;
114  }
115  else if(iSCTMlowhigh == 1){
116   C1= 1.2  ;
117   C2= 0.38 ;
118  }
119
120   //sum the terms for the transfer term
121   *(transfer_node+inode+nstridebin)= C1*TC1 - C1*TC2 - C2*TC3 + C2*TC4 ;
122
123  } //end of loop over nodes
124
125
126     exiting("transfer") ;
```

10.2.2.9 Routine – wall_coordinates.c

Relevant algorithms from wall_coordinates.c routine to calculate the non-dimensional wall units. This routine is only called from user_source_species.c when bin-*m* = 1 to reduce computational overhead.

```
50      entered("wall_coordinates") ;
51
52      nstride = 0 ;
53
54      for(inode=0; inode<= *nnode - 1; ++inode){
55            wd=*(   walldistance+inode);
56            pd=*(porwalldistance+inode);
57            mind=MIN(wd,pd);
58                if(wd == mind){
59                    ibf=*(walldistface0+inode);
```

```
60                      utau=sqrt( *(walltw0+ibf)/ *(rho+inode+nstride) );
61                  }
62                  if(pd == mind){
63                      ibf=*(porwalldistface0+inode);
64                      utau=sqrt( *(porwalltw0+ibf)/ *(rho+inode+nstride) );
65                  }
66
67              *(u_tau+inode) = utau ;
68              *(y_p  +inode) = *(rho+inode+nstride)*utau* mind/
*(vism+inode+nstride);
69
70      }//end loop over nodes
71
72      exiting("wall_coordinates") ;
```

10.2.3 NPHASE-CMFD Routine – user_viscosity_turbulent.c

The NPHASE-CMFD routine user_viscosity_turbulent.c is used to sum over the bin turbulent viscosities (Equation (3.8)) to calculate the total turbulent viscosity distribution for use in the RANS momentum equation. The relevant algorithms from the routine are shown here.

```
075   entered("user_viscosity_turbulent") ;
076
077     carrier_field = 1 ;
078     //sum over the bins to get total turbulent viscosity
079      for(inode=0; inode<= *nnode-1; ++inode){
080       *(vist+inode)= 0.0 ;
081           for(bin=1; bin<= *nspecies; ++bin){
082            nstridebin= (*nnode)*(bin-1) ;
083             *(vist+inode) +=
*(turbulent_viscosity+inode+nstridebin)*Density_InternalNode(inode,carrier_field) ;
084           }
085      }
086
087
088     //if multiphase run -> set the turbulent viscosity of vapor fields to
liquid turbulent viscosity
089         if(*nfield>1){
090          for(ifield=1; ifield<= *nfield-1; ++ifield){
091       nstride = nstride=ifield* *nnode ;
092        for(inode=0; inode<= *nnode-1; ++inode){
093         *(vist+inode+nstride) = *(vist+inode) ;
094        }
095      }
096     }
097
098   exiting("user_viscosity_turbulent") ;
```

10.2.4 NPHASE-CMFD Routine – user_monitor.c

The NPHASE-CMFD routine user_monitor.c has been used in the past for simulation control (i.e. stopping the simulation on divergence) as well as printing output at stream-wise locations in the

wall-normal direction. The existing user_monitor.c routine was used here and altered to provide output relevant to SCTM performance such as wave number bin TKE values, energy spectra, etc. The routine is expansive and is not shown.

10.2.5 NPHASE-CMFD Routine – user_liftforce.c

The NPHASE-CMFD routine user_liftforce.c allows the user to input a lift force formulation. As discussed, an existing lift force formulation was used with modification of the lift coefficient close to the solid wall boundary. The relevant portion of the lift force algorithm where the lift coefficient is modified is shown here.

```
160         //modified for LRN model
161         y_hat =
2.*DistanceClosestWall_InternalNode(inode)/BubbleDiameter_InternalNode(inode,field_
dispersed)-1.;
162         y_hat = MIN(y_hat,1.) ;
163
164         if(usermult<0.0){
165             y_hat = 1.0 ;
166         }
167
168         //evaluate lift terms
169         term = usermult* cl* y_hat* vfhat*
Density_InternalNode(inode,field_continuous) ;
```

10.3 Appendix C

The TKE spectra from HT11 and HT21 are further compared at ten different spatial locations where the two-phase results were obtained with the Lahey BIT source term. Figure 10.2 is a schematic of the 25 mm diameter pipe with non-dimensional spatial locations labeled that correspond to locations where the TKE spectra are presented in Figure 10.3 – Figure 10.4. Single-phase spectra are shown as black square symbols and two-phase spectra are shown as blue diamond symbols.

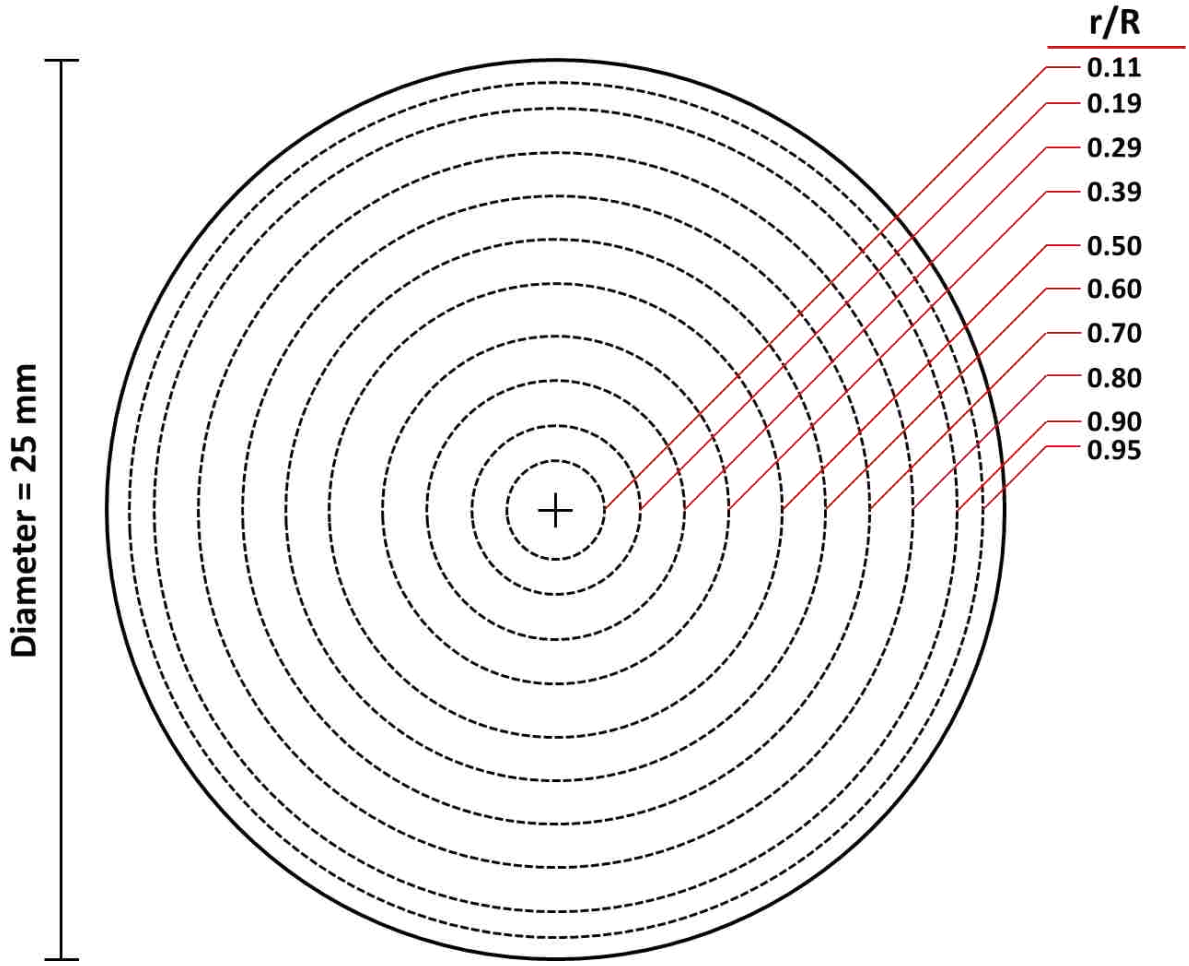

Figure 10.2. 25 mm diameter pipe with spatial locations for TKE spectra comparison labeled.

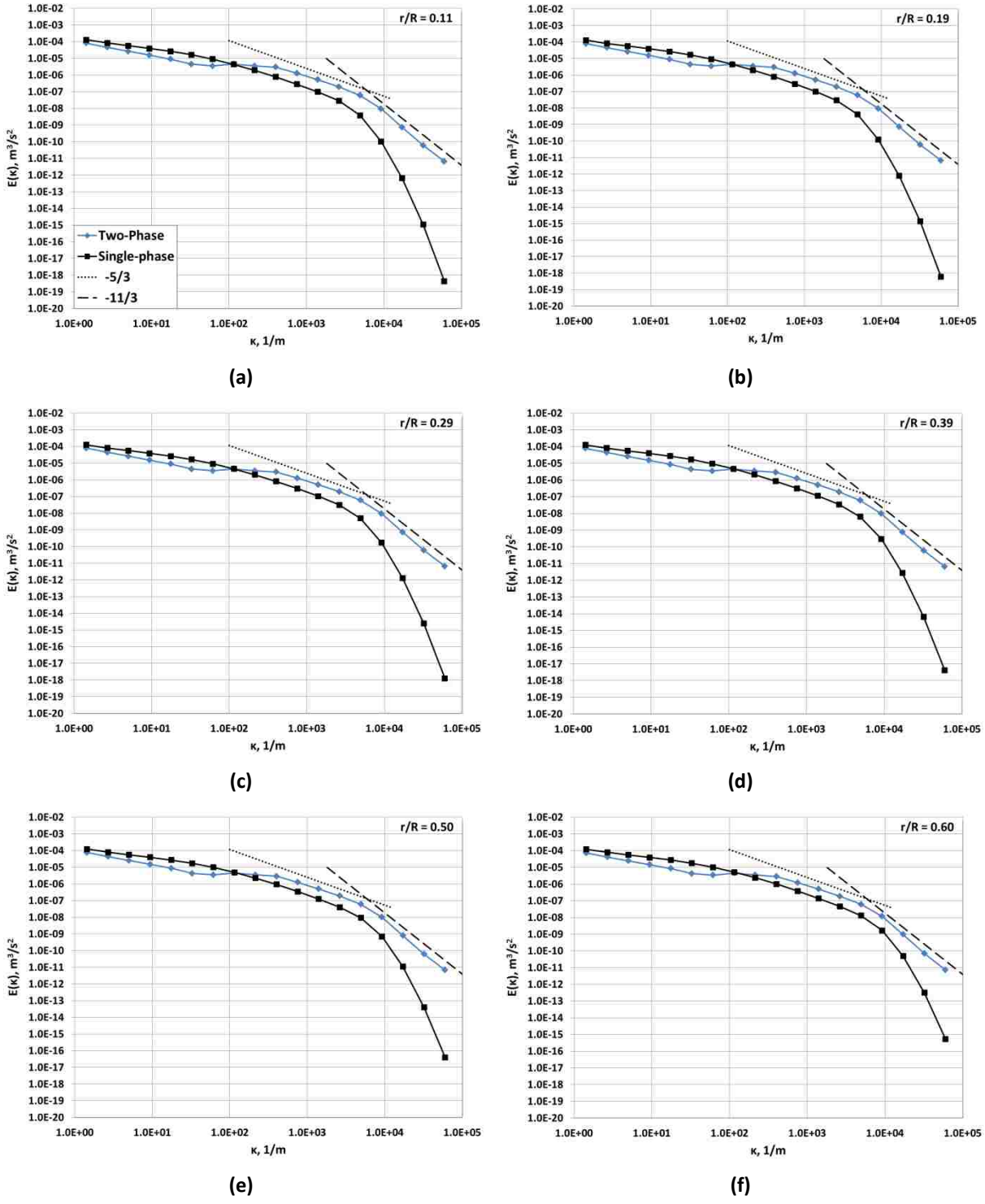

Figure 10.3. TKE spectra comparison for HT11 and HT21 cases at r/R = 0.11 – r/R = 0.60.

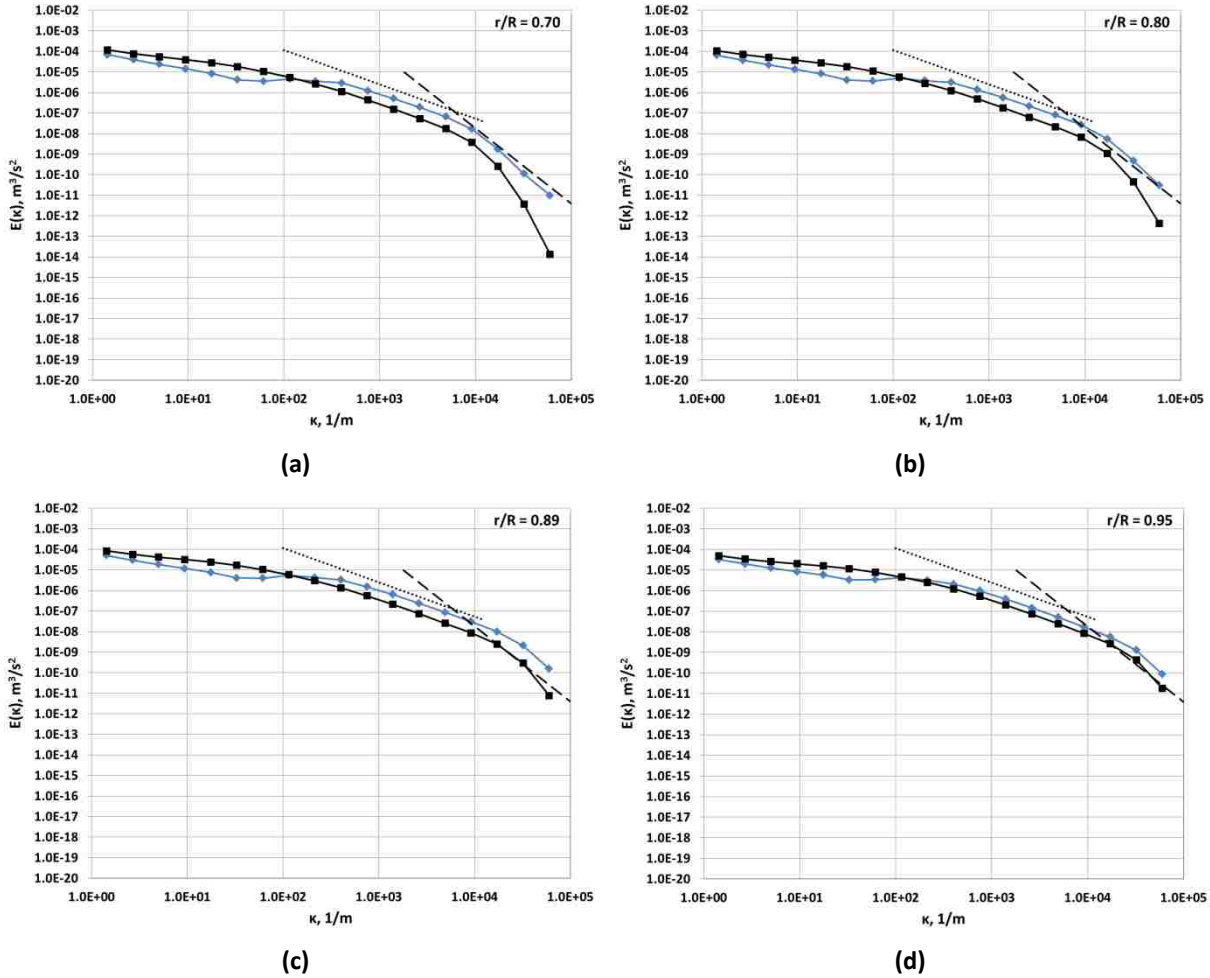

Figure 10.4. TKE spectra comparison for HT11 and HT21 cases at r/R = 0.70 – r/R = 0.95.

10.4 Appendix D

The Maple (www.maplesoft.com) algorithm used to calculate the equivalent bubble diameter for a monodispersed case in comparison to polydispersed (two bubble group) case:

```
> restart :
> #Find equivalent bubble diameter for a monodispersed case from
polydispersed case
>
> #Inputs
> #pipe diameter (mm)
> d := 25 :
> #LOD
> lod := 50 :
> #bubble diameter 1 (mm)
> d1 := 3 :
> #bubble diameter 2 (mm)
> d2 := 6 :
> #average volume fraction - group 1
> a1 := 0.04 :
> #average volume fraction - group 2
> a2 := 0.01 :
>
>
> #Geometric values
> l := d·lod :
> V := π·(d/2)^2·l :
>
> #Total amount of volume occupied by each group
> V1 := a1·V :
> V2 := a2·V :
>
> #Total gas volume
> Vg := V1 + V2 :
>
> #Number of bubbles
> T1 := V1/(π·(d1/2)^2) :
> T2 := V2/(π·(d2/2)^2) :
> T := T1 + T2 :
>
```

```
> #Equivalent diameter for monodispersed case with same number of
bubbles
```

$$> diameter\_eqn := \frac{Vg}{\pi \cdot \left(\frac{de}{2}\right)^2} = T :$$

$$> equivalent\_diameter := fsolve(diameter\_eqn, de) :$$

```
>
> #Void fraction for equivalent case
```

$$> ae := \frac{Vg}{V} :$$

10.5 Appendix E

Supplemental figures are shown here for polydispersed two-phase flow between parallel plates with 100 mm plate spacing (§ 6.5.2). The subscripts are indicated as "L" for liquid, "g,1" for the small bubble group of 3 mm diameter, and "g,2" for the large bubble group of 6 mm diameter. Figure 10.5 – Figure 10.7 are mean flow parameters shown across the channel width. Figure 10.7 is the total bin BIT source term given by Equation (6.14).

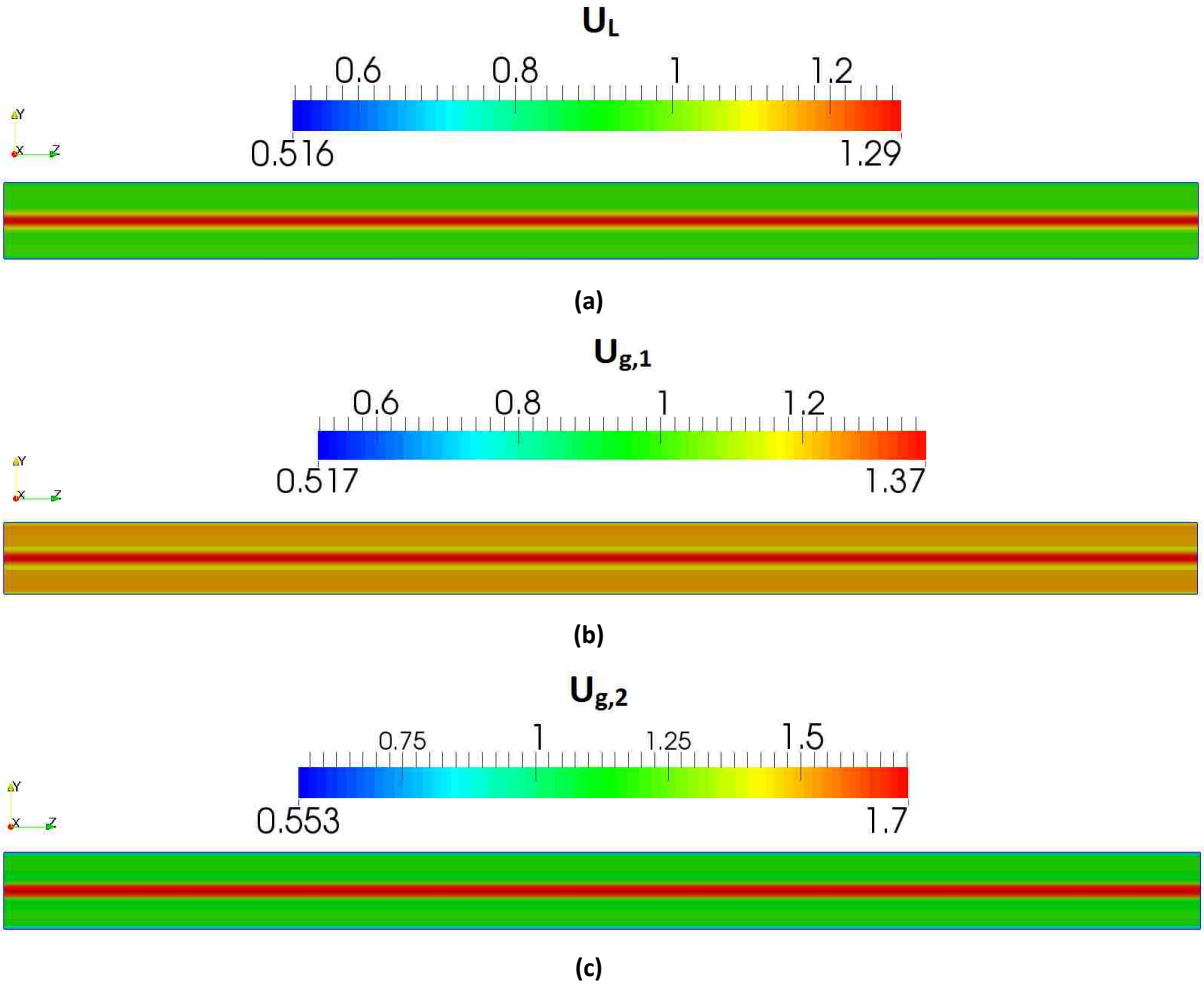

Figure 10.5. Stream-wise velocity distributions for polydispersed two-phase flow between parallel plates with 100 mm spacing (*y* direction is normal to duct walls). The *z*-axis has been scaled shorter for enhanced viewing.

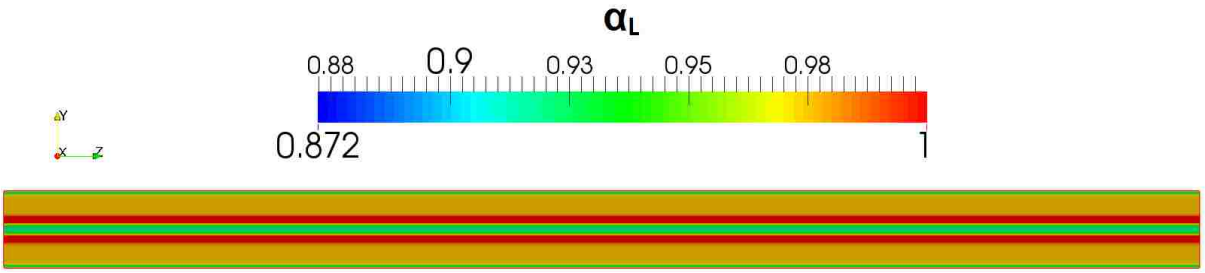

(a)

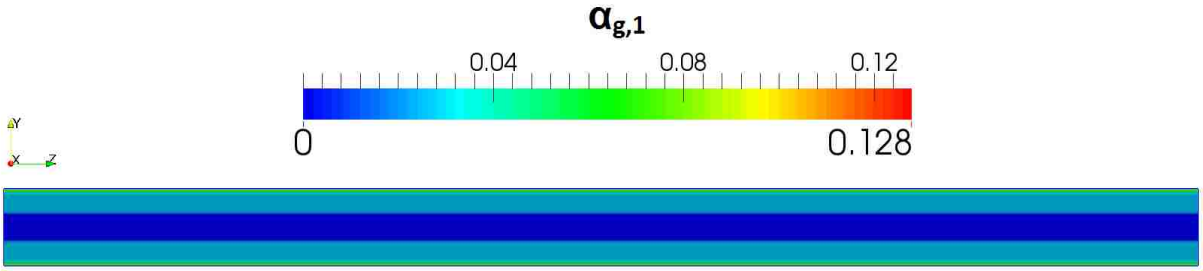

(b)

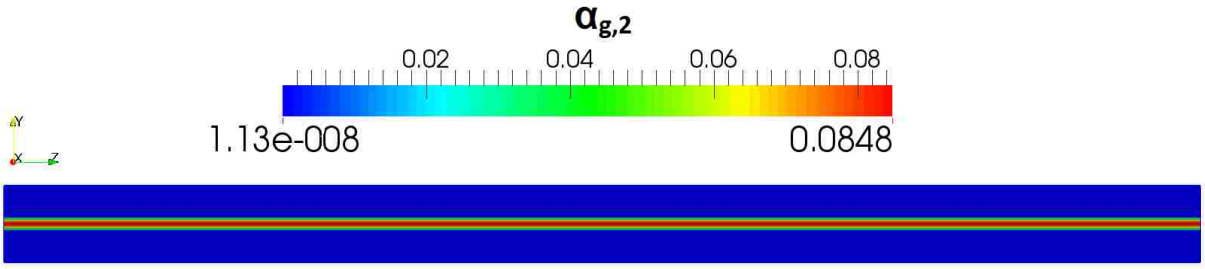

(c)

Figure 10.6. Volume fraction distributions for polydispersed two-phase flow between parallel plates with 100 mm spacing (*y* direction is normal to duct walls). The *z*-axis has been scaled shorter for enhanced viewing.

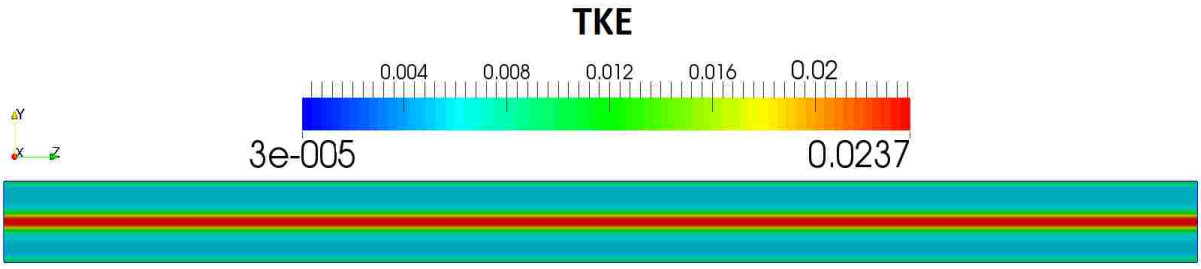

Figure 10.7. TKE distribution for polydispersed two-phase flow between parallel plates with 100 mm spacing (*y* direction is normal to duct walls). The *z*-axis has been scaled shorter for enhanced viewing.

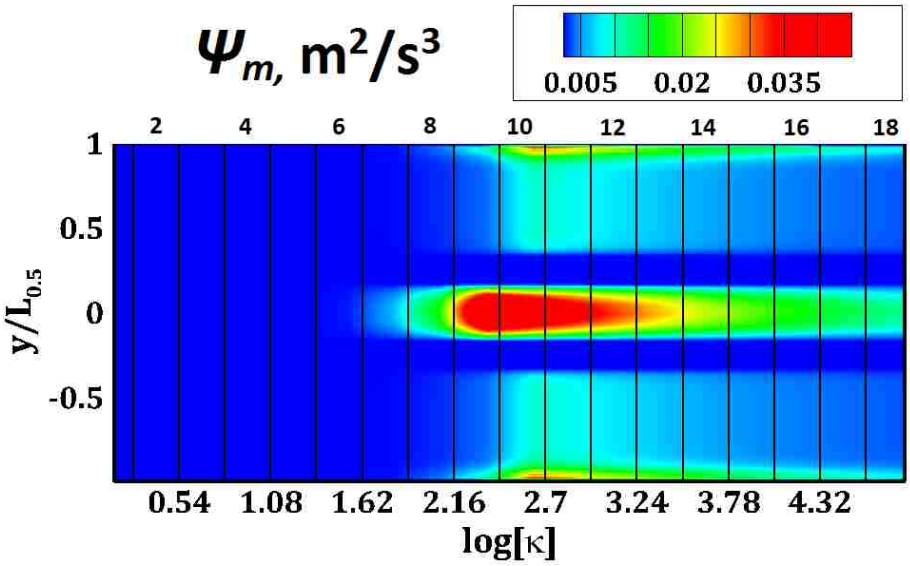

Figure 10.8. Contour levels of the total bin BIT source terms in the spatial and spectral domains in polydispersed two-phase simulation in parallel plate geometry. The vertical lines represent wave number boundaries that are defined along the top of the plot.